

Ca_v1.3 gating modulation by S1475 phosphorylation
and disease-associated *CACNA1D* missense
mutations

Inaugural Dissertation

zur

Erlangung des Doktorgrades
philosophiae doctor (PhD) in Health Sciences
der Medizinischen Fakultät
der Universität zu Köln

vorgelegt von

Sarah Salamon
aus Neuss

Copy-Star Druck, Köln

2023

Betreuer: PD Dr. Jan Matthes

Gutachter / Gutachterin: Prof. Dr. Dirk Isbrandt
Prof. Dr. Tatiana Korotkova
Dr. Matteo Mangoni (extern)

Datum der Mündlichen Prüfung: 08.08.2023

Table of content

List of abbreviations	3
Abstract.....	5
Zusammenfassung.....	6
1. Introduction.....	8
1.1. Voltage-gated calcium channels	8
1.1.1. VGCC structure and function	9
1.2. L-type voltage-gated calcium channels.....	11
1.3. Cav1.3 L-type calcium channel	13
1.3.1. Cav1.3 expression and function in different tissues.....	13
1.4. Modulation of Cav1.3 activity.....	20
1.4.1. Cav1.3 modulation by alternative splicing	20
1.4.2. Cav1.3 modulation by calcium-dependent inactivation	22
1.4.3. Cav1.3 modulation by phosphorylation	25
1.4.4. Role of Cav1.3 modulation	27
1.5. Thesis subject.....	28
1.5.1. Novel disease-associated Cav1.3 missense mutations.....	28
1.5.2. Functional relevance and modulation of phosphorylation site S1475	30
1.6. Aim of the thesis.....	32
2. Methods and Material.....	33
2.1. Molecular biological methods and material	33
2.1.1. Plasmid information.....	33
2.1.2. Investigation of S1475 phosphorylation states via mutation.....	34
2.1.3. Plasmid cloning and mutagenesis	35
2.2. Eukaryotic cell culture and transfection	36
2.2.1. Cultivation of HEK-293 cells.....	36
2.2.2. Transient transfection of VGCCs into HEK-293 cells.....	37
2.3. Electrophysiology	38
2.3.1. Overview of the patch-clamp technique	38
2.3.2. Patch-clamp configurations and principle of data acquisition.....	39
2.3.3. Single-channel patch-clamp recordings.....	41
2.3.4. Whole-cell patch-clamp recordings.....	49
3. Results.....	56
3.1. Cav1.3 gating modulation by disease-associated <i>CACNA1D</i> missense mutations.....	56
3.1.1. L271H missense mutation shifted Cav1.3 single-channel gating towards more hyperpolarized voltages.....	57

3.1.2. A749T missense mutation shifted Cav1.3 single-channel gating towards more hyperpolarized voltages and increased open probability.....	61
3.1.3. F747S missense mutation induced positive cooperative channel-channel gating	64
3.1.4. Structural modelling of L271H, A749T and F747S	71
3.2. Cav1.3 gating modulation by S1475 phosphorylation.....	74
3.2.1. Imitating phosphorylation states differentially modulates Cav1.3 whole-cell currents	74
3.2.2. CaMKII modulates gating kinetics and current densities in dependence of residue at position 1475	76
3.2.3. Single-channel conductance and open probability were modulated by S1475 phosphorylation imitation.....	78
3.2.4. Calmodulin is necessary and sufficient for S1475 modulation of Cav1.3 activity	82
3.2.5. Role of Ca ²⁺ in CaM-dependent S1475 modulation of Cav1.3 activity	85
3.2.6. CaM-dependent reduction of CDI in phosphorylation-mimicking S1475D	90
3.2.7. Decreased Ca ²⁺ -influx through S1475D in response to SAN-like action potentials.....	91
3.2.8. S1475 phosphorylation imitation appears to alter intramolecular interactions	93
4. Discussion.....	96
4.1. Pathophysiological perspective: Disease-associated <i>CACNA1D</i> missense mutations induce gain-of-function through individual gating phenotypes	97
4.1.1. Single-channel data unmask the mechanism underlying changes at whole-cell level.	98
4.1.2. Different disease-associated Cav1.3 mutations differ in clinical phenotype, single-channel gating and intramolecular interactions	102
4.2. Physiological perspective: Phosphorylation site S1475 has functional relevance in human Cav1.3 gating modulation	107
4.2.1. S1475 has functional relevance in human Cav1.3 channels	108
4.2.2. Functional roles of S1475 in human channels compared to S1486 described in rat channels	110
4.2.3. S1475 modulation of Cav1.3 activity in a cellular context.....	112
4.3. Conclusions on the role of Cav1.3 gating modulation.....	115
5. Supplemental material.....	118
References.....	134
Acknowledgements.....	155
Eidesstattliche Erklärung	156

List of abbreviations

A	Ampere
A/D	analog-to-digital
Ala (A)	alanine
AIP	autocamtide-2-inhibitor protein
AP	action potential
apo-CaM	calcium free calmodulin
ASD	autism spectrum disorder
Asp (D)	aspartic acid
ATP	adenosine triphosphate
AUC	area under curve
AVN	atrioventricular node
Ba ²⁺	barium ion
bp	base pair
bpm	beats per minute
BTZ	benzothiazepine
Ca ²⁺	calcium ion
CABPs	Ca ²⁺ -binding proteins
CaM	calmodulin
CaMKII	Ca ²⁺ /calmodulin-dependent protein kinase II
Ca _v	voltage-gated calcium channel
CDI	calcium-dependent inactivation
CREB	cAMP response element-binding protein
Cdk5	cyclin-dependent kinase 5
CI	confidence interval
cm	centimeter
CT	C-terminus
CTM	C-terminal modulatory domain
Da	Dalton
dB	decibel
DCRD	distal C-terminal regulatory domain
DHP	dihydropyridine
DMEM	Dulbecco's modified Eagle's medium
DMSO	dimethyl sulfoxide
DNA	deoxyribonucleic acid
<i>E.coli</i>	<i>Escherichia coli</i>
EDTA	ethylenediaminetetraacetic acid
EGFP/GFP	(enhanced) green fluorescent protein
fA	femto Ampere
f _{active}	fraction of active sweeps
FBS	fetal bovine serum
FRET	Förster/Fluorescence resonance energy transfer
G	giga
g	gramm
Hz	Hertz
HBS	HEPES buffered saline
HEK	human embryonic kidney
HVA	high-voltage activated
I	current
IFG-1	insulin-like growth factor 1
IC ₅₀	half-maximal inhibitory concentration
IHC	inner hair cells
IP ₃	inositol trisphosphate

k	kilo
l	liter
LB	Lysogeny broth
LTCC	L-type calcium channel
LTP	long-term potentiation
LVA	low-voltage activated
m	meter /milli
M	molar / mega
MCT	mean closed time
MFL	mean first latency
min	minutes
MOT	mean open time
ms	millisecond
n	nano
NSCaTE	N-terminal spatial Ca ²⁺ -transforming element
Ω	Ohm
p	pico / statistical probability
P _{open}	open probability
p.	position
PAA	phenylalkylamine
PBS	phosphate buffered saline
PCR	polymerase chain reaction
PCRD	proximal C-terminal regulatory domain
PD	Parkinson's disease
pA/pF	picoampere/picofarad
PKA	protein kinase A
PKC	protein kinase C
PKG	protein kinase G
R	resistance
RFP	red fluorescent protein
rpm	revolutions per minute
RT	room temperature
RTK	receptor tyrosine kinase
s	second
S	Siemens
SAN	sinoatrial node
SEM	standard error of the mean
Ser (S)	serine
TBE	Tris/Borate/EDTA
TIRF	total internal reflection fluorescence
TRIS	tris(hydroxymethyl)aminomethane
τ	time constant tau
μ	micro
V	Volt
V _{0.5act/inact}	voltage of half-maximal (in-) activation
VDI	voltage-dependent inactivation
VGCC	voltage-gated calcium channel
V _{rev}	reversal potential
vs	versus
WT	wildtype

Abstract

Ca²⁺-influx through Cav1.3 voltage-gated calcium channels is indispensable for physiological functions including auditory transduction, hormone secretion, and cardiac and neuronal pacemaking. Accordingly, altered Cav1.3 function can lead to sinoatrial-node-dysfunction, deafness, primary hyperaldosteronism, and neurodevelopmental disorders. Unique electrophysiological properties of Cav1.3 and a complex modulation of its activity suggest that differential (dys-) regulation is crucial for the (patho-) physiological role of Cav1.3. Therefore, this thesis aimed at contributing to the detailed understanding of Cav1.3 gating modulation from a physiological and pathophysiological perspective with a human emphasis. Using single-channel and whole-cell patch-clamp recordings in transiently transfected HEK-293 cells, phosphorylation-state imitating mutations of S1475 were investigated with respect to their role in Cav1.3 modulation. Furthermore, disease-associated Cav1.3 missense mutations L271H, A749T and F747S were electrophysiologically characterized in detail. Each disease-associated mutation displayed gain-of-function characteristics, but with individual gating phenotypes, i.e. leftward-shifted activation (L271H), additional increase of open probability (A749T), or induction of a novel kind of gating cooperativity (F747S), respectively. Differential dysregulation suggests the need for differential modulation as a putative treatment option in mutation-associated disorders. S1475 turned out to be relevant for modulating gating of human Cav1.3. The phosphorylation-mimicking S1475D mutation led to decreased, the phosphorylation-resistant S1475A mutation to increased current density, both mainly due to altered open probability on single-channel level. Notably, it became apparent, that S1475 is crucially involved in CaMKII- and calmodulin-mediated modulation of Cav1.3. Ca²⁺-currents in response to stimuli mimicking sinoatrial-node-like action potentials indicate a putative role of S1475 phosphorylation state for heart-rate regulation. Structural modeling suggests altered intramolecular interaction to be linked to functional changes of both, disease-associated mutations and S1475 phosphorylation state. The findings of this thesis thereby contribute to the understanding of Cav1.3 modulation by resolving underlying molecular mechanisms and by proposing indications for therapeutically targeting Cav1.3 channels. Herein, unravelling the complexity of Cav1.3 gating modulation in a cellular context imposes a challenge, but is a prerequisite to eventually harness this knowledge to specifically modulate the channel in Cav1.3-associated diseases.

Zusammenfassung

Calcium-Einstrom durch spannungsgesteuerte Cav1.3 Calcium Kanäle initiiert unter anderem physiologische Funktionen wie Hormonsekretion, auditorische Transduktion, kardiale Schrittmacherpotentiale und moduliert neuronale Aktivität. Dementsprechend kann eine veränderte Cav1.3 Funktion zu Erkrankungen wie Taubheit, Bradykardie, primärem Hyperaldosteronismus sowie neuronalen Entwicklungsstörungen führen. Spezifische elektrophysiologische Eigenschaften des Cav1.3 Kanals und die komplexe Modulation dessen Aktivität lassen vermuten, dass eine differenzierte (Dys-)Regulation für die (patho-) physiologische Funktion des Kanals entscheidend ist. Ziel dieser Arbeit war es daher, einen Beitrag zum detaillierten Verständnis der Modulation des humanen Cav1.3-Schaltverhaltens aus physiologischer und pathophysiologischer Sicht zu leisten. Mit Hilfe von Einzelkanal- und Ganzzell-Patch-Clamp-Aufnahmen in transient transfizierten HEK-293 Zellen wurde die Rolle phosphorylierungs-imitierender S1475 Mutationen auf das Cav1.3-Schaltverhalten untersucht. Darüber hinaus wurden die krankheitsassoziierten Cav1.3-Missense-Mutationen L271H, A749T und F747S elektrophysiologisch detailliert charakterisiert. Alle drei krankheitsassoziierten Mutationen erhöhten die Einzelkanal Aktivität („gain-of-function“), jedoch mit individuellem Phänotyp hinsichtlich des Schaltverhaltens, d. h. eine links-verschobene Aktivierung (L271H), zusätzlich eine erhöhte Offenwahrscheinlichkeit (A749T), bzw. Induktion einer neuartigen Kanal-Kooperativität (F747S). Die unterschiedliche Dysregulation legt die Notwendigkeit einer differenzierten Modulation als mögliche Behandlungsoption bei mutationsassoziierten Störungen nahe. Hinsichtlich der Phosphorylierungsstelle S1475, stellte sich heraus, dass diese für die Modulation des humanen Cav1.3-Schaltverhaltens relevant ist. Die phosphorylierungs-imitierende S1475D Mutation führte zur einer Verringerung, die phosphorylierungs-resistente S1475A Mutation zu einer Erhöhung der Stromdichte, beides hauptsächlich aufgrund veränderter Offenwahrscheinlichkeit auf Einzelkanal-Ebene. Insbesondere wurde deutlich, dass S1475 entscheidend an der CaMKII- und Calmodulin-vermittelten Modulation des Cav1.3 beteiligt ist. Veränderter Calcium-Einstrom als Reaktion auf Stimuli, die Sinusknoten-Aktionspotentiale imitieren, deuten auf eine mögliche Rolle des S1475 Phosphorylierungsstatus in der Regulation der Herzfrequenz hin. Strukturelle Modellierung deutet darauf hin, dass veränderte intramolekulare Interaktionen mit funktionellen Veränderungen sowohl der krankheitsassoziierten Mutationen, als auch des S1475-Phosphorylierungszustands einhergehen.

Die Ergebnisse dieser Arbeit tragen somit zum Verständnis der Modulation des Cav1.3-Schaltverhaltens bei, indem sie die zugrunde liegenden molekularen Mechanismen aufklären und Anhaltspunkte für zu entwickelnde therapeutische Einflussnahme auf den Kanal liefern. Die Komplexität dieser Modulation im zellulären Kontext zu entschlüsseln, stellt zwar eine Herausforderung dar, ist aber Voraussetzung, um dieses Wissen für die gezielte Kanal-Modulation in Cav1.3-assoziierten Krankheiten nutzen zu können.

1. Introduction

Calcium influx into mammalian cells initiates various physiological responses including gene expression (Finkbeiner & Greenberg, 1998) hormone release (Ashcroft et al., 1994), cell differentiation (Schulla et al., 2003), excitation-contraction coupling (Reuter, 1967), cardiac functions and neuronal signaling (Bean, 1989). The calcium homeostasis is therefore tightly regulated. Ca²⁺-influx through voltage-gated calcium channels (VGCCs) is essential for these physiological responses and is based on electrical membrane excitation. The indispensable tissue-specific adaption of calcium signaling is achieved by different channel types. Each calcium channel type can be modified e.g. by posttranslational modification. This allows fine-tuning of the calcium signal for specific cellular needs. Accordingly, understanding signaling through VGCCs is essential to understand physiological functions and pathophysiological alterations resulting from altered Ca²⁺-influx through VGCCs.

1.1. Voltage-gated calcium channels

Voltage-gated calcium channels were first identified after discovering that ions besides sodium contribute to the electrical properties of the crustacean muscle (Fatt & Katz, 1953). Revealing their importance in cell-signaling, VGCCs were subsequently found to be distributed in all types of excitable cells (Catterall, 2011).

VGCCs are classified into high-voltage activated (HVA) and low-voltage activated (LVA) channels, depending on their activation threshold (Carbone & Lux, 1984; Catterall, 2011). VGCCs are further subgrouped based on electrophysiological and pharmacological characteristics of the pore forming α_1 -subunit. HVA channels are grouped into L-type (Cav1.1 – Cav1.4) (Birnbaumer et al., 1994), P/Q-type (Cav2.1) (Dubel et al., 1992; Randall & Tsien, 1995), N-type (Cav2.2) (Llinas et al., 1989; Mori et al., 1991) and E/R-type (Cav2.3) (Schneider et al., 1994; Williams et al., 1994) channels. LVA channels consist of so-called T-type VGCCs (Cav3.1 – Cav3.3) (Llinas & Yarom, 1981; Perez-Reyes, 2003). With a few exceptions, most VGCC types are expressed in various tissues and contribute to various physiological functions (Catterall, 2011; Hofmann et al., 1999) (Fig. 1).

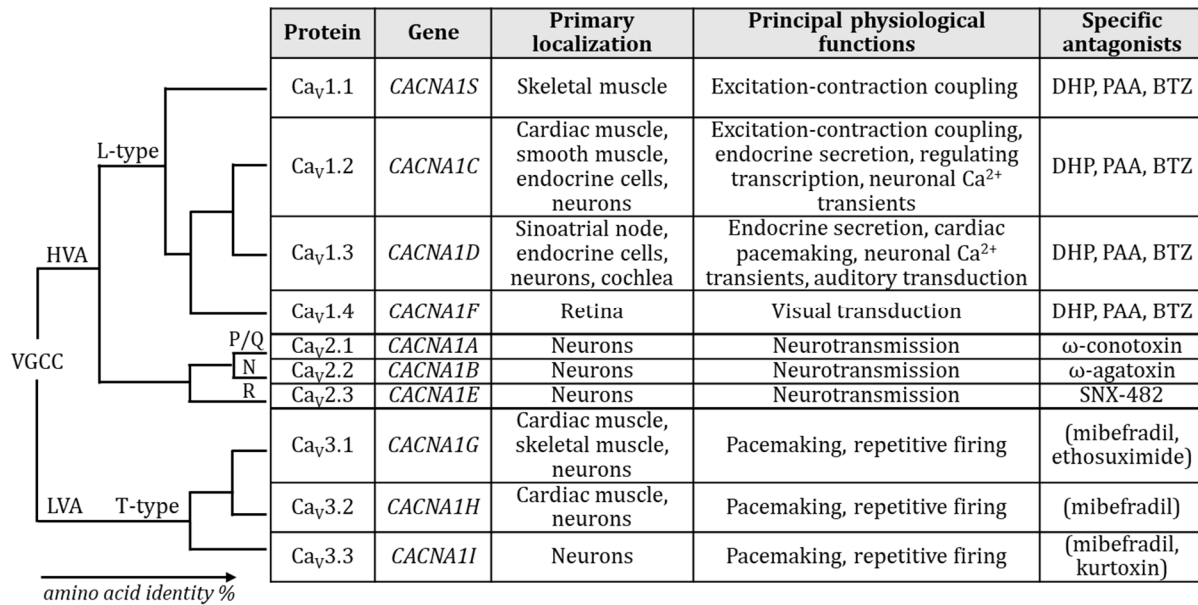


Figure 1. Overview of VGCC classes and types. VGCC classes and their subtypes are arranged in genealogy with increasing amino acid identity, providing information on primary tissue expression and corresponding physiological functions and specific antagonists mibefradil, ethosuximide and kurtoxin inhibit T-type channels, but not exclusively. DHP = dihydropyridine, PAA = phenylalkylamine, BTZ = benzothiazepine, SNX-482 = toxin of tarantula *Hysteroocrates gigas*. Modified according to Birnbaumer et al., 1994; Catterall et al., 2005; Ertel et al., 2000; Hille, 2001; Koh et al., 2021.

1.1.1. VGCC structure and function

VGCCs are hetero-multimeric, transmembrane protein complexes (Fig. 2). Besides the pore-forming α_1 -subunit, there are auxiliary β -, $\alpha_2\delta$ - and γ -subunits (Catterall, 2022). While LVA channels do not assemble auxiliary subunits, HVA channels usually pair with one β - and one $\alpha_2\delta$ - subunit. The γ -subunit is mainly expressed in skeletal muscle HVA channels (Tanabe et al., 1987; Flucher & Beam, 2022).

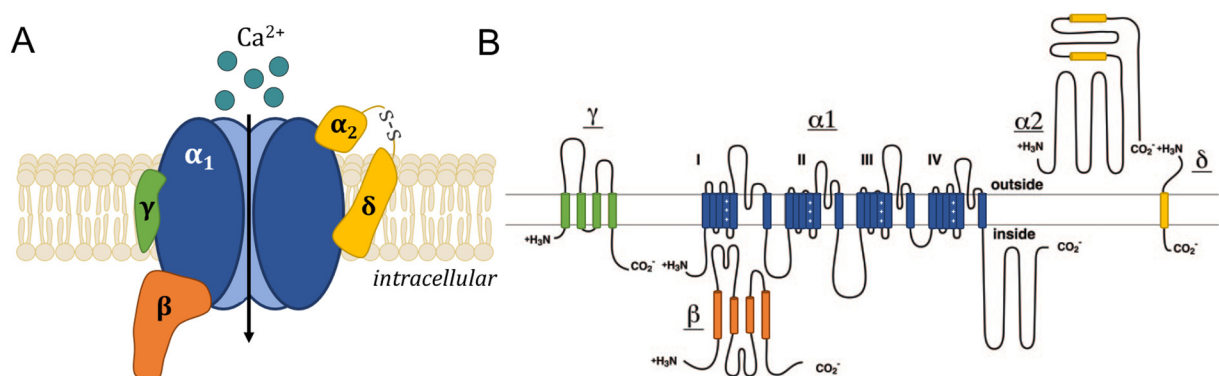


Figure 2. Schematic composition of a VGCC complex. (A) Schematic organization of the pore-forming α_1 -subunit and all known auxiliary subunits. (B) Schematic 2D color-matched subunit structure (modified according to Catterall et al., 2005).

Pore-forming α_1 -subunit

The pore-forming α_1 -subunit defines the majority of channel properties. It is encoded by ten different *CACNA1* genes. The α_1 -subunit is composed of four cylindrically arranged repetitive homologous domains (I-IV). Each domain contains six α -helical transmembrane segments (S1-S6) (Tanabe et al., 1987). Each segment S4 contains an arrangement of positively charged amino acid residues. These form the voltage sensor and initiate a conformational change upon depolarization (Garcia et al., 1997). The extracellular loops connecting segments S5 and S6 contain negatively charged amino acid residues and form the selectivity filter (Ellinor et al., 1995; Yang et al., 1993). The intracellular N-terminus, the inter-domain regions and the C-terminus are important signaling sites (Catterall, 2000).

Auxiliary subunits

Auxiliary subunits bind to the α_1 -subunit and modulate membrane expression, channel trafficking, and biophysical gating properties (Catterall, 2022).

β -subunits are encoded by four *CACNB* genes (*CACNB1-4*). Alternative splicing results in multiple β -subunit variants, which differentially modulate HVA channels (Dolphin, 2003). The β -subunit is composed of five distinct domains (D1-D5) and binds to the α_1 -subunit at the cytosolic loop between domains I and II at a conserved consensus motif called α -interaction domain (AID) (Buraei & Yang, 2010; Pragnell et al., 1994; Van Petegem et al., 2004). The β -subunit modulates the biophysical gating properties of the pore-forming subunit and the trafficking of the pore from the endoplasmic reticulum to the (surface-) membrane (Birnbaumer et al., 1998; Neely et al., 1993). Furthermore, the β -subunit is involved in the regulation of transcription and interacts with RGK proteins, which also influence the modulation of channel activity and trafficking (Buraei & Yang, 2010).

The $\alpha_2\delta$ -subunit is encoded by three *CACNA2D* genes (*CACNA2D1-3*). The protein is post translationally cleaved into an α_2 - and δ -part, linked by a disulfide bond (Brickley et al., 1995; Ellis et al., 1988). The α_2 -part binds extracellularly to the α_1 -subunit, while the δ -part has a transmembrane location. The $\alpha_2\delta$ -subunit increases channel expression and modulates activation and inactivation kinetics and thereby alters the current amplitude (Bourdin et al., 2010; Dolphin, 2013, 2016; Felix et al., 1997; Shistik et al., 1995). Additionally, it binds the anticonvulsant drug gabapentin (Dolphin, 2012).

The γ -subunit is encoded by eight *CACNG* genes (*CACNG1–8*), while only two protein variants are known. It is primarily located at VGCCs in the skeletal muscle, but occasionally also in neuronal calcium channel complexes (Tanabe et al., 1987; Van Petegem et al., 2004). The γ -subunit is composed of four transmembrane domains. Functionally, the γ -subunit downregulates channel activity (Kang & Campbell, 2003).

1.2. L-type voltage-gated calcium channels

Cav1.1, *Cav1.2*, *Cav1.3* and *Cav1.4* form the group of L-type calcium channels (LTCCs) (Hess et al., 1984). The name is based on their long-lasting activity upon depolarization, due to small scale voltage-dependent inactivation (VDI). LTCCs are expressed in various tissues. *Cav1.1* is expressed in the skeletal muscle, where it mediates excitation-contraction coupling (Rios et al., 1992; Seitter & Koschak, 2018; Tanabe et al., 1987). *Cav1.2* is primarily expressed in cardiac and smooth muscle, endocrine cells and neurons, where it mediates cardiac excitation-contraction coupling, endocrine secretion, transcription and neuronal Ca^{2+} -transients (Striessnig, 1999). *Cav1.3* is primarily expressed in the sinoatrial node (SAN), endocrine cells, neurons and inner hair cells of the cochlea (Huang et al., 2022; Mangoni et al., 2003; Matthes et al., 2004; Takimoto et al., 1997). *Cav1.4* is expressed in the retina, where it mediates visual transduction (Strom et al., 1998).

Pathological LTCC activity causes various diseases, including hypokalemic periodic paralysis (*Cav1.1*) (Morrill & Cannon, 1999), Timothy Syndrome (*Cav1.2*) (Splawski et al., 2004), congenital deafness (*Cav1.3*) (Baig et al., 2011; Platzer et al., 2000) and stationary night blindness (*Cav1.4*) (Strom et al., 1998). Altered LTCC function also contributes to the pathophysiology of cardiovascular, neurodegenerative, and neurodevelopmental diseases, including autism spectrum disorder (Breitenkamp et al., 2014; Breitenkamp et al., 2015; Despang et al., 2020; Despang et al., 2022; Striessnig et al., 2004; Striessnig et al., 2010).

LTCCs are sensitive to the therapeutically used Ca^{2+} channel antagonists, chemically defined as phenylalkylamines (PAA), benzothiazepines (BTZ), and dihydropyridines (DHP) (Fleckenstein, 1983; Hess et al., 1984). LTCC agonists include, among other compounds, S-BayK 8644, a structural analog of a DHP with positive inotropic activity (Lauven et al., 1999; Thomas et al., 1985).

While *Cav1.1* and *Cav1.4* are expressed in distinct tissues with individual functions, *Cav1.2* and its closest relative, *Cav1.3*, co-localize in various tissues and contribute to similar physiological responses (Catterall et al., 2005). Nevertheless, both channel types

contribute to these responses at different states. For example, the cardiac Cav1.3 contributes to SAN action potentials, which then excite the myocardium, in which Cav1.2 contributes to the ventricular action potential and is essential for contraction-coupling (Marx, 2018). This specificity is achieved by distinct electrophysiological properties of Cav1.2 and Cav1.3. Compared to Cav1.2, Cav1.3 activates at more hyperpolarized voltages, for which reason Cav1.3 is also described as intermediate-voltage-activated (Koschak et al., 2001; Xu & Lipscombe, 2001) (Fig. 3A). Therefore, Cav1.3 can contribute to pacemaking and mediate sub-threshold activity. Given their different physiological properties and functions, both Cav1.2 and Cav1.3 contribute to different pathophysiological mechanisms in different diseases. LTCC antagonists can be therapeutically used in cardiovascular diseases, i.e. verapamil and DHPs like amlodipine. While these drugs differ in their affinity to cardiac and vascular LTCCs based on resting membrane potential and splice variants (Wirtz & Herzig, 2004), they are not specific for any LTCC subtype. Although the DHP affinity differs among channel subtypes, e.g. the IC_{50} of nimodipine is twenty-fold larger for Cav1.3 than for Cav1.2 (Xu & Lipscombe, 2001) (Fig. 3B), no specific inhibitor of Cav1.2 or Cav1.3 has been discovered yet. To be able to distinguish between Cav1.2- and Cav1.3-mediated effects in research, scientists created DHP-insensitive variants of both channel types (Martinez-Rivera et al., 2023; Toyoda et al., 2017; Zhang et al., 2005). Nevertheless, to find a specific inhibitor, distinguishing features between Cav1.2 and Cav1.3 need to be investigated further.

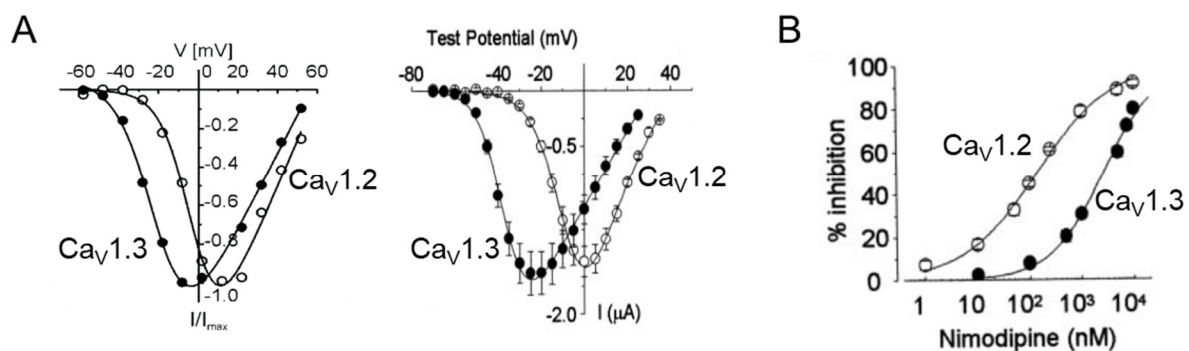


Figure 3. Comparison of Cav1.2 and Cav1.3 LTCCs. (A) Cav1.3 channels activate at more hyperpolarized voltages, as the left-shifted IV-curves of two independent studies show (*right*: Koschak et al., 2001, *middle*: Xu and Lipscombe, 2001). Full symbols: Cav1.3 and open symbols: Cav1.2. **(B)** Cav1.3 has lower affinity for nimodipine than Cav1.2 (Xu and Lipscombe, 2001).

1.3. Cav1.3 L-type calcium channel

This thesis focuses on Cav1.3 LTCCs. Cav1.3 was first identified in neurons in 1992 (Yaney et al., 1992). Cav1.3 is encoded by the *CACNA1D* gene, with a full-length protein of 2138 amino acids and a molecular weight of ~250 kDa. Since its discovery, Cav1.3 was found to be expressed in cell types beyond neurons (Avery & Johnston, 1996; Hell et al., 1993), including endocrine β -pancreatic and adrenal cells (Chik et al., 1997; Garcia-Palomero et al., 2001), sensory cochlea cells (Michna et al., 2003), SAN and smooth muscle cells (Mangoni et al., 2003; Takimoto et al., 1997), as well as kidney and ovary cells (Moosmang, 2009). Cav1.3's unique electrophysiological properties, foremost its activation at lower voltages, were first described in 2001, 10 years after its discovery (Koschak et al., 2001; Xu & Lipscombe, 2001). This electrophysiological characteristic enables Cav1.3 to substantially contribute to the initiation of cardiac and neuronal pacemaking, hormone release and autonomous activity in different tissues (Helton et al., 2005; Olson et al., 2005; Putzier et al., 2009).

1.3.1. Cav1.3 expression and function in different tissues

Cav1.3 in endocrine cells

Cav1.3 channels are expressed in various endocrine cells, including pineal, pituitary, β -pancreatic Langerhans, adrenal cortex and chromaffin cells (Zamponi et al., 2015). In cooperation with Cav1.2 they orchestrate hormone release (Catterall et al., 2005). While in β -pancreatic cells Cav1.3 mRNA levels are ~10-fold higher than Cav1.2 mRNA levels (Braun et al., 2008; Yang et al., 2015), the role of functional Cav1.3 channels in β -pancreatic cells has not yet been fully understood. It was reported that Cav1.2 knock-out mice have impaired insulin release (Schulla et al., 2003), while in Cav1.3 knock-out mice insulin secretion persisted, likely due to a compensatory upregulation of Cav1.2 channels (Namkung et al., 2001). At the same time, however, Cav1.3 knock-out mice were glucose intolerant and had hypo-insulinemia (Namkung et al., 2001). Both LTCCs are also thought to have a role in Ca^{2+} -mediated β -cells apoptosis (Yang et al., 2015).

More studies were conducted on the role of Cav1.3 in adrenal tissue. Cav1.3 contributes to cellular excitability, initiating catecholamine and aldosterone secretion (Felizola et al., 2014; Vandael et al., 2013). Due to its low activation threshold, Cav1.3 mediates the pacemaker current in chromaffin cells. Ca^{2+} -influx through Cav1.3 initiates K^{+} -efflux through large and small conductance Ca^{2+} -activated potassium channels, which depolarizes the membrane and subsequently activates Cav1.2 channels, leading to

catecholamine secretion. Thereby, Cav1.3 contributes to shaping adrenal action potentials (Comunanza et al., 2010; Vandael et al., 2013). Cav1.3 dysfunction can lead to primary hyperaldosteronism and with > 60 identified somatic *CACNA1D* missense-mutations, it is a risk gene in development of aldosterone-producing adenomas (Ortner et al., 2020; Tan et al., 2017).

Cav1.3 in inner hair cells

Cav1.3 is the most common VGCC in sensory cells of the cochlea, namely inner hair cells (IHC). Sound induces tilting of the stereocilia bundles through movement of the cochlear endolymph fluid, which is conveyed by mechano-transduction through K⁺-efflux into IHCs. This depolarizes the membrane potential, which opens Cav1.3 channels, resulting in Ca²⁺-influx triggering glutamate release. Thereby, the signal is transmitted to the auditory cortex in the temporal lobe via the auditory nerve (Brandt et al., 2003; Dou et al., 2004; Michna et al., 2003).

As > 90 % of the Ca²⁺-influx in adult and immature IHCs is mediated through Cav1.3, loss of Cav1.3 leads to deafness (Engel et al., 2002). Cav1.3 global and cochlea-specific knock-out mice are deaf (Eckrich et al., 2018; Platzer et al., 2000). Additionally, in Pakistani families with sinoatrial node dysfunction and deafness (SANDD-syndrome), a homozygous 3-bp insertion of glycine in *CACNA1D* was identified (p.403_404insGly), which led to loss of Cav1.3 function and deafness in affected individuals (Baig et al., 2011).

Cav1.3 in the heart

Cav1.3 and Cav1.2 are both expressed in the heart with different tissue distribution. In prenatal cardiac tissue, Cav1.3 is the primarily expressed LTCC. In adult hearts, however, Cav1.2 is the predominant LTCC in the ventricles, while Cav1.3 expression is restricted to the sinoatrial- and atrioventricular-node (SAN and AVN) (Mangoni et al., 2003; Marx, 2018; Platzer et al., 2000; Takimoto et al., 1997; Zhang et al., 2002).

Within the sinoatrial node, Cav1.3 carries the depolarization of the SAN action potential (SAN-AP). Thereby, Cav1.3 contributes to cardiac pacemaking, as autonomous SAN activity mediates heart beat and rhythm (Marx, 2018). The SAN-AP is initiated by Na⁺- and T-type Ca²⁺-influx in the early depolarization phase, followed by Ca²⁺-influx through Cav1.3 to the peak. The repolarization is carried by K⁺-efflux, which is in the end counteracted by Na⁺-influx. The SAN depolarization spreads through the atria to the AVN, where the excitation is delayed to allow atrial contraction to completely fill the ventricles

with blood. The excitation then spreads through the bundle of His, along the bundle branches towards the apex and along the Purkinje fibers. This causes ventricular contraction mediated by Cav1.2 in the T-tubule and sarcoplasmic ryanodine receptors, namely cardiac excitation-contraction coupling (Bers, 2002) (Fig. 4).

Loss of Cav1.3 current in the heart leads to a pathophysiological reduction in heart rate, called bradycardia. Cav1.3 knock-out mice show severe bradycardia with a ~35 % reduction of heart rate, while contractility is intact. Further, Cav1.3 knock-out mice show disrupted atrioventricular conduction with supraventricular and ventricular extrasystoles (Matthes et al., 2004). This phenotype originates in the lack of Ca²⁺-influx through Cav1.3, which reduces SAN-AP frequency and causes spontaneous SAN arrhythmia (Mangoni et al., 2003). As the SANDD-syndrome shows, a similar pathophysiological phenotype is observed in human loss of Cav1.3 function. Individuals carrying p.403_404 glycine insertion had resting bradycardia and increased heart rate variability. The detected abnormalities in the electrocardiogram also suggest disturbed atrioventricular conduction (Baig et al., 2011).

In human coronary heart disease, LTCCs are therapeutically targeted with mentioned antagonists, e.g. DHP amlodipine, PAA verapamil and BZT diltiazem (Garcia-Donaire, 2008).

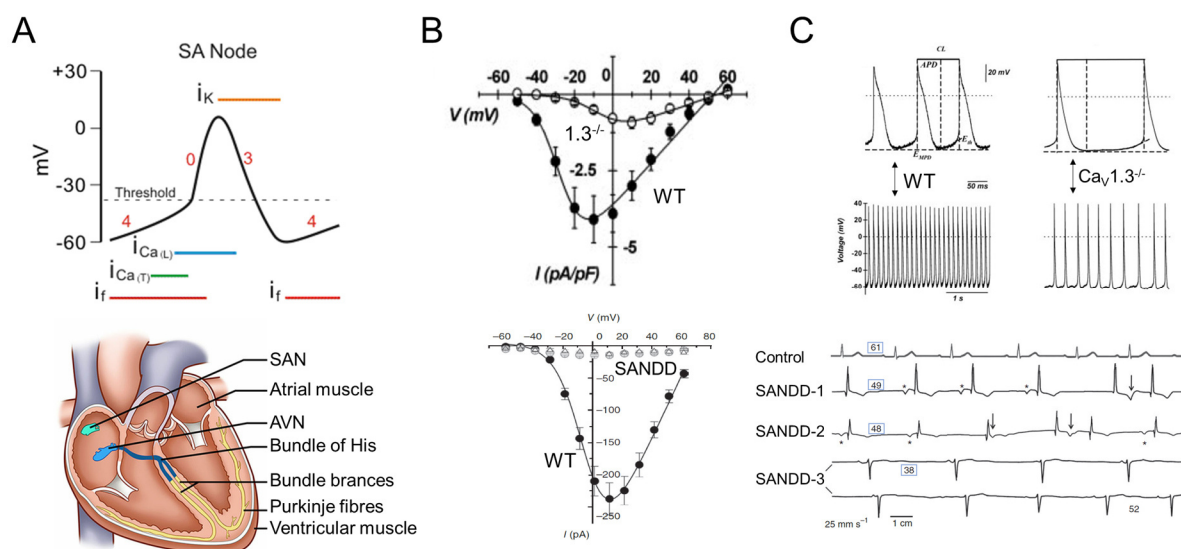


Figure 4. Cav1.3 function in the sinoatrial node. (A) Top: Schematic SAN-AP with corresponding current flow (Klabunde, 2016). **Bottom:** Anatomical structures involved in heart excitation (Labser, 2018). **(B)** Reduced Ca_v1.3 currents in Ca_v1.3 knock-out mice (Ca_v1.3^{-/-}) and SANDD patients. **(C)** Reduced SAN frequency in Ca_v1.3^{-/-} mice and electrocardiogram alterations in SANDD patients, numbers in squares indicate resting heart rate. (Data Ca_v1.3^{-/-} mice: Mangoni et al., 2003, data SANDD: Baig et al., 2011.)

Cav1.3 in neurons

Cav1.3 makes up for ~10 % of neuronal LTCCs, while ~90 % are Cav1.2 channels. Both types overlay in their neuronal expression, but have different functions based on the distinct electrophysiological properties (Koh et al., 2021).

Cav1.3 channels are expressed throughout the brain (Moreno et al., 2016; Tan et al., 2001). On the sub-cellular level Cav1.3 channels localize in two populations: Predominantly somatodendritic, at cell bodies and proximal dendrites (Catterall et al., 2005; Hell et al., 1993), and at distal synapses (Obermair et al., 2004). Surface expression of Cav1.3 co-localizes with synaptic scaffolding proteins, foremost shank-1B or densin-180 (Stanika et al., 2016). In contrast to the rather punctual expression of Cav1.2, Cav1.3 is expressed area-covering (Koh et al., 2021). Neuronal tissue beholds the largest diversity of Cav1.3 splice variants. These splice variants differ among mammalian species, especially between *Homo sapiens* and *Rattus norvegicus* (Koh et al., 2021; Tan et al., 2011). Most splice variants have individual electrophysiological properties, thereby contributing to distinct neuronal functions. For example, the shortest human C-terminal Cav1.3 splice variant can arrange in channel clusters and gate cooperatively to augment neuronal excitability by sustained firing in motoneurons (Binder et al., 2020; Dixon et al., 2022).

The function of Cav1.3 in neurons is as diverse as its expression implies. In dopaminergic neurons, Ca²⁺-influx through Cav1.3 shapes repetitive firing, modulates resting membrane potentials and amplifies synaptic currents (Guzman et al., 2009; Moreno et al., 2016; Olson et al., 2005; Striessnig et al., 2006). Especially in the substantia nigra, Cav1.3 shapes neuronal firing by controlling spike width and firing patterns (Chan et al., 2007; Guzman et al., 2009; Koh et al., 2021; Ortner et al., 2017). Hereto, for example, Ca²⁺-influx through Cav1.3 can inhibit dopaminergic D2 receptor endocytosis through neuronal-calcium-sensor-1 (Dragicevic et al., 2014; Koh et al., 2021). Further, LTCC inhibition can reduce cytosolic dopamine concentrations in the substantia nigra (Koh et al., 2021; Mosharov et al., 2009). Given these Cav1.3 functions in dopaminergic neurons of the substantia nigra, it is not surprising, that Cav1.3 is involved in the pathophysiology of neurodegenerative diseases, including Parkinson's disease (PD) (Surmeier et al., 2010). Herein, the dysregulation of Ca²⁺-homeostasis seems to be crucial. Cav1.2 and Cav1.3 expression was found to be upregulated in a drug-induced model of PD (Wang et al., 2017). Interestingly, inhibiting Cav1.3 currents in *in vivo* and *in vitro* PD models, altered the form of pacemaking and prevented neuronal loss in these models (Chan et al., 2007; Moosmang, 2009).

Following these promising findings, the LTCC antagonist isradipine was tested in treatment of early-stage PD patients in a clinical trial. However, isradipine did not delay PD progression (Parkinson Study Group, 2020). Notably, the trial was conducted with immediate-release isradipine, while the sustained-release form might have been more promising or suitable regarding pharmacokinetic characteristics, especially elimination half-life (Johnson et al., 2005; Nagasamy Venkatesh et al., 2021).

In addition to functions in dopaminergic neurons, Cav1.3 has distinct tasks in learning, memory and reward by influencing synaptic plasticity and long-term potentiation. Cav1.3 is required for memory consolidation in fear learning and activates pathways required for cocaine-conditioned place preference in the ventral tegmental area (Martinez-Rivera et al., 2023; McKinney et al., 2009). In the hippocampus, Cav1.3 modulates gene expression, mediates neurogenesis and dendritic spine elongation, as well as modest synaptic stimuli and constitutes evoked spike activity (Avery & Johnston, 1996; Liljelund et al., 2000). Dysregulated Ca²⁺-influx through Cav1.3 is also involved in the pathophysiology of aging-related diseases, like Alzheimer's disease. Cav1.3 surface expression and thereby Ca²⁺-influx increases in the hippocampus with age, while neuronal excitability weakens (Hurley et al., 2013; Koh et al., 2021; Sahu et al., 2017). Herein, the interaction of amyloid-precursor-protein with the calcium-channel-auxillary- β_3 -subunit mediates A β -increased functional LTCC expression (Kim & Rhim, 2011). Furthermore, Cav1.3 has physiological functions in neuronal development. Ca²⁺-influx through Cav1.3 initiates and stabilizes dendritic outgrowth but then also mediates synaptic pruning and refinement, e.g. by controlling inhibitory input in the auditory pathway (Hirtz et al., 2012; Hung et al., 2008; Sala et al., 2001; Stanika et al., 2015). Further, Cav1.3 also modulates dendritic spine morphology (Stanika et al., 2016).

In fact, neuronal development seems to be crucially susceptible to altered Cav1.3 activity. All ten reported high-risk disease-causing germline *de novo* CACNA1D missense-mutations are associated with neurodevelopmental delay, paired with endocrine symptoms, seizures and/or autism spectrum disorder (ASD). Eight of these ten variants have been functionally characterized on whole-cell level (Ortner et al., 2020; Pinggera et al., 2017; Pinggera et al., 2018). Contrary to the mentioned p.403_404insGly in SANDD-syndrome, the high-risk disease-causing germline *de novo* CACNA1D missense-mutations induce gain-of-function (Pinggera et al., 2015; Striessnig et al., 2022). Gating changes on whole-cell level, induced by somatic and germline CACNA1D missense variants, are

classified into four types of typical gating changes (Striessnig, 2021): Type 1 gating changes are characterized by a significant inactivation-deficiency, in some cases accompanied by a shift of voltage-dependent activation towards more negative voltages (Fig. 5A). Type 2 gating changes are characterized a pronounced shift in voltage-dependent activation towards more negative voltages, which in some cases is also seen for the voltage-dependent inactivation. Additionally, type 2 gating changes can include an altered inactivation (Fig. 5B). Type 3 gating changes include a slowed and partially incomplete inactivation. Type 4 gating changes are displayed by mutations in the voltage-sensor, which induce different degrees of voltage-sensor movements, thereby promoting the transition probability into the open or inactivated state (Pinggera et al., 2018; Striessnig, 2021). Type 1-3 gating changes have been reported in pathogenic *CACNA1D* variants, while type 4 gating changes have only been observed in non-pathogenic variants. The majority of functionally characterized high-risk disease-causing germline *de novo* *CACNA1D* missense-mutations induces type 2 gating changes, while G403D and G407R induce type 1 gating changes. This classification, however, does not allow conclusions on the combination of exhibited symptoms (Ortner et al., 2020) (Tab. 1).

Table 1. Reported high-risk disease-causing germline *de novo* *CACNA1D* missense-mutations. Missense variants are listed sequentially, providing information on gender, symptoms (ND: Neurodevelopmental delay, ASD: Autism spectrum disorder, S: Seizures, ES: Endocrine symptoms), type of gating change and reference.

Variant	Sex	Symptoms				Gating change	Reference
		ND	ASD	S	ES		
V259A	m	+	-	+	+	Type 2	Semenova et al., 2018
L271H	f	+	-	-	+	<i>unknown</i>	De Mingo Alemany et al., 2020
V401L	m	+	+	+	-	Type 2	Pinggera et al., 2017
G403D	f	+	+	+	+	Type 1	Scholl et al., 2013
G407R	m	+	+	-	-	Type 1	Pinggera et al., 2015
S652L	m	+	+	-	-	Type 2	Hofer et al., 2020
F747S	m	+	-	-	+	Type 2	Török et al., 2022
A749G	f	+	+	-	-	Type 2	Pinggera et al., 2018
A749T	f	+	+	-	-	<i>unknown</i>	Ortner et al., 2020
I750M	f	+	-	+	+	Type 2	Scholl et al., 2013

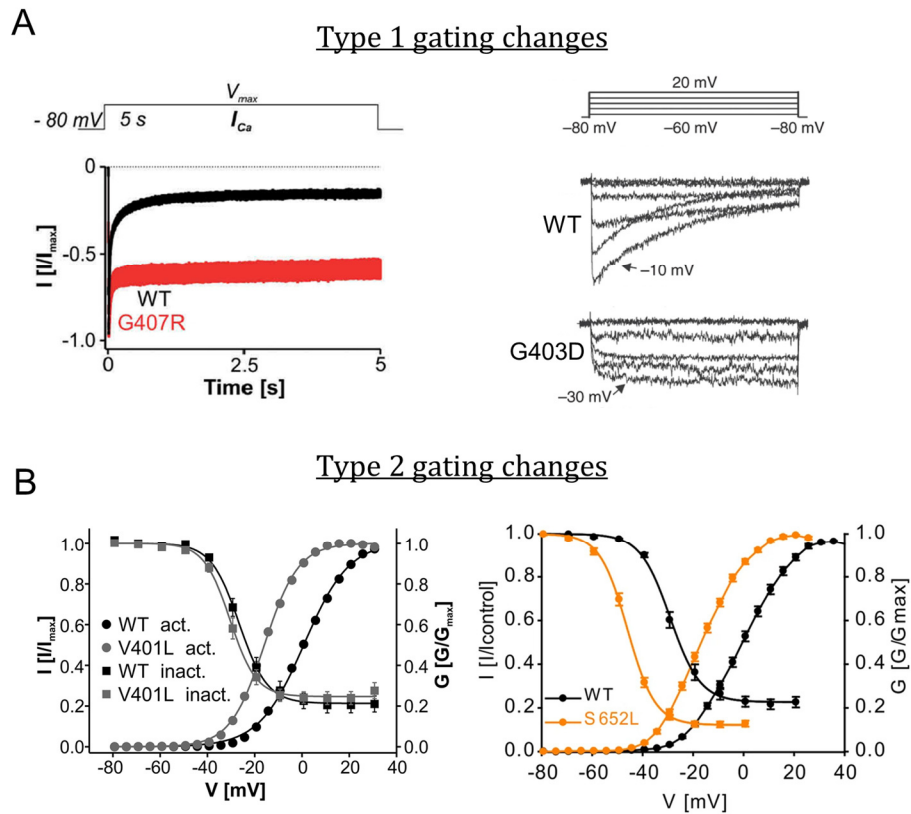


Figure 5. Type 1 and 2 gating changes induced by neurodevelopmental disorder associated *CACNA1D* missense mutations. (A) Type 1 gating changes for G403D (Scholl et al., 2013) and G407R (Pinggera et al., 2018). Both show inactivation-deficiency and G403D also voltage-dependence of activation shifted to more negative voltages. (B) Type 2 gating changes for V401L (Pinggera et al., 2017) and S652L (Hofer et al., 2020). Both show pronounced shifts in voltage-dependent activation towards more negative voltages, for S652L this also seen for voltage-dependent inactivation.

1.4. Modulation of Cav1.3 activity

To fulfill the various tissue-specific needs, Cav1.3 activity is modulated by different mechanisms. Foremost, Cav1.3 activity is modulated by alternative splicing, calcium-dependent inactivation and phosphorylation.

1.4.1. Cav1.3 modulation by alternative splicing

As mentioned, Cav1.3 undergoes alternative splicing, which influences its electrophysiological properties and physiological functions. In these splice variants, certain exons are mutually exclusive (exactly one out of two exons is retained), while others are alternatively spliced sites. Regarding the transmembrane segments and connecting loops, mutually exclusive exons are 8A/8B, 22/22A and 31A/31B, while alternative exons include exon 11 and exon 32 (Huang et al., 2022; Jurkat-Rott & Lehmann-Horn, 2004; Koh et al., 2021; Koschak et al., 2001). Further, Cav1.3 activity is profoundly modulated by alternative splicing of its C-terminus. Herein mutually exclusive exons are only 42/42A. Exon 42A contains a stop codon. Therefore, Cav1.3 channels comprising exon 42A have the shortest C-terminus, while exon 42 produces the full-length C-terminus. In both splice variants, exon 41 can be skipped ($\Delta 41$) and channels containing exon 42 can further contain alternative exons 43S, 43-2, $\Delta 44$ or 48S, all resulting in different C-terminal lengths (Bock et al., 2011; Singh et al., 2008; Tan et al., 2011) (Fig. 6A).

As the Cav1.3 C-terminus is composed of different regulatory domains, alternative splicing modulates the composition of these domains, which alters electrophysiological properties. Proximally located domains include the EF-hand motif, followed by the pre-IQ and IQ domain and hereafter the proximal C-terminal regulatory domain (PCRD). The EF-hand is a highly conserved Ca^{2+} -binding motif and the pre-IQ and IQ domains are structured by coiled amphipathic α -helices. Both, the EF-hand and the IQ domain bind calcium-regulatory proteins, most abundant calmodulin (CaM) (Ben-Johny & Dick, 2022; Huang et al., 2022; Rhoads & Friedberg, 1997). Distal Cav1.3 domains include the distal C-terminal regulatory domain (DCRD) and a PDZ binding sequence, which is an interaction site for postsynaptic scaffolding proteins (Singh et al., 2008; Stanika et al., 2016; Tan et al., 2011). An intramolecular interaction between PCRD and DCRD forms the C-terminal modulatory domain (CTM) (Lieb et al., 2012; Singh et al., 2006) (Fig. 6B).

Alternative C-terminal splicing influences open probability, current density, voltage-dependent activation and calcium-dependent inactivation (CDI) (Bock et al., 2011;

Scharinger et al., 2015; Singh et al., 2008). Rule-of-thumb is, the shorter the C-terminus, the higher the open probability, current density and CDI. Comparing Cav1.3₄₂ and Cav1.3_{42A} shows that the short splice variant Cav1.3_{42A} displays a 10-fold higher open probability and stronger CDI. Further, Cav1.3_{42A} activates at even more hyperpolarized voltages than Cav1.3₄₂, while the conductance is similar. The differences originate in the presence of the CTM. The intramolecular interaction between PCRD and DCRD, which forms the CTM, reduces binding of CaM to the EF-hand and IQ motif, which mediates CDI (Bock et al., 2011; Sang et al., 2021; Singh et al., 2006; Singh et al., 2008) (Fig. 6C). In rat Cav1.3 channels, a single amino acid difference (exon 49, p. 2075 V>A) renders the CTM ineffective, which leftward-shifts voltage-dependent activation, reduces voltage-dependent inactivation (VDI) and accelerates CDI kinetics. These differences in biophysical gating limit cross-species applicability of Cav1.3 findings obtained in humans and rats (Lieb et al., 2012; Tan et al., 2011).

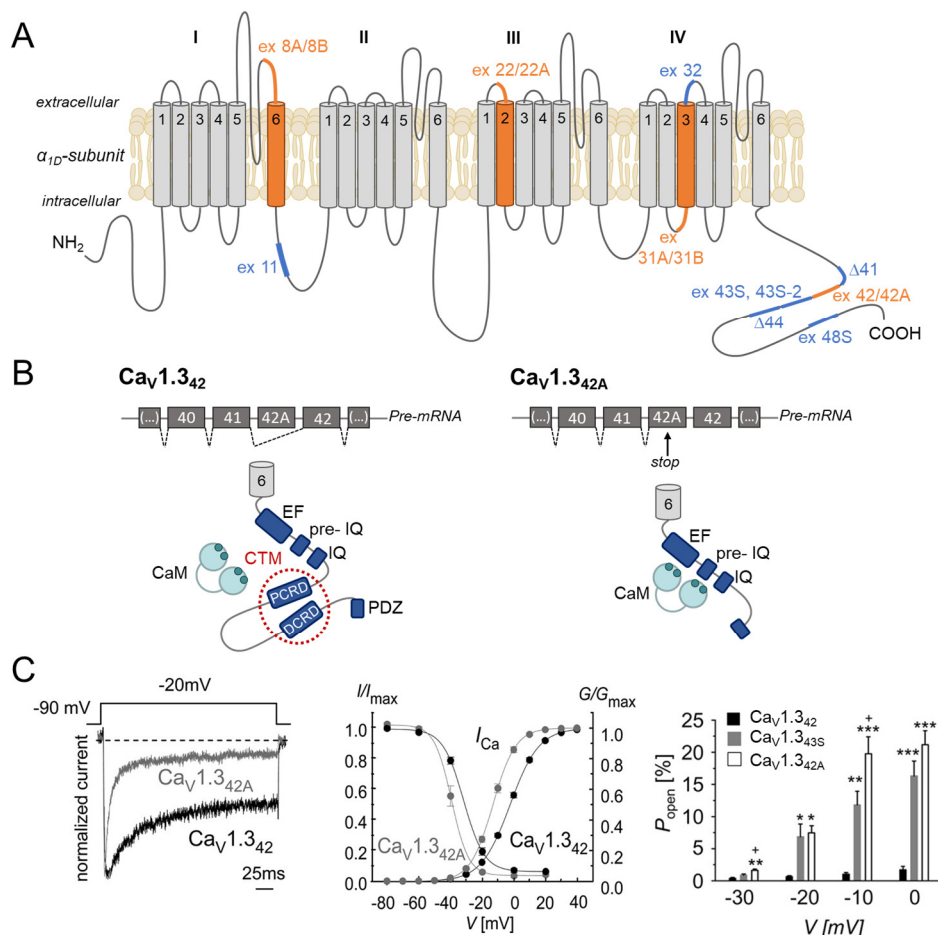


Figure 6. Cav1.3 alternative splicing and resulting gating alterations. (A) Schematic of mutually exclusive (orange) and alternative spliced (blue) exons. **(B)** Alternative C-terminal splicing and resulting domains. CTM reduces CaM binding to EF-hand and IQ-domain. **(C)** Gating differences of Cav1.3₄₂ and Cav1.3_{42A}. *Left:* Increased CDI in Cav1.3_{42A} (Singh et al., 2008). *Middle:* Activity shifted to more negative voltages in Cav1.3_{42A} (Singh et al., 2008). *Right:* Increased open probability (P_{open}) for short C-terminal variants Cav1.3_{42A} and Cav1.3_{43S} (Bock et al., 2011).

1.4.2. Ca_v1.3 modulation by calcium-dependent inactivation

Ca²⁺-influx through VGCCs is dependent on different gating states. Herein, channels are either in a non-conducting state (resting/closed or inactivated) or in a conducting state (open) (Fig. 7). The closed state features multiple closed time constants, revealing different depths of closing states. The transition into the conducting state prolongs with deeper closing states. The open state is characterized by different gating modes. Gating mode 0 is silent, mode 0a displays very low activity with occasional, short openings, mode 1 is characterized by low P_{open} with frequent, brief openings (~ 0.3 ms) and mode 2 features high P_{open} with long channel openings (≥ 2 ms). Mode 2 gating is typically observed in the presence of LTCC agonists e.g. S-BayK 8466 (Herzig et al., 1993; Hess et al., 1984; Tanskanen et al., 2005). The inactivated state is initiated by intrinsic (voltage) and extrinsic (calcium) feedback mechanisms.

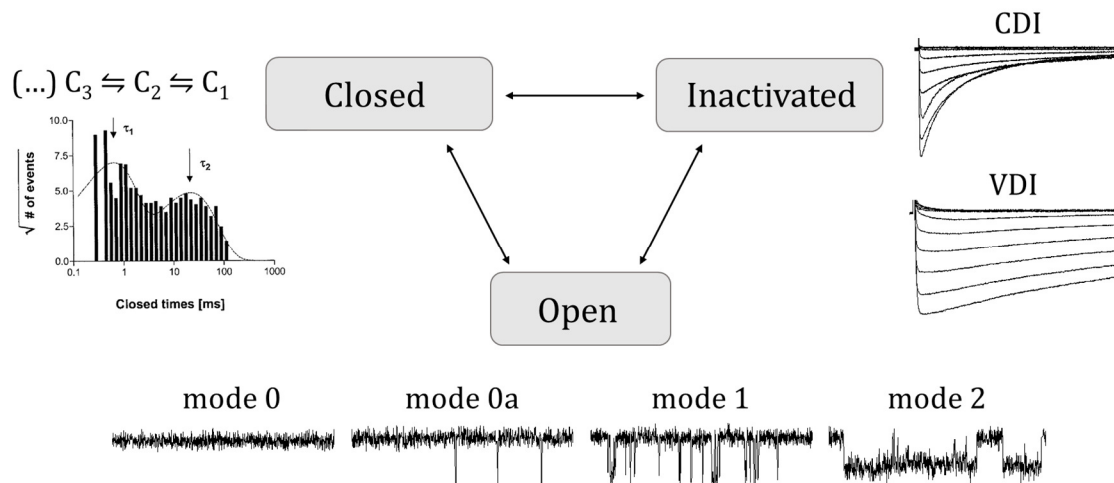


Figure 7. Overview of LTCC gating states. Closed, open and inactivated state with individual characteristics reported aside. Closed state: Different depths of closing states indicated by closed time constants (τ) (Michels et al., 2002). Open state: Gating modes 0–2 with corresponding single-channel activity examples (own recordings). Inactivated state: Exemplary recordings showing calcium- and voltage-dependent inactivation (CDI and VDI) (own recordings).

Channel inactivation is crucially important to prevent cytotoxic increase in intracellular Ca²⁺ through VGCCs (Evans & Zamponi, 2006; Matthes & Herzig, 2010). This transition into a non-conducting state is mediated via voltage-dependent inactivation (VDI) and calcium-dependent inactivation (CDI) (Zamponi et al., 2005).

VDI is an intrinsic mechanism to the pore-forming α_1 -subunit, thought to prevent Ca²⁺-influx like a “hinged lid”. Herein, the “lid” is closed by attachment of the domain I-II linker to the S6 transmembrane segments (Stotz et al., 2000; Zamponi et al., 2005). The intracellular domain III-IV loop and the auxiliary β -subunit influence VDI kinetics, i.e.

β_{2a} -subunit slows inactivation kinetics, while β_{1b} - and β_3 -subunits slightly increase VDI (Buraei & Yang, 2010; Hullin et al., 2003; Jangsongthong et al., 2010). Both, HVA and LVA channels exhibit VDI.

HVA-channels, including Cav1.3, additionally exhibit CDI. CDI is a negative feedback mechanism, triggered by a local increase in the intracellular Ca^{2+} -concentration (≥ 500 nM Ca^{2+}) (Ben-Johny & Yue, 2014). CDI occurs faster than VDI and is not an intrinsic mechanism, but mediated through binding of calmodulin (CaM).

CaM is a 17 kDa, highly conserved, ubiquitously expressed calcium sensor protein. It has a bi-lobe structure, composed of four EF-hand motifs, in which motif I and II form the N-lobe and III and IV form the C-lobe of CaM. Intracellular signaling to the majority of CaM targets requires only one lobe, while signaling to Cav1.3, requires both lobes: CaM N-lobe binds the EF-hand motif and CaM C-lobe binds the IQ-domain in the Cav1.3 C-terminus. Herein, the affinity of C-lobe to IQ-domain is higher than N-lobe to EF-hand and ablation of either domain or lobe abolishes CDI (Banerjee et al., 2018; Ben-Johny & Yue, 2014; Ben Johny et al., 2013; Cens et al., 2006; Kim et al., 2004; Kim et al., 2008; Peterson et al., 1999; Peterson et al., 2000).

CaM pre-associates with Cav1.3 in its Ca^{2+} -free form (apo-CaM). Herein, apo-CaM C-lobe binds the IQ domain, followed by apo-CaM N-lobe binding to the EF-hand. This is thought to extend the C-terminus conformationally, which increases channel P_{open} (Adams et al., 2014). The resulting Ca^{2+} -influx triggers CDI by Ca^{2+} binding to apo-CaM. Thereby, both Ca^{2+} -bound CaM lobes relocate at the proximal C-terminus and additionally associate with the N-terminal spatial Ca^{2+} -transforming element (NSCaTE) (Dick et al., 2008). This conformationally bends the C-terminus, resulting in channel inactivation (Adams et al., 2014; Imredy & Yue, 1994; Lee et al., 1999; Peterson et al., 1999; Peterson et al., 2000; Zuhlke et al., 1999).

Latest research shows, that Ca^{2+} binding to a single CaM lobe (half-calcified CaM) modulates Cav1.2 activity, thereby suggesting that the current CDI model may not reflect the actual complexity of CDI (Bartels et al., 2022).

As indicated by the equilibrium arrows in figure 8 below, CaM regulation is dynamic. In fact, CaM (dis-) association to Cav1.3 C-terminus occurs on a minute timescale. Herein, CaM competes with other channel-interacting proteins, including CaM-like Ca^{2+} -binding proteins (CaBPs) and the CTM of long Cav1.3 splice variants (Kuzmenkina et al., 2019). This competition shapes CDI and enables tissue specific CDI modulation, i.e. inner hair cell currents exhibit weak CDI, and SAN currents strong CDI (Sang et al., 2021; Yang et al.,

2006). Disrupting the C-terminal interaction with CaM alters CDI and has pathophysiological consequences. In Cav1.4, a mutation in the CTM increases CDI in photoreceptors and bipolar cells, leading to stationary night blindness (Hoda et al., 2005; Sang et al., 2021). Vice versa, mutations in the gene encoding CaM (*CALM 1-3*) can disrupt CDI and are associated with cardiac diseases, including long-QT syndrome (Limpitikul et al., 2017; Sang et al., 2021).

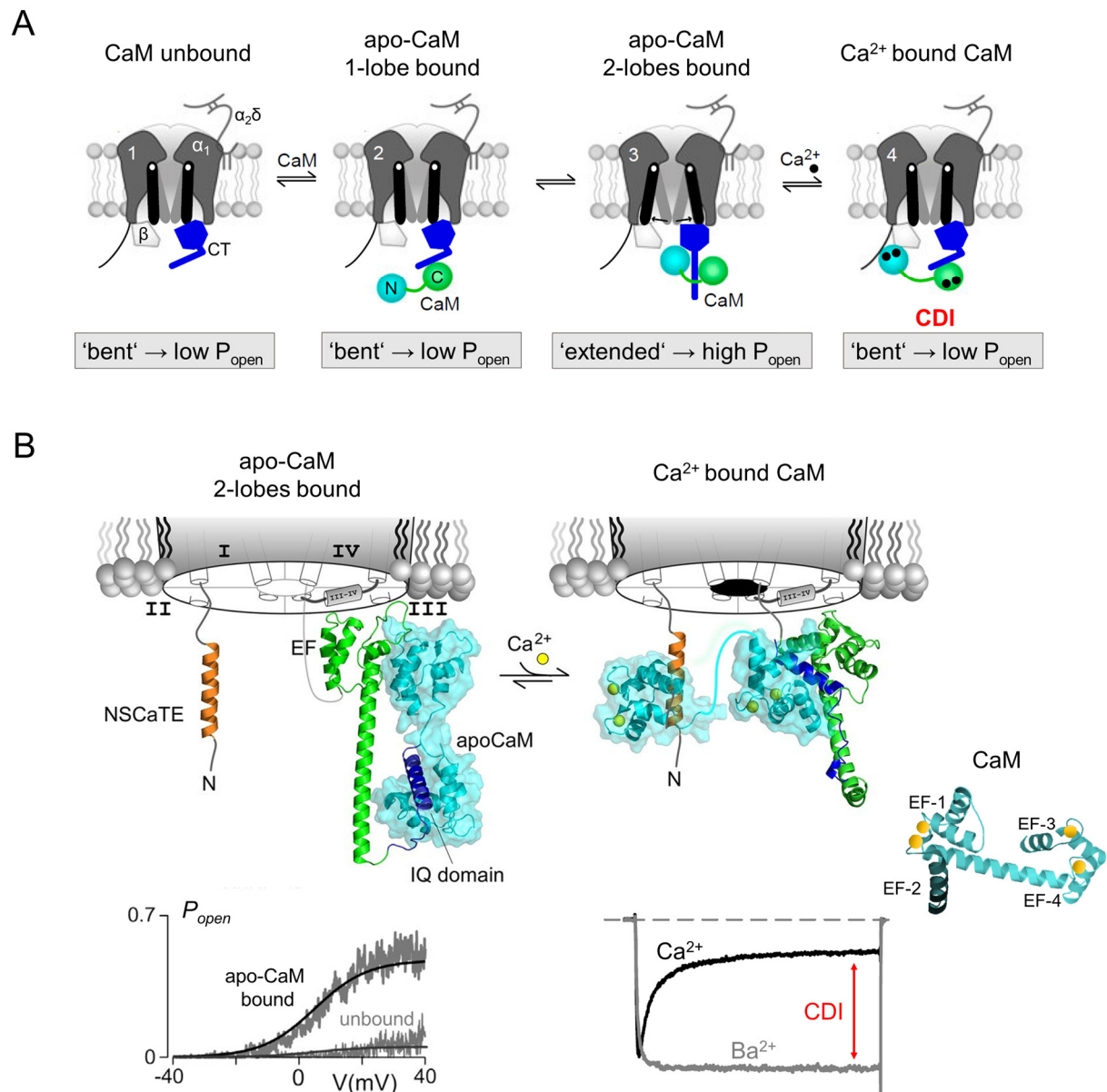


Figure 8. Calcium dependent inactivation of Cav1.3. (A) Schematic of apo-CaM and CaM binding and resulting conformation of Cav1.3 C-terminus (CT) with corresponding P_{open} (modified from Banerjee et al., 2018). (B) Proposed model of apo-CaM and CaM binding to EF-hand, IQ-domain and NSCaTE (Ben-Johny and Yue, 2014). Below, left: Single-channel patch-clamp data showing increased P_{open} upon apo-CaM binding (Adams et al., 2014); right: CDI shown by difference in inactivation of Ba²⁺ and Ca²⁺ whole-cell currents (Ben-Johny et al., 2013). Schematic on the right shows structure of CaM (modified from Yang & Poovaiah, 2003).

1.4.3. Cav1.3 modulation by phosphorylation

Phosphorylation is a posttranslational modification in which a phosphate group (PO_3^{2-}) is enzymatically attached to amino acid residues by phosphodiester binding. Most abundantly phosphorylated amino acids in eukaryotes are serine, threonine, tyrosine and histidine. In contrast to mechanisms relying on protein biosynthesis, phosphorylation enables rapid and reversible modulation of VGCC activity (Cohen, 2002; Catterall, 2011). In LTCCs, phosphorylation of Cav1.2 has been broadly researched. Herein, serine at position 1928 is exemplary of the impact that phosphorylation has on physiological and pathophysiological gating modulation: S1928 phosphorylation uncouples channels from β -adrenergic receptors (Patriarchi et al., 2016) and is thereby involved in catecholamine-dependent β -adrenergic signaling in cardiomyopathy (Borchert et al., 2017). Additionally, it stimulates vasoconstriction during acute hyperglycemia and diabetes (Nystoriak et al., 2017) and was recently found to orchestrate spatial reorganization of vascular LTCCs in diabetes (Martin-Aragon Baudel et al., 2022). Further, increased S1928 phosphorylation was found in the dentate gyrus of the hippocampus and is critical for molecular mechanisms underlying long-term potentiation (Qian et al., 2017).

Phosphorylation of Cav1.3, however, is largely unexplored. Although phosphorylation sites have been identified, their role in physiological or pathophysiological responses remain widely unknown. Further, all known Cav1.3 phosphorylation sites were identified and studied in rat Cav1.3. Herein, N-terminally located S81 is a protein kinase C (PKC) phosphorylation site, which mediates inhibition of Cav1.3 currents (Baroudi et al., 2006). Further, activation of NO-cGMP-PKG pathway inhibits Cav1.3 currents and may impair insulin release via protein kinase G (PKG) phosphorylation of S793 and S860. PKG inhibition and phosphorylation resistant mutation of these residues prevented this current inhibition (Sandoval et al., 2017). Additionally, Ca^{2+} /calmodulin-dependent protein kinase II (CaMKII) phosphorylation of S1486 in rat Cav1.3 mediates insulin-like growth factor 1/receptor tyrosine kinase (IGF-1/RTK) induced current increase in rat hippocampal and cortical neurons. When preventing S1486 phosphorylation via mutation, IGF-1 fails to potentiate Cav1.3 currents (Gao et al., 2006). Further, protein kinase A (PKA) activation increased Cav1.3 channel activity (Qu et al., 2005), possibly via C-terminally identified PKA phosphorylation sites S1743 and S1816 (Ramadan et al., 2009). Additionally, inhibition of cyclin-dependent kinase 5 (Cdk5) phosphorylation of S1947 in substantia nigra neurons, increased Cav1.3 currents (Loya-Lopez et al., 2020) (Fig. 9).

As mentioned, all Cav1.3 phosphorylation sites were identified in rat Cav1.3, although the lack of a functional CTM in rat Cav1.3 limits cross-species applicability (Lieb et al., 2012; Tan et al., 2011). The identified phosphorylation sites are yet unconfirmed for human channel variants.

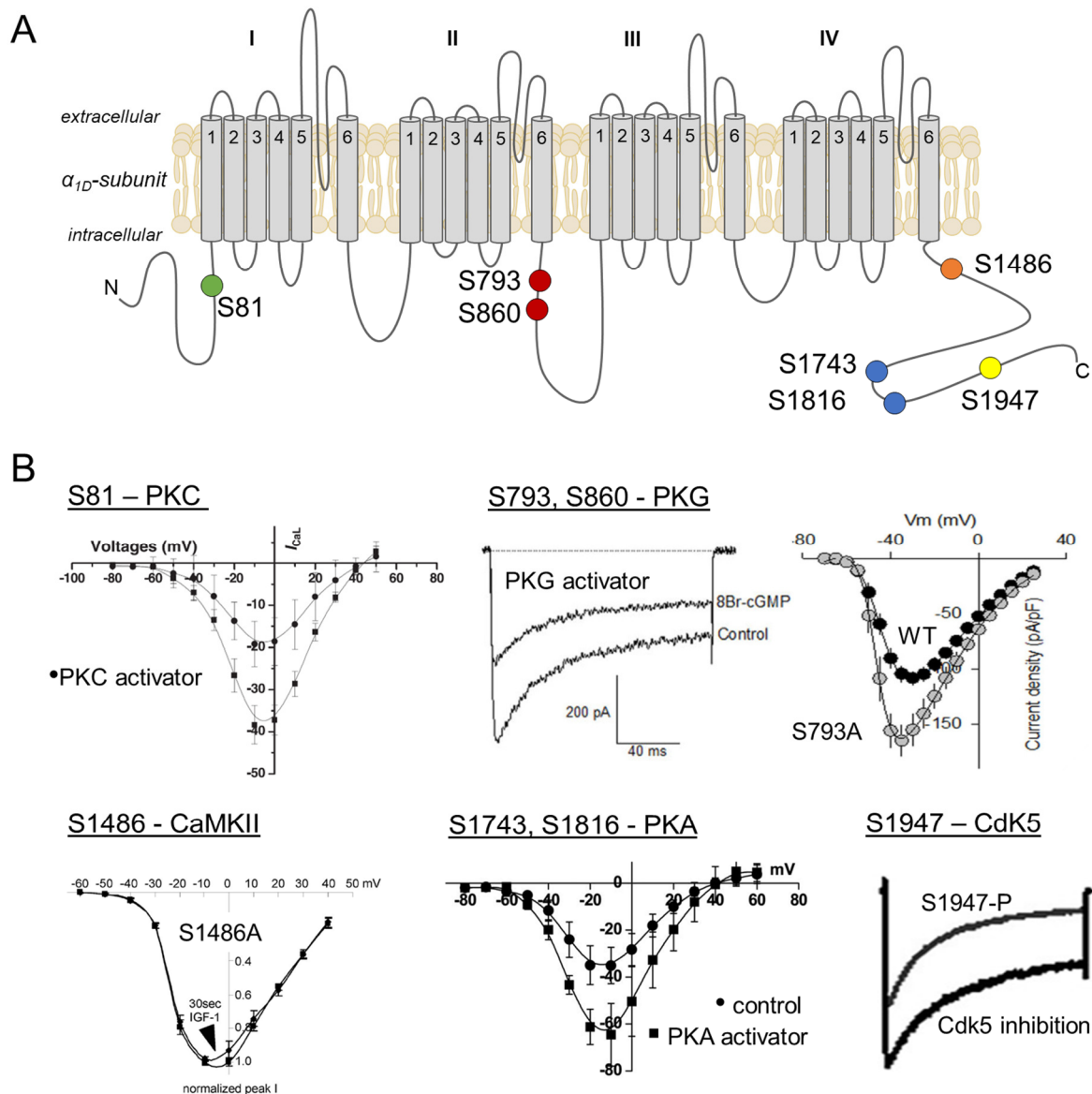


Figure 9. Cav1.3 phosphorylation sites and corresponding gating changes. (A) Schematic localization of phosphorylation sites in Cav1.3 α_{1D} -subunit and **(B)** corresponding gating changes. PKC activation reduces current via S81 (Baroudi et al., 2006); PKG activation reduces current, which is inhibited when S793 cannot be phosphorylated (Sandoval et al., 2017); IGF-1 fails to potentiate currents when S1486 cannot be phosphorylated (Gao et al., 2006); PKA activation increases current (Qu et al., 2005), likely via S1743 and S1816 phosphorylation (Ramadan et al., 2009); Cdk5 inhibition reverses current decrease caused by S1947 phosphorylation (Loya-López et al., 2020).

1.4.4. Role of Cav1.3 modulation

Research shows impressively, that Cav1.3 gating modulation is the central element of Cav1.3 function to meet cellular requirements. In addition to the examples provided in this introduction, the search for a specific Cav1.3 inhibitor is evident for this.

Compound 8 (Cp8) was thought to be a selective inhibitor of Cav1.3. Cp8 is a derivative of pyrimidine-2,4,6-trione, a hit obtained in a non-commercial compound library screening. The selective inhibition of Cav1.3 was shown in electrophysiological recordings of rat Cav1.3 in stably transfected human embryonic kidney cells (HEK-293) (Kang et al., 2012). Cp8 was further investigated by other research groups. Within these studies, Cp8 did not inhibit Cav1.3 currents, despite efforts aligning experimental conditions. A second study even reported that Cp8 acts as an LTCC agonist (Ortner et al., 2014), and a third study revealed further, that Cav1.3 modulation by Cp8 depends crucially on the C-terminal splice variant and the associated auxiliary β -subunit isoform (Huang et al., 2014).

So far, the conflicting results could not be explained. A possible explanation is a potential yet unknown Cav1.3 modulation. For example, the study identifying Cp8 as an inhibitor, recorded Ba^{2+} currents (Kang et al., 2012), while the other studies recorded Ca^{2+} -currents (Huang et al., 2014; Ortner et al., 2014). In fact, Ortner et al. also recorded Ba^{2+} -currents and in a few of those recordings Cp8 slightly reduced Cav1.3 current as well. The authors suggested that Cp8 might be a state dependent Cav1.3 modulator and that inhibition requires a gating state only present when using Ba^{2+} as a charge carrier (Ortner et al., 2014). Further, although Cp8 was investigated in similar Cav1.3 isoforms, it was expressed differently, i.e. stable transfection, transient transfection and in murine tissue. An unrelated previous study gives reason to assume that Cav1.3 loses its characteristic electrophysiological properties in stably transfected conditions (Bell et al., 2001). This observation and possibly other yet unknown Cav1.3 alterations depending on the expression form, may have impacted Cp8 to be an inhibitor in one, and an activator in other studies.

Taken together, these findings verify that Cav1.3's susceptibility to its own modulation is the central element of its function. Researching Cav1.3 modulation will provide novel insights on modulatory mechanisms, which is the key to determine Cav1.3 function in physiological and pathophysiological processes. Herein, unravelling the complexity of Cav1.3 gating modulation is challenging. Eventually, however, therapeutically targeting Cav1.3 will critically depend on the understanding of Cav1.3 gating modulation.

1.5. Thesis subject

As stated, understanding Cav1.3 gating modulation is a prerequisite to comprehend Cav1.3 function in health and disease. Therefore, studying Cav1.3 gating modulation is best approached from both, the physiological and pathophysiological perspective. Further, given the limited cross-species applicability, Cav1.3 gating modulation is preferably studied in the human channel variant. In this context, disease-associated *CACNA1D* mutations are valuable clues because functional characterization of Cav1.3 gating modulation induced by these mutations can provide important insight on Cav1.3 modulatory mechanisms of pathophysiological relevance.

1.5.1. Novel disease-associated Cav1.3 missense mutations

The novel germline *de novo* missense mutations L271H, A749T and F747S are associated with neurodevelopmental disorders. In all cases, no other genetic alteration could explain the combination of exhibited symptoms. When this study was planned, all three mutations had only been described clinically, but not functionally. Very recently, F747S has been characterized on whole-cell level (Török et al., 2022).

Regarding the clinical phenotype, L271H was detected in a female patient, diagnosed at birth with neurodevelopmental delay, elevated blood pressure, facial dysmorphism, muscle hypotonia, hyporeactivity, hyperinsulinemic hypoglycemia, and primary hyperaldosteronism. Treatment included the antihypoglycemic drug diazoxide and at six months of age, nifedipine was administered, improving muscle hypotonia and blood pressure (De Mingo Alemany et al., 2020).

A749T missense-mutation was detected in two individuals. For only one case details are reported, describing a female patient with symptom onset at one year of age, showing neurodevelopmental delay, autism spectrum disorder, binocular vision disorder, hyperactivity, and auto-aggression but no cardiac or endocrine symptoms. Treatment included the antipsychotic drugs risperidone and quetiapine, the antiepileptic drug gabapentin, further memantine, amantadine and buspirone. Immediate-release isradipine was administered too, but terminated as it worsened the symptoms (Ortner et al., 2020).

F747S missense-mutation was detected in a male patient, diagnosed at four weeks with neurodevelopmental delay, elevated blood pressure, hypoglycemia and primary hyperaldosteronism. Additionally, the patient exhibited touch-induced jittering, a novel

symptom in disease-associated *CACNA1D* missense mutations. No information was provided on the drug treatment (Török et al., 2022).

The electrophysiological characterization of these mutations on whole-cell level was conducted in parallel to this thesis by Prof. Dr. Jörg Striessnig and his research group at the University of Innsbruck. Whole-cell characterization of F747S was recently published, showing that F747S does not alter current density but decreases inactivation. Further, F747S shifts voltage-dependent activation and inactivation towards more hyperpolarized voltages, thus identifying type 2 gating changes on whole-cell level (Török et al., 2022). L271H and A749T have also been characterized on whole-cell level. The results are still unpublished but known through personal communication with Prof. Striessnig, who gave me permission to describe the quality of whole-cell effects in this thesis. On whole-cell level, L271H shifts voltage-dependent activation and inactivation towards more hyperpolarized voltages, without increasing whole-cell current density. A749T also shifts voltage-dependent activation and inactivation towards more hyperpolarized voltages but increases current density.

All three mutations are located in highly conserved LTCC regions (Fig. 10). While the associated diseases share certain symptoms, other symptoms are distinct, including the touch-induced jittering in F747S. This is especially interesting considering the proximity of residues A749 and F747 and the similarity of functional changes induced by F747S and L271H. Herein originates the hypothesis that each mutation may alter different innate biophysical channel properties leading to the functional and clinical phenotypes. However, since the whole-cell current is a product of the number of channels in the membrane and the single-channel conductance, availability and open probability (Karmazinova & Lacinova, 2010), it cannot be used to determine different innate biophysical channel properties. Therefore, to address this hypothesis, Cav1.3 currents for all mutations are investigated in patch-clamp recordings at the single-channel level in this thesis.

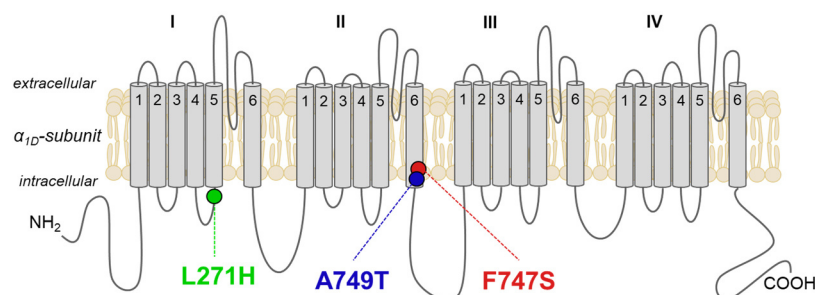


Figure 10. Location of disease-associated Cav1.3 missense mutations. L271H is located in the S4-S5 connecting loop of domain I. A749T and F747S are located in segment S6 of domain II.

1.5.2. Functional relevance and modulation of phosphorylation site S1475

To approach gating modulation from a physiological perspective, this thesis further investigates the functional relevance of phosphorylation site S1475 in Cav1.3 modulation. It is the human equivalent of the previously identified CaMKII phosphorylation site that mediates IGF-1 induced current potentiation in the rat (Gao et al., 2006). All known Cav1.3 phosphorylation sites were found in the rat isoform and are yet unconfirmed for human Cav1.3. The cross-species applicability, however, is limited because rat and human Cav1.3 differ in their structural and electrophysiological properties. Thus, investigating residue S1475 with human emphasis is a prerequisite to allow physio-pathological implications of how phosphorylation site S1475 modulates Cav1.3 currents in humans.

Further, S1475 is a potentially crucial Cav1.3 residue in itself. It is highly conserved only in Cav1.3, while Cav1.2 has a highly conserved alanine at the corresponding position. In fact, both channel types are sequence identical in this C-terminal region, except for S1475. Therefore, phosphorylation of S1475 is a potentially distinguishing feature of Cav1.3 and Cav1.2, specifically modulating Cav1.3 activity as alanine residues cannot be phosphorylated. In addition, except for Cav1.4, S1475 is also absent in all other HVA channels (L-, P/Q-, N-, and R-type) (Fig. 11). Therefore, S1475 is absent in all HVA channel types that co-express with Cav1.3 in similar tissues.

	IV S6	E-helix
Cav1.3	(...) M D N F D Y L T R D W S I L G P H H L D E F K R I W S E Y D (...)	
Cav1.2	(...) M D N F D Y L T R D W S I L G P H H L D E F K R I W A E Y D (...)	
Cav1.1	(...) M D N F D Y L T R D W S I L G P H H L D E F K A I W A E Y D (...)	
Cav1.4	(...) M D N F D Y L T R D W S I L G P H H L D E F K R I W S E Y D (...)	
Cav2.1	(...) M D N F E Y L T R D S S I L G P H H L D E Y V R V W A E Y D (...)	
Cav2.2	(...) M D N F E Y L T R D S S I L G P H H L D E F I R V W A E Y D (...)	
Cav2.3	(...) M D N F E Y L T R D S S I L G P H H L D E F V R V W A E Y D (...)	

Figure 11. Sequence comparison of proximal C-terminus among HVA channels. S1475 and corresponding position in other HVA channels highlighted in yellow. Cav1.3 is sequence identical to Cav1.2 except for S1475 in this region. Only Cav1.4 also contains a serine at this position, while all other HVA channels contain an alanine.

Further, S1475 is located in the E-helix of the EF-hand motif in the proximal Cav1.3 C-terminus. Therefore, it is present in all known (i.e. long and short) splice variants. Furthermore, the EF-hand binds calmodulin to mediate calcium-dependent inactivation. Herein originates the hypothesis, that S1475 phosphorylation could also be functionally relevant in human channels by modulating Cav1.3 gating via CaM-interaction, consequently altering CDI (Fig. 12). To address this hypothesis, S1475 phosphorylation-dependent modulation of Cav1.3 currents is investigated in whole-cell and single-channel

patch-clamp recordings in this thesis. Herein, the human full-length splice variant Cav1.3₄₂ was chosen because it contains the functional CTM, which is absent in the rat and therefore most likely imposes species-specific gating modulation by S1475 phosphorylation.

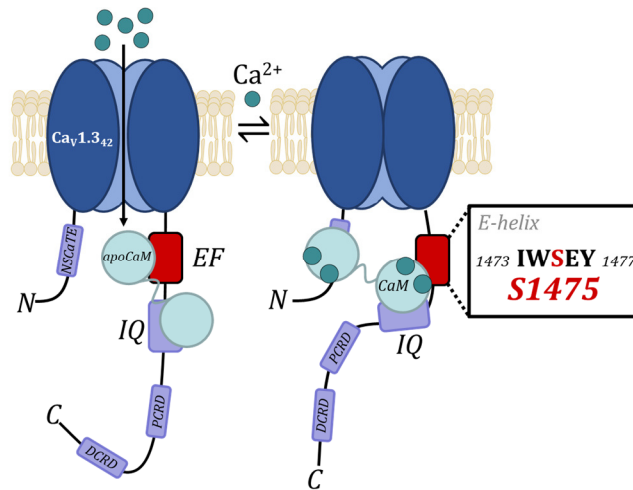


Figure 12. Location of phosphorylation site S1475. S1475 is located within the E-helix of the EF-hand motif with the C-terminus. Both, the EF-hand motif and the IQ-domain are binding sites for calmodulin, which initiates CDI upon Ca²⁺ entry through the channel.

1.6. Aim of the thesis

In this thesis, Cav1.3 gating modulation is investigated from a physiological and pathophysiological perspective with a human emphasis. The intention herein is, to contribute to the understanding of Cav1.3 modulatory mechanisms to eventually harness this knowledge in treatment of Cav1.3-associated diseases. To reach this aim, Cav1.3 pathophysiological gating modulation is investigated for the disease-associated Cav1.3 missense mutations L271H, A749T and F747S, and physiological gating modulation is addressed by investigating human phosphorylation site S1475.

The specific aims with respect to investigating pathophysiological gating modulation by Cav1.3 missense mutations are (1) to characterize Cav1.3 single-channel gating to identify individual gating phenotypes induced by each mutation to thereby explain the effects on whole-cell level and (2) to compare the individual gating phenotypes to draw conclusions on the hypothesis that different gating modulations might be linked to the different clinical phenotypes.

The specific aims with respect to investigating physiological gating modulation via Cav1.3 phosphorylation site S1475 are (1) to characterize the behavior of S1475 (de-) phosphorylation imitating Cav1.3 mutants using a human isoform and physiological charge carrier (2 mM Ca²⁺), (2) to investigate the role of CaMKII modulation of human Cav1.3 channels via S1475 and (3) to test the hypothesis that S1475 modulation involves CaM-interaction and CDI.

2. Methods and Material

To reach the aim of this thesis, to investigate Cav1.3 gating modulation from a physiological and pathophysiological perspective with a human emphasis, molecular biological techniques, structural modeling and electrophysiological patch-clamp recordings were used.

Molecular biological techniques were employed to create plasmid constructs to investigate disease-associated missense mutations L271H, A749T and F747S, as well as S1475 phosphorylation. These plasmids were transfected into human embryonic kidney (HEK-293) cells and used for single-channel and whole-cell patch-clamp recordings.

2.1. Molecular biological methods and material

Molecular biological techniques were used to create extrachromosomal DNA plasmids, containing the sequence for the respective protein of interest.

2.1.1. Plasmid information

As LTCCs assemble as channel complexes, Cav1.3 α_1 -subunits were transfected alongside auxiliary subunits. To obtain a strictly human channel composition, S1475 phosphorylation was investigated in human Cav1.3₄₂ α_1 -subunits, co-expressed with human auxiliary β_{1b} - and $\alpha_2\delta_1$ -subunits. S1475 phosphorylation states were imitated by mutation to alanine (S1475A) and aspartic acid (S1475D). Both, Cav1.3 α_1 - and auxiliary subunits were made by myself (see chapter 2.1.3.).

Gating modulation by *CACNA1D* missense-mutations was investigated in cooperation with the research group of Prof. Dr. Jörg Striessnig at the University of Innsbruck. They identified two of the three mutations and performed whole-cell recordings, while single-channel recordings were performed within the scope of this thesis. To align experimental conditions, Cav1.3₄₂ α_1 -subunits were co-expressed with rat β_3 and rabbit $\alpha_2\delta_1$ auxiliary subunits. Cav1.3 α_1 -subunits containing L271H, A749T and F747S were provided by Prof. Striessnig's post-doctoral researcher Dr. Nadine Ortner. Notably, I was blinded for the mutant constructs and whole-cell effects when performing single-channel experiments and analysis.

Cav1.3₄₂ α_1 -subunits were expressed in pGFP⁻ vector (plasmid map supplemental S1), β_{1b} was expressed in pIRES_EGFP, human $\alpha_2\delta_1$ was expressed in pIRES_RFP, β_3 was expressed in pCMV6, and rabbit $\alpha_2\delta_1$ was expressed in pcDNA3. Detailed plasmid information is provided in table 2.

Table 2. Overview of plasmid constructs.

Plasmids used for investigation of disease associated Cav1.3 missense mutations			
Plasmid	Protein	Species	Origin and Accession No.
pGFP_CACNA1D_42	Cav1.3 ₄₂	<i>Homo sapiens</i>	Koschak et al. 2001 Accession No.: EU363339
pGFP_CACNA1D_42_L271H	Cav1.3 ₄₂ p. 271 L > H	<i>Homo sapiens</i>	J. Striessnig, N. Ortner
pGFP_CACNA1D_42_A749T	Cav1.3 ₄₂ p. 749 A > T	<i>Homo sapiens</i>	J. Striessnig, N. Ortner
pGFP_CACNA1D_42_F747S	Cav1.3 ₄₂ p. 747 F > S	<i>Homo sapiens</i>	J. Striessnig, N. Ortner
pCMV6_CACNB3	Cavβ ₃	<i>Rattus Norvegicus</i>	Castellano et al., 1993 Accession No.: NM_012828
pcDNA3_CACNA2D1	Cavα ₂ δ1	<i>Oryctolagus cuniculus</i>	Ellis et al., 1988 Accession No.: NM_001082276
pcDNA3_GFP	GFP	<i>Aequorea victoria</i>	Research group J. Matthes
Plasmids used for investigation of phosphorylation site S1475			
Plasmid	Protein	Species	Origin and Accession No.
pGFP_CACNA1D_42	Cav1.3 ₄₂	<i>Homo sapiens</i>	Koschak et al. 2001 Accession No.: EU363339
pGFP_CACNA1D_42_S1475A	Cav1.3 ₄₂ p. 1475 S > A	<i>Homo sapiens</i>	This PhD thesis (S. Salamon)
pGFP_CACNA1D_42_S1475D	Cav1.3 ₄₂ p. 1475 S > D	<i>Homo sapiens</i>	This PhD thesis (S. Salamon)
pIRES_CACNB1B_EGFP	Cavβ _{1b}	<i>Homo sapiens</i>	Despang et al., 2022 Accession No.: NM_000723
pIRES_CACNA2D1_RFP	Cavα ₂ δ1	<i>Homo sapiens</i>	This PhD thesis (S. Salamon) Accession No.: NM_000722
pcDNA3_CALM1	CaM	<i>Rattus Norvegicus</i>	Peterson et al. 1999 Accession No.: NM_031969
pcDNA3_CALM1_1234	CaM ₁₂₃₄	<i>Rattus Norvegicus</i>	Peterson et al., 1999
pcDNA3_BSCaM _{IQ}	BSCaM _{IQ}	<i>n.a.</i>	Black et al., 2006
pRSV-CaMKII(1-290)	CaMKII	<i>Rattus Norvegicus</i>	Richard Maurer via Addgene

2.1.2. Investigation of S1475 phosphorylation states via mutation

Investigation of Cav1.3 gating modulation by S1475 phosphorylation included a phosphorylation-imitating approach. Hereto, wildtype (WT) serine at p.1475 was mutated to aspartic acid (Asp; D) or alanine (Ala; A). Aspartic acid has a side chain resembling a serine in a phosphorylated state. Contrary, alanine (Ala; A) lacks such a residue and is therefore phosphorylation resistant (Fig. 13). S1475A mutation required a point mutation (*tca > gca*) and S1475D a triplet exchange (*tca > gac*). This approach allowed investigation without interference of upstream or downstream regulators.

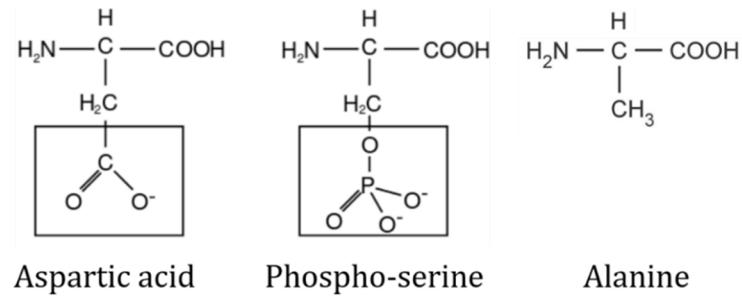


Figure 13. Structure of amino acid side chains in phosphorylation-mimicking approach. Squares highlight similarity of a phosphorylated serine and aspartic acid.

2.1.3. Plasmid cloning and mutagenesis

To create plasmid constructs, polymerase chain reaction (PCR) was used to amplify an intentional misread to introduce e.g. mutations into genes of interest, which is called mutagenesis. Mutagenesis was performed using *QuikChange II XL Site Directed Mutagenesis Kit* (Agilent Technologies, CA, USA). First, primers were designed with ~40 % CG content and weak secondary structure and ordered from Sigma (St. Louis, USA) (Tab. 3). Second, mutagenesis reaction and PCR protocol were performed, based on amount of base pair exchange (Tab. 4). Third, template DNA was eliminated via *DpnI* digest (37°C for 1 hr; 1 µg DNA, 10 U *DpnI*, 1x CutSmart® Buffer (New England Biolabs, MA, USA)). *DpnI* cuts DNA at methylation sites, which were present in template DNA, given previous *Escherichia coli* (*E.coli*) amplification, but absent in the PCR product.

Table 3. Overview mutagenesis primers.

Construct	Primer 5' → 3'
pGFP_CACNA1D_42_S1475A	forward: gaattcaaaagaatatgggcagaatatgaccctgaggc
	reverse: gcctcagggtcatattctgccatattctttgaattc
pGFP_CACNA1D_42_S1475D	forward: gaattcaaaagaatatgggacgaatatgaccctgaggc
	reverse: gcctcagggtcatattctgccatattctttgaattc

Table 4. PCR protocol for mutagenesis reactions.

Components	PCR cycle protocol		
	Step	Temp.	Duration
10x reaction buffer [1x]	1. Initial Denaturation	95°C	1 min
Quick Solution® [0.6x]			
dNTPs [200 µM]	2. Denaturation	95°C	50 s
Template DNA [10 ng]	3. Annealing	60°C	50 s
Forward primer [0.625 µM]	4. Elongation	68°C	10 min
Reverse primer [0.625 µM]	5. Final Elongation	68°C	7 min
PfuUltra High-Fidelity DNA polymerase [0.04 U]	Steps 2. - 4. were repeated 18 x		
Aqua dest. [added to 25 µl reaction volume]			

After mutagenesis reaction, and to amplify plasmids in general, plasmids were transformed into chemically competent *E. coli* for amplification by 30 min incubation on ice followed by 10 min incubation at room temperature (RT) and 60 min at 37°C in SOC media (100 µl *E. coli*, 5 µl PCR product, 20 µl KCN buffer, 80 µl H₂O). The transformation mixture was distributed on agar plates (15 g/l, Sigma-Aldrich) and incubated at 37°C overnight. Since a specific antibiotic resistance was encoded on the plasmid, adding the corresponding antibiotic (ampicillin, 150 µg/ml) enabled identification of successfully transformed bacteria. Single colonies were picked and amplified in Lysogeny broth (LB) medium (20 g/l, pH 7.5, Sigma-Aldrich) at 37°C, 180 rpm overnight. Afterwards DNA was harvested and prepared following instructions of *Qiagen Plasmid Miniprep Kit* and *Macherey-Nagel NucleoBond® Xtra Maxiprep Kit*. Plasmids were diluted in water and their concentration was measured by NanoDrop2000 (Thermo Fisher Scientific, MA, USA). Plasmid DNA was then verified by restriction digest and sequencing. During restriction digest, enzymes cut DNA at palindromic sequences, thus linearizing it in a predictable band pattern (200 ng DNA cut by 0.5 U restriction enzyme in 1x reaction buffer at 37°C for 90 min). Digested DNA was loaded onto 1 % TBE gel (TRIS [0.1 M], Borat [0.1 M], EDTA [2 mM], 1 % agarose) to separate DNA fragments by electrophoresis (100 V, ~45 min). Fragments were visualized by 5 % ethidium bromide (5 min, 60°C) and imaged using *Image Studio Light* hard- and software (LI-COR Biosciences, NE, USA). DNA sequence was confirmed by Sanger sequencing (Microsynth Seqlab GmbH, Göttingen, Germany).

2.2. Eukaryotic cell culture and transfection

In this thesis, experiments were performed in HEK-293 cells. These eukaryotic cells were immortalized by an adenovirus and have been used in scientific research for 50 years. They were chosen as the mammalian expression system because of their amenability to transfection and protein expression.

2.2.1. Cultivation of HEK-293 cells

HEK-293 cells were cultured at 37°C and 5 % CO₂ in Dulbecco's Modified Eagle's Medium (DMEM) providing nutrition, growth factors and antibiotics to prevent bacterial contamination. Since adherent cell lines, like HEK-293, die in overcrowding conditions they were passaged twice a week. Hereto, cells were washed with PBS (pre-warmed to 37°C), detached by incubation with trypsin-EDTA (2 min, 37°C) and distributed in DMEM onto new dishes in smaller amounts (Tab. 5).

Table 5. Overview of solutions and devices for cultivation of HEK-293 cells.

Solution / Device	Composition / Manufacturer
Dulbecco's Modified Eagle's Medium (DMEM)	Gibco Thermo Fisher, Waltham, MA, USA
Trypsin (0.02 % in PBS)	GE Healthcare Life Science, UT, USA
Penicillin/streptomycin	GE Healthcare Life Science, UT USA
Fetal bovine serum (FBS)	Biochrom GmbH, Berlin Germany
Growth medium	DMEM 500ml, FBS 50ml, 100x Pen/Strep 2.75ml
CO ₂ -Incubator: HERAcell 150i	Thermo Scientific, Waltham, MA, USA
Sterile bench: HS 12/2	Heraeus Instruments, Hanau, Germany

2.2.2. Transient transfection of VGCCs into HEK-293 cells

HEK-293 cells were transiently transfected at 60 % confluence using calcium phosphate precipitate (Graham & van der Eb, 1973; Koch et al., 2016). Hereto, plasmids were pipetted into 380 μ l HEPES buffered saline (HBS [mM]: HEPES 21, NaCl 137, KCl 49, Glucose 5.5, Na₂HPO₄ x 7 H₂O 0.75). After 1 min incubation at RT, 20 μ l CaCl₂ [2.5 M] was added dropwise, mixed thoroughly and incubated for 20 min at RT. The transfection mixture was applied to cells in DMEM and removed after 5 h at 37°C, by washing twice with pre-warmed PBS. One day post transfection, cells were distributed onto 350 mm culture dishes and used for electrophysiological recordings 48 to 72 hours afterwards.

For disease-associated missense mutations 1 μ g pore-forming α_1 -subunit (WT, L271H, A749T or F747S) was transfected alongside 0.5 μ g β_3 - and 1.5 μ g $\alpha_2\delta_1$ -subunit. Since neither subunit carried a fluorescent reporter, 0.5 μ g GFP was co-transfected to identify successfully transfected cells.

For S1475 investigation, 0.9 μ g pore-forming α_1 -subunit (WT, S1475A or S1475D) was transfected alongside 0.45 μ g β_{1b} - and 1.35 μ g $\alpha_2\delta_1$ -subunit. Additional plasmids CaM, CaM₁₂₃₄, BSCaM_{IQ} and CaMKII were transfected in a 1:1 ratio with the α_1 -subunit. Both auxiliary subunits were encoded on bicistronic vectors expressing a fluorescent reporter labelling successfully transfected cells (β_{1b} + EGFP (green) and $\alpha_2\delta_1$ + RFP (red)).

2.3. Electrophysiology

Cellular excitability is based on the distribution of ion concentrations at the cell membrane. It results in a capacitor-like charge difference between the intracellular and extracellular space, called the resting membrane potential. Changes in the membrane potential e.g. via action potentials, result in voltage-dependent ion gating through the membrane, which can be measured by electrophysiological techniques. Here, the patch-clamp technique was used to investigate Cav1.3 gating modulation.

2.3.1. Overview of the patch-clamp technique

The patch-clamp technique can be used to examine the voltage-dependent ion gating in excitable cells. It was developed by Erwin Neher and Bernd Sakmann, based on the voltage-clamp method by Hodgkin and Huxley (Hodgkin & Huxley, 1952). In 1976 Neher and Sakmann first recorded single-channel activity from a frog skeletal muscle (Neher & Sakmann, 1976). Further refinements allowed different patch-clamp configurations resolving microscopic single-channel and macroscopic whole-cell currents (Hamill et al., 1981; Neher et al., 1978): Single-channel recordings in cell-attached configuration allow channel investigation in an intact cell, while inside-out configuration exposes the cytoplasm, and outside-out configuration exposes the extracellular space. The whole-cell configuration allows investigation of all channels in the membrane (Fig. 14).

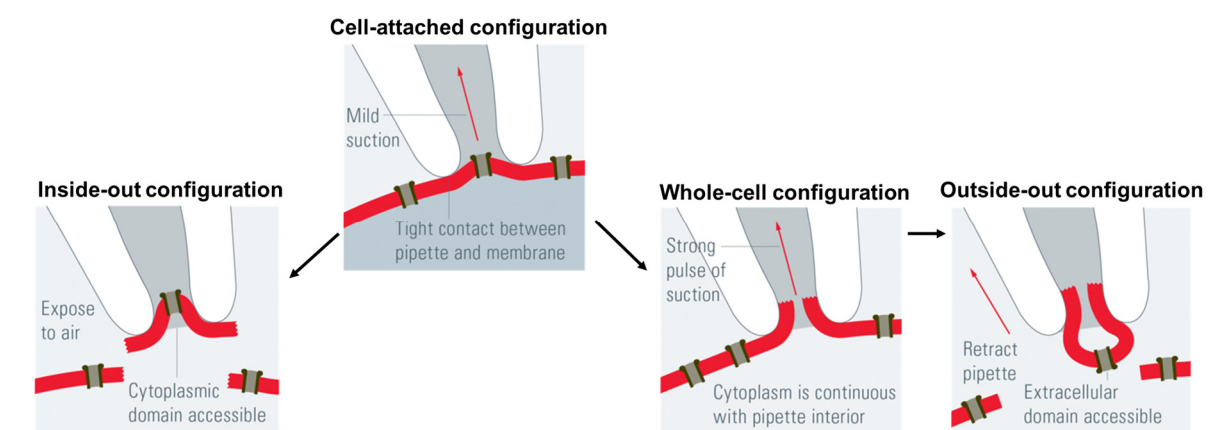


Figure 14. Overview of patch-clamp configurations. The cell-attached configuration allows investigation of single ion channels in an intact cell. By retracting the pipette the inside-out configuration can be achieved. Instead, by applying suction the whole-cell configuration can be achieved and by then retracting the pipette the outside-out configuration is reached (modified from Veitinger, 2011).

2.3.2. Patch-clamp configurations and principle of data acquisition

In this thesis, patch-clamp recordings were performed in the cell-attached single-channel and whole-cell configuration.

Single-channel patch-clamp in the cell-attached configuration allowed investigation of current through single channels of an intact cell. Hereto, a micropipette was used to make contact to a small membrane area, called patch. By sucking the membrane into the pipette, a seal with gigaohm ($G\Omega$) resistance was formed, which electrically isolated the membrane patch from its surroundings. Thus, all ions that flew were conducted by the channel in the patch. The resulting tiny electrical current of 0.5–1 picoampere (pA) was detected by a connected amplifier. Proceeding from the cell-attached status, the whole-cell configuration was achieved by further suction to rupture the membrane inside the pipette. Thereby the cytoplasm and the solution inside the pipette became continuous. The whole-cell configuration then allows either investigation of current through all channels in the membrane (voltage-clamp) or changes in the membrane potential (current-clamp) (Hill & Stephens, 2021; Ogden, 1994). In this thesis, voltage-clamp was used, namely voltage was applied and the resulting current was measured.

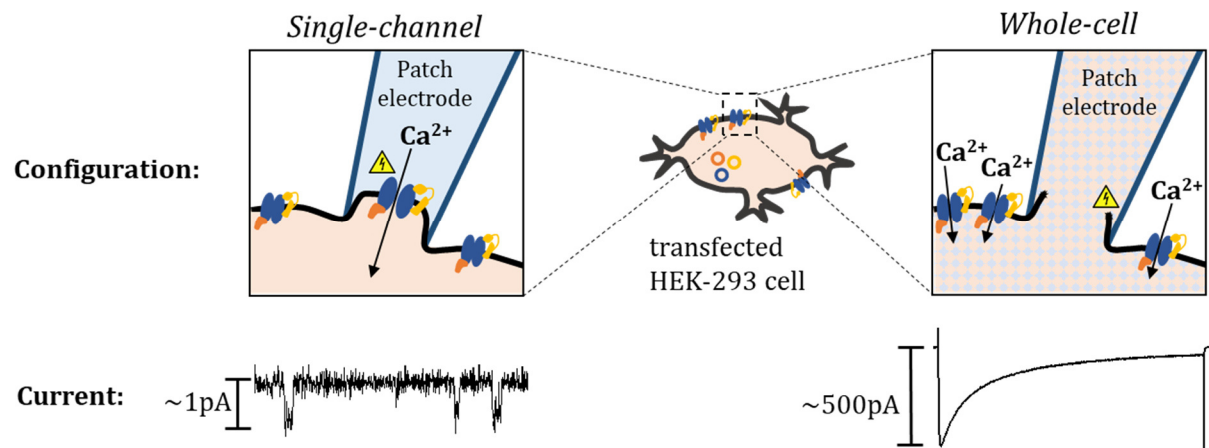


Figure 15. Schematics of cell-attached single-channel and whole-cell patch-clamp configuration and corresponding current. Schematic of how a transfected HEK-293 cell, expressing VGCCs in the cell membrane, is patched in the single-channel and whole-cell configuration showing $G\Omega$ seal and voltage induction, causing channel opening. *Below:* Current resulting from -20 mV stimulation in both configurations with approximate scale.

Principle of data acquisition

The components of a patch-clamp setup included a computer with acquisition software, pre- and main-amplifier, analog-to-digital (A/D) converter, bath electrode (silver chloride wire) and a patch electrode (pipette with solution on silver chloride wire). The patch electrode was moved by a micromanipulator to position it close to the membrane. The recording chamber was placed in a Faraday cage and on an anti-vibration table to shield it from electrical pickup and vibration. During a recording, the acquisition software was used to command a defined voltage to the patch to induce channel openings. The patch electrode and the bath electrode, which serves as a reference electrode, were connected to the pre-amplifier. The potential difference between these electrodes, caused by the ion flow through channels formed the signal. The current through ion channels is small (single-channel ~ 1 pA, whole-cell ~ 500 pA). Therefore, the pre-amplifier has the highest input resistance, thus stabilizing the signal. To minimize pickup noise, it was directly located at the patch electrode (“headstage”). Past the pre-amplifier, the signal could be further amplified or filtered via the main amplifier. The amplified signal was converted by the A/D converter and transmitted to the computer (Hill & Stephens, 2021; Hille, 2001; Ogden, 1994).

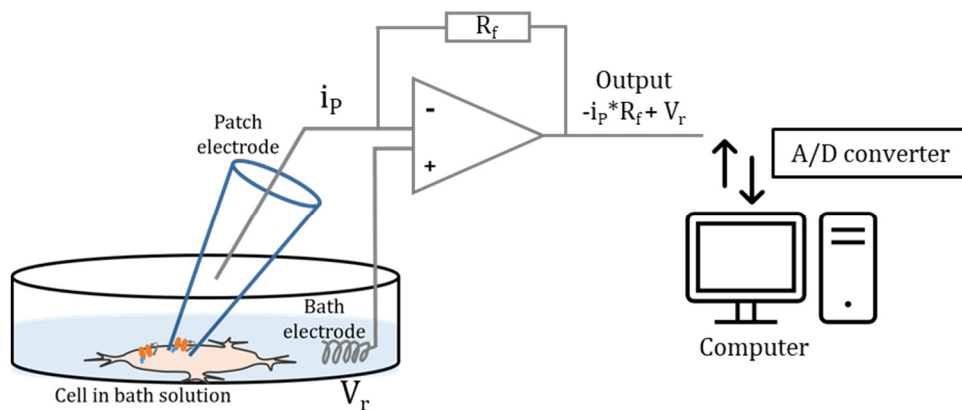


Figure 16. Schematic of data acquisition. Ion flow is registered as potential difference between patch electrode (i_p) and bath electrode (V_r). The amplification gain is set by the feedback resistor R_f . The output signal is formed by $-i_p * R_f + V_r$. Conversion and transmission through A/D converter and computer visualize the current (modified according to Ogden, 1994).

2.3.3. Single-channel patch-clamp recordings

Single-channel patch-clamp recordings were performed to investigate biophysical gating parameters modulating Cav1.3 activity via missense mutations L271H, A749T and F747S, as well as phosphorylation site S1475.

Single-channel patch-clamp recordings: Patch-clamp setup

Single-channel recordings were performed in the research group of PD Dr. Jan Matthes at the Department of Pharmacology at the University Hospital of Cologne. Figure 17 allocates components to the used equipment.

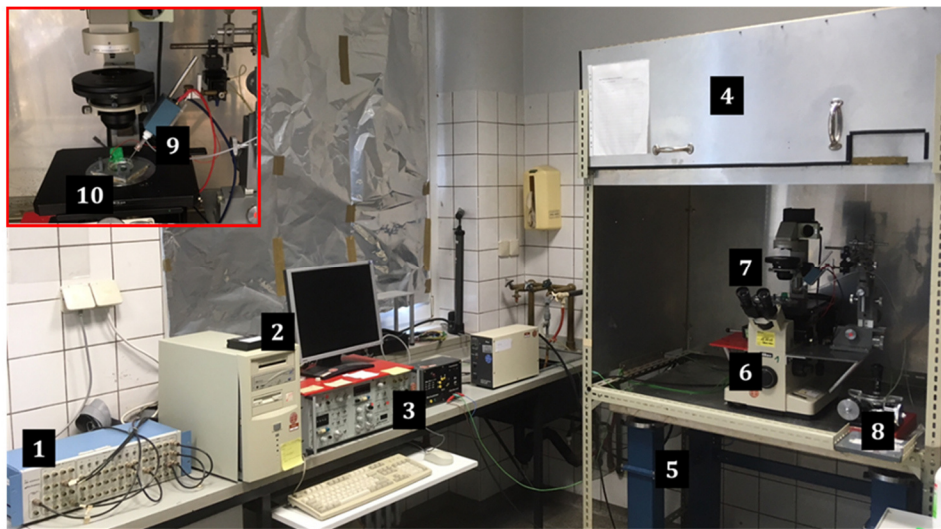


Figure 17. Components of single-channel patch-clamp setup. (1) A/D converter, (2) computer with acquisition software, (3) main amplifier, (4) Faraday cage, (5) anti-vibration table, (6) fluorescence microscope, (7) patching area – see red framed insert, (8) hydraulic micromanipulators, (9) patch electrode and pre-amplifier (headstage), (10) bath electrode in recording chamber.

Table 6. Overview of devices and manufacturers. Coating of the silver wires with a chloride layer for patch- and bath-electrode was performed via galvanic cell reaction: $\text{Ag} + \text{Cl}^- \leftrightarrow \text{AgCl} + \text{e}^-$ in 3 M KCl at 1 mA/cm².

Device	Manufacturer
Faraday cage and recording chamber	Self-supplied
Anti-vibration table	Barry Controls GmbH, Raunheim, Germany
Fluorescence microscope	Nikon Corporation Instrument Company, Japan
Hydraulic micromanipulator: MHW-103	Narishige International, Tokyo, Japan
Amplifier: Axopatch 1D	Molecular Devices & Axon Instruments, CA, USA
A/D converter: DMA interface	Molecular Devices & Axon Instruments, CA, USA
Computer (MS-DOS)	Microsoft, NM, USA
Acquisition software: pClamp 5.5	Molecular Devices & Axon Instruments, CA, USA
Silver wire: AG-15W	Science Products, Hofheim, Deutschland

Single-channel patch-clamp recordings: Patch pipettes

Micropipettes for single-channel and whole-cell recordings were made from borosilicate glass capillaries. Borosilicate glass can be handled at high temperatures, which meets the requirements for manufacturing pipettes for patch-clamp recordings (Ogden, 1994; Stanfield, 1987). Pipettes for single-channel recordings had an opening diameter of less than 1 μm , resulting in a pipette resistance of 7–9 M Ω . Hereto, they were manufactured on the experimental day in three steps: First, 8.5 cm long capillaries were pulled apart vertically in a double pull procedure (step 1: heating 12.40, step 2: heating 9.30). Second, the pipette tip was coated with hydrophobic Sylgard® and heat-hardened. Coating prevented stray capacitance at the pipette wall in solution, which would disturb single-channel currents (Fig. 18). Third, the opening edges were smoothed by fire-polishing.

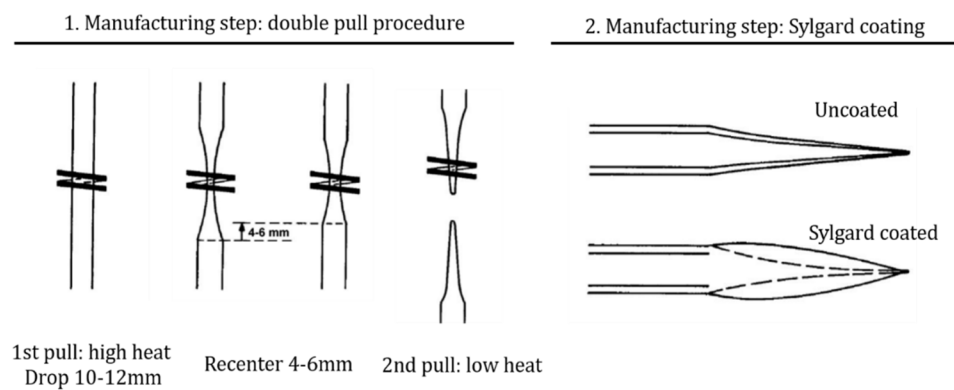


Figure 18. Schematic step 1 and 2 in single-channel pipette manufacturing. *Left:* Double pull procedure requires filament re-adjustment. *Right:* Sylgard coating (from Ogden, 1994).

Table 7. Overview of devices, fabricators and solutions for pipette manufacturing

Device	Specifications, Manufacturer
Vertical pipette puller	Type: PP-83, Narishige Scientific Instruments, Tokyo, Japan
Micropipette polisher	Type: MF-83, Narishige Scientific Instruments, Tokyo, Japan
Glass capillaries	Borosilicate, OD/ID: 1.7/1.3 mm, wall thickness 0.283 mm (thin), Hilgenberg, Malsfeld, Germany
Sylgard®	Sylgard® 184 Curing Agent Silicone Elastomere 100 μl per gram Sylgard® 184 Base Silicone Elastomer, Dow Corning, MI, USA

Single-channel patch-clamp recordings: Solutions

Patch-clamp experiments required a bath solution surrounding the cells and a pipette solution inside the patch electrode. The bath solution contained 120 mM K⁺, thus disabling its driving force and resulting in a membrane potential of 0 mV. Thereby physiological interference with the commanded voltage was avoided. The bath solution additionally contained ATP and glucose to retain cell viability and avoid rundown of

current. The pipette solution contained the charge carrier 15 mM Ba²⁺. LTCCs are permeable for both, Ca²⁺ and Ba²⁺, while they have a higher affinity for Ca²⁺ but a higher conductance for Ba²⁺ (Bourinet et al., 1996). Therefore, single-channel current amplitudes are two-fold larger with Ba²⁺ than with Ca²⁺, and Ba²⁺ can be used to detect openings over broader voltage ranges (Fig. 19). Additionally, 15 mM Ba²⁺ is among the lowest reported concentration to reliably measure Cav1.3 single-channel activity. Using lower concentrations reduces the amplitude size and using higher concentrations results in the surface charge screening effects, masking Cav1.3's unique feature of activation at lower voltages.

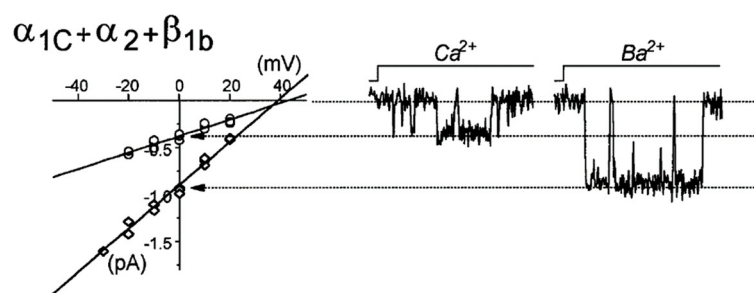


Figure 19. Single-channel conductance in dependence of charge carrier. Exemplary single-channel openings using 100 mM Ca²⁺ or Ba²⁺ and corresponding voltage-dependence indicating larger conductance for Ba²⁺ in Cav1.2 LTCCs (Bourinet et al., 1996).

Table 8. Overview single-channel solutions. Bath solution was freshly made on each experimental day. Pipette solution was stored for three months at 4°C.

	Chemical	Conc. [mM]	Manufacturer
Pipette solution	BaCl ₂ x 2H ₂ O	15	Roth, Karlsruhe, Germany
	HEPES	10	Sigma-Aldrich, St. Louis, USA
	TEA-Cl	120	Sigma-Aldrich, St. Louis, USA
	TEA-OH	pH adjustment: 7.4	Sigma-Aldrich, St. Louis, USA
	Osmolarity: 295 mOsm/L		
Bath solution	K-glutamate	120	Sigma-Aldrich, St. Louis, USA
	HEPES	10	Sigma-Aldrich, St. Louis, USA
	Glucose	10	Roth, Karlsruhe, Germany
	ATP disodium salt	1	Roth, Karlsruhe, Germany
	EGTA	2	Sigma-Aldrich, St. Louis, USA
	CaCl ₂ x 2H ₂ O*	1	Roth, Karlsruhe, Germany
	MgCl ₂ x 6 H ₂ O*	2	Merck, Darmstadt, Germany
	KCl*	25	Sigma-Aldrich, St. Louis, USA
	KOH	pH adjustment: 7.3	Sigma-Aldrich, St. Louis, USA
	Osmolarity: 308 mOsm/L		
	Device		Manufacturer
	pH-meter		Mettler Toledo, Gießen, Germany
	Osmometer: OM 807		Löser Messtechnik, Berlin, Germany

Single-channel patch-clamp recordings: Data collection

Single-channel recordings were obtained 48 to 72 hours post transfection at 19–23°C. Culture medium was removed and 3 ml bath solution was added. GFP or EGFP and RFP fluorescence labeled successfully transfected cells. Only attached, fluorescent cells with stretched shape and without surface debris were patched. The bath electrode was placed inside the dish in the recording chamber and the pipette was tip- and back-filled and slid on the silver chloride wire. Positive pressure was applied via tubing connected to the pipette holder to prevent pipette blockage. Upon positioning the pipette over the cell membrane, the pressure was released and the membrane was hoisted into the pipette by mild suction, forming the gigaohm seal $>1\text{ G}\Omega$. A repetitive depolarizing pulse was applied to test if the patch contained a channel, visible as a downshift from the baseline signal. Each voltage alteration caused capacity transients, which were compensated through the amplifier. Patches containing a channel were depolarized stepwise. The potential in the membrane patch (V_{patch}) results from the subtraction of the pipette potential (V_{ref}) from the cell's interior potential (V_{cell}): $V_{\text{patch}} = V_{\text{cell}} - V_{\text{ref}}$ (Hille, 2001; Stanfield, 1987).

In this thesis, patches were depolarized from -100 mV holding potential 180 times per test potential from -50 mV to +10 mV in 10 mV steps. Pulses lasted 150 ms, following 500 ms holding potential. The sampling rate was 10 kHz and the signal was filtered at 2 kHz, -3 dB with 4-pole Bessel, resulting in a point discrimination of 0.1 ms. *Clampex 5.5* was used as acquisition software. Notably, if vital channel activity was already detected at -50 mV, lower test potentials were included to determine the activity threshold.

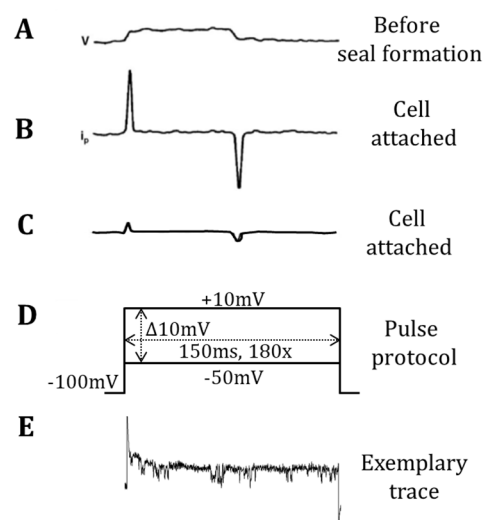


Figure 20. Transients and current during single-channel recordings. (A) Square current before seal formation. (B) Transients in the cell-attached configuration resulting from pipette stray capacity before and (C) after compensation. (D) Pulse protocol used in this thesis and (E) raw data trace of own recording. Modified from Odgen, 1994.

Single-channel patch-clamp recordings: Quality and inclusion criteria

Recordings had to fulfill the following pre-defined inclusion criteria:

1. Minimum trace criterion: ≥ 120 traces had to remain after eliminating traces disturbed by electrical or mechanical pickup.
2. Test potential criterion: Test potentials -50 mV to 0 mV had to be recorded gapless. If seal leakage terminated the recording prematurely, it was excluded completely.
3. Holding potential criterion: Recordings had to have a stable current in response to the holding potential (± 0.3 pA) and no baseline shift.
4. Channel amount criterion: Patches containing > 3 channels were excluded to reliably mathematically correct for the number of channels in the patch.
5. Transfection criterion: Data had to be obtained of ≥ 3 independent transfections for each group. All groups were recorded on the same experimental days.

Recordings were evaluated for these criteria and analyzed only after obtaining sufficient numbers of experiments to reduce analysis bias. Notably, being blinded for the mutant constructs L271H, A749T and F747S and their whole-cell effects while I performed single-channel experiments and analysis, further reduced experimental bias.

Single-channel patch-clamp recordings: Data analysis

Recordings were analyzed using pClamp 10.7 (Axon Instruments, Molecular Devices, Sunnyvale CA, USA). Initially, raw data was recorded with pClamp 5.5 and had to be exported to be compatible with pClamp 10.7.

Recordings were subtracted by the average leakage across blank traces and analyzed for openings. Each downshift from the baseline reaching 50 % of the voltage-specific amplitude level was considered a channel opening. By this half-height criterion also not fully resolved openings (based on the sampling rate) were included (Herzig et al., 2007). Detected openings were stacked onto a spread sheet, containing information about trace number, level, start and end time, duration and amplitude (Fig. 21). This information was used to calculate single-channel gating parameters.

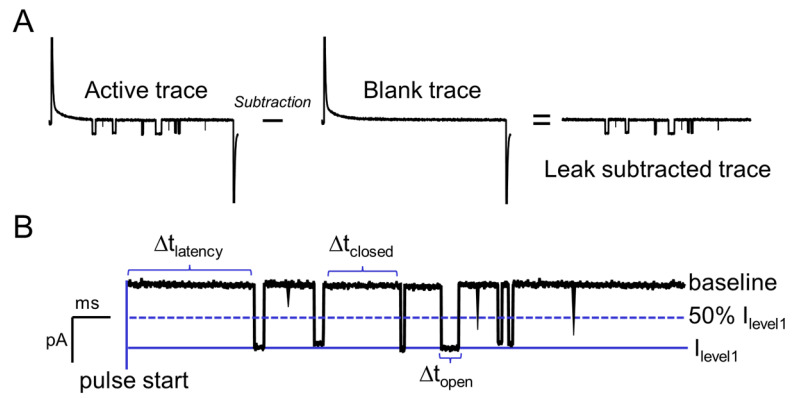


Figure 21. Schematical leak subtraction and event analysis. (A) Leak subtraction. **(B)** Currents with time elapsed between pulse start and first channel opening ($\Delta t_{\text{latency}}$), time between openings (Δt_{closed}) and opening duration (Δt_{open}), showing the half-height criterion.

The single-channel parameters provide information on the channel in its open, closed and inactivated state or transitions between them. Figure 22 schematically shows the three channel states, which are minimally required to describe the single-channel gating behavior. For example, the channel availability describes the arousal of the channel to transition from the closed into the open state. Within the active traces, the open probability describes the proportion the channel spends in the open state. Open and closed times further reveal how long the channel stays in either state on average. Additionally, the latency measures the time elapsed until the channel activates upon depolarization, i.e. its first transition from the closed into the open state. The ensemble average current includes all these parameters and shows the channel activity over time.

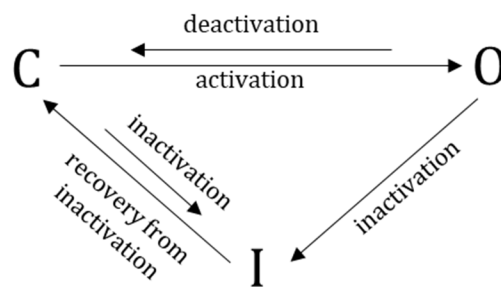


Figure 22. Schematic of transitions into gating states. O: open or activated states, C: closed or resting state, I: inactivated state (modified from Karmazina & Lacinova, 2010).

Single-channel gating parameters were calculated by a custom written Python script (supplemental S2), Microsoft Excel and GraphPad Prism 9 (GraphPad Software, Inc., CA, USA). Equations (1) – (6) according to Herzig et al. (Herzig et al., 2007).

- (1) Fraction of active sweeps (f_{active}): Reports the percentage of all traces containing at least one channel opening. f_{active} represents the channel availability at a given test potential.

$$f_{active} = 100 * \frac{Ma}{M0} \quad [\%] \quad \text{Corrected for } k > 1 : \quad f' = 1 - \sqrt[k]{1 - f_{active}}$$

- (2) Mean open probability (P_{open}): Percentage of open state occupancy in active traces at a given test potential.

$$P_{open} = 100 * \frac{\Sigma t_{open}}{Ma * t0} \quad [\%] \quad \text{Corrected for } k > 1 : \quad P'_{open} = \frac{P_{open}}{k} * \frac{f}{f'}$$

- (3) Mean open time (MOT): Average duration of channel openings at a given test potential.

$$MOT = \frac{\Sigma t_{open}}{\Sigma openings} \quad [\text{ms}]$$

- (4) Mean first latency (MFL): Average duration until first opening upon depolarization in active sweeps at a given test potential. Calculated usually for $k = 1$ only, as openings of individual channels cannot be distinguished in $k > 1$ patches.

$$MFL = \frac{\Sigma t_{latency}}{Ma} \quad [\text{ms}]$$

- (5) Mean closed time (MCT): Mean time interval between two consecutive openings at a given test potential. Calculated usually for $k = 1$ only, as openings of individual channels cannot be distinguished in $k > 1$ patches.

$$MCT = \frac{\Sigma t_{closed}}{\Sigma closures} \quad [\text{ms}]$$

- (6) Ensemble average current: Mean current flowing at a given time after onset of a depolarizing test pulse.

$$I_{sum}(t) = \frac{\Sigma_{m=1}^{M0} i(\Delta t_j) m}{M0} \quad [fA]$$

- (7) Open time constants (τ_{open}): Open time histograms plotted according to Sigworth and Sine (Sigworth & Sine, 1987) with $\log_{10} open\ times$ to \sqrt{count} , fitted by maximum likelihood fit to obtain open time constants per test potential.

$$f(t) = \sum_{i=1}^n P_i e^{[\ln(t) - \ln(\tau_i)]} e^{\ln(t) - \ln(\tau_i)}$$

- (8) Coupling coefficient (κ): Coupled Markov chain model reporting probability of coupled channel openings on a scale of 0 to 1 according to Navedo et al. 2010, based on Chung & Kennedy, 1996.

(9) Conductance and reversal potential: The conductance (in pS) is the slope of the linear regression of single-channel amplitudes versus test potentials. The x-intercept of this regression indicates the reversal potential (V_{rev}).

$$V_{rev} = \frac{0 - I_{0mV}}{dV}$$

(10) Voltage of half-maximal activation ($V_{0.5 act}$): f_{active} fitted by Boltzmann sigmoidal equation reveals the potential at which of half-maximal activation occurs.

$$I_V = \frac{1}{1 + e^{\frac{V_{0.5} - V}{dV}}}$$

Legend:

k = number of channels in patch, m = trace index, $i[\Delta t_j]$ = time-dependent amplitude of the j^{th} first open levels, t_0 = pulse duration, M_0 = total number of traces, M_a = number of active traces, I_V = current at voltage V, I_{0mV} = current at 0mV, dV = slope, $V_{0.5}$ = voltage of half-maximal activation, V = voltage.

Single-channel patch-clamp recordings: Statistical analysis and data visualization

Single-channel parameters were tested for normal distribution by D'Agostino-Pearson K2 normality test (D'Agostino, 1986). After confirming normal distribution and equal variance, data was analyzed by parametric tests. Differences were considered statistically significant with p-values $p \leq 0.05$. Two independent groups were compared by calculating unpaired Student's t-test. Multiple comparisons were corrected by Bonferroni-Dunn's test. Three independent groups were compared by calculating one-way ANOVA. Only if the ANOVA indicated statistical significance, post hoc correction was applied by Bonferroni's multiple comparisons test.

Data was visualized either as mean with 95 % confidence interval (CI) or as boxplots with whiskers from min to max with all data points. Figures report p-values of post hoc correction by Bonferroni's multiple comparisons test following statistically significant ANOVA. Values are reported as mean \pm standard error of the mean (SEM), with up to two decimal digits and p-values are reported with up to three decimal digits, thus smaller p-values will be reported as $p < 0.001$. Detailed tables are included in the supplemental material (S5 and S6), reporting all data values, results of unpaired t-tests, results of ANOVA with F-value and degrees of freedom F (DFn, DFd), and p-values of post hoc correction by Bonferroni's multiple comparisons test.

2.3.4. Whole-cell patch-clamp recordings

Whole-cell patch-clamp recordings were performed to investigate S1475 modulation of Cav1.3 gating.

Whole-cell patch-clamp recordings: Patch-clamp setup

Whole-cell recordings were obtained in the research group of PD Dr. Jan Matthes. Figure 23 allocates components to equipment. Due to temporary equipment deficiencies, some recordings were also obtained at the setup of the research group of Prof. Dr. Dirk Isbrandt. Here data was recorded with pClamp 11, Axopatch 700B and Digidata 1550 (Molecular Devices & Axon Instruments, CA, USA).

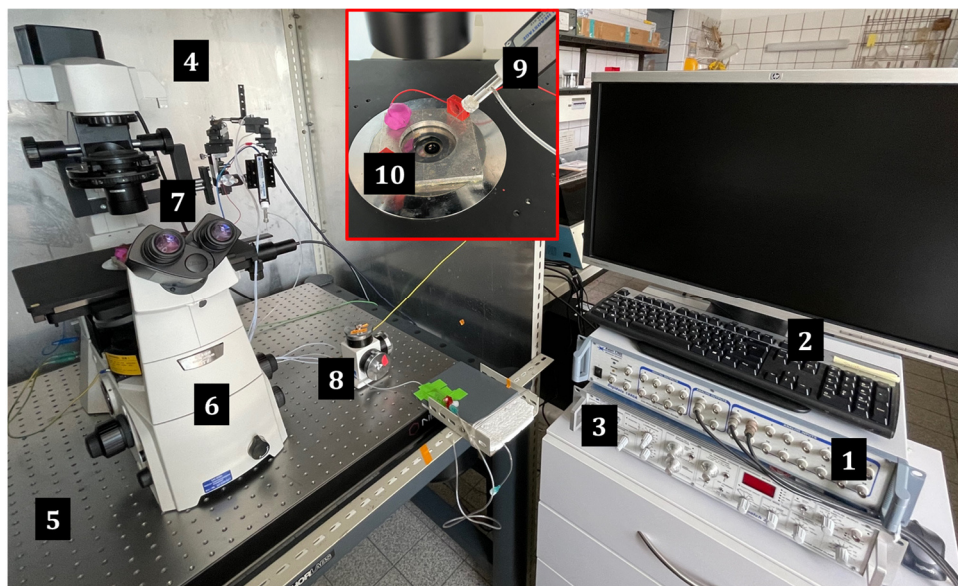


Figure 23. Components whole-cell patch-clamp setup AG Matthes. (1) A/D converter, (2) computer with acquisition software, (3) main amplifier, (4) Faraday cage, (5) anti-vibration table, (6) fluorescence microscope, (7) patching area – see red framed insert, (8) hydraulic micromanipulators, (9) patch electrode and pre-amplifier (headstage), (10) bath electrode in recording chamber.

Table 9. Overview of devices and manufacturers of whole-cell patch-clamp setup.

Device	Manufacturer
Faraday cage and recording chamber	Self-supplied
Anti-vibration table	Thorlabs, NJ, USA
Fluorescence microscope: Eclipse Ti	Nikon Corporation Instrument Company, Japan
Hydraulic micromanipulator: MHW-103	Narishige Scientific Instruments, Tokyo, Japan
Amplifier: Axopatch 200B	Molecular Devices & Axon Instruments, CA, USA
Headstage: CV 203BU	Molecular Devices & Axon Instruments, CA, USA
A/D converter: Digidata 1440A	Molecular Devices & Axon Instruments, CA, USA
Computer (Windows 10)	Microsoft, NM, USA
Acquisition software: Clampex 10.7	Molecular Devices & Axon Instruments, CA, USA
Silver wire AG-15W (Chloride layer via galvanic cell: 3 M KCl, at 1 mA/cm ²)	Science Products, Hofheim, Deutschland

Whole-cell patch-clamp recordings: Patch pipettes

Borosilicate glass capillaries were manufactured to obtain a pipette resistance of 2.5–5 M Ω . First, 8.5 cm long capillaries were pulled apart horizontally in a triple-pull-procedure. The heating steps were -5 to +30°C of the filament ramp temperature and at mid-point velocity. Second, pipettes were fire-polished over a heated platinum wire.

Table 10. Overview of devices and manufacturers for pipette manufacturing.

Device	Manufacturer
Micropipette Puller: P-97	Sutter Instrument, CA, USA
Box-filament: 3.0x3.0 mm (FB330B)	Sutter Instrument, CA, USA
Micropipette polisher: MF-83	Narishige Scientific Instruments, Tokyo, Japan
Borosilicate glass capillaries	Glass: OD/ID: 1.7/1.3 mm, wall thickness 0.283 mm (thin), Hilgenberg, Malsfeld, Germany

Whole-cell patch-clamp recordings: Solutions

Whole-cell currents were recorded with physiological extracellular charge carrier at physiological concentrations (2 mM Ca²⁺). Additionally, 2 mM Ba²⁺-currents were recorded to distinguish between Ca²⁺- and voltage-dependent gating. The pipette solution contained glucose and ATP to retain cell viability and avoid rundown, as the pipette interior becomes continuous with the cell cytoplasm.

Table 11. Overview of solutions and composition. Bath solution was prepared fresh on experimental days. Pipette solution was aliquoted and stored for up to three months at -20°C.

	Chemical	Conc. [mM]	Manufacturer
Bath solution	CaCl ₂ x 2H ₂ O or BaCl ₂ x 2H ₂ O	2	Roth, Karlsruhe, Germany
	CsCl	95	Roth, Karlsruhe, Germany
	TEA-Cl	50	Sigma-Aldrich, St. Louis, USA
	Glucose	12	Roth, Karlsruhe, Germany
	HEPES	10	Sigma-Aldrich, St. Louis, USA
	MgCl ₂ x 6H ₂ O	1	Merck, Darmstadt, Germany
	CsOH	pH adjustment: 7.3	Sigma-Aldrich, St. Louis, USA
	Osmolarity: 311 mOsm/L		
Pipette solution	CsCl	140	Roth, Karlsruhe, Germany
	Mg-ATP	4	Sigma-Aldrich, St. Louis, USA
	EGTA	10	Sigma-Aldrich, St. Louis, USA
	HEPES	9	Sigma-Aldrich, St. Louis, USA
	MgCl ₂ x 6H ₂ O	1	Merck, Darmstadt, Germany
	CsOH	pH adjustment: 7.35	Sigma-Aldrich, St. Louis, USA
	Osmolarity: 301 mOsm/L		
Devices	pH-meter		Mettler Toledo, Gießen, Germany
	Osmometer: OM 807		Löser Messtechnik, Berlin, Germany

CaMKII activation and inhibition

To investigate, whether S1475 was phosphorylated by CaMKII, CaMKII was either co-expressed in a constitutively active form (CaMKII₁₋₂₉₀) or inhibited by KN-93. CaMKII₁₋₂₉₀ is a constitutively active mutant of CaMKII α . It is truncated after amino acid 290 and thus lacks the self-regulatory region and is constitutively active (Sun et al., 1994). pRSV-CaMKII₁₋₂₉₀ plasmid was a gift from Richard Maurer (Addgene plasmid #45065). KN-93 is a competitive and reversible CaMKII inhibitor (K_i : 370 nM). It is selective for CaM-kinases relative to PKA and PKC. KN-93 inhibits CaMKII autophosphorylation and thereby activation of the enzyme. KN-93 concentrations ranging between 0.5 and 10 μ M were reported to inhibit CaMKII (Gao et al., 2006; Pellicena & Schulman, 2014; Sumi et al., 1991; Tokumitsu et al., 1990). Here, 1 μ M KN-93 was sufficient to inhibit CaMKII activity. KN-93 was diluted in DMSO and added to the bath solution. The final KN-93 concentration was 1 μ M and 0.07 % DMSO. Control experiments were performed with bath solution and 0.07 % DMSO without KN-93. Recordings were obtained at comparable incubation durations (\sim 10 min) to exclude time-dependent effects of KN-93 incubation on Cav1.3 currents.

Table 12. Overview of KN-93 solution composition.

KN-93 was stored light-protected at -80°C, dilutions were prepared fresh on experimental days.

Chemical	Concentration	Manufacturer
KN-93 (CAS 139298-40-1)	1 μ M	Calbiochem-Millipore, CA, USA
DMSO	0.07 %	Sigma-Aldrich, St. Louis, USA

Whole-cell patch-clamp recordings: Data collection and pulse protocols

Since whole-cell configuration was reached by rupturing the membrane in the cell-attached configuration, seal formation was the same as mentioned, followed by strong suction. Rupturing the membrane was indicated by appearance of wide capacity transients. These were composed of whole-cell capacitance (C_M) and series resistance (R_S). The whole-cell capacitance is defined as $C_M = \epsilon_o A/d$, including lipid properties (ϵ_o) and thickness (d) of the membrane, thus giving an estimate of the cell surface (A). The series resistance is composed of the pipette resistance and the access resistance, which results from accessing the cell interior with the pipette. A command voltage to the membrane is interfered by the series resistance, and changes in the command voltage are delayed by time-constant τ resulting from whole-cell capacitance and series resistance $\tau = C_M * R_S$. Accordingly, whole-cell capacitance and series resistance needed to be

compensated to ensure clamping the membrane to the commanded voltage. The recorded whole-cell current was normalized to the cell size indicated by C_M , resulting in current density (Ogden, 1994; Rosholm et al., 2021).

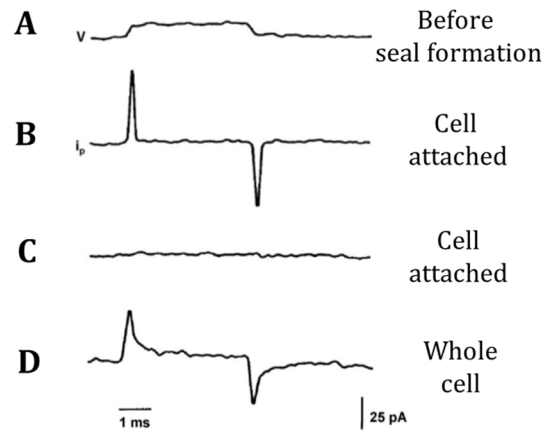


Figure 24. Transients during whole-cell configuration. (A) Square current in response to 5 mV pulse before seal formation. (B) Transient currents in the cell-attached configuration resulting from pipette stray capacity before and (C) after compensation. (D) Wide capacity transients indicating access to cell interior (modified from Ogden, 1994).

To investigate Cav1.3 gating modulation, three different pulse protocols were applied:

- (1) Current-voltage relationship (IV-protocol): From -100 mV holding potential, cells were depolarized for 500 ms from -80 mV to +50 mV in 10 mV steps, followed by 50 ms pulse to -70 mV and a 50 ms pulse to -120 mV as leak subtraction reference. This resulted in 14 traces per recording, with 10 kHz sampling rate, 2 kHz lowpass filter (Fig. 25).

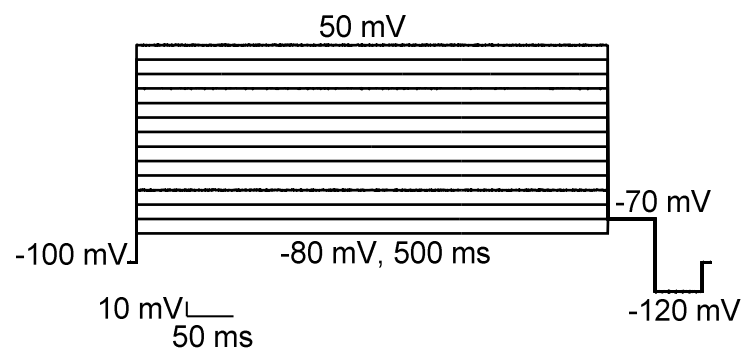


Figure 25. Schematic of IV-protocol.

(2) Steady-state inactivation (SSI-protocol): From -90 mV holding potential, cells were depolarized for 2 s from -90 mV to +20 mV in 10 mV steps, each time followed by a 200 ms pulse to 10 mV, followed by a 100 ms pulse to -120 mV and a 100 ms pulse to -70 mV as leak subtraction reference. This resulted in 12 traces per recording with 10 kHz fast and 5 kHz slow sampling rate, 2 kHz lowpass filter (Fig. 26).

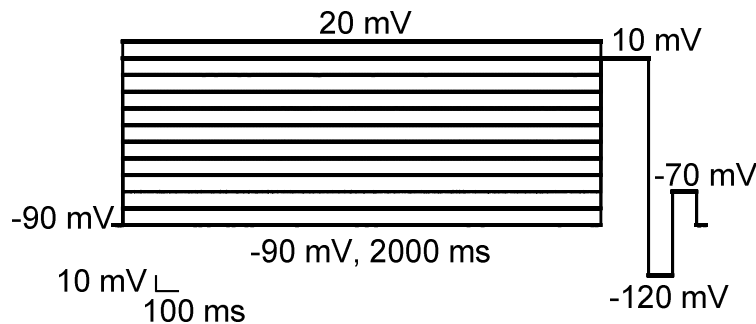


Figure 26. Schematic of SSI-protocol.

(3) SAN-like action potential (SAN-protocol): To measure Cav1.3 current induced by SAN-like action potential, cells were stimulated by 5 times 2 stimulus waves designed after human SAN-AP (Verkerk et al., 2007). Peak to peak duration of 0.8 s simulated a heart rate of 75 bpm. Sampling rate 50 kHz, 500 Hz lowpass filter (Fig. 27).

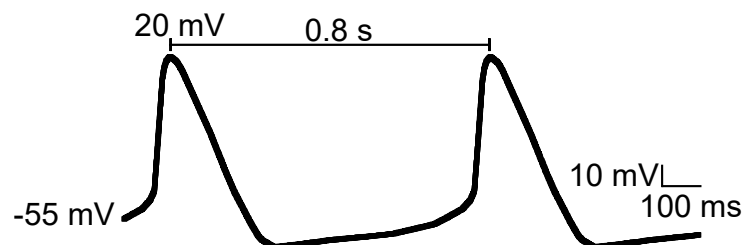


Figure 27. Schematic of SAN-protocol.

Whole-cell patch-clamp recordings: Quality and inclusion criteria

The whole-cell data had to fulfill the following pre-defined inclusion criteria:

1. Protocol criterion: Recordings had to be obtained in the order IV → SSI → SAN for the same cell. Each protocol had to be completed, namely 14 traces for IV, 12 traces for SSI and 5 traces for SAN. Further, SSI and SAN recordings were only included if the corresponding IV was included. If leakage terminated the recording prematurely, only completed protocols were included, resulting in different numbers of experiments (IV > SSI > SAN).

2. Holding potential and leak criterion: Recordings had to have a stable current at holding potential (± 50 pA) and a leak < 20 %, comparing raw and leak-subtracted data.

3. Resistance criterion: Recordings had to have an access resistance of $R_a \leq 20$ M Ω , because at 20 M Ω the ΔV between the commanded voltage and the actual membrane potential was < 2 mV. Recordings had no restrictions regarding whole-cell capacitance C_M . In fact, varying C_M values were included to exclude cell size-dependent effects on whole-cell currents.

4. Transfection criterion: Data had to be obtained from ≥ 3 independent transfections for each group. All groups were recorded on the same experimental days.

Recordings were evaluated for these criteria and analyzed only after obtaining sufficient numbers of experiments to reduce analysis bias.

Whole-cell patch-clamp recordings: Data analysis

Whole-cell parameters provide information about the gating states and the transition between them for the whole population of channels in the membrane. For example, the peak current density reports the maximum current through all open channels in response to depolarization and the inactivation reports the transition from the open state into the inactivated or closed state over time.

Recordings were analyzed using pClamp10.7 (Axon Instruments, Molecular Devices, Sunnyvale CA, USA). Leak and capacity currents were subtracted offline using Microsoft Excel and data was fitted using GraphPad Prism 9 (GraphPad Software, Inc., CA, USA).

- (1) Current-voltage relationship: Peak current in response to depolarization was normalized to cell size, thus indicating current density (pA/pF) and fitted by Boltzmann-Ohm equation according to Karmazanova and Lacinova (Karmazanova & Lacinova, 2010) to obtain IV-curves.

$$I_V = G_{max} * \frac{(V - V_{rev})}{1 + \exp\left(\frac{V_{0.5 act} - V}{dV}\right)}$$

- (2) Voltage-dependent activation kinetics: Conductance at each test potential was normalized to its maximum (G/G_{max}) and fitted by Boltzmann equation to obtain activation slope and voltage of half-maximal activation ($V_{0.5 act}$).

$$G = \frac{I}{V - V_{rev}}$$

- (3) Steady-state inactivation: Current remaining at 10 mV after pre-pulses, normalized to its maximum (I/I_{\max}) and fitted by Boltzmann equation to obtain inactivation slope, non-inactivating current and voltage of half-maximal inactivation ($V_{0.5 \text{ inact}}$).

$$\frac{I_V}{I_{\max}} = \frac{1}{1 + e^{\frac{V - V_{0.5 \text{ inact}}}{dV}}} + I_0$$

- (4) Remaining current at 300 ms (r_{300}): Percentage of peak current remaining after 300 ms depolarization to voltage V . Amount of time-dependent inactivation at 300 ms thus equals $1 - r_{300}$.

$$r_{300} = 100 * (I_{\text{peak}(V)} - I_{300(V)})$$

- (5) Calcium-dependent inactivation: Subtracting remaining current at 300 ms of Ca^{2+} recordings from that of Ba^{2+} recordings reflects amount of CDI.

$$f = r_{300}(\text{Ba}^{2+}) - r_{300}(\text{Ca}^{2+})$$

Legend:

I_V = current at voltage V , V_{rev} = reversal potential, G_{\max} = maximum conductance, $V_{0.5}$ = voltage of half-maximal (in-) activation, dV = slope factor of Boltzmann term, I_{\max} = maximum current, I_0 = non-inactivating current, $I_{\text{peak}(V)}$ = peak current density at voltage V , $I_{300(V)}$ = current after 300 ms depolarization to voltage V .

Whole-cell patch-clamp recordings: Statistical analysis and data visualization

Whole-cell gating parameters were tested for normal distribution by D'Agostino-Pearson K2 normality test (D'Agostino, 1986). After confirming normal distribution and equal variance, data was analyzed by parametric tests. Differences were considered statistically significant with p -values $p \leq 0.05$. Three independent groups were compared by calculating one-way ANOVA. Only if the ANOVA indicated statistical significance, post hoc correction was applied by Bonferroni's multiple comparisons test.

Data was visualized either as mean with 95% confidence interval (CI) or as boxplots with whiskers from min to max with all data points. Figures report p -values of post hoc correction by Bonferroni's multiple comparisons test following statistically significant ANOVA. Values are reported as mean \pm SEM, with up to two decimal digits and p -values are reported with up to three decimal digits, thus smaller p -values will be reported as $p < 0.001$. Detailed tables are included in the supplemental material (S7), reporting data values, results of ANOVA with F -value and degrees of freedom F (DFn, DFd), and p -values of post hoc correction by Bonferroni's multiple comparisons test.

3. Results

As stated, the aim of this thesis is to investigate Cav1.3 gating modulation from a physiological and pathophysiological perspective with a human emphasis. The results on Cav1.3 pathophysiological gating modulation by disease-associated missense mutations are presented first, followed by the physiological perspective reporting gating modulation depending on phosphorylation site S1475.

3.1. Cav1.3 gating modulation by disease-associated *CACNA1D* missense mutations

As mentioned, L271H, A749T and F747S are *CACNA1D* germline *de novo* missense-mutations associated with neurodevelopmental disorders, with (L271H and F747S) or without (A749T) endocrine and other symptoms (Fig. 28). In a collaboration with Prof. Dr. Jörg Striessnig and his research group at the University of Innsbruck, we functionally characterized Cav1.3 gating modulation by these mutations. The whole-cell recordings obtained by Jörg Striessnig's group (not part of this thesis) indicate gain-of-function alterations. However, whole-cell currents are a product of the number of channels in the membrane (N), and the conductance (i), availability (f_{active}) and open probability (P_{open}) at single-channel level ($I = N * i * f_{active} * P_{open}$) (Karmazinova & Lacinova, 2010). Therefore, I performed single-channel recordings to unmask the biophysical gating properties of the respective Cav1.3 mutations leading to the observed alterations on whole-cell level.

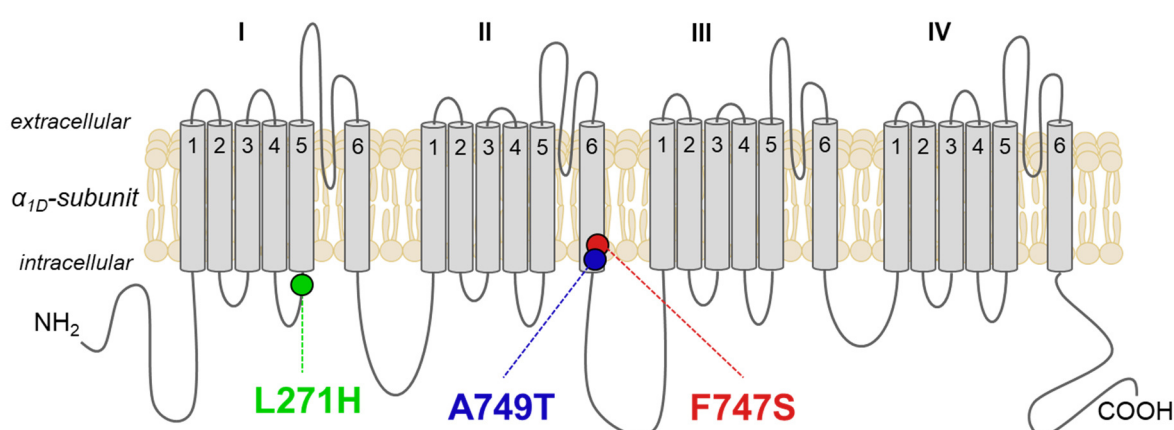


Figure 28. Location of disease associated missense mutations L271H, A749T, and F747S.

3.1.1. L271H missense mutation shifted Cav1.3 single-channel gating towards more hyperpolarized voltages

To characterize L271H gating modulation of Cav1.3, single-channel gating parameters were calculated and compared to WT. Hereto, availability, open probability, conductance, open and closed times, latency, reversal potential and voltage of half-maximal activation were included. As mentioned, detailed tables listing data values and p-values are included in the supplemental material (S5).

The exemplary traces and corresponding ensemble average currents of the single-channel experiments visually displayed an increase of single-channel activity for L271H compared to WT (Fig. 29). Interestingly, despite the obvious increase in activity, the representative traces also revealed a smaller unitary current amplitude for L271H compared to WT (at -20 mV, WT: -0.88 ± 0.02 pA, L271H: -0.67 ± 0.01 pA, $p < 0.001$).

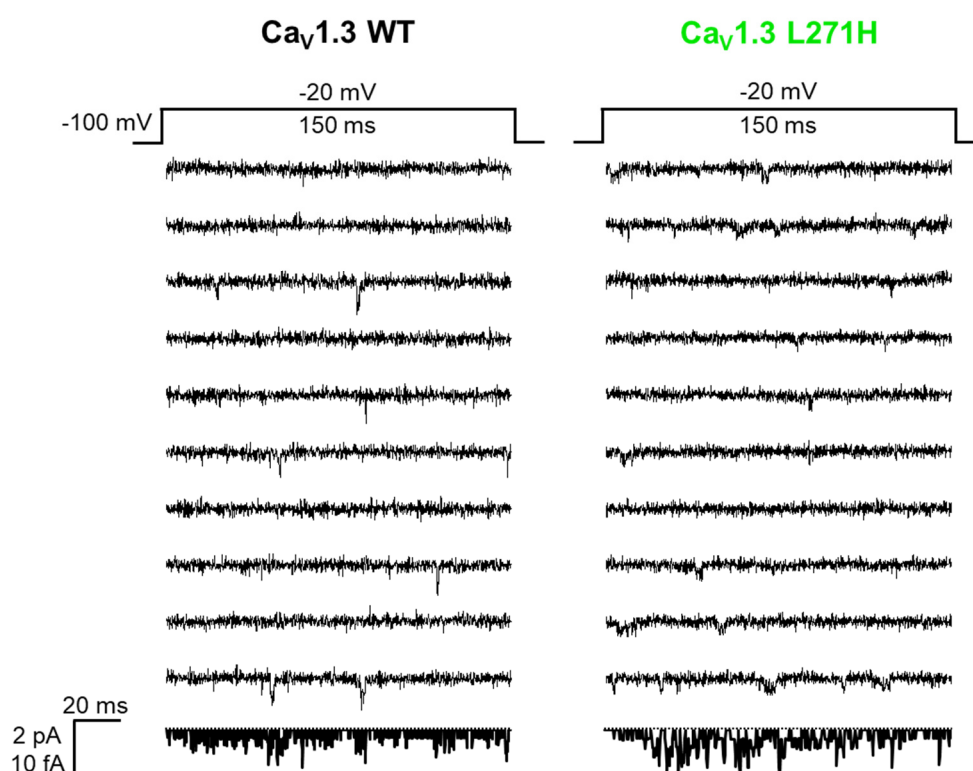


Figure 29. Exemplary traces and ensemble average current of Cav1.3 WT and L271H single-channel recordings. Ten exemplary and consecutive traces of 15 mM Ba²⁺ currents at -20 mV and corresponding ensemble average current below dotted line. Schematic of pulse protocol shown above. Traces show increased single-channel activity for L271H, despite smaller current amplitude. Scale bar indicates 20 ms and 2 pA for individual traces or 10 fA for ensemble average currents.

In line with the visual observations, L271H had an increased single-channel availability in terms of fraction of active sweeps (f_{active}) at all test potentials (Fig. 30). For example, at -20 mV test potential, WT availability was at 65 %, while channel availability of L271H was at 90 % ($p < 0.001$).

The corresponding voltage of half-maximal activation ($V_{0.5\text{act}}$) was shifted to more hyperpolarized voltages by ~ 10 mV (WT: -24.54 ± 0.70 mV, L271H: -33.24 ± 1.02 mV, $p < 0.001$). This means that L271H channels were aroused to transition into the open state by less depolarization compared to the WT. Interestingly, values of single-channel availability converged when “correcting” for the observed shift in activation (e.g. WT: 31.38 ± 1.52 % at -30 mV and L271H: 32.75 ± 5.20 % at -40 mV).

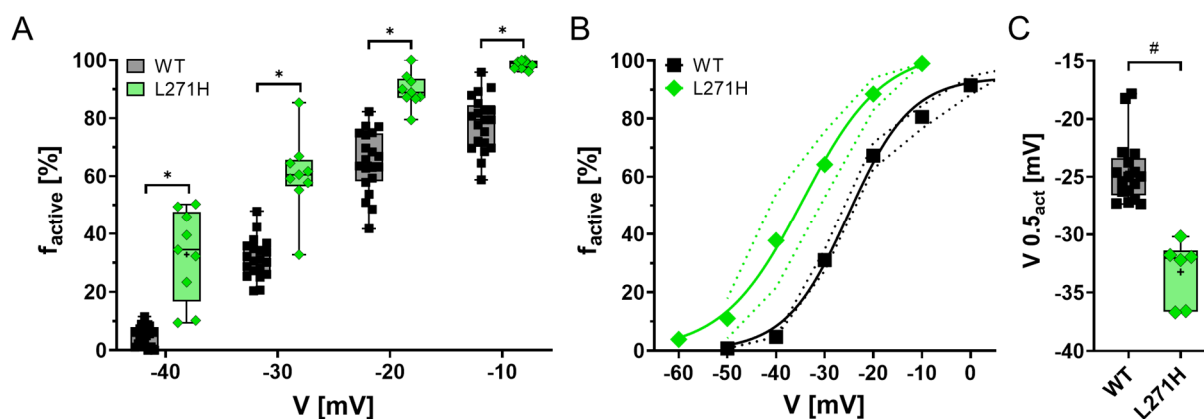


Figure 30. Comparing single-channel availability for L271H and WT. (A) Fraction of active sweeps (f_{active}) is increased for L271H across test potentials (WT: $n = 20$, L271H: $n = 9$). **(B)** f_{active} fitted by Boltzmann-equation and **(C)** corresponding $V_{0.5\text{act}}$ are shifted towards more hyperpolarized potentials (WT: $n = 17$, L271H: $n = 6$). Charge carrier: 15 mM Ba^{2+} . Data shown as mean and 95 % CI or as boxplots from min to max with all data points, + marks mean. * $p \leq 0.05$ in Bonferroni-Dunn’s test following multiple unpaired t-test and # $p \leq 0.05$ in unpaired t-test.

Analyzing the open probability (P_{open}) revealed an increase for L271H compared to WT across test potentials (Fig. 31). At -20 mV, L271H displayed a nearly two-fold higher P_{open} compared to WT (WT: 0.58 ± 0.04 %, L271H: 1.14 ± 0.16 %, $p < 0.001$). Similar to f_{active} , when considering the shift in voltage-dependent activation, P_{open} of L271H and WT nearly converged, except for -40 mV. Since L271H displayed an increased P_{open} but similar mean open time (MOT) compared to WT, the differences in P_{open} resulted from an increased opening frequency. Affirmative hereof was a decreased mean first latency (MFL) and a decreased mean closed time (MCT) for L271H. This means that within active traces, L271H channels spent more time in the open state due to a more frequent transition into the open state compared to the WT.

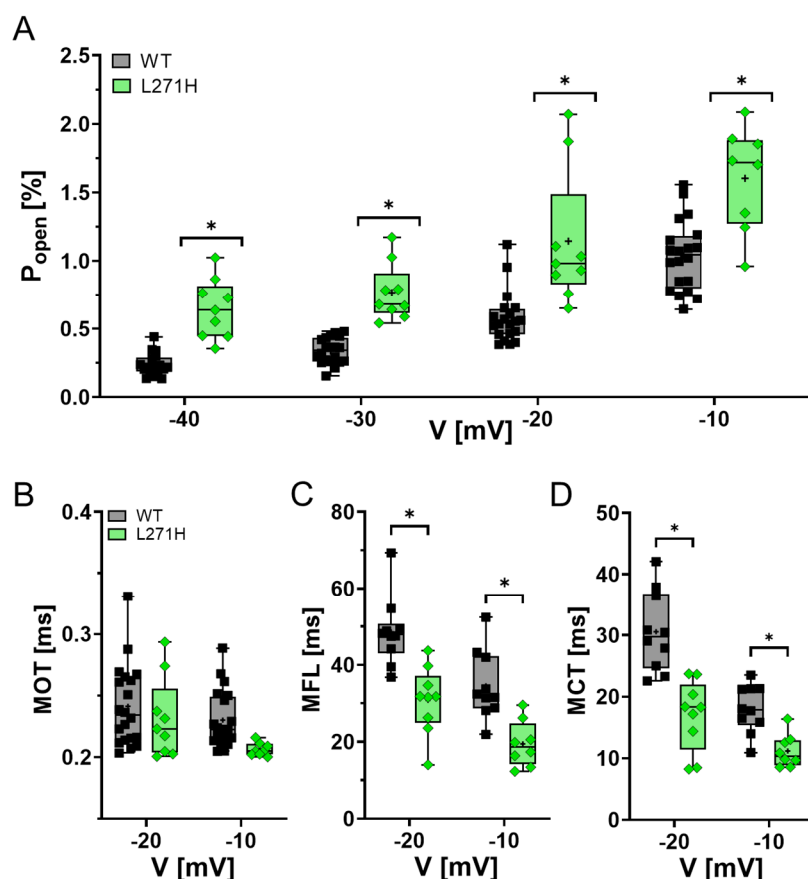


Figure 31. Comparison of open probability, mean open time, mean first latency and mean closed time. (A) Open probability (P_{open}) is increased for L271H, while (B) mean open time (MOT) is similar (WT: $n = 20$, L271H: $n = 9$). (C) Mean first latency (MFL) and (D) mean closed time (MCT) are decreased for L271H (WT: $n = 10$, L271H: $n = 9$). Charge carrier: 15 mM Ba^{2+} . Data shown as boxplots from min to max with all data points, + marks mean. * $p \leq 0.05$ in Bonferroni-Dunn's test following multiple unpaired t-test.

Conductance is defined as the slope of the linear regression of the single-channel current amplitudes plotted against the membrane potential. It thus describes the relationship between the current through a single-channel and the voltage as a major driving force. Despite smaller current amplitudes, the single-channel conductance of L271H was similar to WT (WT: 11.02 ± 0.67 pS, L271H: 10.23 ± 0.78 pS, $p = 0.489$). The smaller current amplitudes resulted in a parallel-leftward shift of linear regression for L271H compared to WT. The corresponding reversal potential (V_{rev}) of L271H was shifted 16 mV towards less positive values, however, not reaching statistical significance (WT: 64.34 ± 5.22 mV, L271H: 48.34 ± 4.88 mV, $p = 0.076$) (Fig. 32).

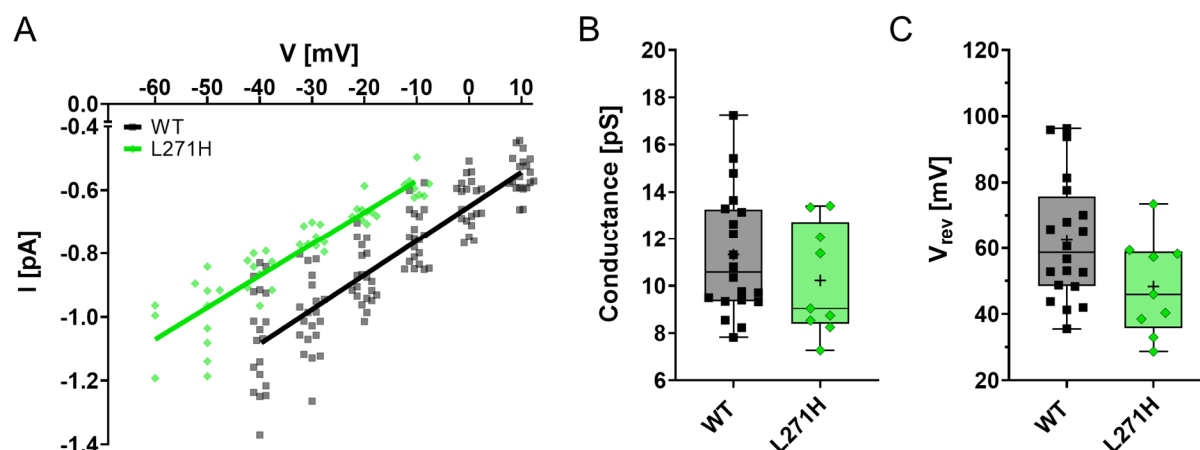


Figure 32. Comparison of current amplitudes, conductance and reversal potential. (A) Linear regression through current amplitudes is parallel leftward-shifted for L271H. (B) Conductance is similar for WT and L271H. (C) X-intercept of linear regression (reversal potential V_{rev}) is non-significantly shifted for L271H ($p = 0.076$). WT: $n = 20$, L271H: $n = 9$. Charge carrier: 15 mM Ba^{2+} . Data shown as boxplots from min to max with all data points, + marks mean. No statistically significant differences detected in unpaired t-test.

The radar chart in figure 33 summarizes Cav1.3 single-channel gating modulation by missense mutation L271H. The radar chart displays an increased single-channel activity of L271H compared to WT. Conductance and mean open time were unaffected. First latency and closed times were decreased, while availability, peak current and P_{open} were increased for L271H. The increase in activity at a given potential can be sufficiently explained by a shift of voltage-dependent activity towards more hyperpolarized potentials for L271H.

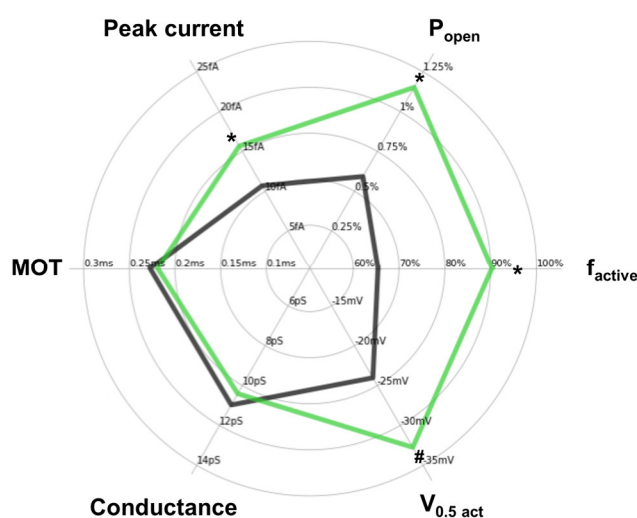


Figure 33. Radar chart comparison of single-channel parameters for L271H and WT. Peak current, P_{open} , f_{active} and MOT are shown at -20 mV for WT (black) and L271H (green). Chart displays mean values. * $p \leq 0.05$ in Bonferroni-Dunn's test following multiple unpaired t-test and # $p \leq 0.05$ in unpaired t-test.

3.1.2. A749T missense mutation shifted Cav1.3 single-channel gating towards more hyperpolarized voltages and increased open probability

To characterize A749T gating modulation of Cav1.3, single-channel availability, open probability, conductance, open and closed time, latency, reversal potential and voltage of half-maximal activation were compared to WT. As mentioned, detailed tables listing data values and p-values are included in the supplemental material (S5).

The exemplary traces and corresponding ensemble average currents visually displayed an increase in single-channel activity for A749T (Fig. 34). The peak ensemble average current was three-fold larger compared to WT (at -20 mV, WT: 10.44 ± 0.82 fA, A749T: 31.93 ± 2.61 fA, $p = 0.001$).

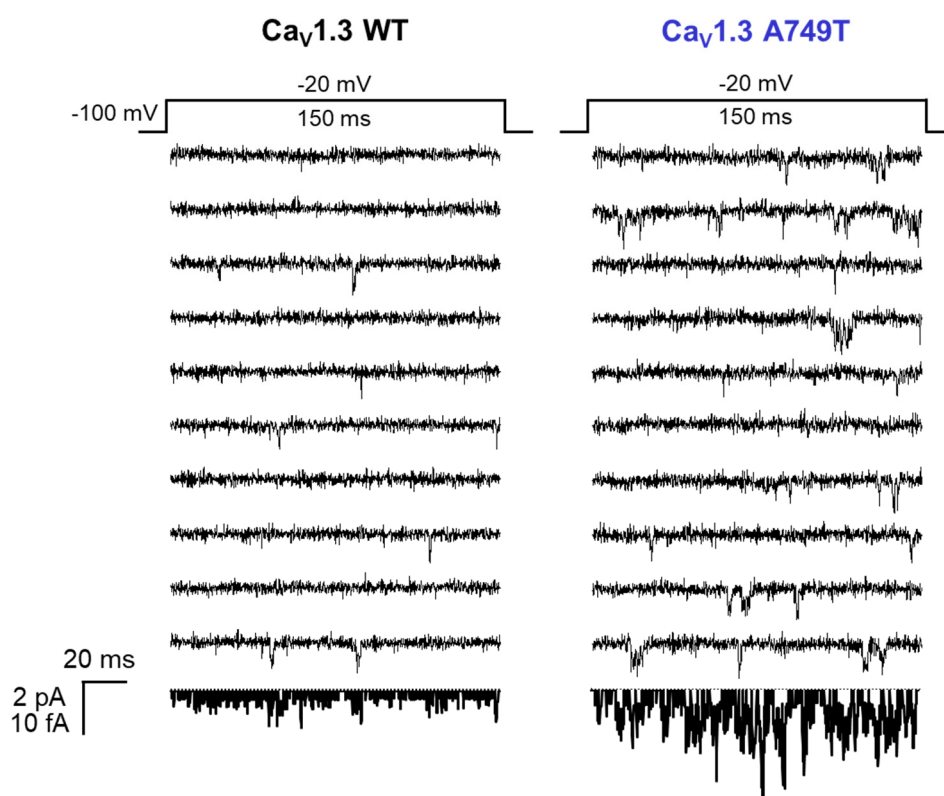


Figure 34. Exemplary traces and ensemble average current of Cav1.3 WT and A749T single-channel recordings. Ten exemplary and consecutive traces of 15 mM Ba²⁺ currents at -20 mV and corresponding ensemble average current below dotted line. Schematic of pulse protocol shown above. A749T displays increased single-channel activity. Scale bar indicates 20 ms and 2 pA for individual traces or 10 fA for ensemble average currents.

Further, the fraction of active sweeps revealed increased single-channel availability for A749T across test potentials. A749T f_{active} at -30 mV was 36 % larger compared to WT (WT: 31.38 ± 1.52 %, A749T: 67.72 ± 5.99 %, $p < 0.001$). The corresponding voltage of half-maximal activation ($V_{0.5 \text{ act}}$) of A749T was shifted by 9 mV towards more hyperpolarized voltages (WT: -24.54 ± 0.70 mV, A749T: -33.21 ± 3.56 mV, $p < 0.001$). This means that A749T had an increased arousal to transition into the open state at less depolarization than the WT (Fig. 35).

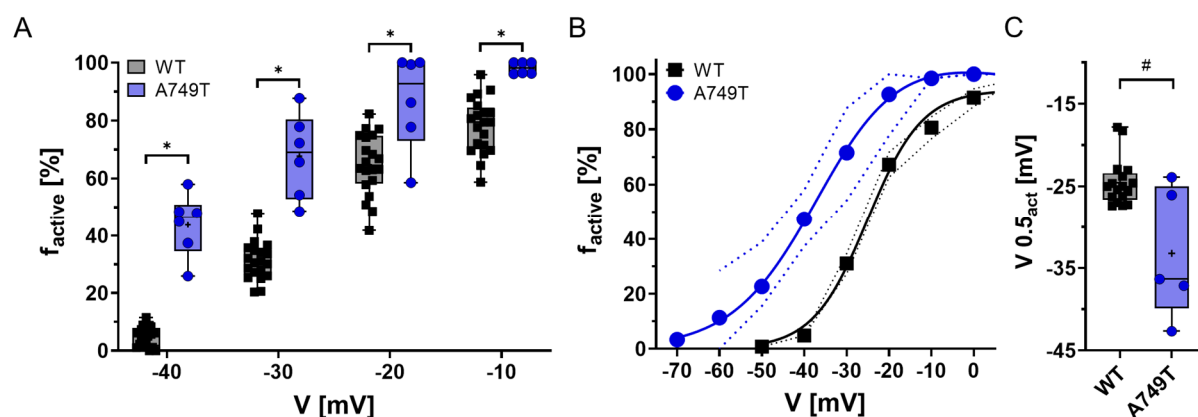


Figure 35. Comparing single-channel availability for A749T and WT. (A) f_{active} is increased for A749T across test potentials (WT: $n = 20$, A749T: $n = 6$). (B) f_{active} fitted by Boltzmann-equation and (C) corresponding $V_{0.5 \text{ act}}$ are shifted towards more hyperpolarized potentials (WT: $n = 17$, L271H: $n = 5$). Charge carrier: 15 mM Ba^{2+} . Data shown as mean and 95 % CI or as boxplots from min to max with all data points, + marks mean. # $p \leq 0.05$ in unpaired t-test and * $p \leq 0.05$ in Bonferroni-Dunn's test following multiple unpaired t-test.

In addition to the availability, the open probability was increased for A749T compared to WT (Fig. 36). At all test potentials P_{open} of A749T was four-fold larger than P_{open} of the WT (e.g. -20 mV, WT: 0.58 ± 0.04 %, A749T: 2.41 ± 0.17 %, $p < 0.001$). At -40 mV, A749T already exceeded the open probability observed for WT at -10 mV (WT: 1.04 ± 0.06 % at -10 mV, A749T: 1.16 ± 0.12 % at -40 mV). Accordingly, in contrast to L271H, the leftward shift in activation only partially explained the increased single-channel activity. Further, while the mean open time was similar between WT and A749T, mean first latency and mean closed time were decreased for A749T, suggesting that the increase in P_{open} originated in an increased opening frequency. This means that within active traces, A749T channels, similar to L271H, spend more time in the open state due to a more frequent transition into the open state compared to the WT.

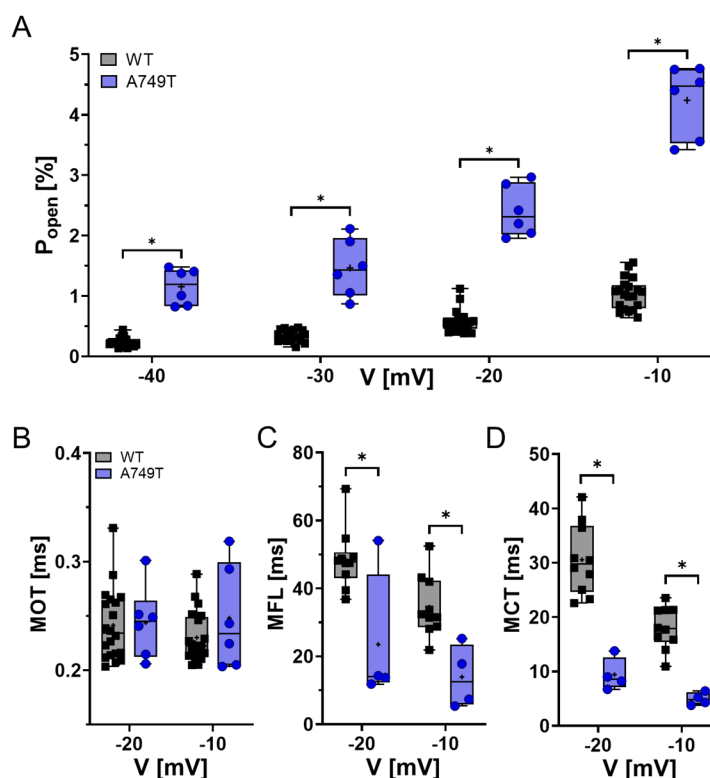


Figure 36. Comparison of open probability, mean open time, mean first latency and mean closed time. (A) P_{open} is increased for A749T, while (B) mean open time is similar (WT: $n = 20$, A749T: $n = 6$). (C) Mean first latency and (D) mean closed time are decreased for A749T (WT: $n = 10$, A749T: $n = 4$). Charge carrier: 15 mM Ba^{2+} . Data shown as boxplots from min to max with all data points. * $p \leq 0.05$ in Bonferroni-Dunn's test following multiple unpaired t-test.

A749T displayed slightly reduced current amplitudes but had a similar conductance as the WT (WT: 11.02 ± 0.67 pS, A749T: 10.09 ± 1.13 pS, $p = 0.329$). The corresponding reversal potentials were also similar (WT: 64.34 ± 5.22 mV, A749T: 61.28 ± 4.71 mV, $p > 0.9$) (Fig. 37).

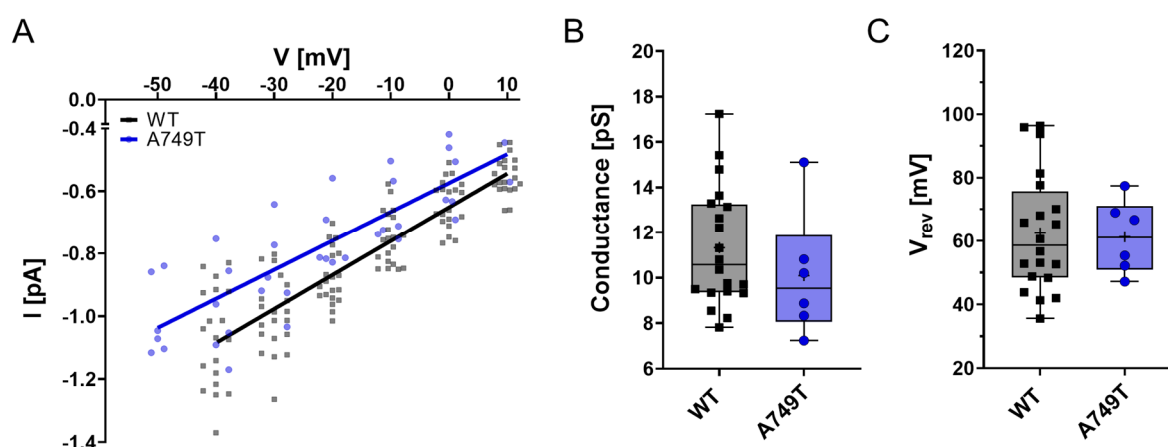


Figure 37. Comparison of current amplitudes, conductance and reversal potential. (A) Current amplitudes across test potentials and corresponding linear regression for WT and A749T. (B) Conductance and (C) reversal potential are similar between WT and A749T. WT: $n = 20$, A749T: $n = 6$. Charge carrier: 15 mM Ba^{2+} . Data shown as boxplots from min to max with all data points, + marks mean. No statistically significant differences were detected in unpaired t-test.

Radar chart comparison of WT and A749T summarizes, that missense mutation A749T shifted Cav1.3 activity towards more negative voltages and increased peak current, availability and open probability, while mean open time and conductance are unaffected (Fig. 38).

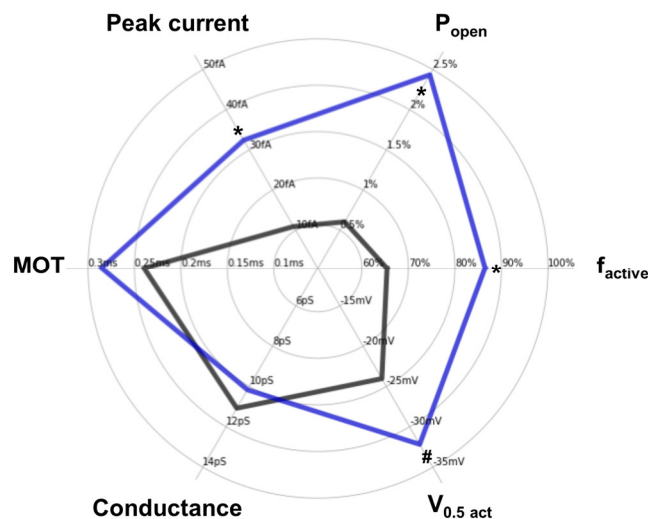


Figure 38. Radar chart comparison of single-channel parameters for A749T and WT. Peak current, P_{open} , f_{active} and MOT are shown at -20mV for WT (black) and A749T (blue). Chart displays mean values. * $p \leq 0.05$ in Bonferroni-Dunn's test following multiple unpaired t-test and # $p \leq 0.05$ in unpaired t-test.

3.1.3. F747S missense mutation induced positive cooperative channel-channel gating

To characterize F747S gating modulation of Cav1.3, various single-channel parameters were compared to WT. Interestingly, measuring F747S channel activity displayed two deviant observations: First, only a small amount of GΩ seals revealed channel activity. Second, among the seals showing channel activity, the extent of activity varied strongly, depending on the number of channels in the patch. Notably, single-channel parameters were mathematically corrected for the apparent number of channels in the patch (2.2.3. according to Herzig et al., 2007).

The exemplary traces and corresponding ensemble average currents visually displayed these differences in channel activity (Fig. 39). Within one-channel patches ($k = 1$), activity of WT and F747S was similar. Within patches containing two or three channels ($k > 1$), however, F747S displayed immensely increased channel activity compared to WT. F747S _{$k > 1$} showed activity at lower test potentials and increased opening durations with rising test potentials. Further, the peak ensemble average current at -20 mV was eight-fold larger compared to WT (WT: $10.44 \pm 0.82\text{ fA}$, F747S _{$k > 1$} : $75.36 \pm 17.59\text{ fA}$, $p < 0.001$).

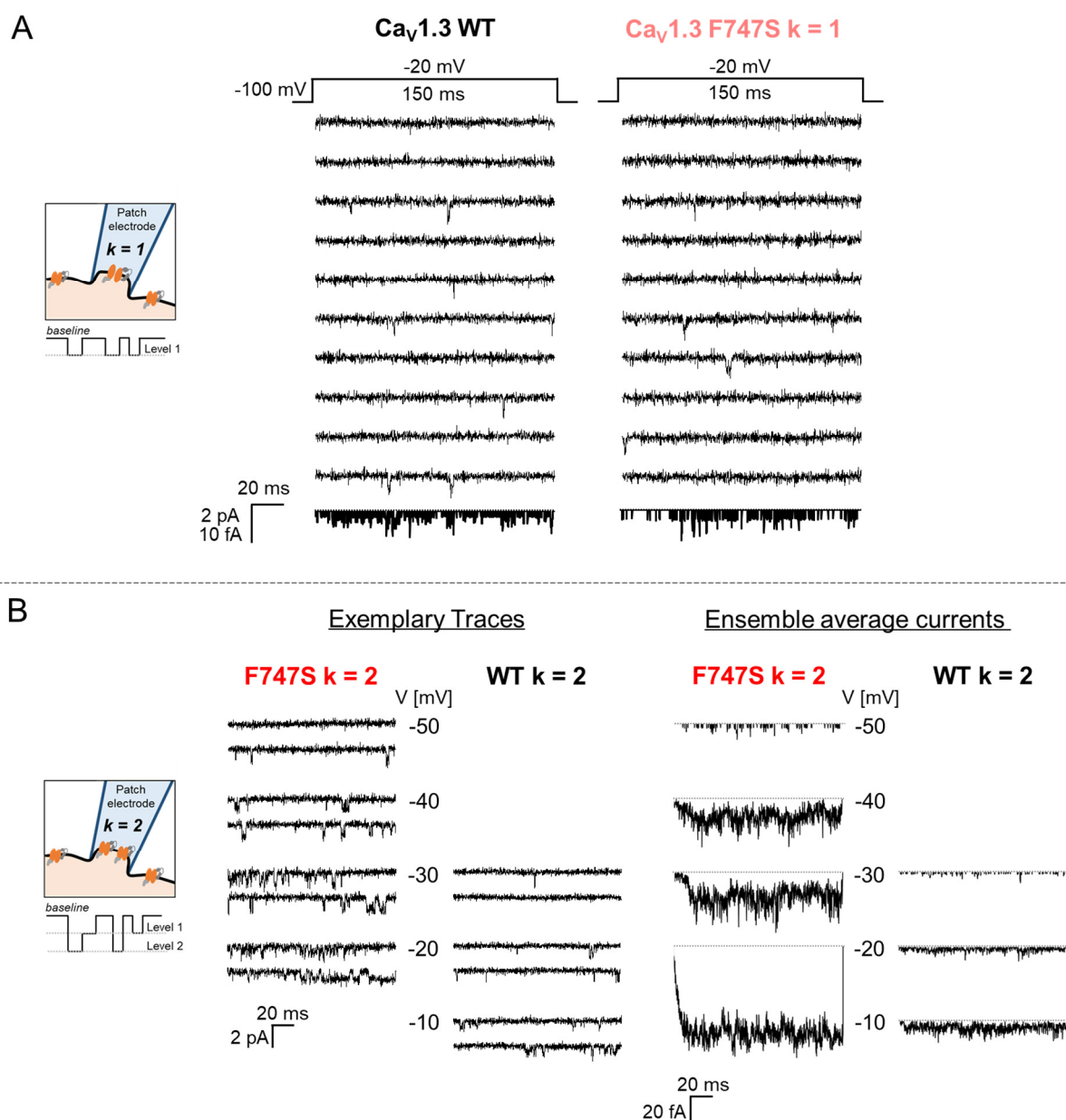


Figure 39. Exemplary traces and ensemble average currents of Ca_v1.3 WT and F747S single-channel recordings. Charge carrier: 15mM Ba²⁺. **(A)** Ten exemplary and consecutive traces and corresponding ensemble average current below dotted line at -20 mV display similar channel activity of WT and F747S in one-channel patches (k = 1). Schematic of pulse protocol shown above. Schematic on the left illustrates k = 1, recognized by level 1 openings. **(B)** Exemplary traces and ensemble average currents for WT and F747S two channel patches (k = 2). Schematic illustrates k = 2, recognized by level 1 and level 2 openings. *Left:* Two exemplary, consecutive traces at different test potentials reveal F747S activity at lower voltages and prolonged channel openings compared to WT. *Right:* Ensemble average currents across test potentials display immensely increased currents for F747S_{k=2} compared to WT. Scale bar indicates 20 ms and 2 pA for individual traces or 10 fA or 20 fA in ensemble average currents.

Observing fewer active seals was quantified by seal statistics, i.e. the amount of patches without channel activity ($k = 0$), containing one channel ($k = 1$) or multiple channels ($k > 1$) within all obtained $G\Omega$ seals. Cells expressing F747S displayed 71 % patches without channel activity, significantly more compared to the WT, which showed 36 % patches without channel activity ($p < 0.001$ in χ^2 -test) (Fig. 40). Seal statistics at whole-cell level were normal, making effects on overall transfection success unlikely. The observation at the single-channel level thus indicates altered membrane distribution of F747S channels, which will be further discussed in section 4.1.2.

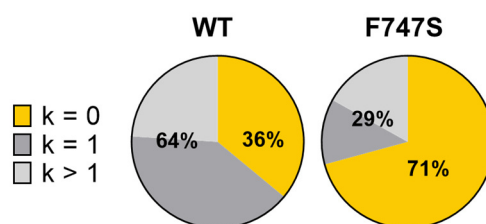


Figure 40. Seal statistics for WT and F747S. Percentage of $G\Omega$ seals without ($k = 0$, yellow) and with channel activity ($k = 1$, gray; $k > 1$, light gray). F747S shows significantly increased $k = 0$ patches compared to WT ($p < 0.001$ in χ^2 test).

Further, the varying activity observed for different channel numbers in the patch was quantified by comparing P_{open} of WT and F747S one- and multi-channel patches. The equations used to correct parameters for the number of channels in the patch, reliably correct parameters for $k \leq 3$. The equations are based on assuming that multiple channels in a patch gate independently. The results showed that $WT_{k=1}$ and $WT_{k>1}$ have similar P_{open} across test potentials ($p > 0.9$ at all voltages), whereas compared to $F747S_{k=1}$, $F747S_{k>1}$ had significantly increased P_{open} ($p < 0.001$ at all voltages) (Fig. 41).

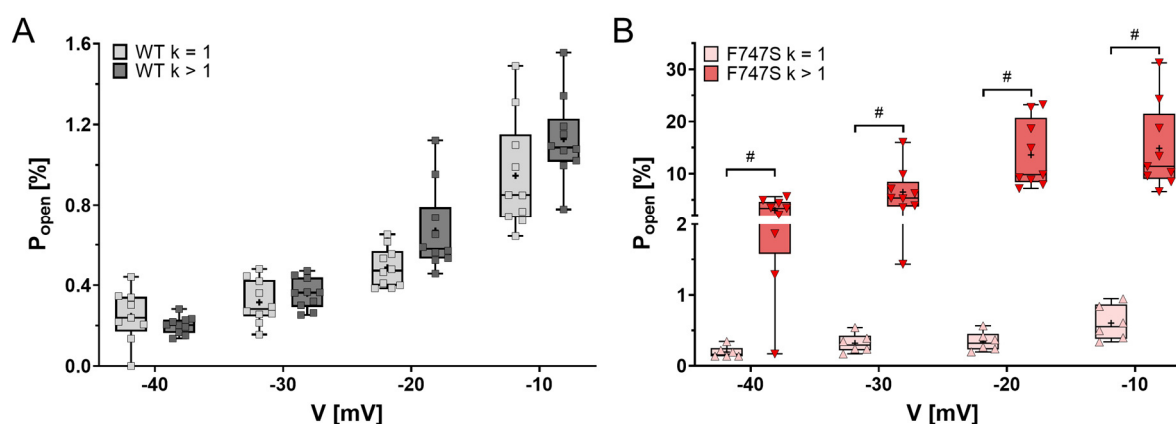


Figure 41. Comparison of WT and F747S P_{open} separated by channel number in patches. (A) P_{open} of $WT_{k=1}$ and $WT_{k>1}$ is similar at all voltages. **(B)** P_{open} of $F747S_{k>1}$ is significantly increased at all voltages compared to $F747S_{k=1}$. P_{open} was mathematically corrected for the number of channels in patch. Note differences in the scaling of y-axes. Charge carrier 15mM Ba^{2+} . # $p \leq 0.05$ in unpaired t-test.

Since single-channel gating of F747S in either one- or multi-channel patches was significantly different, they were compared separately to WT and each other. Data on WT Cav1.3 obtained from single- or multi-channel patches were pooled because the number of channels did not affect gating of single channels.

Analyzing the fraction of active sweeps revealed that F747S_{k=1} had similar availability at all test potentials compared to WT. The corresponding voltage of half-maximal activation was therefore also similar for WT and F747S_{k=1} (WT: -24.54 ± 0.70 mV, F747S_{k=1}: -24.04 ± 1.34 mV, $p > 0.9$). F747S_{k>1} had increased availability compared to WT at -40 mV, -30 mV and -10 mV and compared to F747S_{k=1} at -40 mV. Further, F747S_{k>1} showed a shift in $V_{0.5act}$ of 10 mV towards more negative voltages compared to WT and F747S_{k=1} (F747S_{k>1}: -34.08 ± 3.70 mV, $p = 0.002$ vs WT and $p = 0.006$ vs F747S_{k=1}) (Fig. 42).

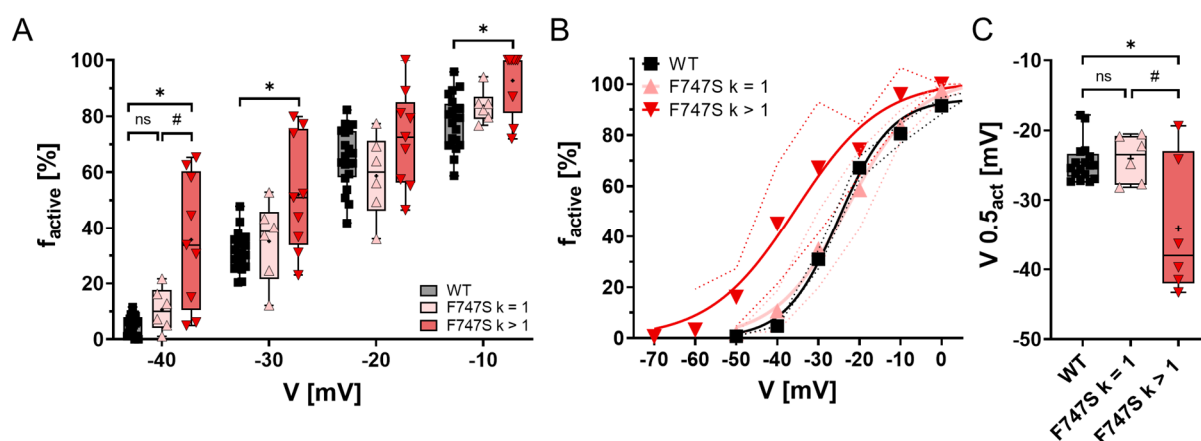


Figure 42. Comparing single-channel availability for F747S and WT. (A) f_{active} is comparable for WT and F747S_{k=1}, while F747S_{k>1} displays increased availability (WT: $n = 20$, F747S_{k=1}: $n = 6$, F747S_{k>1}: $n = 9$). (B) Accordingly, f_{active} fitted by Boltzmann-equation and (C) corresponding $V_{0.5act}$ are similar for WT and F747S_{k=1} but shifted towards more negative potentials for F747S_{k>1} (WT: $n = 17$, F747S_{k=1}: $n = 6$, F747S_{k>1}: $n = 6$). Charge carrier: 15 mM Ba²⁺. Data shown as mean and 95 % CI or as boxplots from min to max with all data points, + marks mean. * $p \leq 0.05$ vs WT and # $p \leq 0.05$ F747S_{k=1} vs F747S_{k>1} in Bonferroni's post hoc test following one-way ANOVA.

Further, the open probability of WT and F747S_{k=1} was similar at all test potentials ($p > 0.9$), while F747S_{k>1} had an up to 25-fold increased P_{open} . At -20 mV, F747S_{k>1} displayed a P_{open} of ~14 %, while WT and F747S_{k=1} had open probabilities below 0.6 % (WT: 0.58 ± 0.04 %, F747S_{k=1}: 0.34 ± 0.06 %, F747S_{k>1}: 13.61 ± 2.15 %, WT vs F747S_{k=1} $p > 0.9$, F747S_{k>1} vs WT and vs F747S_{k=1} $p < 0.001$).

For F747S_{k>1}, the changes in P_{open} originated in an increase in both, opening duration and opening frequency. The mean open time was significantly increased for F747S_{k>1} compared to WT and F747S_{k=1}. At -20 mV F747S_{k>1} openings had an average duration of

0.58 ± 0.11 ms, while WT and F747S_{k=1} had an average opening duration of 0.21 ± 0.01 ms (WT vs F747S_{k=1} $p > 0.9$, F747S_{k>1} vs WT and vs F747S_{k=1} $p < 0.001$). Affirmative of the increased opening frequency was the decrease in mean first latency and mean closed time for F747S_{k>1} compared to WT and F747S_{k=1}. Interestingly, MCT of F747S_{k=1} was significantly increased compared to WT at -10 mV (WT: 18.03 ± 1.23 ms, F747S_{k=1}: 25.91 ± 3.88 ms, $p = 0.023$). Notably, MFL and MCT were usually calculated for one-channel patches only, as in multi-channel patches it cannot be determined which channel opened or closed. For F747S_{k>1}, both MFL and MCT were calculated to provide further information on gating behavior changes in multi-channel patches (Fig. 43).

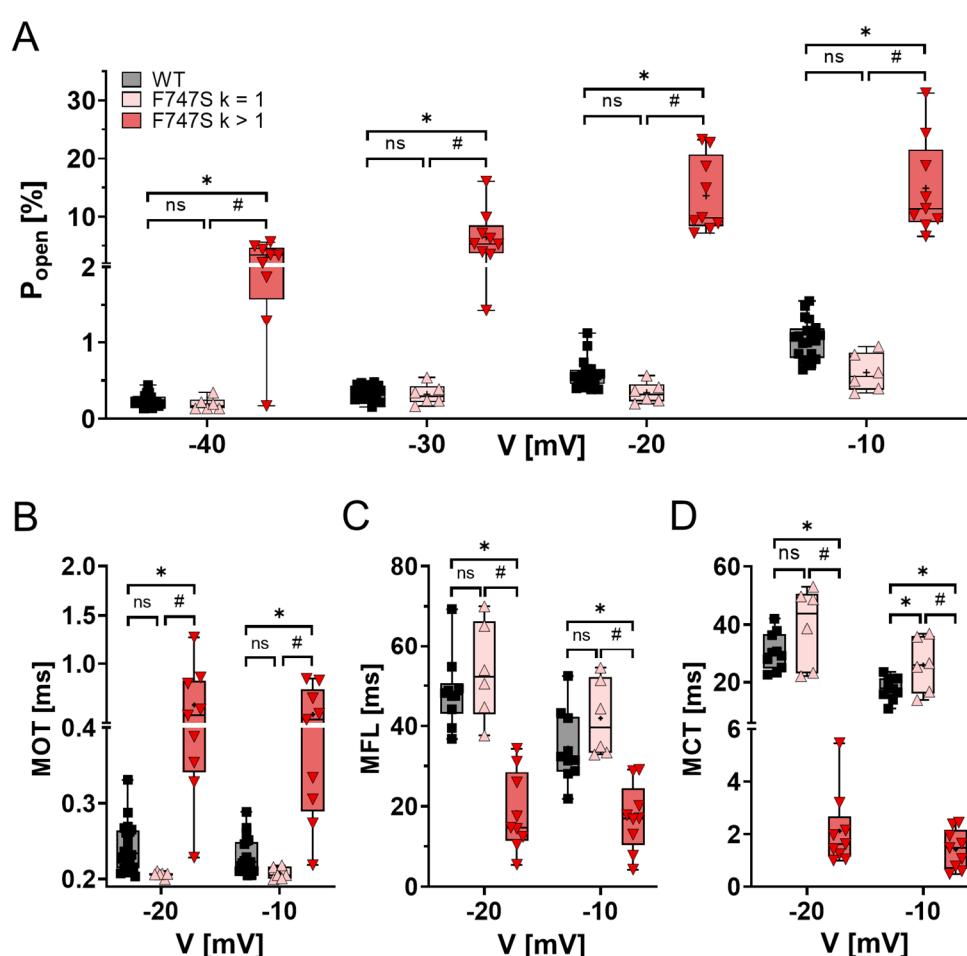


Figure 43. Comparison of open probability, mean open time mean first latency and mean closed time. (A) P_{open} is similar for WT and F747S_{k=1} but up to 25-fold increased for F747S_{k>1} (WT: $n = 20$, F747S_{k=1}: $n = 6$, F747S_{k>1}: $n = 9$). (B) Mean open time is similar for WT and F747S_{k=1} but increased for F747S_{k>1}. (C) Mean first latency and (D) mean closed time are decreased for F747S_{k>1} (WT: $n = 10$, F747S_{k=1}: $n = 6$, F747S_{k>1}: $n = 9$). Charge carrier: 15 mM Ba²⁺. Data shown as boxplots from min to max with all data points, + marks mean. * $p \leq 0.05$ vs WT and # $p \leq 0.05$ F747S_{k=1} vs F747S_{k>1} in Bonferroni's post hoc test following one-way ANOVA.

The results showed that changes in P_{open} originated in an increased opening frequency and opening duration. While the mean open time was significantly increased for $F747S_{k>1}$, the parameter reports the average opening duration. Regarding the large data variance in MOT and the observation within the exemplary traces for $F747S_{k>1}$, the mean open time might not sufficiently describe the changes in opening durations. Therefore, the opening durations were related to their count in open time histograms for further analysis. These histograms, plotted according to Sigworth and Sine (Sigworth & Sine, 1987), were fitted to obtain open time constants (τ) (Fig. 44). Interestingly, WT and $F747S_{k=1}$ were most appropriately fitted mono-exponentially, resulting in one open time constant τ_1 (WT: 0.18 ± 0.01 ms, $F747S_{k=1}$: 0.11 ± 0.01 ms). Contrary, fitting $F747S_{k>1}$ resulted in two open time constants τ_1 and τ_2 ($F747S_{k=1}$ τ_1 : 0.12 ± 0.03 ms and τ_2 : 1.24 ± 0.24 ms). This revealed that $F747S_{k>1}$ had indeed two populations of opening durations, namely short and long openings, rather than an increased average opening duration. Additionally, τ_1 values of all variants were similar, thus indicating no differences in short opening durations (WT vs $F747S_{k=1}$ and vs $F747S_{k>1}$ $p = 0.1$, $F747S_{k=1}$ vs $F747S_{k>1}$ $p > 0.9$). Taken together, the open time distribution accompanied by the increased open probability was considered to reveal mode 2 gating for $F747S_{k>1}$.

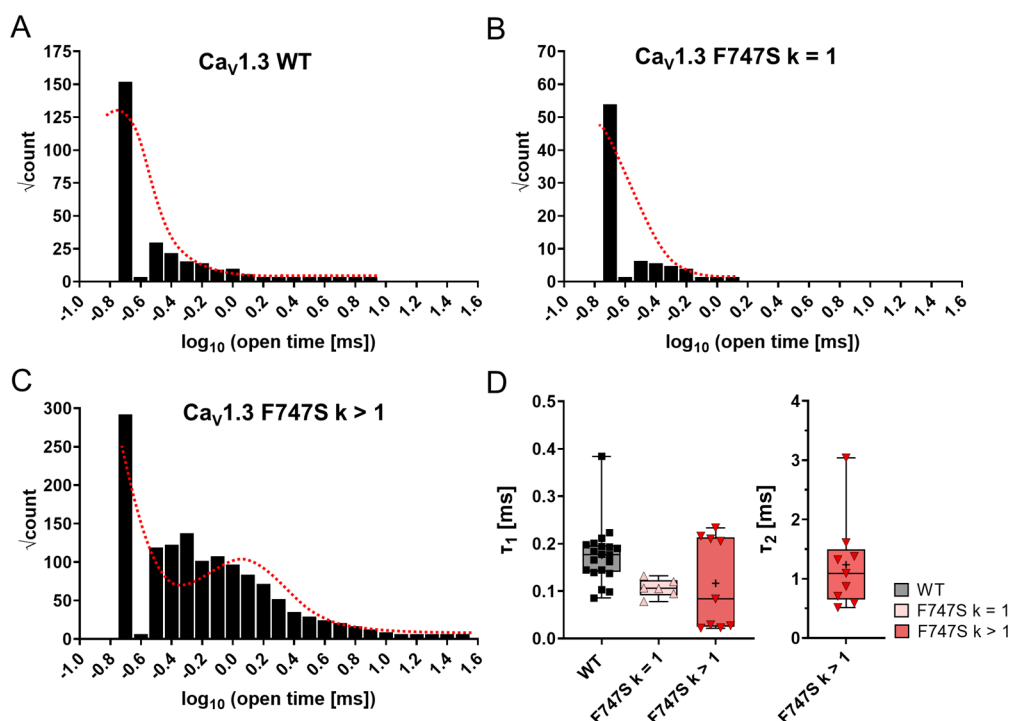


Figure 44. Distribution of opening durations for WT and F747S. (A-C) Open time histograms according to Sigworth and Sine, 1987 of \log_{10} open times against square root count at -10 mV for all experiments pooled. Fit indicated by dotted red line. Peaks of fits correspond to tau values. **(D)** Open time constant τ_1 is similar among variants, while τ_2 is only determined for $F747S_{k>1}$. WT: $n = 20$, $F747S_{k=1}$: $n = 6$, $F747S_{k>1}$: $n = 9$. Data shown as boxplots from min to max with all data points, + marks mean. No statistically significant differences found among τ_1 values.

To further characterize apparent gating cooperativity, a coupling coefficient (κ) was calculated. κ indicates the coupling probability based on simultaneously occurring openings of multiple channels (according to Navedo et al. 2010 based on Chung & Kennedy, 1996). Calculating the coupling coefficient for $WT_{k>1}$ and $F747S_{k>1}$ revealed $\kappa < 0.02$ for both isoforms ($WT_{k>1}$: 0.013 ± 0.005 and $F747S_{k>1}$: 0.01 ± 0.004), i.e. no difference between WT and F747S was observed in this respect.

Regarding conductance and reversal potential, all variants were similar (conductance: WT: 11.02 ± 0.67 pS, $F747S_{k=1}$: 11.11 ± 1.28 pS, $F747S_{k>1}$: 12.10 ± 0.89 pS, ANOVA $p = 0.735$). Accordingly, there was no F747S mutation-dependent nor channel-number-dependent difference in current amplitude across test potentials (Fig. 45).

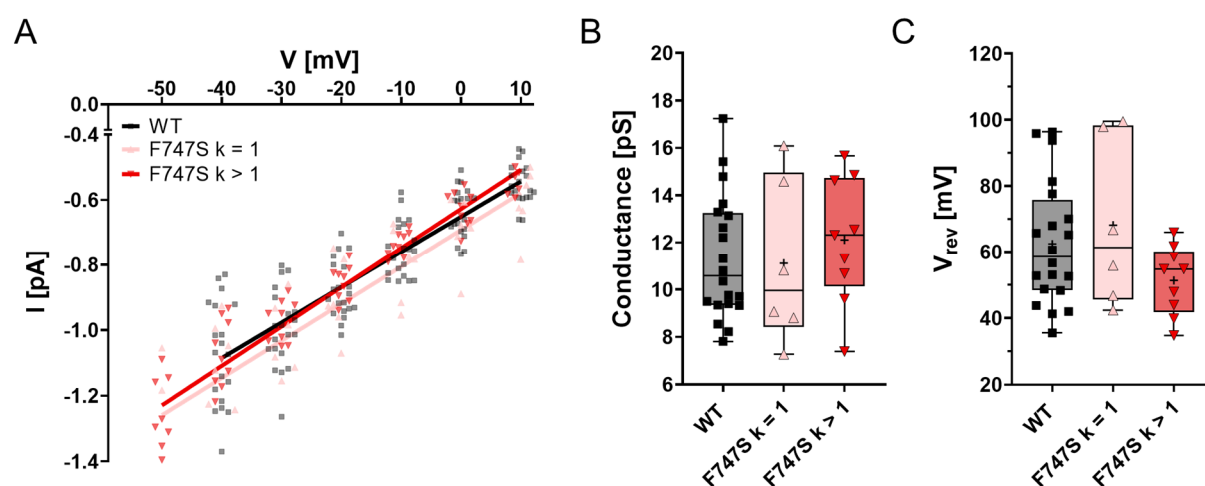


Figure 45. Comparison of current amplitudes, conductance and reversal potential. (A) Current amplitudes and corresponding linear regression for WT and F747S are similar. (B) Conductance and (C) V_{rev} are also similar. WT: $n = 20$, $F747S_{k=1}$: $n = 6$, $F747S_{k>1}$: $n = 9$. Charge carrier: 15 mM Ba^{2+} . Data shown as boxplots from min to max with all data points. No statistically significant differences detected in one-way ANOVA.

The radar chart comparison of WT, $F747S_{k=1}$ and $F747S_{k>1}$ summarizes the depicted gating changes (Fig. 46). For WT and $F747S_{k=1}$, both webs are almost congruent, revealing that in one-channel patches, F747S gates similarly to the WT. Contrary, for $F747S_{k>1}$ the radar chart shows that two or three F747S channels in the patch increased peak current, MOT and P_{open} and further shifted $Cav1.3$ activity towards more negative voltages. Together with the indication of altered membrane distribution and depicted mode 2 gating, the results reveal positive-cooperative channel-channel interaction for F747S.

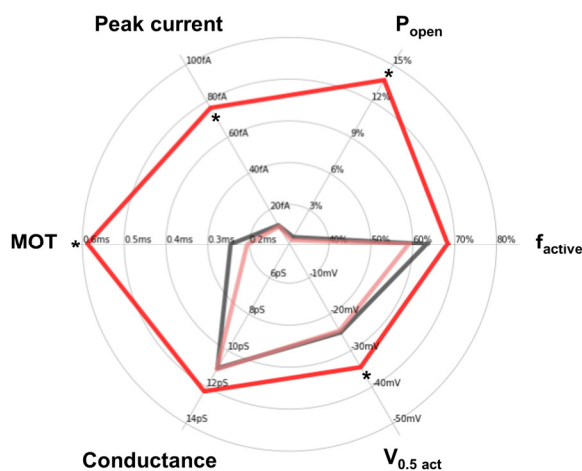


Figure 46. Radar chart comparison of single-channel parameters for F747S and WT. Peak current, P_{open} , f_{active} and MOT are shown at -20 mV for WT (black), F747S_{k=1} (rose) and F747S_{k>1} (red). * $p \leq 0.05$ vs WT in Bonferroni's post hoc test following one-way ANOVA.

3.1.4. Structural modelling of L271H, A749T and F747S

All three disease-associated missense mutations in Cav1.3 showed gain-of-function phenotypes, however, through different changes of single-channel gating. While all mutations caused a shift in activity towards more negative voltages compared to WT, they differed in the modulation of P_{open} and gating modes. For L271H, the increased activity could be sufficiently explained by the leftward-shifted voltage dependence alone. The increase of A749T was only partly explained by the leftward shift in voltage dependence and was mainly caused by an overall increased open probability. For F747S, the increase in activity obviously originated in positive cooperative channel-channel interaction, a novel observation for disease-associated *CACNA1D* missense mutations, stating the importance of single-channel analysis in revealing Cav1.3 pathophysiological gating modulation, as further discussed in section 4.1.1. Taken together, disease-associated missense mutations L271H, A749T and F747S modulate Cav1.3 activity with individual gating phenotypes.

These individual gating phenotypes may originate in structural intramolecular changes and therefore the residues were modeled in the recently published Cav1.3 cryo-EM structure using *PyMol* (7UHG, Yao et al., 2022). Figure 47 shows the location of all three amino acids from a top view and a transmembrane view. Both angles showed that the mutation-prone amino acids cluster at the intracellular side in the pore-forming segments S5 and S6.

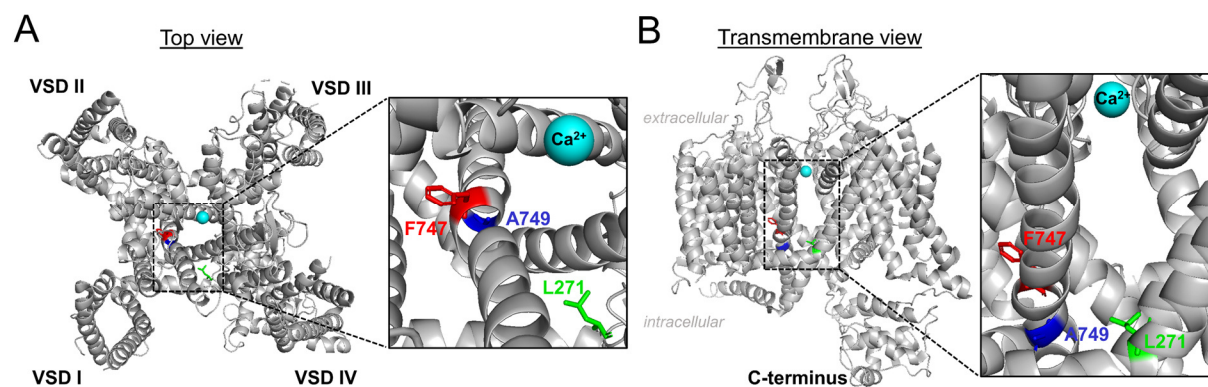


Figure 47. Structural modeling of L271H, A749T and F747S within the Cav1.3 α_1 -subunit. (A) 3D cryo-EM structure of Cav1.3 in a top view with highlighted region and enlargement showing location of L271 (green), A749 (blue) and F747 (red). (B) Residues visualized in the transmembrane view.

Each site was structurally modeled with the WT and the mutated residue (Fig. 48). L271 is located at the bottom of S5 in domain I and connected to its neighboring residue I274 within its own α -helix. It further interacts with V401 and L405 in segment S6. Upon mutation to H271, the interacting residues remained the same, but the mutation-induced imidazole ring of histidine influenced the distance to these residues. A similar observation was made for A749T, which is located in segment S6 of domain II. The polarity of T749 suggested a stronger interaction with L653 at the bottom of segment S5. F747 is also located in segment S6 of domain II, two amino acids upstream of A749. F747 carries one of three benzene rings forming an interaction, the other two being attached to F1141 and F1142 in segment S6 of domain III. Since serine lacks a benzene ring, S747 changes the interacting residue in favor of N1145.

In summary, all three examined Cav1.3 mutations exhibit potentially altered intramolecular amino acid interactions that may be linked to altered function.

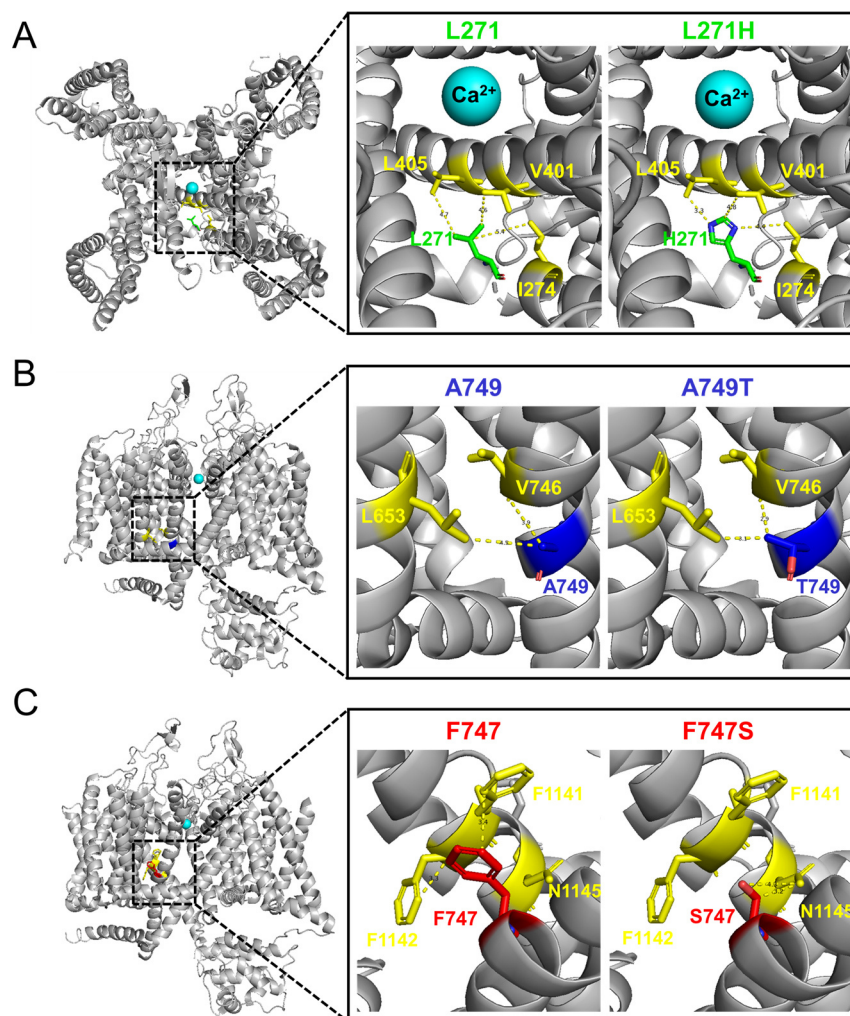


Figure 48. Structural modeling intramolecular interactions of L271H, A749T and F747S. (A) Top view: L271 and H271 interact with residues in the same and the neighboring transmembrane segment. The imidazole ring of H271 leads to a shorter distance to the neighboring segment compared to L271. (B) Transmembrane view: T749 is in closer proximity to L653 in the neighboring segment. (C) Transmembrane view: S747 disrupts three interacting benzene rings and instead interacts with N1145 in a segment of a different domain.

3.2. Cav1.3 gating modulation by S1475 phosphorylation

After investigating pathophysiological Cav1.3 gating modulation in disease-associated mutations, the following results will address S1475 modulation of Cav1.3 gating. S1475, the human equivalent of a CaMKII phosphorylation site of Cav1.3 identified in rats, is investigated with respect to its effect on the electrophysiological properties of Cav1.3 and its role for the interaction with calmodulin (CaM) and potential consequences on calcium-dependent inactivation (CDI) (Fig. 49).

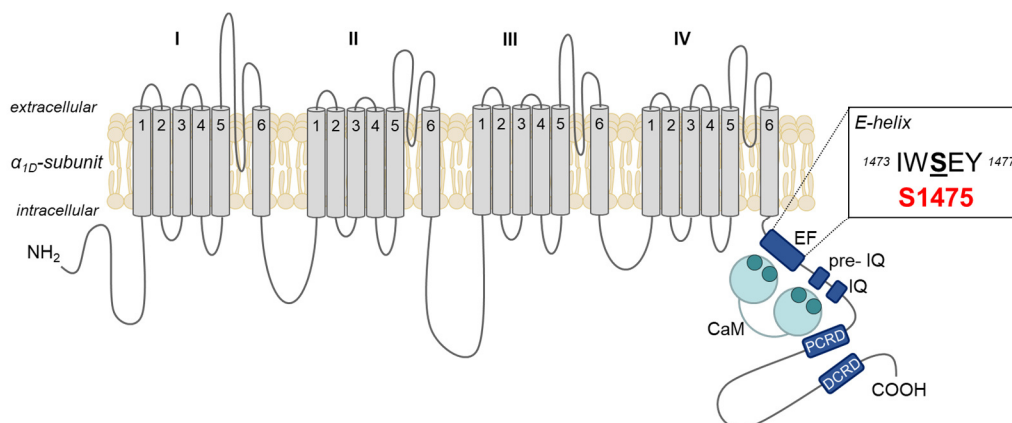


Figure 49. Schematic localization of S1475 inside the EF-hand.

3.2.1. Imitating phosphorylation states differentially modulates Cav1.3 whole-cell currents

To investigate S1475 effects of Cav1.3 gating, S1475 phosphorylation states were imitated by mutations to alanine or aspartic acid. The three Cav1.3 variants WT (S1475), phosphorylation-resistant S1475A and phosphorylation-mimicking S1475D were first investigated by recording 2 mM Ca^{2+} whole-cell currents, resembling the physiological extracellular Ca^{2+} concentration. As mentioned, detailed tables listing data values and p-values are included in the supplemental material (S7).

All Cav1.3 variants were functional but differed significantly in their current density. In comparison to WT, the IV-curves revealed an increase of peak current density by 50 % for phosphorylation-resistant S1475A, whereas peak current density of phosphorylation mimicking S1475D channels was reduced by 55 % (WT: 21.91 ± 1.06 pA/pF, S1475A: 33.03 ± 2.05 pA/pF, S1475D: 9.93 ± 0.60 pA/pF, $p < 0.001$ between all groups). Further, the remaining current after 300 ms pulse duration (r_{300}) was increased by ~10 % for S1475D at all test potentials, reaching statistical significance at -30 mV and -20 mV. An increased remaining current was equated with a reduced inactivation ($1 - r_{300}$).

Analyzing the activation kinetics revealed that phosphorylation-mimicking S1475D channels had a steeper activation slope compared to both, WT and S1475A (WT: 5.25 ± 0.28 mV, S1475A: 5.57 ± 0.28 mV, S1475D: 6.75 ± 0.25 mV, WT vs S1475A $p > 0.9$, WT vs S1475D $p = 0.005$, S1475A vs S1475D $p = 0.03$). Regarding the inactivation kinetics, S1475D showed increased non-inactivating current ($I_{\text{non-inact}}$) compared to S1475A, and the voltage of half-maximal inactivation was shifted to more depolarized potentials for S1475D compared to WT.

In summary, this means that imitating the phosphorylated state at p.1475 decreased current density and foremost affected inactivation parameters. Thus, analysis of basal calcium currents showed that imitating (de-) phosphorylation states of S1475 has an impact on Cav1.3 whole-cell gating (Fig. 50).

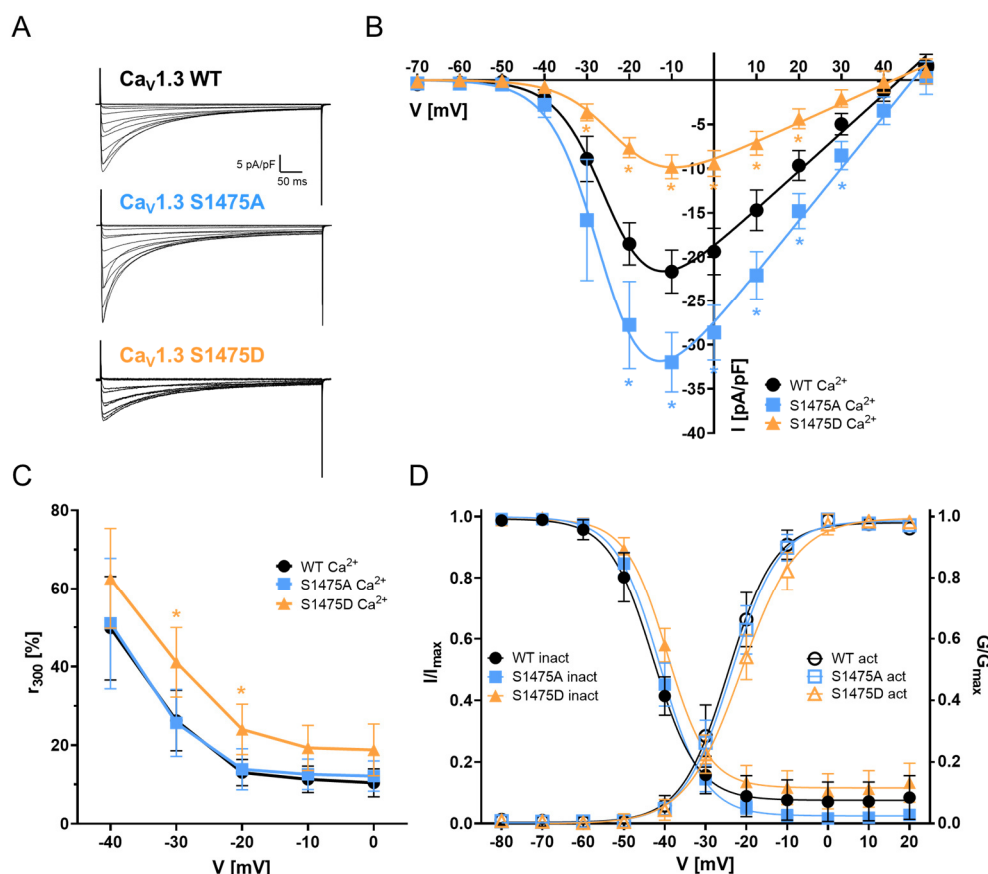


Figure 50. Imitating phosphorylation states modulates 2 mM Ca^{2+} whole-cell currents. (A) Representative recordings of WT, phosphorylation-resistant S1475A and phosphorylation-mimicking S1475D. (B) Current-voltage relationships fitted by Boltzmann-Ohm equation (IV-curves) show current density increase for S1475A and decrease for S1475D (WT: $n = 13$, S1475A: $n = 15$, S1475D: $n = 9$). (C) Remaining current after 300 ms (r_{300}) is increased for S1475D at -30 mV (WT vs S1475D: $p = 0.045$, S1475A vs S1475D $p = 0.029$) and at -20 mV (WT vs S1475D: $p = 0.01$, S1475A vs S1475D $p = 0.02$). (D) Slope of voltage-dependent activation (G/G_{max}) is steeper for S1475D (WT: $n = 13$, S1475A: $n = 13$, S1475D: $n = 9$). Steady-state inactivation (I/I_{max}) is shifted towards more depolarized potentials for S1475D vs WT and the non-inactivating current is increased for S1475D vs S1475A (WT: $n = 12$, S1475A: $n = 15$, S1475D: $n = 8$). Charge carrier: 2 mM Ca^{2+} . Data shown as mean and 95% CI, * $p \leq 0.05$ vs WT in Bonferroni's post hoc test following significant one-way ANOVA.

3.2.2. CaMKII modulates gating kinetics and current densities in dependence of residue at position 1475

Analysis of basal calcium currents revealed that imitating S1475 phosphorylation states impacts electrophysiological properties. To investigate whether S1475 is also a CaMKII target in human Cav1.3 channels, modulation by CaMKII was examined. Hereto, CaMKII was either inhibited by KN-93 or co-expressed in the constitutively active form CaMKII₁₋₂₉₀.

CaMKII inhibition by 1 μ M KN-93 reduced current density by \sim 60 % for all variants. This reduction was expected (Hao et al., 2008; Yokokura et al., 1996) and can be attributed to the fact that KN-93 also acts as a CaM antagonist. It thus indicated the use of effective KN-93 concentrations. Further, as KN-93 was diluted in DMSO, control experiments were performed with DMSO (0.07 %) alone, which showed no effect on Cav1.3 currents (supplemental S3). With respect to S1475, CaMKII inhibition approximated the peak current density of WT to that of phosphorylation-resistant S1475A, whereas the peak current density of S1475D remained reduced by \sim 55 %, thus to a similar extent as observed under basal conditions (WT: 10.73 ± 0.48 pA/pF, S1475A: 11.37 ± 0.48 pA/pF, S1475D: 4.43 ± 0.14 pA/pF, WT vs S1475A $p = 0.9$, S1475D vs WT and vs S1475A $p < 0.001$) Accordingly, the WT behaved like the phosphorylation-resistant S1475A Cav1.3 variant upon CaMKII inhibition by KN-93 (Fig. 51A).

Oppositely, co-expression of constitutively active CaMKII₁₋₂₉₀ approximated the peak current density for WT to that of phosphorylation-mimicking S1475D, while current density of S1475A remained higher (WT: 10.96 ± 1.10 pA/pF, S1475A: 30.81 ± 1.70 pA/pF, S1475D: 10.11 ± 0.72 pA/pF, WT vs S1475D $p > 0.9$, S1475A vs WT and vs S1475D $p < 0.001$) (Fig. 51B). Notably, upon CaMKII₁₋₂₉₀ co-expression S1475A and S1475D peak current densities were similar to recordings under basal conditions (Fig. 50B). Regarding the gating kinetics, the WT displayed a steeper activation slope, increased non-inactivating current and rightward-shifted voltage of half-maximal (in-) activation, thus converging to S1475D, while S1475A then differed significantly. Accordingly, the WT behaved like the phosphorylation-mimicking S1475D Cav1.3 variant upon co-expression of constitutively active CaMKII (Fig. 52).

In summary, the data shows that CaMKII modulates current density via S1475 and could allow conclusions on the partial WT phosphorylation in other experiments, as further addressed in section 4.2.1. In addition, mutants S1475A and S1475D mimic CaMKII modulation in terms of dephosphorylation and phosphorylation at S1475, respectively.

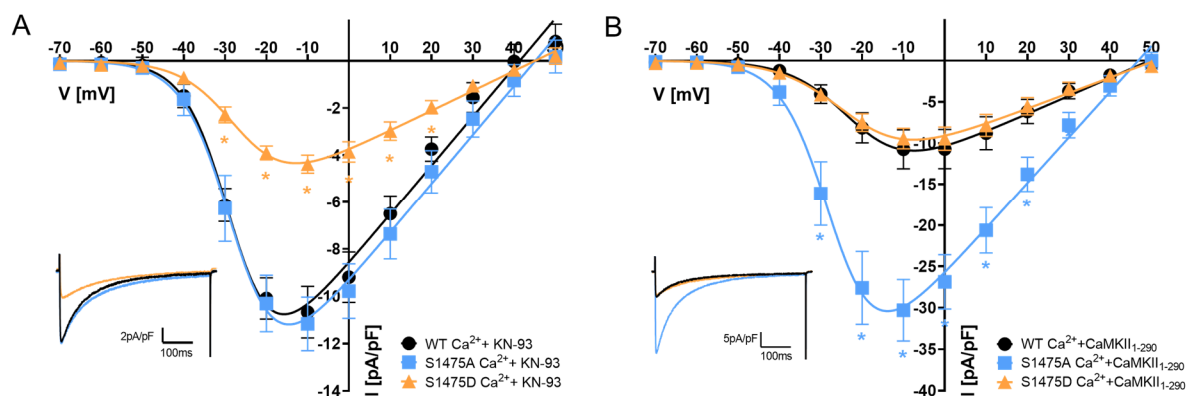


Figure 51. CaMKII modulates current density in dependence of residue at position 1475. (A) CaMKII inhibition by $1 \mu M$ KN-93 approximates WT peak current density to S1475A (WT: $n = 14$, S1475A: $n = 13$, S1475D: $n = 11$). (B) Vice versa, co-expression of constitutively active CaMKII₁₋₂₉₀ approximates WT peak current density to S1475D (WT: $n = 18$, S1475A: $n = 16$, S1475D: $n = 16$). Insets show exemplary traces at -10 mV. Charge carrier: 2 mM Ca^{2+} . Data shown as mean and 95% CI, * $p \leq 0.05$ vs WT in Bonferroni's post hoc test following one-way ANOVA.

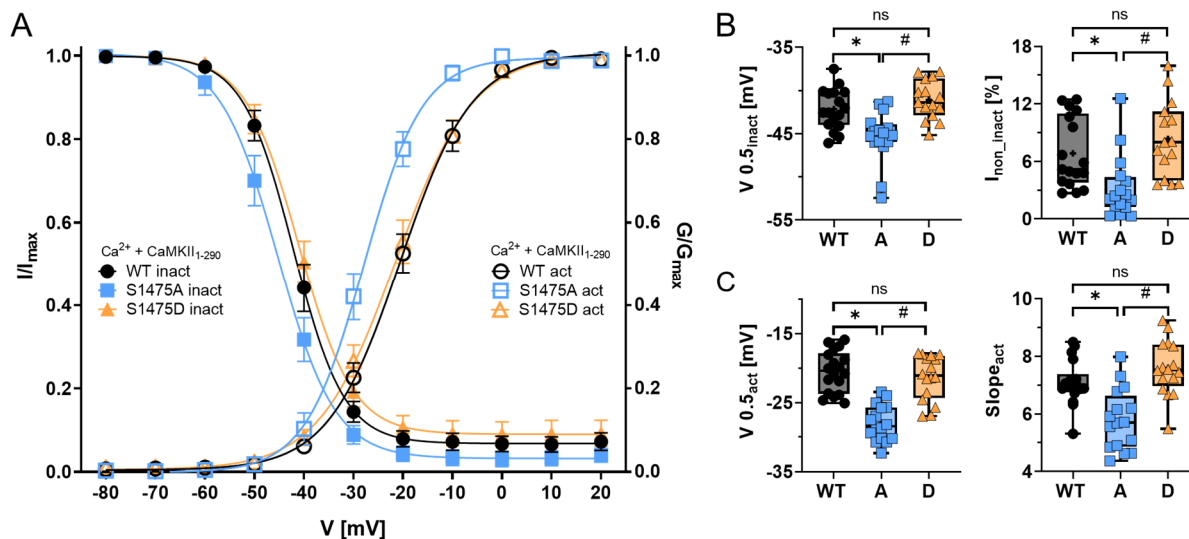


Figure 52. CaMKII modulates gating kinetics in dependence of residue at position 1475. (A) Voltage-dependent activation (G/G_{max}) and steady-state inactivation (I/I_{max}) upon CaMKII₁₋₂₉₀ co-expression approximates WT kinetics to S1475D, also depicted by (B) $V_{0.5_{inact}}$ and non-inactivating current (WT: $n = 17$, S1475A: $n = 16$, S1475D: $n = 15$) and (C) $V_{0.5_{act}}$ and activation slope (WT: $n = 18$, S1475A: $n = 16$, S1475D: $n = 16$). Charge carrier: 2 mM Ca^{2+} . Data shown as mean and 95% CI or boxplots from min to max with all data points. * $p \leq 0.05$ vs WT and # $p \leq 0.05$ S1475A vs S1475D in Bonferroni's post hoc test following one-way ANOVA.

3.2.3. Single-channel conductance and open probability were modulated by S1475 phosphorylation imitation

Since the whole-cell current is composed of the number of channels in the membrane, availability, open probability and conductance, single-channel recordings were required to further investigate underlying mechanisms. Seal statistics did not indicate a difference in the number of channels in the membrane (supplemental S4). Therefore, in a next step, I recorded single-channel activity to address which parameters underlie S1475-dependent modulation of whole-cell currents.

The exemplary traces and corresponding ensemble average currents of these single-channel experiments displayed an increased single-channel activity for S1475A and a decreased activity for S1475D compared to WT (Fig. 53).

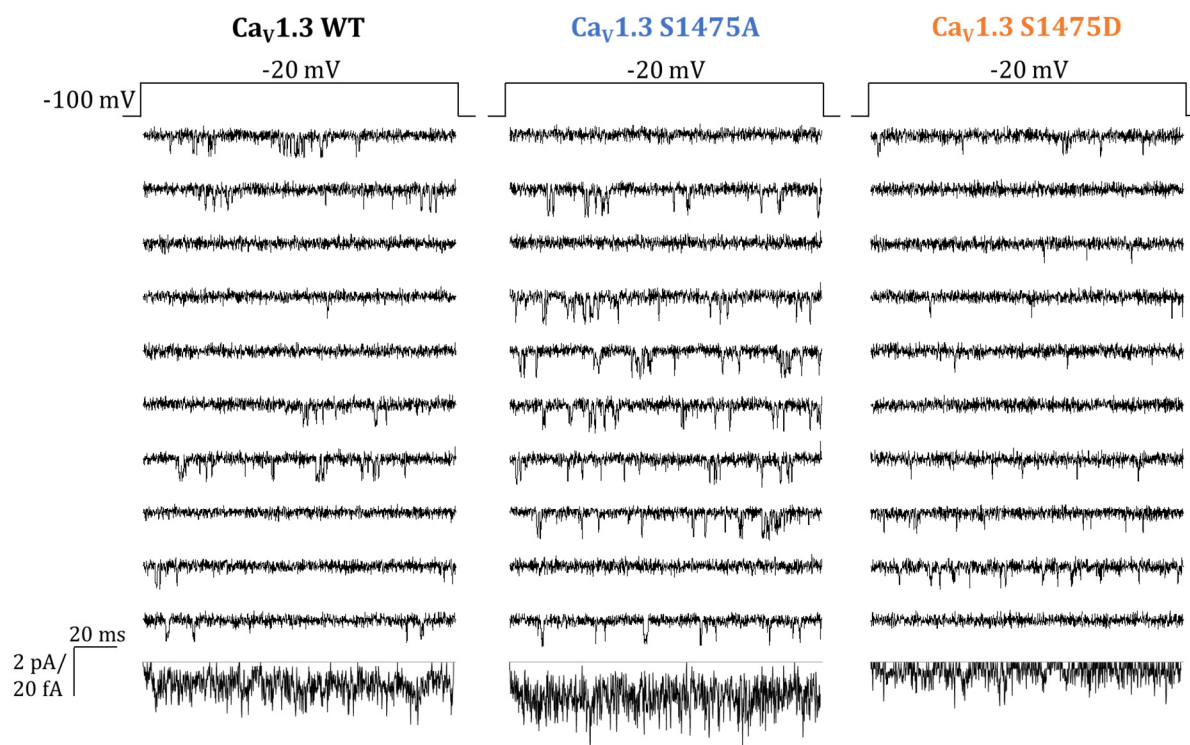


Figure 53. Exemplary traces and ensemble average currents of WT, S1475A and S1475D single-channel recordings. Ten exemplary and consecutive traces of 15 mM Ba²⁺ currents at -20 mV and corresponding ensemble average current below dotted line. Schematic of pulse protocol shown above. Scale bar indicates 20 ms and 2 pA for traces or 20 fA for ensemble average currents.

To address the mechanisms underlying the differences in whole-cell currents, the availability (f_{active}), the open probability (P_{open}) and the conductance were compared for WT, S1475A and S1475D. Analyzing the fraction of active sweeps revealed similar availability (ANOVA $p > 0.05$). Correspondingly, also voltages of half-maximal activation were similar among variants (WT: -27.19 ± 0.81 mV, S1475A: -26.60 ± 0.60 mV, S1475D: -27.60 ± 0.35 mV, ANOVA $p = 0.7$) (Fig. 54).

Accordingly, this means that imitation of S1475 phosphorylation states did not affect single-channel availability, i.e. S1475 phosphorylation states did not alter the arousal to transition into the open state.

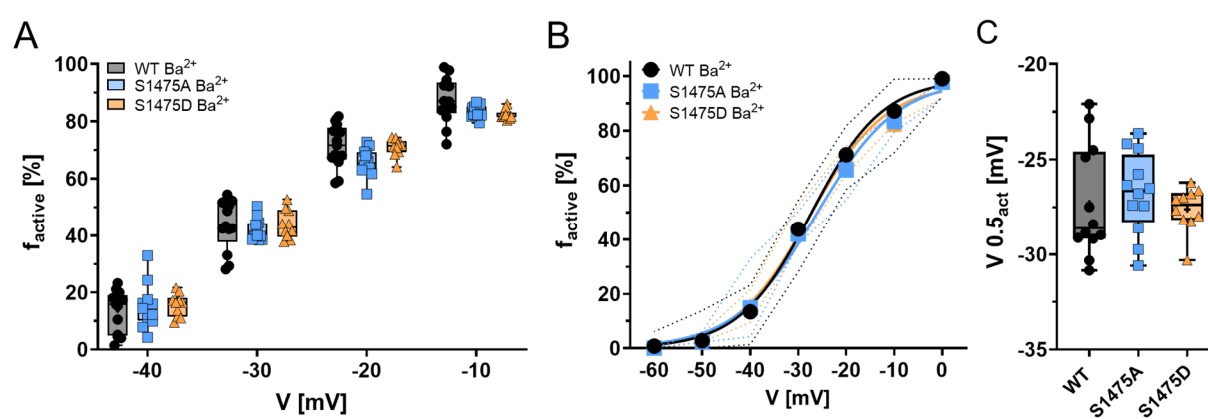


Figure 54. Comparison of single-channel availability. (A) f_{active} is similar for WT, S1475A and S1475D. (B) Accordingly, f_{active} fitted by Boltzmann-equation and (C) $V_{0.5_{\text{act}}}$ are also similar among variants. WT: $n = 13$, S1475A: $n = 12$, S1475D: $n = 10$. Charge carrier: 15 mM Ba²⁺. Data shown as mean and 95 % CI or as boxplots from min to max with all data points, + marks mean. No statistically significant differences detected in one-way ANOVA.

Analyzing the open probability showed an increase for S1475A and a decrease for S1475D, compared to WT and each other across test potentials (at -20 mV WT: 1.37 ± 0.10 %, S1475A: 2.21 ± 0.14 %, S1475D: 0.66 ± 0.03 %, $p < 0.001$ between all groups). As P_{open} describes the percentage of open state occupancy in active sweeps and the availability was unchanged, an alteration in P_{open} could only underlie an alteration in opening frequency or duration. Since the mean open time was unaffected, the P_{open} differences were associated with altered opening frequencies. Affirmative hereof was an increase in the mean first latency, i.e. the time elapsed from pulse start until first opening and an increase in the mean closed time for phosphorylation-mimicking S1475D channels compared to WT (Fig. 55).

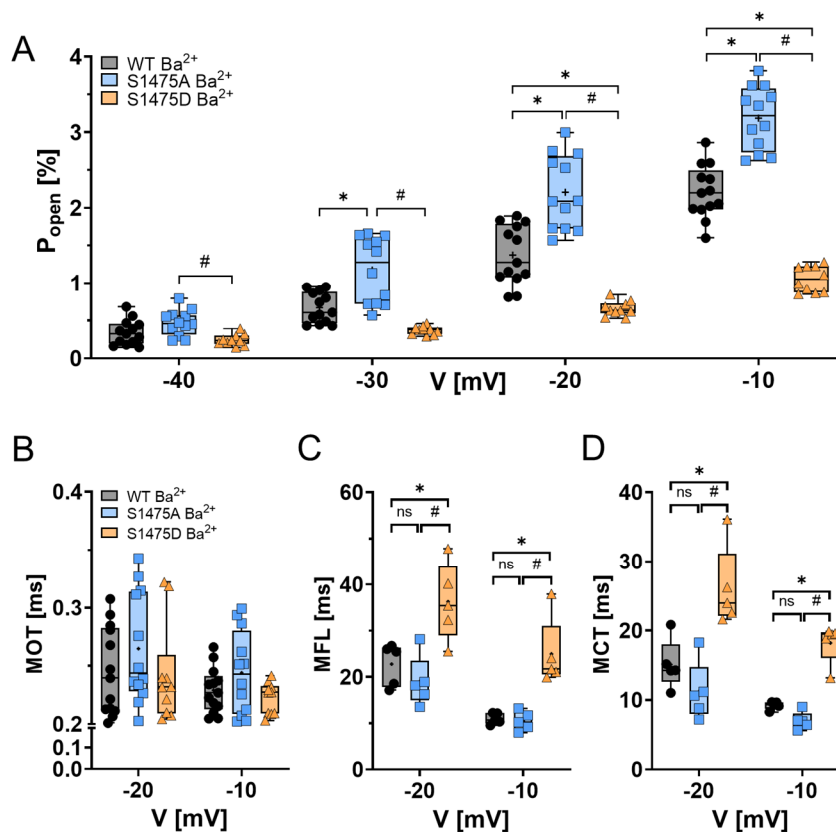


Figure 55. Comparison of open probability, mean open time, mean first latency and mean closed time. (A) P_{open} is increased for S1475A and decreased for S1475D, while (B) mean open time shows no differences (WT: $n = 13$, S1475A: $n = 12$, S1475D: $n = 10$). (C) Mean first latency and (D) mean closed time are increased for S1475D (only for $k = 1$, all $n = 5$). Charge carrier: 15 mM Ba^{2+} . Boxplots from min to max with all data points, + marks mean. * $p \leq 0.05$ vs WT and # $p \leq 0.05$ S1475A vs S1475D in Bonferroni's post hoc test following one-way ANOVA.

In addition, the single-channel conductance appeared to be altered by S1475 phosphorylation state imitation (Fig. 56). S1475A channels displayed an increased conductance and S1475D channels displayed a reduced conductance (WT: 15.84 ± 0.50 pS, S1475A: 18.50 ± 0.89 pS, S1475D: 14.14 ± 0.61 pS, WT vs S1475A: $p = 0.044$, WT vs S1475D: $p = 0.4$, S1475A vs S1475D: $p < 0.001$). Correspondingly, the reversal potential of S1475A was shifted towards more less positive voltages and V_{rev} of S1475D was shifted towards more positive voltages (WT: 31.59 ± 0.96 mV, S1475A: 24.24 ± 1.63 mV, S1475D: 39.17 ± 1.26 mV, WT vs S1475A and vs S1475D: $p = 0.005$, S1475A vs S1475D: $p < 0.001$).

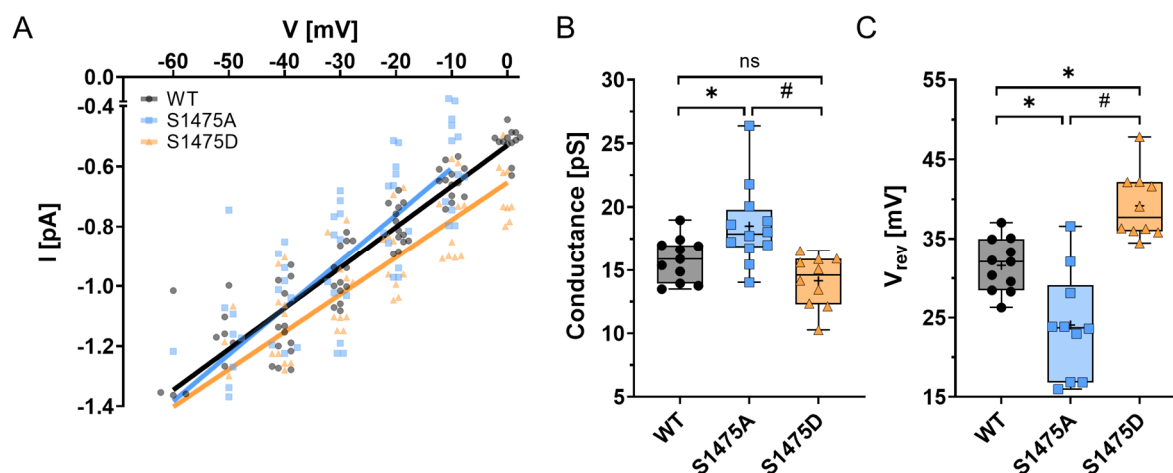


Figure 56. Comparison of current amplitudes, conductance and reversal potential. (A) Current amplitudes and corresponding pooled linear regression reveals **(B)** that conductance was increased for S1475A and decreased for S1475D and that **(C)** the reversal potential was leftward-shifted for S1475A and rightward-shifted for S1475D (WT: n = 13, S1475A: n = 12, S1475D: n = 10). Charge carrier: 15 mM Ba²⁺. Boxplots from min to max with all data points, + marks mean. *p ≤ 0.05 vs WT and #p ≤ 0.05 S1475A vs S1475D in Bonferroni's post hoc test following one-way ANOVA.

The radar chart summarizes the effects of imitating S1475 phosphorylation states on single-channel gating and displays increased single-channel activity for phosphorylation-resistant S1475A and decreased single-channel activity for phosphorylation-mimicking S1475D channels. Herein, channel availability (f_{active}) was unaffected by imitating S1475 phosphorylation states, while conductance and P_{open} were increased for S1475A and decreased for S1475D. In summary, alterations of single-channel conductance and P_{open} explain the changes observed at whole-cell level when imitating S1475 phosphorylation states (Fig. 57).

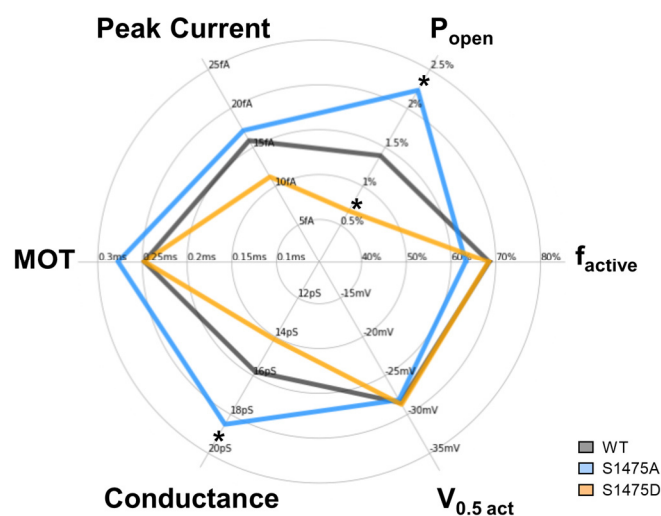


Figure 57. Radar chart comparison of single-channel parameters for WT, S1475A and S1475D. Peak current, P_{open} , f_{active} and MOT are shown at -20 mV. Chart displays mean values showing increased activity for S1475A and decreased activity for S1475D. Charge carrier: 15mM Ba²⁺. * p ≤ 0.05 vs WT in Bonferroni's post hoc test following one-way ANOVA.

3.2.4. Calmodulin is necessary and sufficient for S1475 modulation of Cav1.3 activity

Calmodulin (CaM) is an important modulator of Cav1.3 activity. Since S1475 is located within the C-terminal EF-hand, that is essential for interacting with CaM, I investigated whether imitating S1475 (de-) phosphorylation influenced Cav1.3 modulation by CaM.

CaM co-expression

Although CaM is endogenously expressed in HEK293 cells, CaM was co-expressed in a 1:1 ratio with the α_1 -subunit to allow for saturated CaM effects. For WT and phosphorylation-resistant S1475A, CaM co-expression shifted the IV-curve leftward by ~ 10 mV and increased peak current density, compared to recordings without CaM co-expression. WT peak current density increased by 60 % and S1475A current density increased by 28 %, resulting in similar peak current densities for WT and S1475A upon CaM co-expression. In contrast, CaM co-expression decreased peak current density of phosphorylation-mimicking S1475D by 45 % (WT: 34.94 ± 2.54 pA/pF, S1475A: 42.24 ± 2.98 pA/pF, S1475D: 5.63 ± 0.36 pA/pF, WT vs S1475A $p = 0.5$, S1475D vs WT and vs S1475A $p < 0.001$) (Fig. 58).

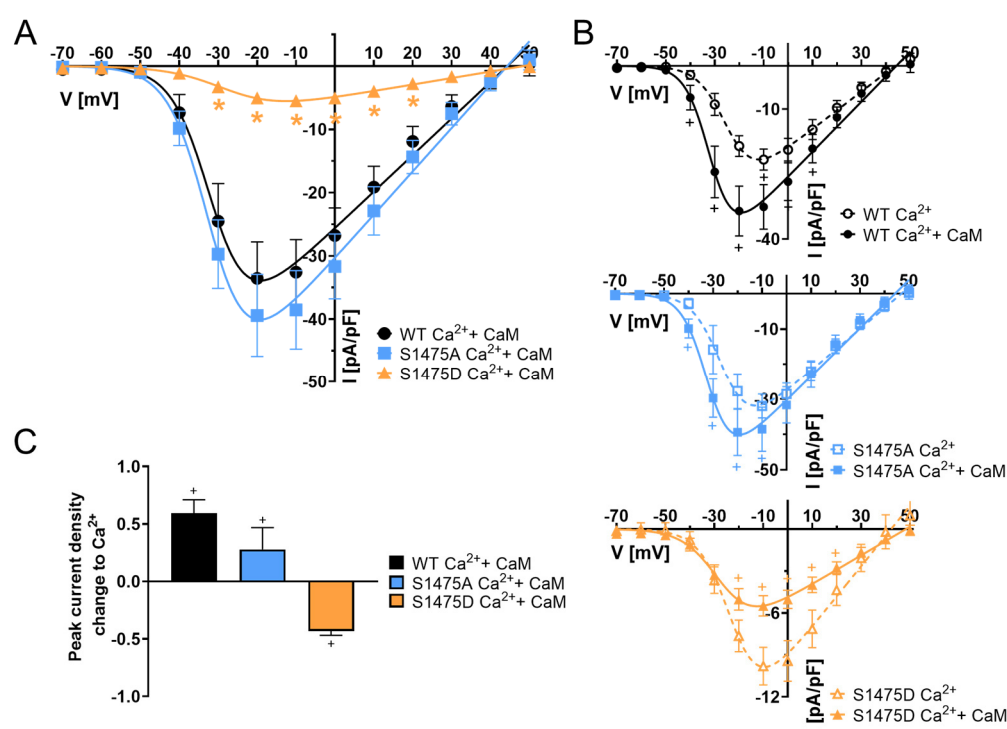


Figure 58. CaM co-expression affects current density in opposite ways depending on residue at p.1475. (A) Co-expressing CaM results in similar peak current densities for WT and S1475A but a decrease for S1475D (WT: $n = 14$, S1475A: $n = 13$, S1475D: $n = 19$). **(B)** Comparing current density with and without CaM co-expression shows increase for WT and S1475A but decrease for S1475D upon CaM co-expression. **(C)** Magnitude of peak current density change upon CaM co-expression. Charge carrier: 2mM Ca²⁺. Data shown as mean and 95 % CI. + $p \leq 0.05$ Ca²⁺ vs Ca²⁺ + CaM in unpaired t-test. * $p \leq 0.05$ vs WT in Bonferroni's post hoc test following one-way ANOVA.

In addition to enhancing differences in peak current density, CaM co-expression also increased the differences in current inactivation (Fig. 59). Phosphorylation-mimicking S1475D channels displayed an increased remaining current, namely a reduced inactivation, at all test potentials compared to WT and S1475A. At -20 mV, S1475D channels had a three-fold larger remaining current compared to WT and S1475A (WT: 13.01 ± 1.71 %, S1475A: 17.27 ± 2.77 %, S1475D: 40.13 ± 2.82 %, WT vs S1475A $p = 0.8$, S1475D vs WT and vs S1475A $p < 0.001$). This was also visualized by comparing exemplary traces with normalized current density.

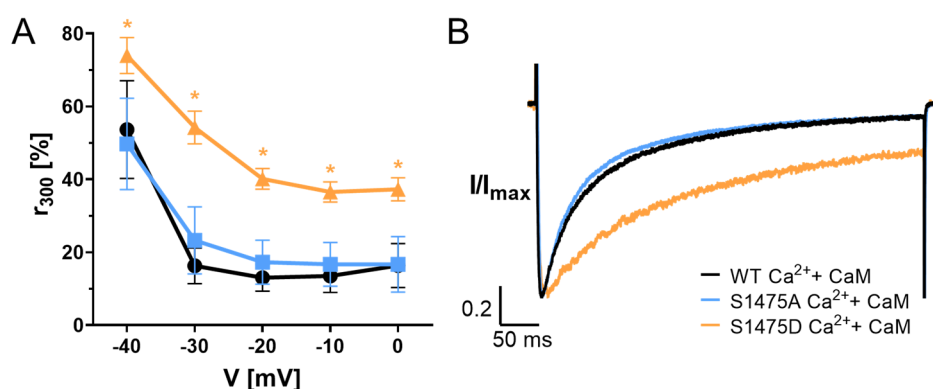


Figure 59. CaM co-expression decreases inactivation of S1475D. (A) Remaining current for S1475D is increased at all test potentials, thus inactivation is decreased (WT: $n = 14$, S1475A: $n = 13$, S1475D: $n = 19$). (B) Normalized exemplary traces (I/I_{max}) at -20 mV display increased remaining current for S1475D. Charge carrier: 2mM Ca²⁺. Data shown as mean and 95 % CI. * $p \leq 0.05$ vs WT in Bonferroni's post hoc test following one-way ANOVA.

Further, in addition to enhancing differences in peak current density and inactivation, co-expressing CaM shifted the activation and inactivation kinetics of S1475D to more depolarized potentials compared to WT and S1475A. The activation slope was steeper and $V_{0.5act}$ was rightward-shifted by 7 mV ($V_{0.5act}$ WT: -30.55 ± 1.31 mV, S1475A: -30.66 ± 1.39 mV, S1475D: -23.84 ± 0.69 mV, WT vs S1475A $p > 0.9$, S1475D vs WT and vs S1475A $p < 0.001$). The steady-state inactivation revealed an elevated non-inactivating current and $V_{0.5inact}$ was rightward-shifted by 8 mV ($V_{0.5inact}$ WT: -44.02 ± 0.84 mV, S1475A: -43.45 ± 0.96 mV, S1475D: -36.30 ± 0.65 mV, WT vs S1475A $p > 0.9$, S1475D vs WT and vs S1475A $p < 0.001$). Similar to the observations on peak current density and inactivation, WT and S1475A displayed comparable activation and inactivation kinetics (Fig. 60).

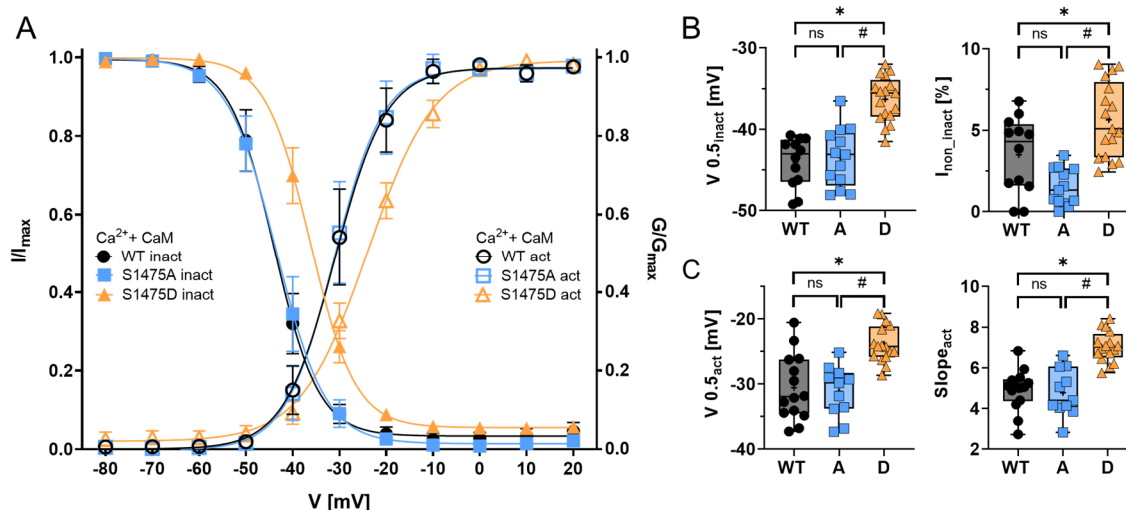


Figure 60. CaM co-expression modulates gating kinetics in dependence of residue at p. 1475. (A) Voltage-dependent activation (G/G_{max}) and steady-state inactivation (I/I_{max}) upon CaM co-expression are shifted towards more depolarized voltages for S1475D, also depicted by (B) $V_{0.5inact}$ and non-inactivating current (WT: $n = 12$, S1475A: $n = 13$, S1475D: $n = 17$) and (C) $V_{0.5act}$ and activation slope (WT: $n = 14$, S1475A: $n = 11$, S1475D: $n = 16$). Charge carrier: 2mM Ca^{2+} . Data shown as mean and 95 % CI or boxplots from min to max with all data points. * $p \leq 0.05$ vs WT and # $p \leq 0.05$ S1475A vs S1475D in Bonferroni's post hoc test following ANOVA.

CaM depletion

In a next step, data obtained under conditions that allowed saturated CaM effects were compared with data collected under conditions that abolished CaM effects. To completely deplete CaM effects, including those of endogenously expressed CaM, BsCaM_{IQ} was co-expressed in a 1:1 ratio with the α_1 -subunit. BsCaM_{IQ} contains the neuromodulin IQ-domain, which binds CaM with high affinity. Since this affinity exceeds those of other intracellular binding partners, including Cav1.3 channels, BsCaM_{IQ} withdraws endogenous CaM, therefore it is also referred to as an IQ-sponge.

Co-expressing BsCaM_{IQ} rightward-shifted the current-voltage relationship and reduced peak current density for all variants. Interestingly, co-expressing BsCaM_{IQ} converged the currents of all variants, resulting in similar peak current density regardless of the residue at position 1475 (WT: 3.77 ± 0.45 pA/pF, S1475A: 4.27 ± 0.17 pA/pF, S1475D: 3.74 ± 0.32 pA/pF, ANOVA $p = 0.41$). Additionally, the inactivation was similar at all test potentials for all variants with $\sim 35\%$ remaining current (-20 mV WT: $35.26 \pm 2.51\%$, S1475A: $33.08 \pm 1.66\%$, S1475D: $36.27 \pm 3.21\%$, ANOVA $p = 0.64$). Further, activation and inactivation kinetics were similar among variants without CaM (Fig. 61). This means, that S1475 dependent modulation of Cav1.3 currents did not occur without CaM.

Taken together, the results of co-expression and depletion of CaM revealed that CaM was necessary and sufficient for S1475 modulation of Cav1.3 activity.

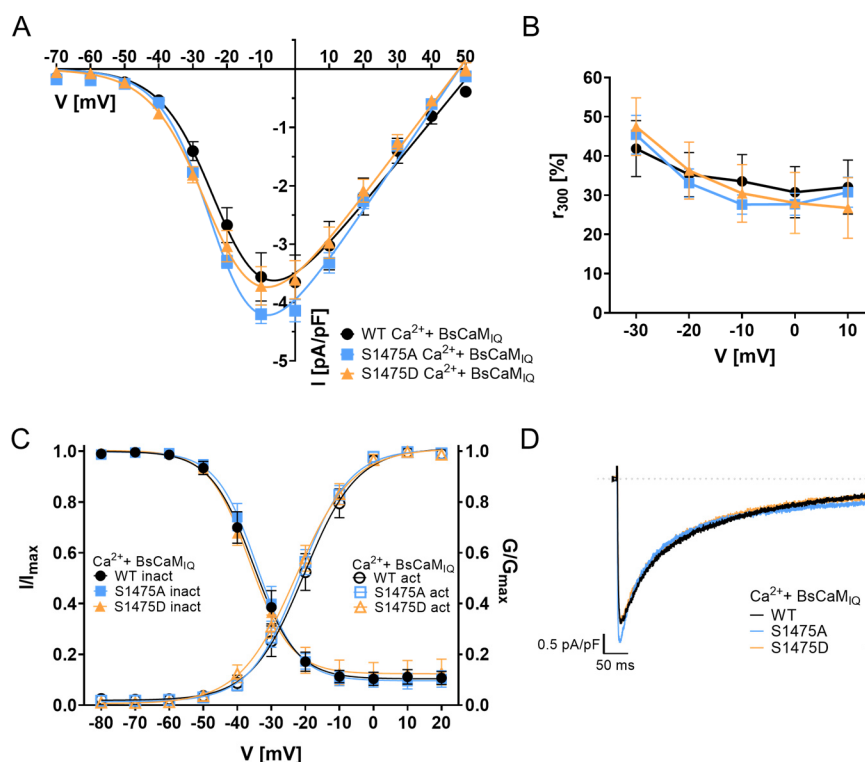


Figure 61. BsCaM_{1Q} co-expression results in similar whole-cell gating for WT, S1475A and S1475D. (A) Without CaM the current density carried by WT, S1475A and S1475D is similar, as well as (B) r_{300} (WT: $n = 14$, S1475A: $n = 18$, S1475D: $n = 13$). (C) Voltage-dependent activation (G/G_{max}) (WT: $n = 13$, S1475A: $n = 18$, S1475D: $n = 12$) and steady-state inactivation (I/I_{max}) (WT: $n = 14$, S1475A: $n = 18$, S1475D: $n = 10$) are also similar. (D) Exemplary traces visually confirm these similarities. Charge carrier: 2 mM Ca²⁺. Data shown as mean and 95 % CI. No statistically significant differences were detected in one-way ANOVA.

3.2.5. Role of Ca²⁺ in CaM-dependent S1475 modulation of Cav1.3 activity

CaM was necessary and sufficient for S1475 modulation of Cav1.3 activity. In those experiments Ca²⁺ was likely bound to CaM. Since Ca²⁺-free CaM (apo-CaM) can also modulate Cav1.3 activity, I investigated the role of Ca²⁺ in CaM-dependent S1475 modulation of Cav1.3 activity. Hereto, Ca²⁺ was withdrawn from CaM in a bilateral approach: First, Ca²⁺-currents were recorded upon co-expressing CaM₁₂₃₄, a CaM variant incapable of binding Ca²⁺. Second, Ba²⁺-currents were recorded upon co-expressing native CaM, which has negligible affinity for Ba²⁺ and thus remained Ca²⁺-free.

Ca²⁺-currents upon CaM₁₂₃₄ co-expression

Co-expressing CaM₁₂₃₄ resulted in similar peak current density for WT and S1475A, while peak current density of S1475D remained significantly lower (WT: 29.94 ± 2.47 pA/pF, S1475A: 35.44 ± 1.10 pA/pF, S1475D: 9.44 ± 0.45 pA/pF, WT vs S1475A $p = 0.06$, S1475D vs WT and vs S1475A $p < 0.001$). The remaining current of all variants was elevated, indicating that CaM₁₂₃₄ could not convey CDI. In comparison to WT and S1475A, however,

inactivation of S1475D remained significantly reduced (r_{300} at -30 mV, WT: 54.11 ± 3.17 %, S1475A: 58.31 ± 2.85 %, S1475D: 76.47 ± 2.15 %, WT vs S1475A $p = 0.85$, S1475D vs WT and vs S1475A $p < 0.001$). Regarding activation and inactivation kinetics, co-expressing CaM₁₂₃₄ resulted in similar gating kinetics for WT and S1475A, while S1475D displayed a rightward-shifted $V_{0.5\text{inact}}$ and $V_{0.5\text{act}}$ towards more depolarized potentials ($V_{0.5\text{inact}}$ WT: -38.57 ± 0.78 mV, S1475A: -38.83 ± 0.51 mV, S1475D: -33.18 ± 0.52 mV, WT vs S1475A $p > 0.9$, S1475D vs WT and vs S1475A $p < 0.001$) (Fig. 62). Despite observing similar effects as with Ca²⁺-bound CaM, CaM₁₂₃₄ effects were less pronounced. Compared to Ca²⁺-bound CaM, S1475D current density was 70 % larger than with CaM₁₂₃₄. Accordingly, in relation to WT and S1475A, peak current density reduction of S1475D was ~20 % smaller than with Ca²⁺-bound CaM. The same applied for CaM₁₂₃₄ effects on remaining current and (in-) activation kinetics. This means that Ca²⁺-binding did not make a qualitative difference but enhanced the actions of CaM in S1475 modulation of Cav1.3 activity.

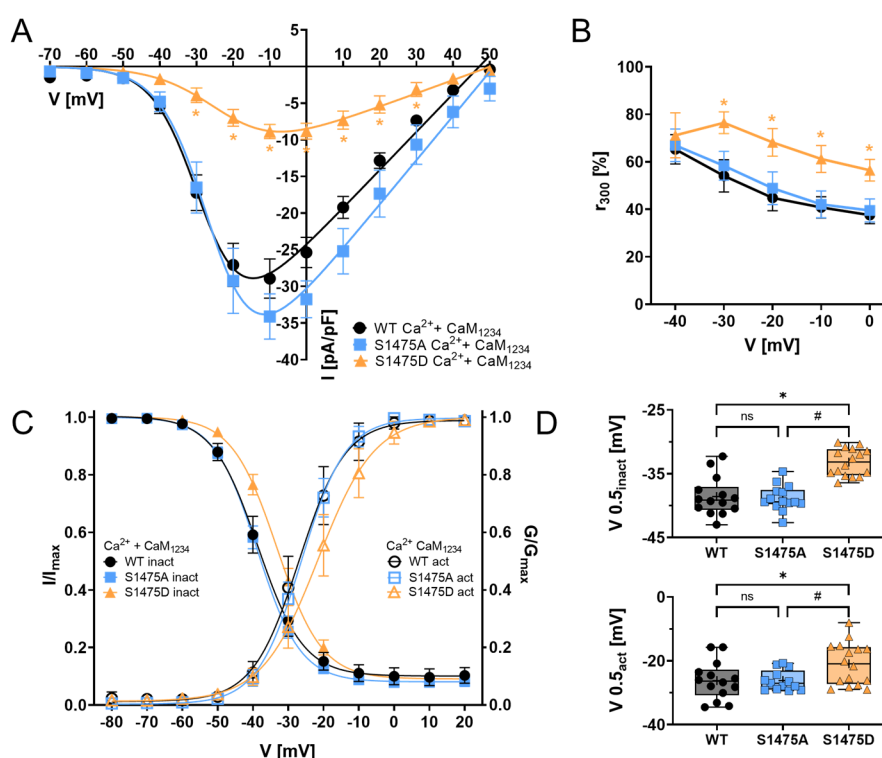


Figure 62. Ca²⁺-currents upon CaM₁₂₃₄ co-expression. (A) Co-expressing CaM₁₂₃₄ reduces current density for S1475D as well as (B) r_{300} (WT: $n = 14$, S1475A: $n = 15$, S1475D: $n = 16$). (C) Voltage-dependent activation (G/G_{max}) and steady-state inactivation (I/I_{max}) and accordingly (D) $V_{0.5\text{inact}}$ and $V_{0.5\text{act}}$ are rightward-shifted for S1475D (WT: $n = 14$, S1475A: $n = 14$, S1475D: $n = 16$). Charge carrier: 2mM Ca²⁺. Data shown as mean and 95 % CI or boxplots from min to max with all data points, + marks mean. * $p \leq 0.05$ vs WT and # $p \leq 0.05$ S1475A vs S1475D in Bonferroni's post hoc test following one-way ANOVA.

Ba²⁺-currents upon CaM co-expression

Since CaM primarily binds Ca²⁺ entering the cell via VGCCs, I used Ba²⁺ instead of Ca²⁺ as a charge carrier to prevent Ca²⁺-binding to CaM. The results on Ba²⁺-currents upon co-expressing native CaM were similar to the observations on Ca²⁺-currents upon CaM₁₂₃₄ co-expression with regard to the current density and (in-) activation kinetics.

Peak current density of WT and S1475A were similar, while S1475D peak current density was reduced, however, less pronounced compared to Ca²⁺-bound CaM (WT: 30.65 ± 3.37 pA/pF, S1475A: 30.91 ± 2.67 pA/pF, S1475D: 9.97 ± 1.03 pA/pF, WT vs S1475A $p > 0.9$, S1475D vs WT and vs S1475A $p < 0.001$). Regarding the activation and inactivation kinetics, Ba²⁺ induced a shift to more hyperpolarized potentials, since Cav1.3 has a higher conductance for Ba²⁺ over Ca²⁺. Compared to WT and S1475A, however, S1475D displayed rightward-shifted voltages of half-maximal (in-) activation ($V_{0.5 \text{ inact}}$ WT: -44.96 ± 0.66 mV, S1475A: -44.99 ± 0.52 mV, S1475D: -39.36 ± 0.81 mV, WT vs S1475A $p > 0.9$, S1475D vs WT and vs S1475A $p < 0.001$).

When Ba²⁺ instead of Ca²⁺ is used as charge carrier, only voltage- but not calcium-dependent inactivation (VDI not CDI) of Cav1.3 channels is conveyed. Therefore, more than ~70 % of the current remained for all variants. Contrary to CaM₁₂₃₄ co-expression, with Ba²⁺ and co-expressing native CaM, phosphorylation-mimicking S1475D showed similar inactivation to WT and S1475A (-30 mV, WT: 75.44 ± 2.70 %, S1475A: 73.64 ± 3.36 %, S1475D: 82.46 ± 2.09 %, ANOVA $p = 0.053$). This suggests that the observed differences in inactivation of S1475D were not caused by differences in VDI (Fig. 63).

Taken together, this means that Ca²⁺-binding did not make a qualitative difference on current density and gating kinetics but enhanced the actions of CaM in S1475 modulation of Cav1.3 activity.

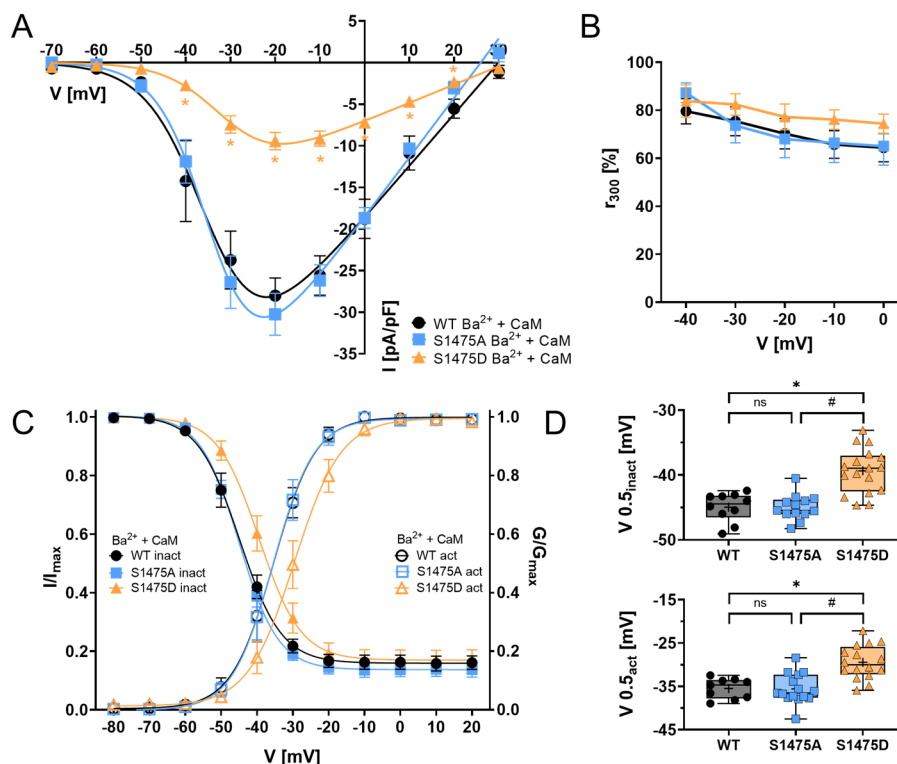


Figure 63. Ba²⁺-currents upon CaM co-expression. (A) Current density is reduced for S1475D, while (B) r_{300} was similar among variants (WT: $n = 10$, S1475A: $n = 15$, S1475D: $n = 17$). (C) (In-) activation kinetics, (D) $V_{0.5 \text{ inact}}$ (WT: $n = 10$, S1475A: $n = 13$, S1475D: $n = 17$) and $V_{0.5 \text{ act}}$ (WT: $n = 9$, S1475A: $n = 15$, S1475D: $n = 16$) are rightward -shifted for S1475D. Charge carrier: 2mM Ba²⁺. Data shown as mean and 95 % CI or boxplots from min to max with all data points, + marks mean. * $p \leq 0.05$ vs WT and # $p \leq 0.05$ S1475A vs S1475D in Bonferroni's post hoc test following one-way ANOVA.

Ba²⁺-currents without CaM co-expression

In addition to the bilateral approach depleting Ca²⁺ from CaM, Ba²⁺-currents were recorded without CaM co-expression as a control. Without Ca²⁺ and without co-expressed CaM, peak current density of S1475D was only reduced by 40 % in comparison to WT and S1475A (WT: 32.17 ± 2.17 pA/pF, S1475A: 35.02 ± 2.24 pA/pF, S1475D: 19.12 ± 1.82 pA/pF, WT vs S1475A $p > 0.9$, WT vs S1475D $p = 0.003$, S1475D vs S1475A $p < 0.001$). No further S1475 dependent differences were observed on the remaining current (ANOVA $p > 0.1$ at all test potentials) or activation (ANOVA $p > 0.1$) and inactivation (ANOVA $p > 0.1$) kinetics (Fig. 64).

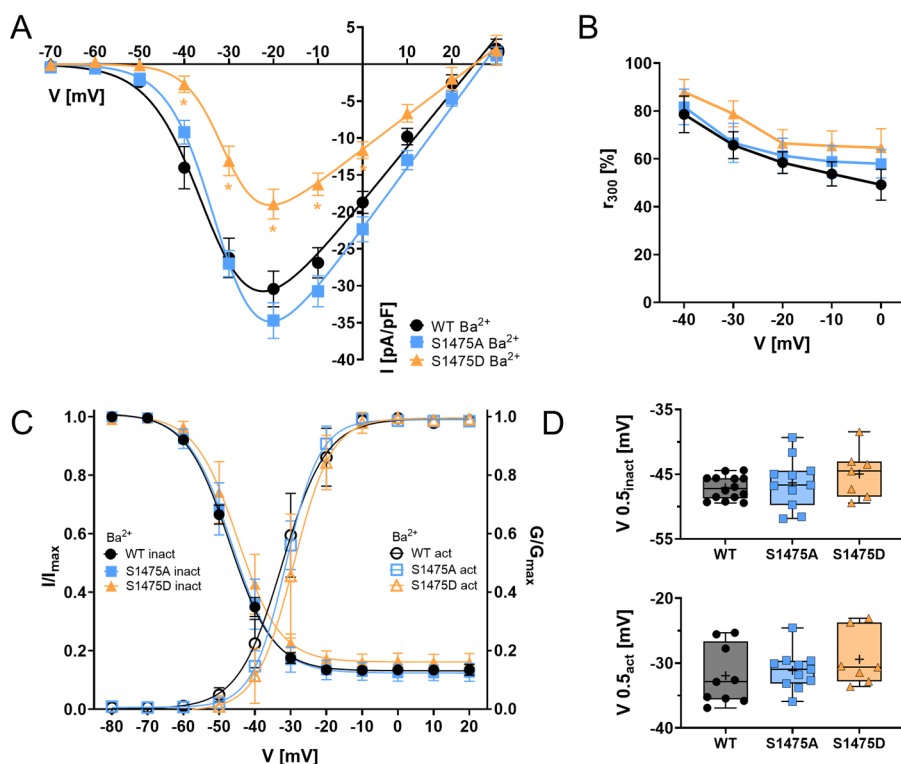


Figure 64. Ba²⁺ whole-cell currents. (A) S1475D current density is reduced by only by 40 % (WT: n = 14, S1475A: n = 12, S1475D: n = 7). (B) r_{300} and (C) (in-) activation kinetics, as well as (D) $V_{0.5\text{ inact}}$ (WT: n = 14, S1475A: n = 11, S1475D: n = 7) and $V_{0.5\text{ act}}$ (WT: n = 9, S1475A: n = 11, S1475D: n = 7) were similar. Charge carrier: 2mM Ba²⁺. Data shown as mean and 95 % CI or boxplots from min to max with all data points, + marks mean. *p ≤ 0.05 vs WT in Bonferroni's post hoc test following one-way ANOVA.

Additionally, comparing Ba²⁺- and Ca²⁺-currents with and without CaM co-expression revealed that CaM co-expression enhanced WT Ca²⁺-currents, while WT Ba²⁺-currents remained similar. For S1475D, however, CaM co-expression reduced peak current density in Ba²⁺- and Ca²⁺-currents. Thus, reduction of peak current density in S1475D seems to be regardless of the charge carrier and only dependent on CaM expression levels (Fig. 65).

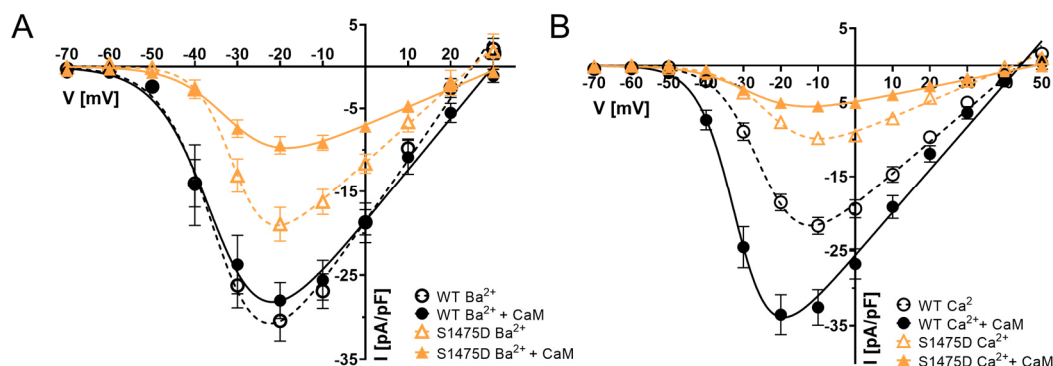


Figure 65. Comparison of Ca²⁺- and Ba²⁺-currents with and without CaM co-expression. (A) CaM co-expression reduces Ba²⁺-currents of S1475D, while WT currents remain similar. (B) CaM co-expression reduces Ca²⁺-currents of S1475D, while WT currents increase. Thus, reduction of current density in S1475D is regardless of the charge carrier. Values shown as mean ± SEM.

In summary, addressing the role of Ca^{2+} in CaM-dependent S1475 modulation of $\text{Cav}1.3$ activity revealed that Ca^{2+} -free CaM was able to modulate current density and (in-) activation kinetics of $\text{Cav}1.3$ currents in phosphorylation-mimicking S1475D channels. Inactivation of S1475D was only decreased when Ca^{2+} was used as a charge carrier, thus suggesting CDI instead of VDI to be affected in S1475D channels. All observed differences, however, were less pronounced compared to Ca^{2+} -bound CaM in both approaches. Consequently, while Ca^{2+} is only essential for certain S1475-modulated parameters, it overall enhances CaM-dependent S1475 modulation of $\text{Cav}1.3$ activity.

3.2.6. CaM-dependent reduction of CDI in phosphorylation-mimicking S1475D

In a next step, calcium-dependent inactivation was analyzed in more detail, as both Ca^{2+} - and CaM-dependent properties modulated $\text{Cav}1.3$ S1475D currents. When using Ca^{2+} as a charge carrier, inactivation of $\text{Cav}1.3$ currents consists of a voltage-dependent and Ca^{2+} -dependent component (VDI and CDI). As mentioned, since CaM barely binds Ba^{2+} , using Ba^{2+} as charge carrier abolishes CDI, with voltage remaining as the driving force for inactivation. Therefore, the difference between the amount of inactivation obtained using either Ba^{2+} or Ca^{2+} indicates the fraction of CDI. Here, the fraction of CDI was calculated using r_{300} at peak current test potentials without (-10 mV) and with (-20 mV) CaM co-expression and is reported by f-values and compared among variants. Without CaM co-expression, f-values were ~40–50 % and thus, similar among variants (WT: 44.05 ± 1.41 , S1475A: 46.17 ± 1.81 , S1475D: 41.78 ± 2.44 , ANOVA $p = 0.28$). Upon CaM co-expression, the remaining Ba^{2+} -current increased for all variants. Consequently, the fraction of CDI increased for WT and S1475A to 50–60 %. For S1475D, however, the remaining Ca^{2+} -currents increased as well, resulting in similar CDI with and without CaM co-expression. Comparing CDI among variants upon CaM co-expression thus revealed a significant reduction in CDI for S1475D (WT: 57.22 ± 1.71 , S1475A: 50.72 ± 2.77 , S1475D: 37.10 ± 2.81 , WT vs S1475A $p = 0.3$, WT vs S1475D $p < 0.001$, S1475A vs S1475D $p = 0.002$) (Fig. 66).

In conclusion, the above-mentioned reduction in inactivation of phosphorylation-mimicking S1475D channels was a modulation of $\text{Cav}1.3$ CDI not VDI.

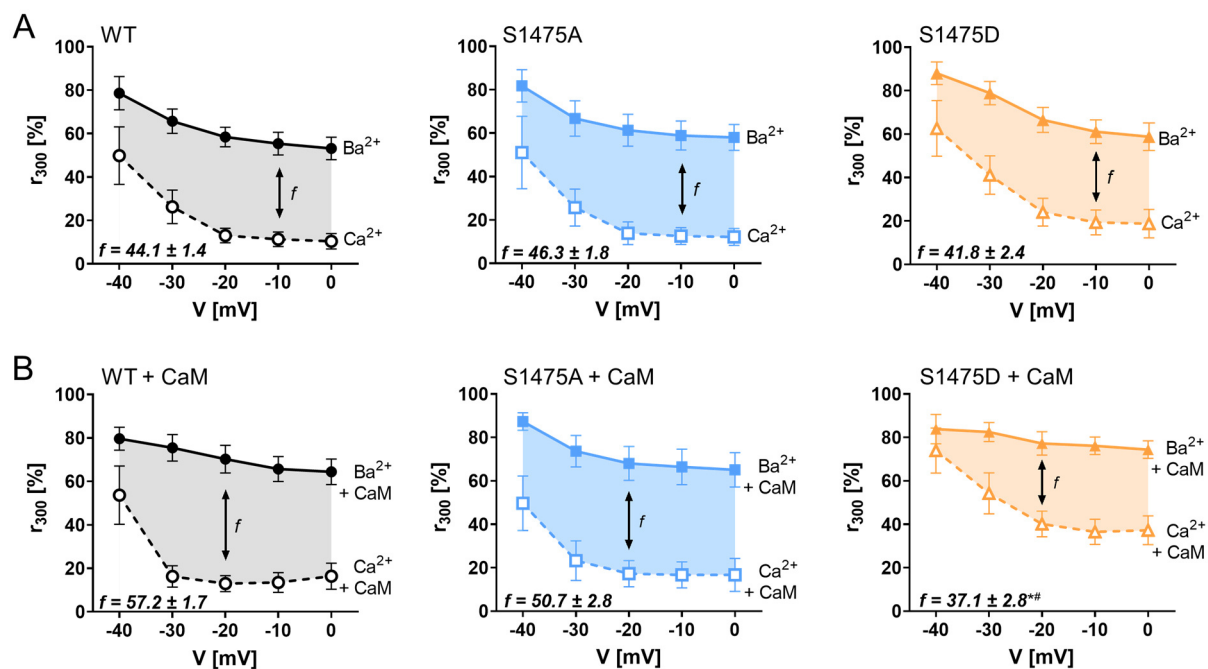


Figure 66. Comparison of CDI with and without CaM co-expression. (A) r_{300} without CaM co-expression compared for Ba^{2+} - and Ca^{2+} -currents. Shaded area reports CDI, which is similar among variants. **(B)** r_{300} with CaM co-expression compared for Ba^{2+} - and Ca^{2+} -currents reveals decreased CDI for S1475D. f -values are reported as mean \pm SEM. Data shown as mean and 95% CI. Number of experiments reported in figures 50, 59, 63 and 64. * $p \leq 0.05$ vs WT and # $p \leq 0.05$ S1475A vs S1475D in Bonferroni's post hoc test following one-way ANOVA.

3.2.7. Decreased Ca^{2+} -influx through S1475D in response to SAN-like action potentials

The previous results characterized how S1475 phosphorylation imitation modulated Cav1.3 gating. How this modulation, however, shapes Cav1.3 currents under more physiological conditions remains unclear. To approach this topic, I recorded Ca^{2+} -currents for WT, S1475A and S1475D in response to sinoatrial-node like action potentials (SAN-APs).

In the heart, the SAN-AP is initiated by Na^{+} - and T-type Ca^{2+} -influx. Upon threshold, the depolarization is carried to the peak by L-type Ca^{2+} -influx, followed by K^{+} -efflux during repolarization, which is in the end counteracted by Na^{+} -influx back to resting membrane potential. As mentioned, Cav1.3 is the predominant L-type channel in the SAN, thereby mediating cardiac pacemaking, as loss of Cav1.3 leads to bradycardia.

A SAN-AP-like pulse protocol was used to stimulate WT, S1475A and S1475D, imitating a heart rate of 75 bpm. Since CaM was necessary and sufficient for S1475-mediated modulation of Cav1.3 currents, CaM was co-expressed for these experiments. In agreement with the physiological role of Cav1.3 in SAN-AP, all variants showed peak

Ca²⁺-currents during the SAN-AP depolarization phase and a second current during early repolarization. Compared to WT and S1475A, S1475D channels displayed a reduced peak current density during depolarization, in line with previous observations (WT: 9.28 ± 1.04 pA/pF, S1475A: 10.71 ± 1.17 pA/pF, S1475D: 2.43 ± 0.39 pA/pF, WT vs S1475A $p = 0.9$, S1475D vs WT and vs S1475A $p < 0.001$). The current during repolarization, however, was similar among variants (WT: 1.74 ± 0.20 pA/pF, S1475A: 1.94 ± 0.20 pA/pF, S1475D: 1.32 ± 0.16 pA/pF, ANOVA $p = 0.09$). To estimate the total Ca²⁺-influx in response to SAN-AP-like stimuli, the area under the curve (AUC) was calculated. S1475D displayed reduced Ca²⁺-influx in response to SAN-AP-like stimuli (WT: 1.16 ± 0.20 , S1475A: 1.63 ± 0.28 , S1475D: 0.48 ± 0.10 , WT vs S1475A $p = 0.3$, WT vs S1475D $p = 0.04$, S1475A vs S1475D $p < 0.001$) (Fig. 67).

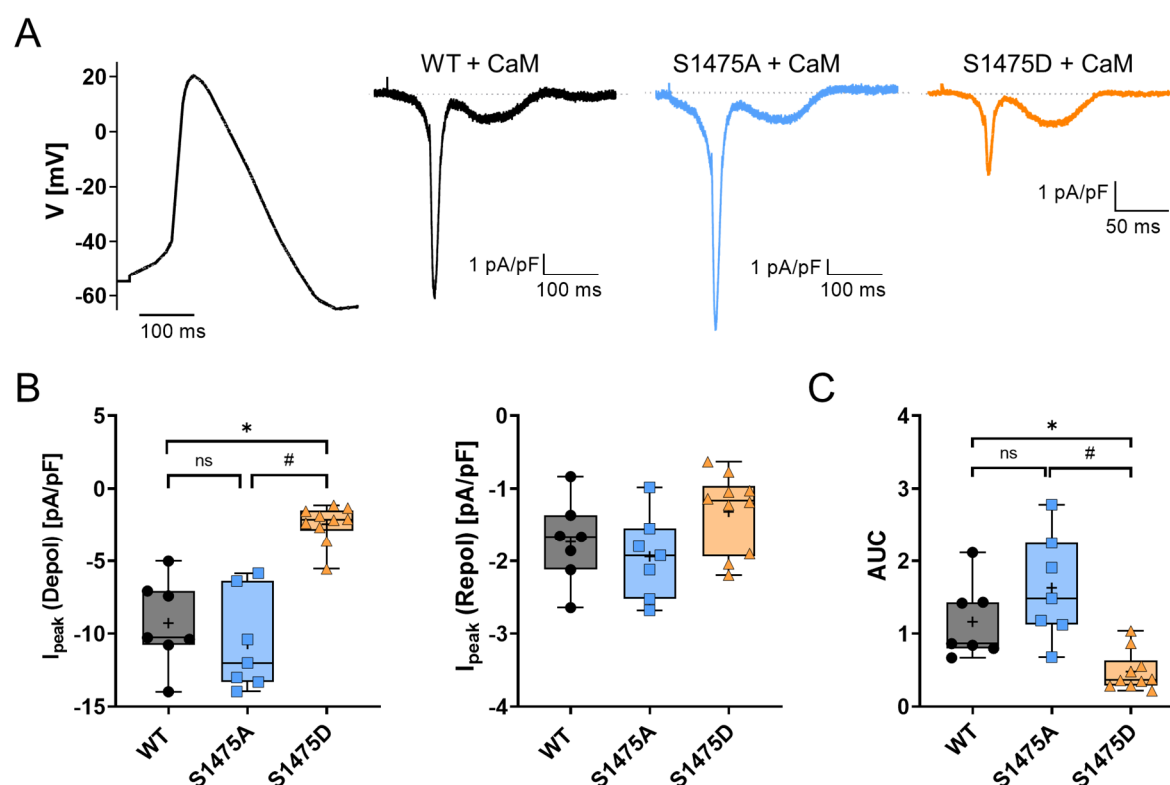


Figure 67. SAN-AP-like stimulation of WT, S1475A and S1475D during CaM co-expression. (A) Pulse protocol of SAN-AP and corresponding exemplary traces. (B) Peak current density during depolarization was reduced for S1475D, while peak current density during repolarization was similar among variants. (C) Area under the curve shows reduced total Ca²⁺-influx for S1475D. WT: $n = 7$, S1475A: $n = 7$, S1475D: $n = 10$. Charge carrier: 2 mM Ca²⁺. Data shown as boxplots from min to max with all data points, + marks mean. * $p \leq 0.05$ vs WT and # $p \leq 0.05$ S1475A vs S1475D in Bonferroni's post hoc test following one-way ANOVA.

3.2.8. S1475 phosphorylation imitation appears to alter intramolecular interactions

While the previous results characterized the mechanisms through which S1475 modulates Cav1.3 gating, these mechanisms may originate in S1475 phosphorylation-dependent intra- or intermolecular changes.

A potential intramolecular change could be an altered interaction with surrounding residues, arising from charge differences between serine and a phosphorylated serine at position S1475. To address such a potential intramolecular change, residues interacting with S1475 or D1475 were structurally modeled in the Cav1.3 cryo-EM structure using *PyMol* and *AlphaFold 2*. The recently published Cav1.3 cryo-EM structure (7UHG, Yao et al., 2022) revealed that the E-helix of the EF-hand is in close structural proximity to the intracellular linker connecting domain III and IV (III-IV linker) (Fig. 68).

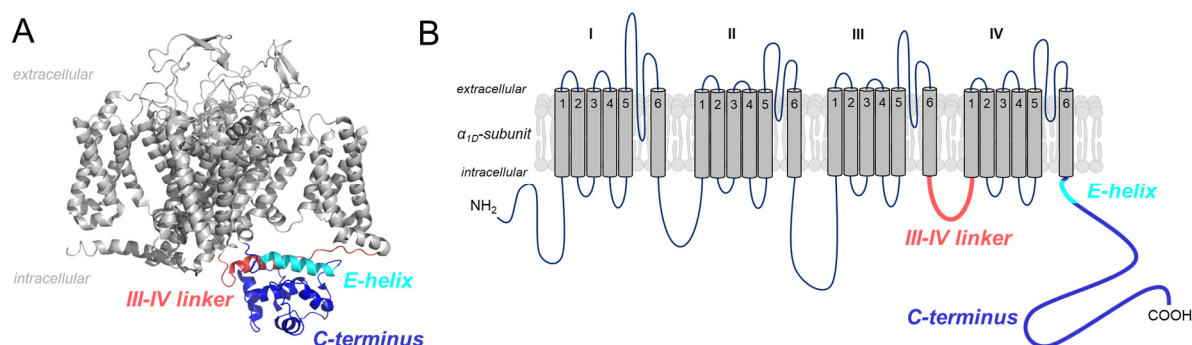


Figure 68. 3D and 2D structure of Cav1.3 α_1 -subunit. (A) 3D cryo-EM structure of Cav1.3 (7UHG, Yao et al., 2022). III-IV linker (red), C-terminus (blue) and E-helix (cyan) are highlighted. III-IV linker and E-helix are in close proximity. **(B)** Same regions highlighted in the 2D structure.

The structural modeling revealed that S1475 was located at the C-terminal end of the E-helix of the EF-hand. S1475 interacted N-terminally with K1471 and R1472 and C-terminally with D1478 and P1479, in line with the known 3.6 residues per turn structure of an α -helix (Sinden, 1994). Modeling S1475D did not affect these intrahelical interactions. Aside from the intrahelical interactions, S1475 interacted with R1187 in the III-IV linker. Modeling S1475D, however, revealed that aspartic acid's COO⁻ side chain tilted away counterclockwise from the α -helix, which resulted in an interaction of D1475 with L1185 instead of R1187 in the III-IV linker (Fig. 69).

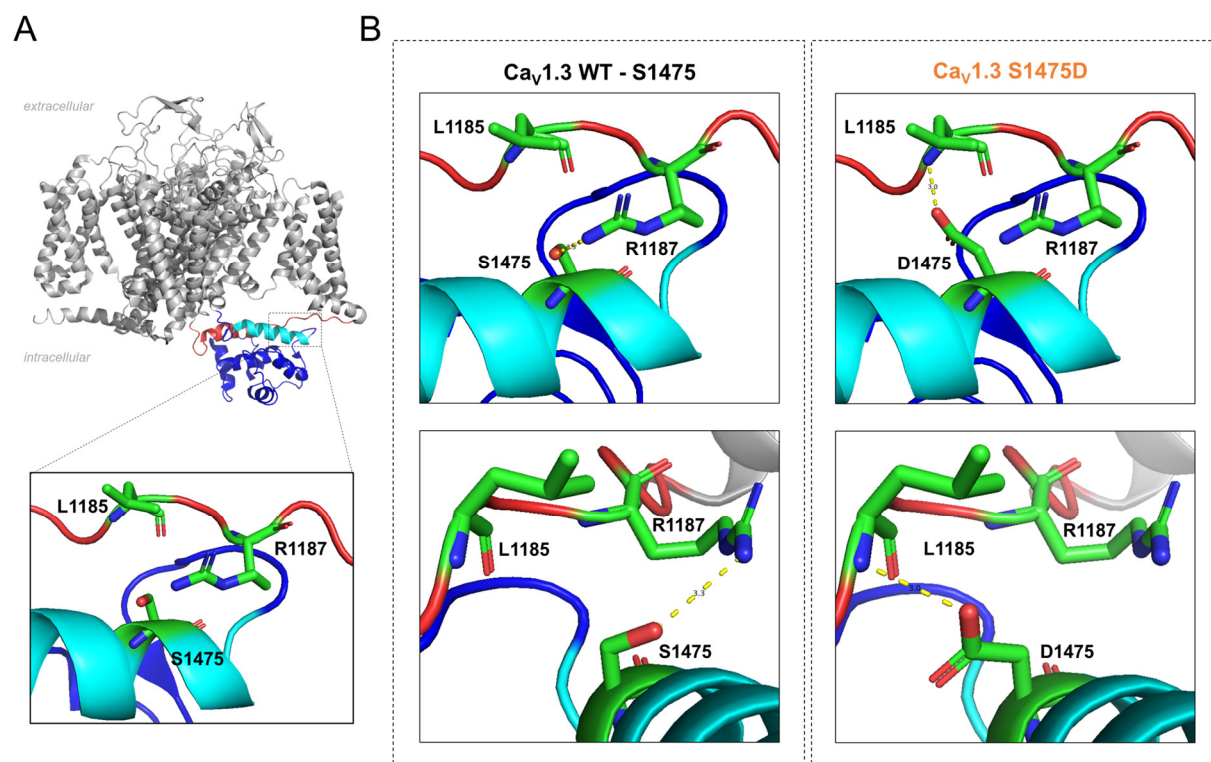


Figure 69. Structurally modeling intramolecular interactions of S1475 and D1475 within the $\text{Ca}_v1.3$ α_1 -subunit. (A) 3D cryo-EM structure of $\text{Ca}_v1.3$ with highlighted regions corresponding to Fig. 68. Enlargement shows L1185 and R1187 in the III-IV linker and S1475 in the E-helix as sticks colored by element (C (green), N (blue), O (red)). (B) S1475 interacts with R1187, while D1475 interacts with L1185 as indicated by dashed yellow line also reporting distance in Ångstroms. Interactions shown in two perspectives (top row and bottom row).

Since L1185 and R1187 were located in an unstructured region of the III-IV linker, *AlphaFold2* was used to determine the accuracy of structural prediction in this region. Hereto, *AlphaFold2* provides the per-residue confidence score (pLDDT). This score is the result of the local *Distance Difference Test* indicating local structural accuracy, thus used to classify the model's confidence.

To estimate the confidence of L1185 and R1187 in structural modeling and therefore also the accuracy of the predicted interaction with S1475 and D1475, respectively, pLDDT-scores were calculated for all residues. As expected, since S1475 is part of an α -helix it had a higher pLDDT-score than L1185 and R1187 (pLDDT S1475: 87.55, L1185: 82.57, R1187: 75.40). All residues, however, had scores between 90 and 70 and were therefore considered to be confident in their local structural accuracy (Fig. 70). Accordingly, also the predicted interactions with S1475 and S1475D, respectively, were considered to be confident.

In conclusion, imitation of S1475 phosphorylation could alter the intramolecular interaction with residues in the III-IV linker, thus potentially linking functional and structural effects of imitating S1475 phosphorylation.

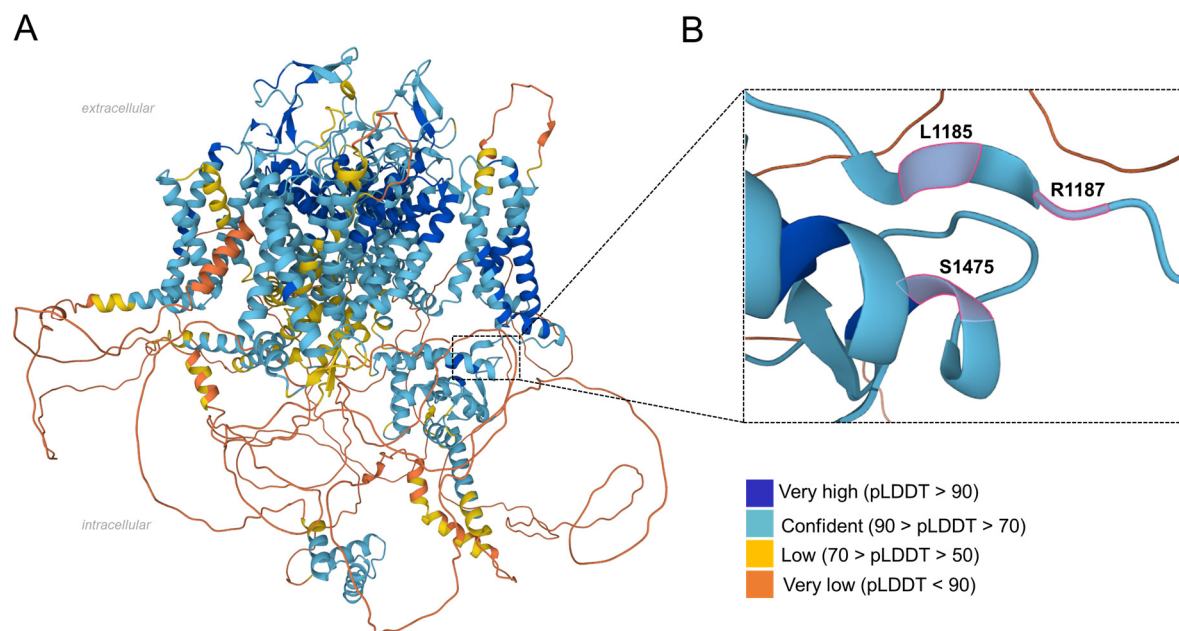


Figure 70. Prediction of structural accuracy within $\text{Ca}_v1.3$ α_1 -subunit. (A) Structural accuracy color coded across 3D structure of $\text{Ca}_v1.3$. Especially the distal C-terminal region has very low structural accuracy. (B) Enlargement shows S1475, L1185 and R1187, highlighted in pink frames. Per-residue confidence score (pLDDT) of all residues is considered confident.

4. Discussion

Cav1.3 L-type voltage-gated calcium channels have an indispensable role in auditory transduction, endocrine responses, cardiac pacemaking and neuronal development (Catterall et al., 2005). Among LTCCs, Cav1.3 has unique electrophysiological properties, foremost its activation at more hyperpolarized voltages than other LTCCs (Koschak et al., 2001; Xu & Lipscombe, 2001). Cav1.3 activity is modulated by alternative splicing, calcium dependent inactivation (CDI) and phosphorylation (Ben-Johny & Yue, 2014; Catterall, 2011; Singh et al., 2008). In fact, Cav1.3's susceptibility to its own gating modulation is the central element of its function. Cav1.3 modulation via CDI involves binding of the Ca²⁺-sensor protein calmodulin (CaM) to the C-terminal EF-hand and IQ-domain to prevent excessive Ca²⁺-influx (Ben Johny et al., 2013). Alternative C-terminal splicing affects the composition of C-terminal domains and thereby alters gating properties (Bock et al., 2011; Singh et al., 2008). Species-dependent differences in the C-terminal structure limit applicability of findings obtained in rat Cav1.3 isoforms to human channel variants (Lieb et al., 2012). Notably, all known phosphorylation sites modulating Cav1.3 activity were identified in the rat and are yet unconfirmed for human channels. From a pathophysiological perspective, Cav1.3 modulation by missense mutations reveals that neuronal development is crucially susceptible to dysregulated Cav1.3 Ca²⁺-currents. Herein, neurodevelopmental pathologies are often accompanied by endocrine symptoms resulting from so-called gain-of-function type 1 or type 2 gating changes on whole-cell level (Ortner et al., 2020). So far, neither Cav1.3 gating behavior under physiological nor pathophysiological conditions are sufficiently understood to e.g. confidently draw conclusions about therapeutically useful modulation of channel activity. In accordance, the aim of this thesis was to investigate the modulation of Cav1.3 gating from a physiological and pathophysiological perspective, using a human Cav1.3 isoform as the most medically relevant species.

4.1. Pathophysiological perspective: Disease-associated *CACNA1D* missense mutations induce gain-of-function through individual gating phenotypes

Pathophysiological gating modulation was investigated for missense mutations L271H, A749T and F747S. All three are associated with neurodevelopmental delay in children, accompanied by hyperaldosteronism (L271H) (De Mingo Alemany et al., 2020), autism-spectrum disorder and auto-aggression (A749T) (Ortner et al., 2020), and hyperaldosteronism and touch-induced jittering (F747S) (Török et al., 2022). Of the ten known high-risk disease-causing germline *de novo* *CACNA1D* missense variants, L271H, A749T and F747S were most recently identified, and have so far been functionally characterized only at the whole-cell level.

While clinical and experimental results show similarities between the cases, the observed differences may indicate that there are relevant biophysical differences of the mutants at the molecular level. To analyze this, I obtained single-channel recordings in this thesis. The objectives were (1) to identify the gating phenotype induced by each mutation, to test whether and to what extent it may explain the effects at whole-cell level, and (2) to compare these gating phenotypes to draw conclusions on the hypothesis that differential gating modulation could explain the different clinical phenotypes. The main findings are that all mutations increase single-channel activity while exhibiting individual gating phenotypes. L271H induces a shift towards more hyperpolarized voltages with respect to availability, voltage of half-maximal activation, open probability, reversal potential and peak current. A749T also induces a shift in voltage of half-maximal activation towards more hyperpolarized voltages, but increases open probability throughout the voltage range, mainly due to an increased opening frequency. While enhanced single-channel activity of L271H appears to be sufficiently explained by the leftward shift in its voltage dependence, activity of A749T appears to be increased beyond the observed leftward shift. F747S findings are striking in terms of positive-cooperative channel-channel interaction, so far unknown for Cav1.3, accompanied by a shift in voltage of half-maximal activation towards more hyperpolarized voltages and a change in the gating mode towards mode 2 gating. With respect to the aims mentioned above, the following discussion focusses on (1) using the identified gating phenotypes to explain the effects observed on whole-cell level and to classify the types of gating changes and on (2) combining single-channel gating phenotypes and structural modeling to draw conclusions on the differential clinical phenotypes.

4.1.1. Single-channel data unmask the mechanism underlying changes at whole-cell level

The results show that all three mutations induce gating phenotypes with gain-of-function characteristics. This is in line with the observations made on whole-cell level, (Jörg Striessnig, personal communication). Of note, I was blinded for the mutant constructs and whole-cell effects when performing single-channel experiments and analysis, thus reducing experimental bias.

On whole-cell level, L271H shifts current activation and inactivation towards more hyperpolarized voltages, but does not increase whole-cell peak current density (Jörg Striessnig, personal communication). On single-channel level, as revealed in this thesis, L271H shifts availability, voltage of half-maximal activation, open probability, reversal potential and peak current towards more hyperpolarized voltages. Of note, differences in L271H single-channel gating compared to WT at a given test potential are sufficiently explained by this leftward shift of voltage-dependence. This fits one-to-one to the observation at whole-cell level, where IV-curves are shifted towards more hyperpolarized potentials while the peak current density is similar to that of WT Cav1.3. L271H can thus be classified to induce so-called type 2 gating changes. Since the short C-terminal isoform of Cav1.3 already causes a leftward-shift in voltage-dependent activation compared to the long isoform used in this study (Singh et al., 2008), L271H should also be investigated for the short isoform in future studies. If the effect of L271H and that of the short C-terminus were additive, this would cause L271H to operate at voltages similar to those activating low-voltage activated T-type channels (Perez-Reyes, 2003).

The exhibited symptoms in the individual carrying L271H are similar to known symptoms caused by other missense variants (Ortner et al., 2020). Based on the increased channel activity revealed in this thesis, administering LTCC inhibitors appears to be reasonable. Indeed, nifedipine improved the clinical condition, mainly by attenuating hypotonia (De Mingo Alemany et al., 2020). L271H channels may have an increased DHP-sensitivity as a leftward-shifted inactivation increases the fraction of inactivated channels. Since DHP-binding depends on the inactivated state, this could thus increase DHP-sensitivity (Tang et al., 2016).

On whole-cell level, A749T shifts voltage-dependent activation and inactivation towards more hyperpolarized voltages and increases whole-cell peak current density (Jörg Striessnig, personal communication). On single-channel level, as revealed in this thesis,

A749T shifts availability and voltage of half-maximal activation towards more hyperpolarized voltages and increases open probability. Plotting the opening probability (P_{open}) against the test potential indicates that, independent of the observed leftward shift, the maximum P_{open} of A749T is increased compared to WT, regardless of the membrane potential. Due to the shift in voltage-dependence, however, A749T can be classified to induce type 2 gating changes, too.

Given the electrophysiological changes observed with A749T, administering LTCC inhibitors in A749T carrying individuals could be beneficial. In the published case, however, isradipine administration was discontinued because symptoms worsened with the concomitant presence of a cold (Ortner et al., 2020). It thus remains unclear whether isradipine application would have been beneficial long-term. Further, immediate-release isradipine was administered as the isradipine formulation used, an issue that has been discussed in the context of a study on early stages of Parkinson's disease in which isradipine failed to show a benefit (Parkinson Study Group, 2020). This thesis suggests, that each investigated mutation differentially alters gating parameters that may affect DHP-binding, and thus perhaps alter the effects of DHP treatment. Therefore, the lack of benefit of isradipine treatment in the case of A749T and early-stage PD may be due to the fact that a modulator of channel gating is needed to rescue the specific gating phenotype, rather than undifferentiated Cav1.3 antagonism.

Regarding electrophysiological characterization of F747S on whole-cell level, F747S shifts voltage-dependent activation and inactivation towards more hyperpolarized voltages. Similar to L271H but in contrast to A749T, F747S does not increase current density. Additionally, F747S reduces inactivation (Török et al., 2022) (Fig. 71).

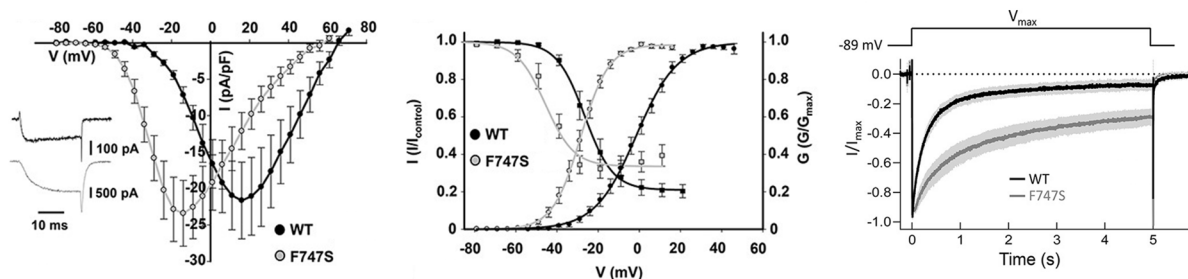


Figure 71. Whole-cell characterization of F747S. F747S shifts voltage-dependent activation and inactivation towards more hyperpolarized voltages and decreases inactivation but does not increase peak current density (Török et al., 2022).

The results obtained in the cell-attached (i.e. single-channel) configuration in this thesis are remarkable. In recordings with only one channel in the patch ($k = 1$), single-channel gating was similar compared to Cav1.3 WT, including a similar voltage-dependence of channel activity. With more than one channel in the patch ($k > 1$), activity was significantly shifted to more hyperpolarized voltages and the open probability increased by 25-fold, despite mathematical correction for the number of channels in the patch. Furthermore, in multi-channel recordings, open-time-histograms revealed two populations of opening durations, indicating the presence of so-called mode 2 gating (Herzig et al., 1993; Hess et al., 1984; Tanskanen et al., 2005). These findings are thus evident of F747S inducing positive cooperative channel-channel interaction leading to enhanced single-channel activity. Using the cell-attached configuration, seal statistics revealed an increased amount of empty patches, indicating an altered distribution of channels in the membrane, e.g. due to arranging in pairs or clusters. Together with the observed cooperativity, these results imply, that not observing increased peak current density for F747S on whole-cell level originates in a decreased number of F747S channels expressed across the membrane.

Cooperative LTCC gating was first reported for Cav1.2 channels in smooth muscle and cardiomyocytes (Koschak et al., 2007; Navedo et al., 2010), then also found in Cav1.3 channels (Moreno et al., 2016). Herein, Cav1.3 cooperative gating was reported to be Ca^{2+} -dependent and to occur only in the short C-terminal splice variant, via interaction of neighboring C-termini (Dixon et al., 2022; Moreno et al., 2016). Thus, for the first time this thesis describes functional cooperativity of full-length Cav1.3 using Ba^{2+} as charge carrier. In addition, the coupling coefficient (κ) was calculated, which indicates the coupling probability on a scale of 0 to 1, based on simultaneously occurring openings of multiple channels (Navedo et al. 2010 based on Chung & Kennedy, 1996). The coupling coefficient for WT and F747S multichannel patches in this thesis was $\kappa < 0.02$ for both variants, while Moreno et al. reported a higher κ of 0.29 for the short Cav1.3 isoform in their study (Moreno et al., 2016). Accordingly, the here observed cooperativity unlikely resembled the channel coupling that Moreno et al. observed. Further, coupled gating has so far only been observed in LTCC clusters containing ~ 8 channels (Moreno et al., 2016; Navedo et al., 2010). In this thesis, cooperative gating was observed in patches containing two or three channels. Both findings thus indicate that the here observed cooperativity is a novel kind of cooperative channel gating, different from that described by Navedo et al. and Moreno et al. (Moreno et al., 2016; Navedo et al., 2010). This novel kind of cooperative

channel gating is certainly interesting to future research. For example, clustering of TRPV4 channels was observed to occur with increased levels of scaffolding protein AKAP5 (Dixon et al., 2022; Mercado et al., 2014; Tajada et al., 2017). The long Cav1.3 isoform contains a PDZ binding domain at the distal C-terminus, which has been shown to interact with the scaffolding proteins densin-180 and shank1b (Stanika et al., 2015; Stanika et al., 2016). Thus, regarding F747S, scaffolding proteins could play a role in the likely altered membrane distribution and positive cooperative channel-channel gating. Of note, seal statistics are limited in their validity to report changes in membrane expression. Super-resolution microscopy would help to conclusively clarify F747S membrane distribution in future studies (Baddeley et al., 2009; Moreno et al., 2016; Vivas et al., 2017). Further, total internal reflection fluorescence (TIRF) microscopy and split-Venus bi-molecular fluorescence complementation can be used to visualize so-called channel sparklets and C-terminal coupling (Moreno et al., 2016).

Given the leftward-shifted voltage-dependence, F747S can be classified as causing type 2 gating changes from a whole-cell perspective, similar to L271H and A749T. However, the single-channel recordings suggest that the shift in activation is a specific feature of cooperativity in the case of F747S. In fact, cooperatively gating LTCCs have been reported to activate at more negative voltages (Dixon et al., 2022). The current findings on cooperative gating of F747S suggest that the leftward shift of its voltage-dependence is due to a different mechanism than that observed with L271H and A749T. Accordingly, perhaps the definition of type 2 gating changes proposed by Pinggera et al. (Pinggera et al., 2018) should be further divided into subtypes based on single-channel observations. As with L271H and A749T, the single-channel results obtained with F747S may explain the changes observed at the whole-cell level. Given the vast enhancement of single-channel activity, however, it is assumed that the expression level of functional or available channels is reduced with F747S compared to WT Cav1.3. This interpretation is supported by the finding that the percentage of empty patches was significantly increased when expressing mutant channels. The single-channel findings further suggest implications for therapeutically targeting F747S. An approach to revoke channel cooperativity could result in F747S channels behaving like WT channels.

Taken together, the findings on single-channel gating provided in this thesis reveal that each of the three mutations causes an individual gating phenotype. Although each of these

phenotypes represents a gain-of-function phenotype, the data could argue for different pathological effects and different channel modulation as a therapeutic approach.

4.1.2. Different disease-associated Cav1.3 mutations differ in clinical phenotype, single-channel gating and intramolecular interactions

Structural modeling paired with single-channel recordings may give first hints towards an association of molecular changes and a certain clinical phenotype.

Not only the position of the mutation, but also the chemical properties of the residue itself seems to determine the clinical and functional consequences. The exchange of alanine to threonine at p.749 (A749T) is associated with neurodevelopmental delay, autism spectrum disorder (ASD) and auto-aggression but without endocrine symptoms (Ortner et al., 2020). Among the ten high-risk disease-causing germline *de novo* *CACNA1D* missense-mutations also an alanine to glycine exchange is reported at the same position (A749G) (Ortner et al., 2020; Pinggera et al., 2015). Clinically, the symptoms caused by A749G and A749T were greatly overlapping. However, while A749G, like A749T, was associated with ASD but not endocrine symptoms, patients with the A749G mutation, unlike A749T mutation carriers, showed neither auto-aggression nor hypotonia but impaired motor skills. Electrophysiological characterization of A749G reveals changes similar to that observed with A749T (Pinggera et al., 2015). It is tempting to speculate that different single-channel gating changes underlie the whole-cell electrophysiological phenotype, perhaps leading to different pathological changes at the cellular level and thus different clinical phenotypes. However, so far, the A749G variant has not been characterized at the single-channel level.

A749T is located in the highly conserved “LAIA” motif and a corresponding mutation was identified in T-type Cav3.1 channels (corresponding position: A961T) (Chemin et al., 2018). Clinically, the seven individuals carrying A961T show severe intellectual impairment, hypotonia, an atrophic cerebellum accompanied by delayed motoric development and oculomotor apraxia (Barresi et al., 2020; Casas-Alba et al., 2021; Chemin et al., 2018). Functionally, current density was not increased, but inactivation was delayed, and activity was shifted to more hyperpolarized voltages, the latter similar to the observations made in Cav1.3 (Chemin et al., 2018). I am currently performing experiments to clarify which single-channel phenotype is caused by Cav3.1 A961T.

In future studies, the relation between functional changes at the molecular or cellular level and the clinical phenotype should be addressed *in vivo*. An A749G knock-in mouse

model was created and is currently characterized by the research group of Jörg Striessnig (Török et al., 2022). Of note, murine but not rat Cav1.3 isoforms contain a functional CTM, thus being closer to the human isoform. Accordingly, mouse model characterization of such high-risk disease-causing sites may help to understand the relation between clinical and functional saliences.

Similar to A749, also different missense variants are known at F747. Clinically, the patient carrying F747S was diagnosed with neurodevelopmental delay, hyperaldosteronism and touch-induced jittering, with the latter being a novel symptom reported in *CACNA1D* missense mutations. The somatic missense variants F747C, F747L and F747V have been reported in a total of 42 individuals with aldosterone producing adenomas or cell clusters (APA/APCC) but without neurodevelopmental delay and without jittering (Azizan et al., 2013; Ortner et al., 2020). F747L was functionally characterized on whole-cell level, also revealing type 2 gating changes, although to a weaker extent (Pinggera et al., 2018). While the electrophysiological characterization reveals similar changes in F747S and F747L, the clinical phenotypes differ greatly. Since touch-induced jittering only occurs in F747S and single-channel gating revealed positive cooperative channel-channel interaction in this mutant, it is once again tempting to speculate that different single-channel changes underlie the whole-cell phenotype, perhaps leading to different pathological changes and thus different clinical phenotypes.

Structural modeling combined with single-channel data further supports the idea of linking molecular changes with functional changes and clinical phenotypes. L>H, A>T and F>S are all changes towards hydrophilic and polar amino acids, which increases their potential for intramolecular binding. Further, L271H is an exchange of an aliphatic to an aromatic amino acid, while F747S is a loss of an aromatic amino acid. The missense mutations introduce potentially new phosphorylation sites. Close to A749 and F747, two PKG phosphorylation sites are known (Sandoval et al., 2017). The packed location of A749T and F747S, however, likely minimizes enzymatic access to these residues.

Modeling these residues revealed that L271H and A749T interact with residues within the same domain, while F747S interacts with residues within the neighboring domain. L271H is located in domain I close to the intracellular site of segment S5. In addition to the interactions within its own α -helix, it interacts with V401 and L405 in segment S6 of the same domain. Interestingly, V401L is another known high-risk disease causing *CACNA1D* missense variant inducing type 2 gating changes (Pinggera et al., 2017). G403D,

located between V401 and L405, and G407R, located distal to V401 and L405, are other known high-risk disease-causing *CACNA1D* missense variants inducing type 1 gating changes (Pinggera et al., 2015; Scholl et al., 2013). Further, p.403_404insGly of SANDD-syndrome patients is located here (Baig et al., 2011). Functionally, L271H induces a shift towards more hyperpolarized potentials for all single-channel gating parameters and structural modeling suggests a stronger interaction with segment S6 residues, which form the channel pore. Thereby the channel could be more prone to open at lower membrane depolarizations, by stabilizing a pre-open state of Cav1.3. This is also supported by the reduced mean first latency (MFL), i.e. L271H opens earlier after onset of depolarization.

A749T is located in the pore-forming segment S6 of domain II, directly adjacent to I750M, another known high-risk disease causing *CACNA1D* missense variant (Scholl et al., 2013). In addition to the interactions within the α -helix that A749T is located in, it interacts with L653 in S5 of domain II. L653P is a known somatic missense variant associated with aldosterone producing adenomas (Omata et al., 2017). Next to L653 lies S652L, another known high-risk disease causing *CACNA1D* missense variant inducing type 2 gating changes, interestingly also accompanied by auto-aggression in affected patients (Hofer et al., 2020). The findings of this thesis reveal that for both mutations, L271H and A749T, the interacting residues do not change upon mutation but the proximity and the polarity of histidine and threonine are likely to change the binding strengths towards these interacting residues. Functionally, A749T induces a shift of the single-channel availability towards more hyperpolarized potentials and increases open probability, while structural modeling suggests a stronger interaction with segment S5 residues. This could reflect a stabilized pre-open state that favors faster transitions to the open state. This is also supported by the reduced first latency and the finding that the increased opening probability is due to an increased number of opening events.

F747S is located in segment S6 of domain II, two amino acids upstream of A749T. Contrary to L271H and A749T it does not interact with residues of the same domain. Instead, F747 interacts with F1141 and F1142 in segment S6 of domain III, forming an interaction between three benzene rings. These belong to a cluster of hydrophobic residues lining the pore (Hering et al., 2018). F747S disrupts this hydrophobic lining since serine is a hydrophilic amino acid. Further, F747S no longer interacts with the residues mentioned above, but interacts with N1145, a binding that due to the polarity of serine appears to be quite strong. At the single-channel level, F747S apparently led to a shift in availability

towards more hyperpolarized potentials only when a cooperative channel-channel interaction occurred, which also caused the shift in gating modes. Therefore, it is more likely, that local depolarization and Ca²⁺-entry through one channel triggers Ca²⁺-influx through the neighboring channel. The disruption of the hydrophobic residues lining the pore may then stabilize the channel in the open state, resulting in the observed prolonged openings and mode 2 gating. However, to understand channel cooperation on a molecular level, further experiments are needed, including surface imaging. Further, heterologous expression of both, WT and F747S channel variants together would provide information whether cooperative gating requires two mutant channels.

While F747S was modeled in the cryoEM structure of Cav1.3 within this thesis, Török et al. modeled F747S in the cryoEM structure of Cav1.1. Modeling residues in Cav1.1 allows to model different gating states, while the cryoEM structure of Cav1.3 supposedly depicts the inactivated state. Thus, knowledge on structural voltage-sensor movements of Cav1.1 may be used to structurally predict F747S in different gating states. Interestingly, Török et al. revealed the same interacting residues for F747 and S747 in the inactivated state as this thesis, including the novel interaction of S747 with N1145. Their modeling of the open state suggests, that the interaction of S747 and N1145 remains, forming an additional hydrogen-bond, thereby stabilizing the open state (Török et al., 2022). Their suggestion is indeed supported by the positive cooperative channel-channel interaction revealed in this thesis.

Taken together, the discussed findings show, that L271H, A749T and F747S cluster in a “hot spot” region alongside all other high-risk disease causing *CACNA1D* missense variants known so far (Fig. 72). While L271H and A749T interact between segments S5 and S6 of their own domain, respectively, F747S interacts with the same pore-forming segment S6 within an adjacent domain and by introducing a novel intramolecular binding. This supports the idea that in the case of F747S a different molecular mechanism underlies the similar leftward shift of the voltage dependence than in the case of L271H and A749T. Further, it supports the idea of a subdivided classification of gating changes based on single-channel gating phenotypes. The findings clearly show that single-channel recordings add indispensable value on human Cav1.3 gating modulation by high-risk disease causing *CACNA1D* missense variants to understand their functional and clinical phenotypes.

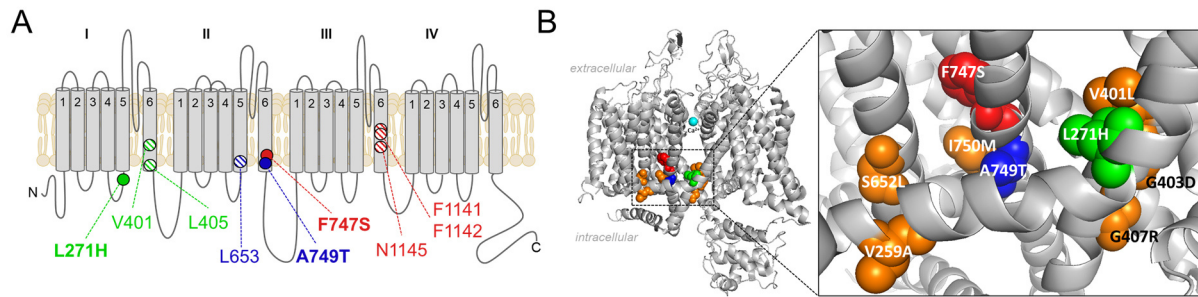


Figure 72. Location of known high-risk disease causing *CACNA1D* missense variants. (A) 2D structure of $\text{Ca}_v1.3$ α_1 -subunit. L271H (green) and interacting residues (striped green), A749T (blue) and interacting residues (striped blue), and F747S (red) and interacting residues (striped red). **(B)** 3D structure reveals that A749T, L271H and F747S lie within the hot spot region alongside known high-risk disease causing *CACNA1D* missense variants (orange).

4.2. Physiological perspective: Phosphorylation site S1475 has functional relevance in human Cav1.3 gating modulation

S1475 is the human equivalent of the previously identified CaMKII phosphorylation site in the rat Cav1.3 (Gao et al., 2006). Given the limited cross-species applicability, it is important to know, that all known Cav1.3 phosphorylation sites were identified in the rat, but are yet unconfirmed for human isoforms. Of interest, S1475 is located within the C-terminal EF-hand motif, which binds CaM during CDI. S1475 is present in all known splice variants and highly conserved in Cav1.3, while all other HVA channel types that show a tissue distribution similar to Cav1.3, contain an alanine at the 1475 corresponding position and thus cannot be phosphorylated at this site. Taken together, these features make S1475 an interesting site to be investigated regarding Cav1.3 gating modulation. Such studies are prerequisites for physio-pathological implications of Cav1.3 modulatory mechanism. This thesis aimed at (1) characterizing gating of S1475 (de-) phosphorylation imitating Cav1.3 mutants using a human isoform and the physiological charge carrier Ca^{2+} , (2) investigating the role of CaMKII modulation of human Cav1.3 channels via S1475 and (3) testing the hypothesis of S1475 modulation involving CaM and CDI. In brief, the main findings are that when using 2 mM Ca^{2+} , the current density of the phosphorylation-mimicking S1475D variant is decreased, while that of the phosphorylation-resistant S1475A variant is increased compared to the WT. This is mainly due to an increased open probability for S1475A and decreased open probability for S1475D, while the single-channel availability is unaffected. At the whole-cell level, CaMKII activation leads to an approximation of the current density of WT and S1475D, while oppositely CaMKII inhibition leads to a similar current density for WT and S1475A. CaM appears to be necessary and sufficient for the observed modulation. Ca^{2+} enhanced the CaM dependent modulation. The phosphorylation-mimicking S1475D variant displays reduced CDI but not VDI and showed reduced Ca^{2+} -influx in response to SAN-AP-like stimulation protocol. Structural modelling suggests that the III-IV linker region could be intramolecularly involved in S1475 mediated modulation of Cav1.3 activity.

4.2.1. S1475 has functional relevance in human Cav1.3 channels

The findings show that S1475 is relevant for functional properties of human Cav1.3 channels. Imitating S1475 (de-) phosphorylation affected current density, gating kinetics and inactivation.

Under basal conditions, the WT current density was between that of the phosphorylation-resistant S1475A and the phosphorylation-mimicking S1475D variant, suggesting phosphorylation of at least some of the WT channels. Indeed, activating or inhibiting CaMKII resulted in an approximation of WT mediated current densities to the respective S1475 mutant. Interestingly, also the overexpression of CaM approximated WT current density to that of S1475A, while completely depleting CaM by co-expression of BsCaM_{IQ} abolished difference between WT, S1475A and S1475D. BsCaM_{IQ} reduced current density for all variants, which is in line with previous observations in literature (Banerjee et al., 2018; Liu et al., 2010). The lack of endogenous CaM profoundly reduces current influx as well as inactivation, thus stating the importance of CaM modulation in Cav1.3 channels. It further shows that under basal conditions CaM concentrations in HEK cells are able to modulate Cav1.3 channels. The findings of this thesis also reveal that CaM induces a leftward shift in voltage-dependent activation kinetics. $V_{0.5\text{act}}$ values are at more hyperpolarized potentials for CaM > CaM₁₂₃₄ > BsCaM_{IQ}. Interestingly, this shift is not observed for S1475D channels. Thus, S1475D seems to be resistant to a CaM-induced shift in voltage-dependent activation kinetics and a CaM-induced increase in CDI.

Interestingly, co-expressing CaM altered current density of S1475 variants in the opposite direction. It increased current density for WT and S1475A and decreased it for S1475D. This was observed in Ba²⁺- and Ca²⁺-currents. The current increase may be triggered by Ca²⁺-free CaM (apo-CaM), since co-expression of CaM also increases apo-CaM, which facilitates channel opening prior to CDI (Adams et al., 2014). The decreased current observed in S1475D suggests an opposite effect of apo-CaM for the phosphorylation-mimicking mutant. However, co-expressing calcium-insensitive CaM₁₂₃₄ only slightly increased current density of the WT, while S1475A and S1475D had comparable current density to basal conditions, i.e. without CaM co-expression. While the current density behaves inconclusive in this regard, inactivation accurately reflects CaM₁₂₃₄ effects, by being attenuated upon CaM₁₂₃₄ co-expression. Recent findings support that apo-CaM effects on LTCC currents may not be fully understood, by revealing that upregulation of channel activity requires half-calcified CaM (Bartels et al., 2022).

Taken together, alteration of CaM levels modulated current density, gating kinetics and CDI in dependence of residue at p.1475. It is tempting to conclude, that S1475 modulates Cav1.3 gating directly via CaM. This thesis, however, does not provide evidence for direct CaM and S1475 interaction. This would require binding studies. In fact, Förster resonance energy transfer (FRET) experiments were conducted. Unfortunately, binding affinity could not be studied up to now, neither *in vitro*, nor in FRET experiments on isolated proteins. While the fluorescently tagged CaM protein was successfully isolated and turned out to be suitable as a marker during native page analysis (Heerwig et al., 2023), the full-length human Cav1.3 C-terminus could not be sufficiently isolated. Despite being supported by Dr. Manu Ben-Johny at Columbia University in New York, who had previously successfully conducted similar experiments with the rat isoform (Banerjee et al., 2018), the full-length human Cav1.3 C-terminus did also not express sufficiently to perform FRET binding studies *in vitro*. While this limits the interpretation of the findings here, it is a crucial observation on the limited cross-species applicability of rat and human Cav1.3 channels. Since this observation is of interest beyond the scope of this thesis, troubleshooting is currently ongoing to address this observation further.

Regarding S1475 modulation of Cav1.3 activity, the findings once more reveal the importance of single-channel recordings. Similar to the conclusions drawn for Cav1.3 missense-mutations, single-channel data unmask the underlying mechanisms of whole-cell changes. Although surface expression of WT, S1475A and S1475D was only addressed via seal-statistics and not super-resolution microscopy, the findings show that the whole-cell changes originate at least in altered single-channel gating. Herein, the changes in open probability can explain the changes in whole-cell current density. Since availability and mean open time are unaffected, but MCT and MFL are decreased, imitating S1475 (de-) phosphorylation modulates Cav1.3's opening frequency.

The findings further confirm the role of CaMKII modulation of Cav1.3 activity via S1475. Co-expressing constitutively active CaMKII resulted in similar current density of WT and S1475D and vice versa CaMKII inhibition by KN-93 resulted in similar current density of WT and S1475A. Including (de-) phosphorylation-imitating mutants in these experiments allows to conclude that CaMKII modulates Cav1.3 current density via phosphorylation of S1475. Further, current density values of S1475A and S1475D were not affected by co-expressing constitutively active CaMKII. It is therefore tempting to speculate that CaMKII modulates Cav1.3 current density only via S1475.

This thesis is limited in concluding, whether CaMKII phosphorylates S1475 *in vivo* or whether phosphorylation could also be catalyzed by other enzymes. Studies suggest that specific sites may not exclusively be phosphorylated by one specific enzyme (Blesneac et al., 2015; Cohen, 2002; Davis et al., 2001; Ismailov & Benos, 1995). Since KN-93 does not inhibit phosphorylating enzymes like PKA, PKG or PKC, the results suggest that CaMKII is the primary phosphorylating enzyme at residue S1475. Although more specific inhibitors of CaMKII such as autocalcine-2-inhibitor protein (AIP) are known, KN-93 is still widely used in VGCC research (Gao et al., 2006; Martinez-Rivera et al., 2023; Yuan et al., 2023). The reported reduction in current density caused by KN-93 acting as a CaM antagonist (Hao et al., 2008; Yokokura et al., 1996), was also observed in this thesis. It is in line with the current reduction observed with BsCaM_{IQ}.

Taken together, interpreting the findings of this thesis supports the functional relevance of S1475 in gating modulation of human Cav1.3 channels. The findings indicate that S1475 modulation involves CaM and alters CDI. They also confirm CaMKII modulation of human Cav1.3 channels via S1475.

4.2.2. Functional roles of S1475 in human channels compared to S1486 described in rat channels

S1475 is the human equivalent of S1486 in rat Cav1.3 channels. S1486 was identified as a potential CaMKII phosphorylation site in rat Cav1.3 channels (Gao et al., 2006). Gao et al. showed that IGF-1 potentiates Cav1.3 currents, likely via CaMKII phosphorylation of S1486. While the current thesis did not address upstream or downstream pathways, Gao et al. did not investigate modulation of channel gating properties via S1486 in more detail. CaMKII modulation of Cav1.3 currents, however, was investigated in both studies. Gao et al. reported that, when co-expressing constitutively active CaMKII, the WT behaved similar to phosphorylation-mimicking S1486D channels. This is in line with the findings in this thesis. Further in Gao et al., IGF-1 failed to potentiate S1486A and S1486D currents via CaMKII. This observation is also in line with the findings of this thesis, showing that current density of S1475A and S1475D are unchanged upon co-expressing constitutively active CaMKII. It can therefore be concluded, that CaMKII modulates Cav1.3 activity via S1486 or S1475, respectively, i.e. across species.

Other findings on CaMKII modulation of Cav1.3 currents, however, appear to differ between species. CaMKII leftward-shifted and increased rat WT Cav1.3 currents (Gao et al.), while it did not shift and decreased human WT Cav1.3 currents (this study). Possible

explanations hereof may be rat isoform specific modulation via S1486, or additional CaMKII interaction sites present in rat but absent in human Cav1.3 channels, or species-specific downstream effects, since the potentiation of rat Cav1.3 currents required Ca²⁺-release from IP₃-sensitive stores. Of note, investigation of signaling downstream of Cav1.3 or CaMKII is beyond the scope of this study.

Limitation of cross-species applicability is mainly due to the non-functional C-terminal modulatory domain (CTM) in rat Cav1.3 channels. The CTM reduces CaM binding to the channel and thereby alters open probability and CDI. The role of rat S1486 modulation, however, was investigated using 20 mM Ba²⁺ as charge carrier, thus not allowing for Ca²⁺- or CaM-mediated effects, including that of Ca²⁺/CaM-dependent CaMKII and CDI. While Ba²⁺ only allows for VDI, the pulse durations of 30–50 ms used by Gao et al., however, are too short to report VDI effects in LTCCs. In conclusion, the CaM dependent CDI reduction observed for S1475D in this thesis is beyond the scope of Gao et al.

Parallels to other studies can be used to approach species dependent consequences in CDI during Cav1.3 modulation. First, a study investigating necessary C-terminal sites for CDI induced triple alanine mutations inside the EF-hand and IQ-motif of rat Cav1.3 channels. The authors also mutated the respective serine (SEY > AAA) and found no change in CDI (Ben-Johny & Yue, 2014). This is in line with the findings for human S1475A in this thesis. Second, with respect to *CACNA1D* missense-mutations, A749G was also investigated in rat Cav1.3 channels (corresponding site: A760G) (Limpitikul et al., 2016). Interestingly, the leftward shift in voltage-dependent activation was regardless of the species, while opposite effects on CDI were observed, thus supporting the role of CTM in human Cav1.3 modulation (Limpitikul et al., 2016; Pinggera et al., 2015).

Taken together, comparing roles of S1486 in rat and S1475 in human Cav1.3 channels may be limited by different study designs, but it reveals functional relevance of this site in both species. It is targeted by CaMKII in both species, therefore up- and downstream pathways of S1475 and S1486 phosphorylation could be similar. Herein, the comparison of S1475 and S1486 can be used to develop new hypotheses, e.g. IGF-1 may potentiate human Cav1.3 channels via S1475 dephosphorylation, or that calcineurin may be the dephosphorylating enzyme. However, the comparison also reveals species specific modulation of current density and activation kinetics. Since these specific effects are crucial to understand Cav1.3 modulatory mechanism in health and disease, it indicates the need to test for findings obtained in the rat in human Cav1.3 channels, too.

4.2.3. S1475 modulation of Cav1.3 activity in a cellular context

The findings obtained from structural modeling and recording currents in response to SAN-AP-like stimuli were used to interpret the putative role of S1475 modulation of Cav1.3 activity in a cellular context.

Structural modeling suggested an interaction of the EF-hand E-helix with the intracellular loop connecting domain III and IV, namely the III-IV linker. S1475 interacts with R1187, while D1475 interacts with L1185. Although the modeling is limited by Cav1.3 being modeled in its inactive state and in the absence of CaM, it suggests that S1475 phosphorylation could alter the intramolecular interaction with the III-IV linker. This interaction together with the observed S1475D mediated differences in CDI, give reason to assume an involvement of the III-IV linker in CDI modulation. This linker was already suggested to mediate fast inactivation in K⁺ and Na⁺ channels, while for Cav1.3 this would be a novel finding. In voltage-gated Na⁺ channels, mutating the hydrophobic IFM residues in the III-IV linker to glutamine abolished fast inactivation (Stotz et al., 2004; West et al., 1992). A similar regulation involving the C-terminal E-helix in III-IV linker interaction could be conceivable for LTCCs and would thus provide a new hypothesis arising from the findings in this thesis, i.e. E-helix interaction with the III-IV linker shapes inactivation in LTCCs.

Aside from wanting to understand the details of S1475 modulation of Cav1.3 activity, the question arises which consequences this modulation could have on a cellular level. Apart from P1499L, which is associated with aldosterone producing adenomas (Omata et al., 2017), no disease-associated mutations of the Cav1.3 EF-hand are known to date, that would suggest physiological or pathophysiological effects due to the alteration caused by the phosphorylation status and thus the intramolecular interaction of S1475. However, applying an SAN-AP-like pulse protocol to S1475D channels resulted in a decreased Ca²⁺-influx during the depolarization phase of the simulated AP. Since Cav1.3 channels are the major type carrying LTCC currents in the depolarization phase of the SAN-AP, these findings suggest that S1475D (or a sustained phosphorylation at S1475) could affect the action potential shape and frequency in the sinoatrial node. Findings on bradycardic effects of Cav1.3 deficiency suggest that S1475D, or a sustained phosphorylation at S1475, could result in similar consequences (Baig et al., 2011; Mangoni et al., 2003; Matthes et al., 2004). Interestingly, computer modelling of SAN-AP and corresponding LTCC currents

($I_{Ca,L}$) based on data obtained from the rabbit, predicted a decrease in SAN-AP frequency to underly reduced Ca^{2+} -influx during depolarization (Noble et al., 1989; Wilders et al., 1991; Wilders, 2007) (Fig. 73). The findings of this thesis thus provide experimental data supporting the model.

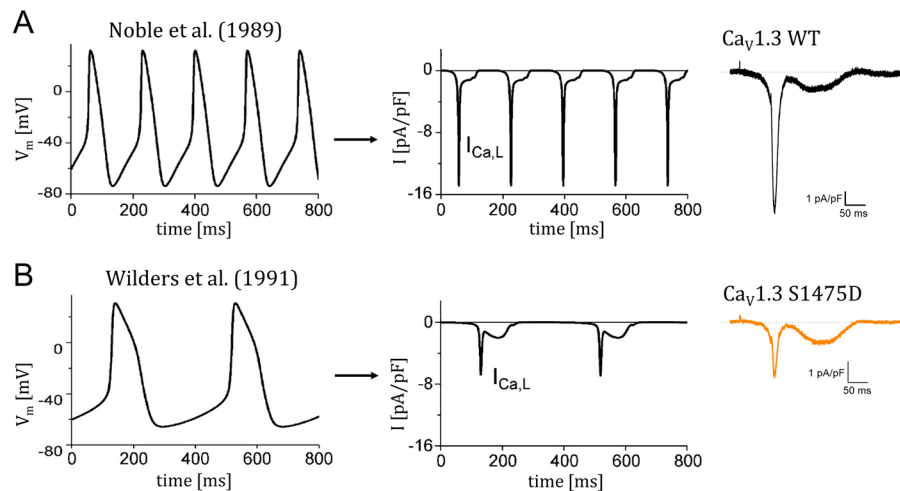


Figure 73. Altered Ca^{2+} -influx during SAN-AP depolarization. SAN action potentials and LTCC currents in the single rabbit SA nodal cell models of Noble et al. (1989) and Wilders et al. (1991), compared to **(A)** $Ca_v1.3$ WT and **(B)** $Ca_v1.3$ S1475D currents in response to SAN-AP-like stimuli obtained in this thesis (modified from Wilders, 2007).

Despite the similarity to bradycardic effects of $Ca_v1.3$ deficiency, for example in patients with SANDD-syndrome, the results do not allow concluding on whether S1475 phosphorylation reduces heart-rate and whether this reduction would occur in a physiological or pathophysiological range. Nevertheless, since $Ca_v1.3$ dysfunction is linked to a variety of diseases, it would be interesting to know, whether the S1475 phosphorylation state is involved in these channelopathies. Hereto, future studies should investigate if increased S1475 (de-) phosphorylation is observed in $Ca_v1.3$ -associated diseases. Tissue analysis using mass spectrometry or Western blot analysis for phosphorylated proteins, as well as phospho-specific antibodies could reveal if S1475 (de-) phosphorylation extent differs from that in healthy controls. A mouse model characterization would provide further insight into the cellular role of S1475 modulation of $Ca_v1.3$ activity. For example, the $Ca_v1.2$ -S1928A mouse model has provided valuable insights into cellular consequences of S1928 phosphorylation (Lemke et al., 2008). Recently, inducing diabetes in this mouse model suggested a beneficial effect of S1928 phosphorylation in the disease (Martin-Aragon Baudel et al., 2022).

Although S1475D reduces CDI, which might be considered a gain-of-function characteristic, it decreases peak current density and induces a rightward shift of activation and inactivation kinetics towards more depolarized potentials, both to be considered loss-of-function characteristics. Therefore, it is tempting to speculate, that S1475 phosphorylation could perhaps reduce Cav1.3's susceptibility towards mildly depolarizing stimuli and therefore may be beneficial in e.g. Parkinson's disease. In this context, it would also be interesting to test, whether S1475 phosphorylation alters DHP sensitivity of Cav1.3 channels. Further, given different sub-cellular localization of Cav1.3, especially in neurons, S1475 modulation of Cav1.3 activity could have local rather than global cellular consequences (Hell et al., 1993; Obermair et al., 2004; Stanika et al., 2016; Zhang et al., 2005). Importantly, S1475 modulation of specific electrophysiological parameters does not directly correlate with specific cellular functions in a one-way scenario. Instead, it should be acknowledged, that S1475 modulation of Cav1.3 activity is one part of the complex Cav1.3 modulation embedded in a cellular context.

Nevertheless, S1475 is present in all Cav1.3 splice variants and highly conserved, while absent in all other high-voltage activating calcium channels that express in similar tissues as Cav1.3. This observation itself certifies the unique potential of this phosphorylation site. In summary, S1475 modulation of Cav1.3 activity employs three important modulatory mechanisms: Phosphorylation, CaM-interaction and CDI. Although direct physiological or pathophysiological consequences of S1475 modulation cannot be concluded from the data at hand, the findings indicate a significant contribution of S1475 in modulating Cav1.3 activity and thus likely also in Cav1.3 dependent responses in health and disease.

4.3. Conclusions on the role of Cav1.3 gating modulation

This thesis adds substantially to the understanding of Cav1.3 modulation by providing insights on underlying mechanisms in pathophysiological and physiological gating modulation. Effects on Cav1.3 gating by modulation of (1) activation threshold, (2) inactivation, and (3) open probability may thus contribute to health or disease.

A unique electrophysiological characteristic of Cav1.3 is its low activation threshold, and an additional leftward shift and thereby Ca^{2+} -influx at even lower voltages, as revealed for Cav1.3 missense mutations, may thus crucially affect Cav1.3 dependent functions. A reduced or abolished inactivation prolongs Ca^{2+} -influx through Cav1.3, thus altering important calcium- and voltage-dependent feedback mechanisms. Because rat Cav1.3 channels have a nonfunctional CTM, inactivation is the parameter most likely to show differences in modulation when comparing rat and human Cav1.3 isoforms (Lieb et al., 2012; Tan et al., 2011). This thesis sheds light on other differences in Cav1.3 gating modulation that may be due to species-dependent differences. Accordingly, previous and future findings on rat Cav1.3 isoforms should be confirmed using human channels, especially if this knowledge is to be harnessed for Cav1.3-associated diseases and their therapies. Changes in open probability mark the alteration of an innate biophysical gating parameter and confirm the importance of single-channel recordings in ion channel research. The knowledge gain added by single-channel recordings in this thesis, justifies the demanding equipment and acquisition requirements, and the time-consuming analysis. This is most obviously highlighted here by discovering positive cooperative channel-channel interaction in F747S.

The results of this thesis suggest that modulation of Cav1.3 may affect drug binding and thus effect potential therapeutic options, like administering DHPs to the patients affected by the Cav1.3 mutations analyzed here. Furthermore, this thesis reveals mechanisms underlying the gain-of-function phenotypes and suggests, that, from a therapeutic perspective, specific gating modulation is needed, rather than undifferentiated Cav1.3 antagonism: Considering that the functional phenotype of L271H relies on a leftward-shifted activity alone, a channel modulator reversing this shift could rescue the gating phenotype. Similarly, F747S channels only exhibit cooperativity in multi-channel patches. A modulator preventing channel cooperativity may also rescue the gating phenotype in F747S. Further, A749T increased current density and open probability, while S1475D

decreased these parameters. Thus, it is tempting to speculate that increased S1475 phosphorylation may rescue the gating phenotype induced by A749T.

Interestingly, Prof. Henry Colecraft and his research group at Columbia University in New York, currently develop a VGCC modulator using divalent nanobodies (Morgenstern & Colecraft, 2021). The so-called Cav- α blocker withdraws specific auxiliary β -subunits from the Cav2.2 pore-forming α_1 -subunit, thereby downregulating channel activity (Morgenstern et al., 2019; Morgenstern et al., 2022). In T-type channels, which do not assemble with auxiliary subunits, the divalent nanobodies are fused to a ubiquitin ligase, and bind to specific intracellular domains, like the C-terminus of specific T-type channels and induce ubiquitination. The channel is then degraded directly out of the membrane by the normal cellular machinery (Morgenstern & Colecraft, 2021). This approach has potential for therapeutic intervention in different channelopathies and has been shown to reduce the development of neuropathic pain in mice (Sun et al., 2022). The necessary technologies seem to evolve with the increasing need for them, unraveled by research investigating modulatory mechanisms that identify putative targets, like this thesis.

In conclusion, this thesis adds to current research by providing novel insights on underlying mechanisms in Cav1.3 gating modulation, foremost by revealing channel cooperativity in F747S via single-channel recordings, and by revealing an interplay of phosphorylation, CaM-interaction and CDI through S1475 (Fig. 74). While these findings increase the understanding of Cav1.3 function in physiological and pathophysiological processes, they further present possible targets for future research on therapeutically used Cav1.3-specific modulators. Herein, unravelling the complexity induced by tissue-specific interplay of different modulatory mechanisms, imposes a challenge in Cav1.3 research, but is a prerequisite to eventually harness this knowledge to specifically modulate the channel in Cav1.3-associated diseases.

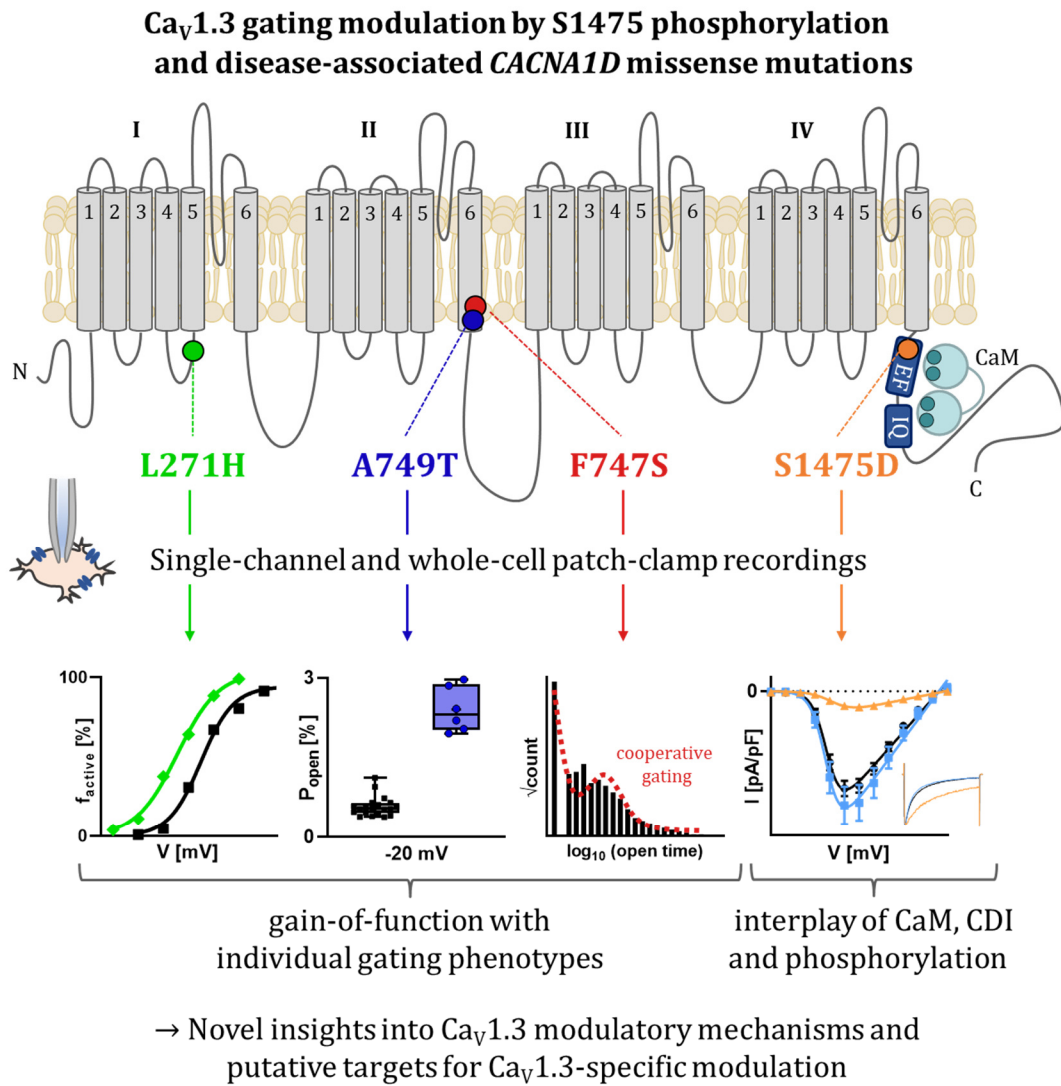


Figure 74. Graphical summary of Cav1.3 gating modulation by S1475 phosphorylation and disease-associated *CACNA1D* missense mutations.

5. Supplemental material

S1 – Plasmid map pGFP-_CACNA1D_42

The human cDNA of Cav1.3₄₂ was previously cloned into the pGFP⁺ expression vector (Grabner et al., 1999; Singh et al., 2008). Unfortunately, a manufacturer plasmid map was unavailable. Therefore, the entire plasmid was sequenced within the scope of this thesis and the resulting plasmid map is shown below.

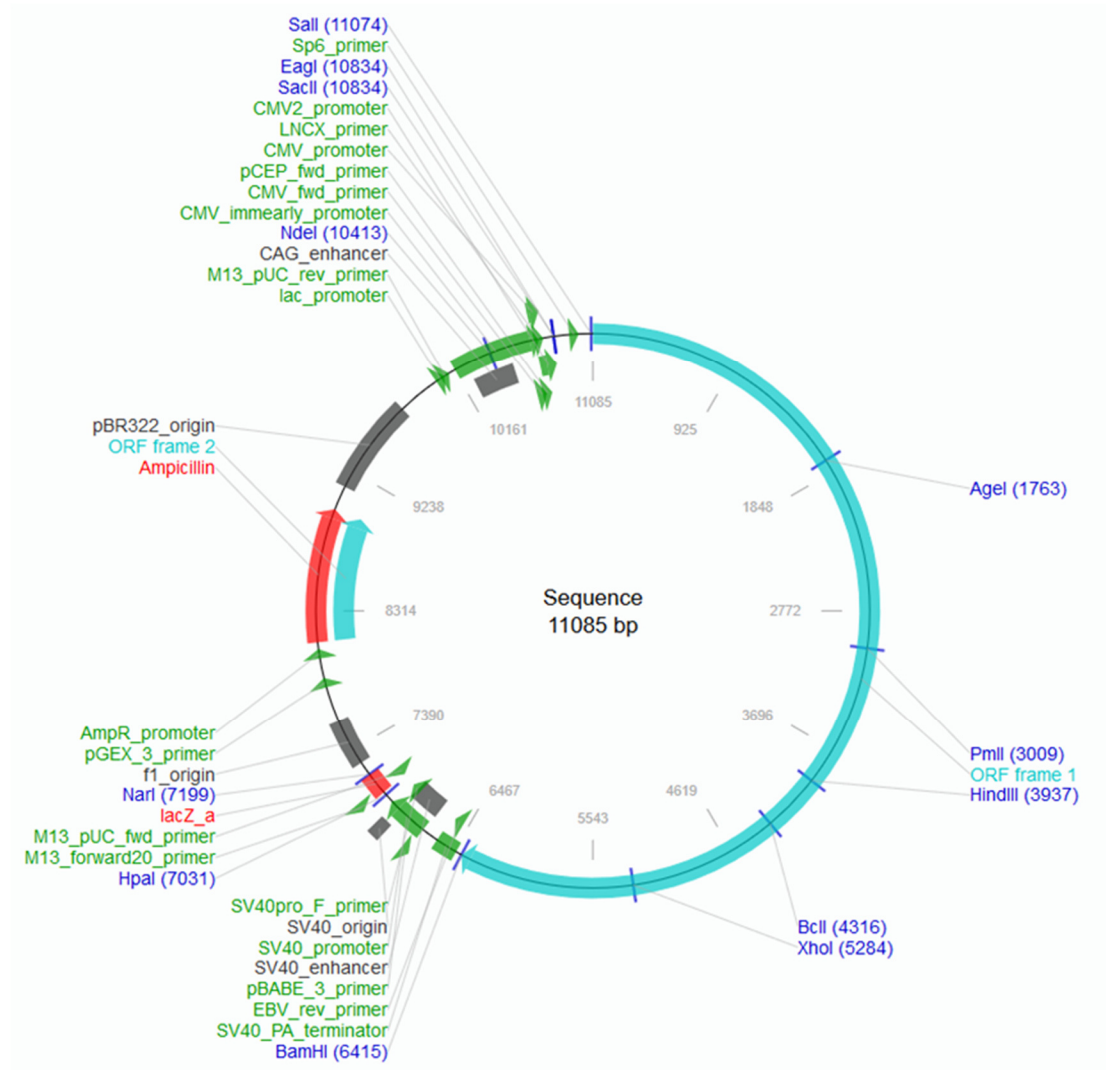


Figure S1. Plasmid map pGFP-_CACNA1D_42.

S2 – Gating parameter calculation by Python script

Single-channel gating parameters were calculated according to the following custom written Python script.

S2. Python code for calculating single-channel gating parameters

```
#SingleChannelGatingParameterAnalysisSarahSalamon
#----- import funtions -----
import pandas as pd
import numpy as np
import matplotlib as mb
import math

#----- load raw data excel sheet -----
SC_data = pd.read_excel(r'C:\Users\[insert_specific_directory]Filename.xlsx',
sheetnames="Tabelle1",names =
["trace","search","level","state","eventstart","eventend","amplitude","ampsd","dwelltime","instfreq",
"interevent"], index=False )

#----- determine channel amount, pulse duration, all traces and active traces -----
k = max(SC_data.level)
t0 = max(SC_data.eventend)
Mo = max(SC_data.trace)
Ma = sum(SC_data.search[(SC_data.level == 1) & (SC_data.interevent == "Not found")])

#----- one_channel_patches -----
if k == 1:
    #----- open state parameters-----
    MOT = np.mean(SC_data.dwelltime[(SC_data.level ==1)])
    Po = 100*(sum(SC_data.dwelltime[(SC_data.level >0)])/(Ma*t0))

    #-----closed state parameters-----
    MCT=np.mean(SC_data.dwelltime[(SC_data.level==0)&(SC_data.eventend<t0)&
(SC_data.interevent != "Not found")])

    #----- availability -----
    Fa = 100*(Ma/Mo)

    #-----latency -----
    MFL=sum(SC_data.eventstart[(SC_data.level>0)&(SC_data.interevent=="Not found")])/(Ma)

#----- two_channel_patches -----
elif k == 2:
    #----- availability -----
    Fa = 100*(1-((1-(Ma/Mo))**(1./2.)))

    #----- open state parameters -----
    MOT = np.mean(SC_data.dwelltime[(SC_data.level ==1)])
    Po=((100*(sum(SC_data.dwelltime[(SC_data.level>0)])/(Ma*t0)))/2)*((100*(Ma/Mo))/Fa)

#----- two_channel_patches -----
elif k == 3:
    #----- availability -----
    Fa = 100*(1-((1-(Ma/Mo))**(1./3.)))

    #----- open state parameters -----
    MOT = np.mean(SC_data.dwelltime[(SC_data.level ==1)])
    Po=((100*(sum(SC_data.dwelltime[(SC_data.level>0)])/(Ma*t0)))/3)*((100*(Ma/Mo))/Fa)
```

S3 – DMSO control experiments within KN-93 inhibition of CaMKII

KN-93 was used to inhibit CaMKII activity. KN-93 was diluted in DMSO and added to the bath solution. The final KN-93 concentration was 1 μM and 0.07 % DMSO. Control experiments were performed with bath solution and 0.07 % DMSO without KN-93. Control experiments showed no effect of 0.07 % DMSO on current density of $\text{Ca}_v1.3$ currents.

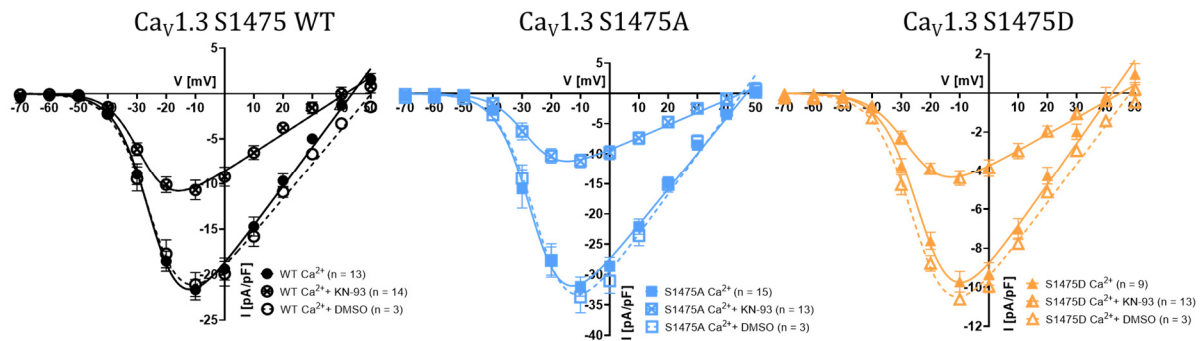


Figure S3. DMSO control experiments. Control experiments showed no effect of 0.07 % DMSO on current density of $\text{Ca}_v1.3$ currents compared to 2 mM Ca^{2+} recordings without DMSO. Therefore, the reduction in current density is attributed to KN-93. Data shown as mean \pm SEM.

S4 - Seal statistics of single-channel recordings investigating S1475 modulation

Seal statistics report the amount of $\text{G}\Omega$ seals without channel activity ($k = 0$), containing one channel ($k = 1$) or multiple channels ($k > 1$) within all $\text{G}\Omega$ seals. No differences were detected among WT, S1475A and S1475D

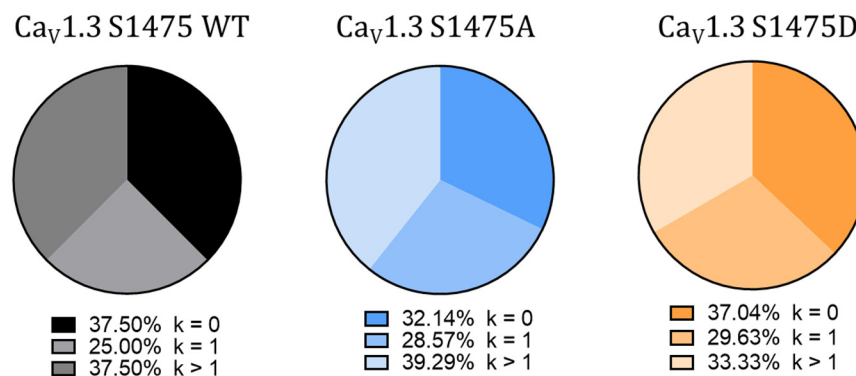


Figure S4. Seal statistics of single-channel recordings investigating S1475 modulation

S5 – Data and p-value overview of single-channel patch clamp recordings investigating Cav1.3 missense mutations

Table S 5.1. Data values of single-channel recordings of WT, L271H and A749T. Table reports parameters as mean \pm SEM. Number of experiments below the respective parameters. * $p \leq 0.05$ vs WT in unpaired t-test. P-values supplement Tab S 5.2.

		WT	L271H	A749T	
15mM Ba²⁺	V_{0.5 act} [mV]	-24.54 \pm 0.70	-33.24 \pm 1.02*	-33.21 \pm 3.56*	
	n	17	6	5	
	Conductance [pS]	11.02 \pm 0.67	10.23 \pm 0.78	10.09 \pm 1.13	
	V_{rev} [mV]	64.34 \pm 5.22	48.34 \pm 4.88	61.28 \pm 4.71	
	Peak ensemble average current at -20 mV [fA]	10.44 \pm 0.82	15.43 \pm 2.49	31.93 \pm 2.61	
	f_{active} [%]	-40 mV	5.06 \pm 0.76	32.75 \pm 5.20*	43.74 \pm 4.49*
		-30 mV	31.38 \pm 1.52	60.42 \pm 4.53*	67.72 \pm 5.99*
		-20mV	64.79 \pm 2.38	89.61 \pm 1.92*	86.98 \pm 6.80*
		-10mV	78.15 \pm 2.11	98.46 \pm 0.52*	98.13 \pm 0.84*
	P_{open} [%]	-40 mV	0.24 \pm 0.02	0.65 \pm 0.07*	1.16 \pm 0.12*
		-30 mV	0.34 \pm 0.02	0.77 \pm 0.07*	1.46 \pm 0.20*
		-20mV	0.58 \pm 0.04	1.14 \pm 0.16*	2.41 \pm 0.17*
		-10mV	1.04 \pm 0.06	1.60 \pm 0.13*	4.24 \pm 0.24*
	MOT [ms]	-20mV	0.24 \pm 0.01	0.23 \pm 0.01	0.24 \pm 0.01
		-10mV	0.23 \pm 0.01	0.21 \pm 0.01	0.25 \pm 0.02
	n	20	9	6	
	MCT [ms]	-20mV	30.56 \pm 2.05	16.97 \pm 1.90*	9.43 \pm 1.53*
		-10mV	18.03 \pm 1.23	11.19 \pm 0.95*	4.92 \pm 0.58*
MFL [ms]	-20mV	48.56 \pm 2.81	30.77 \pm 2.93*	23.50 \pm 10.21*	
	-10mV	34.55 \pm 2.81	19.44 \pm 2.11*	13.94 \pm 4.65*	
n (only k = 1)	10	9	4		

Table S 5.2. Results of unpaired Student's t-test comparing single-channel recordings investigating L271H and A749T. Table reports p-values up to three decimal places. Smaller p-values are reported as $p < 0.001$.

		WT vs L271H	WT vs A749T	
15mM Ba²⁺	V_{0.5 act} [mV]	< 0.001	< 0.001	
	Conductance [pS]	0.489	0.329	
	V_{rev} [mV]	0.076	0.974	
	Peak ensemble average current at -20 mV [fA]	0.027	0.001	
	f_{active} [%]	-40 mV	< 0.001	< 0.001
		-30 mV	< 0.001	< 0.001
		-20mV	< 0.001	< 0.001
		-10mV	< 0.001	< 0.001
	P_{open} [%]	-40 mV	< 0.001	< 0.001
		-30 mV	< 0.001	< 0.001
		-20mV	< 0.001	< 0.001
		-10mV	< 0.001	< 0.001
	MOT [ms]	-20mV	0.752	0.099
		-10mV	0.082	0.802
	MCT [ms]	-20mV	< 0.001	< 0.001
		-10mV	0.014	< 0.001
MFL [ms]	-20mV	< 0.001	< 0.001	
	-10mV	0.001	< 0.001	

Table S5.3. Data values of single-channel recordings of WT, and F747S. Table reports parameters as mean \pm SEM. Number of experiments below the respective parameters. * $p \leq 0.05$ vs WT and # $p \leq 0.05$ F747S_{k=1} vs F747S_{k>1} in Bonferroni's multiple comparisons test following one-way ANOVA. N.a.: Value not applicable. P-values supplement Tab S 5.5.

		WT	F747S k = 1	F747S k > 1	
15mM Ba ²⁺	V_{0.5 act} [mV]	-24.54 \pm 0.70	-24.04 \pm 1.34	-34.08 \pm 3.70*#	
	n	17	6	6	
	Conductance [pS]	11.02 \pm 0.67	11.11 \pm 1.28	12.10 \pm 0.89	
	V_{rev} [mV]	64.34 \pm 5.22	68.24 \pm 9.30	51.36 \pm 3.27	
	Peak ensemble average current at -20 mV [fA]	10.44 \pm 0.82	9.79 \pm 1.72	75.36 \pm 17.59	
	f_{active} [%]	-40 mV	5.06 \pm 0.76	10.67 \pm 3.11	35.62 \pm 7.88*#
		-30 mV	31.38 \pm 1.52	35.04 \pm 5.91	52.04 \pm 6.95*
		-20mV	64.79 \pm 2.38	58.70 \pm 6.05	72.14 \pm 5.74
		-10mV	78.15 \pm 2.11	83.59 \pm 2.40	92.72 \pm 3.87*
	P_{open} [%]	-40 mV	0.24 \pm 0.02	0.19 \pm 0.03	3.02 \pm 0.60*#
		-30 mV	0.34 \pm 0.02	0.32 \pm 0.05	6.52 \pm 1.43*#
		-20mV	0.58 \pm 0.04	0.34 \pm 0.06	13.61 \pm 2.15*#
		-10mV	1.04 \pm 0.06	0.60 \pm 0.10	14.89 \pm 2.75*#
	MOT [ms]	-20mV	0.24 \pm 0.01	0.21 \pm 0.01	0.58 \pm 0.11*#
		-10mV	0.23 \pm 0.01	0.21 \pm 0.01	0.49 \pm 0.08*#
	τ [ms]	τ_1	0.18 \pm 0.01	0.11 \pm 0.01	0.12 \pm 0.03
		τ_2	n.a.	n.a.	1.24 \pm 0.24
	n	20	6	9	
	MCT [ms]	-20mV	30.56 \pm 2.05	39.28 \pm 5.60	2.12 \pm 0.48*#
		-10mV	18.03 \pm 1.23	25.91 \pm 3.88*	1.42 \pm 0.25*#
MFL [ms]	-20mV	48.56 \pm 2.81	53.65 \pm 4.99	18.48 \pm 3.27*#	
	-10mV	34.55 \pm 2.81	41.90 \pm 3.90	17.17 \pm 2.79*#	
n	10	6	9		

Table S 5.4. ANOVA results of comparing single-channel recordings investigating F747S. Table reports F-values and degrees of freedom F (DFn, DFd) and corresponding p-value.

ANOVA results comparing WT, F747S k = 1 and F747S k > 1			
15mM Ba ²⁺	Conductance [pS]		F (2, 32) = 0.312 and p=0.735
	V _{rev} [mV]		F (2, 32) = 1.795 and p=0.182
	V _{0.5 act} [mV]		F (2, 26) = 8.592 and p=0.001
	Peak current at -20 mV [fA]		F (2, 32) = 17.83 and p<0.001
	f _{active} [%]	-40 mV	F (2, 32) = 18.89 and p<0.001
		-30 mV	F (2, 32) = 7.949 and p=0.002
		-20mV	F (2, 32) = 1.946 and p=0.159
		-10mV	F (2, 32) = 7.194 and p=0.003
	P _{open} [%]	-40 mV	F (2, 32) = 29.13 and p<0.001
		-30 mV	F (2, 32) = 27.82 and p<0.001
		-20mV	F (2, 32) = 55.01 and p<0.001
		-10mV	F (2, 32) = 38.24 and p<0.001
	MOT [ms]	-20mV	F (2, 32) = 14.33 and p<0.001
		-10mV	F (2, 32) = 16.01 and p<0.001
τ ₁		F (2, 32) = 3.703 and p=0.036	
MCT [ms]	-20mV	F (2, 22) = 50.02 and p<0.001	
	-10mV	F (2, 22) = 45.37 and p<0.001	
MFL [ms]	-20mV	F (2, 22) = 29.58 and p<0.001	
	-10mV	F (2, 22) = 16.18 and p<0.001	

Table S 5.5. p-values of Bonferroni's multiple comparisons test following significant one-way ANOVA investigating F747S. Table reports p-values up to three decimal places. Smaller p-values are reported by p < 0.001.

		WT vs F747S k = 1	WT vs F747S k > 1	F747S k = 1 vs F747S k > 1	
15mM Ba ²⁺	V _{0.5 act} [mV]		>0.999	0.002	0.006
	Peak current at -20 mV [fA]		>0.999	<0.001	<0.001
	f _{active} [%]	-40 mV	>0.999	<0.001	0.002
		-30 mV	>0.999	0.001	0.056
		-10mV	0.695	0.002	0.240
	P _{open} [%]	-40 mV	>0.999	<0.001	<0.001
		-30 mV	>0.999	<0.001	<0.001
		-20mV	>0.999	<0.001	<0.001
		-10mV	>0.999	<0.001	<0.001
	MOT [ms]	-20mV	>0.999	<0.001	<0.001
		-10mV	>0.999	<0.001	<0.001
	τ ₁		0.110	0.117	>0.999
	MCT [ms]	-20mV	0.124	<0.001	<0.001
		-10mV	0.023	<0.001	<0.001
MFL [ms]	-20mV	>0.999	<0.001	<0.001	
	-10mV	0.367	<0.001	<0.001	

S6 – Data and p-value overview of single-channel patch clamp recordings investigating S1475 modulation of Cav1.3

Table S 6.1. Data values of single-channel recordings investigating S1475 modulation of Cav1.3. Table reports parameters as mean \pm SEM. Number of experiments below the respective parameters. * $p \leq 0.05$ vs WT and # $p \leq 0.05$ S1475A vs S1475D in Bonferroni's multiple comparisons test following one-way ANOVA. P-values supplement Tab. S 6.3.

		WT	S1475A	S1475D	
15mM Ba ²⁺	Conductance [pS]	15.84 \pm 0.50	18.50 \pm 0.89*	14.14 \pm 0.61#	
	V_{rev} [mV]	31.59 \pm 0.96	24.24 \pm 1.63*	39.17 \pm 1.26**	
	V_{0.5 act} [mV]	-27.29 \pm 0.81	-26.60 \pm 0.60	-27.60 \pm 0.35	
	Peak ensemble average current at -20 mV [fA]	15.63 \pm 2.17	16.93 \pm 1.52	10.97 \pm 1.05	
	f_{active} [%]	-40 mV	13.41 \pm 1.97	14.86 \pm 2.11	15.52 \pm 1.19
		-30 mV	43.88 \pm 2.38	41.99 \pm 1.06	43.87 \pm 1.52
		-20mV	71.24 \pm 2.00	65.66 \pm 1.36	70.93 \pm 0.91
		-10mV	87.22 \pm 2.11	83.45 \pm 0.58	82.39 \pm 0.52
	P_{open} [%]	-40 mV	0.34 \pm 0.04	0.47 \pm 0.05	0.24 \pm 0.02 [#]
		-30 mV	0.67 \pm 0.05	1.17 \pm 0.12*	0.37 \pm 0.02**
		-20mV	1.37 \pm 0.10	2.21 \pm 0.14*	0.66 \pm 0.03**
		-10mV	2.21 \pm 0.09	3.18 \pm 0.12*	1.06 \pm 0.05**
	MOT [ms]	-20mV	0.25 \pm 0.02	0.27 \pm 0.02	0.25 \pm 0.02
		-10mV	0.23 \pm 0.01	0.24 \pm 0.01	0.22 \pm 0.00
	n		13	12	10
MCT [ms]	-20mV	15.11 \pm 1.43	11.22 \pm 1.70	26.11 \pm 2.34**	
	-10mV	9.22 \pm 0.23	7.01 \pm 0.50	18.20 \pm 1.13**	
MFL [ms]	-20mV	22.76 \pm 1.82	18.99 \pm 2.21	36.25 \pm 3.35**	
	-10mV	10.98 \pm 0.47	10.45 \pm 0.82	24.94 \pm 2.97**	
n (only k = 1)		5	5	5	

Table S 6.2. ANOVA results of comparing single-channel recordings investigating S1475 modulation of $Ca_v1.3$. Table reports F-values and degrees of freedom F (DFn, DFd) and corresponding p-value up to three decimal places. Smaller p-values are reported by $p < 0.001$.

ANOVA results comparing WT, S1475A, S1475D			
15mM Ba ²⁺	Conductance [pS]		F (2, 32) = 8.887 and p<0.001
	V _{rev} [mV]		F (2, 32) = 23.51 and p<0.001
	V _{0.5 act} [mV]		F (2, 32) = 0.373 and p=0.692
	Peak current at -20 mV [fA]		F (2, 32) = 2.949 and p=0.067
	f _{active} [%]	-40 mV	F (2, 32) = 0.303 and p=0.740
		-30 mV	F (2, 32) = 0.331 and p=0.721
		-20mV	F (2, 32) = 3.639 and p=0.038
		-10mV	F (2, 32) = 2.968 and p=0.066
	P _{open} [%]	-40 mV	F (2, 32) = 6.660 and p=0.004
		-30 mV	F (2, 32) = 22.61 and p<0.001
		-20mV	F (2, 32) = 46.12 and p<0.001
		-10mV	F (2, 32) = 108.2 and p<0.001
	MOT [ms]	-20mV	F (2, 32) = 0.541 and p=0.587
		-10mV	F (2, 32) = 2.224 and p=0.125
	MCT [ms]	-20mV	F (2, 12) = 13.74 and p<0.001
		-10mV	F (2, 12) = 53.01 and p<0.001
MFL [ms]	-20mV	F (2, 12) = 10.18 and p=0.003	
	-10mV	F (2, 12) = 16.65 and p<0.001	

Table S 6.3. p-values of Bonferroni's multiple comparisons test following significant one-way ANOVA investigating S1475 modulation of $Ca_v1.3$. Table reports p-values up to three decimal places. Smaller p-values are reported by $p < 0.001$.

		WT vs S1475A	WT vs. S1475D	S1475A vs. S1475D	
15mM Ba ²⁺	Conductance [pS]		0.044	0.368	<0.001
	V _{rev} [mV]		0.005	0.005	<0.001
	f _{active} [%]	-20mV	0.059	>0.999	0.113
	P _{open} [%]	-40 mV	0.108	0.360	0.003
		-30 mV	<0.001	0.053	<0.001
		-20mV	<0.001	<0.001	<0.001
		-10mV	<0.001	<0.001	<0.001
	MCT [ms]	-20mV	0.635	<0.001	<0.001
		-10mV	0.236	<0.001	<0.001
	MFL [ms]	-20mV	>0.999	0.017	0.003
-10mV		>0.999	0.001	<0.001	

S7 – Data and p-value overview of single-channel patch clamp recordings investigating S1475 modulation of Cav1.3

Table S 7.1. Data values of whole-cell recordings investigating S1475 modulation of Cav1.3. Table reports parameters as mean \pm SEM. Number of experiments below the respective parameters. *p \leq 0.05 vs WT and #p \leq 0.05 S1475A vs S1475D in Bonferroni's multiple comparisons test following one-way ANOVA. Exact p-values see supplemental Tab. S 7.3.

		WT	S1475A	S1475D	
2mM Ca ²⁺	Peak current density [pA/pF]	21.91 \pm 1.06	33.03 \pm 2.05*	9.93 \pm 0.60**	
	r₃₀₀ (%)	-40 mV	49.85 \pm 6.08	51.03 \pm 7.78	62.58 \pm 5.66
		-30 mV	26.28 \pm 3.53	25.68 \pm 3.98	41.11 \pm 3.91**
		-20 mV	13.03 \pm 1.54	13.87 \pm 2.45	24.03 \pm 2.71**
		-10 mV	12.40 \pm 1.65	12.59 \pm 1.81	19.32 \pm 2.54
		0 mV	10.42 \pm 1.57	12.15 \pm 1.80	16.91 \pm 3.17
	n	13	15	9	
	Activation (G/G_{max})	V_{0.5 act} [mV]	-24.42 \pm 1.16	-23.54 \pm 0.98	-21.07 \pm 0.97
		Slope [mV]	5.25 \pm 0.28	5.57 \pm 0.28	6.75 \pm 0.25**
		n	13	13	9
	Inactivation (I/I_{max})	V_{0.5 inact} [mV]	-43.33 \pm 0.86	-40.91 \pm 0.67	-39.59 \pm 0.67*
		Slope [mV]	-5.27 \pm 0.36	-5.35 \pm 0.24	-5.02 \pm 0.09
		I_{non-inact} [%]	8.21 \pm 2.64	2.81 \pm 0.79	11.53 \pm 2.26#
		n	12	15	8
KN-93	Peak current density [pA/pF]	10.73 \pm 0.48	11.37 \pm 0.48	4.43 \pm 0.14**	
	n	14	13	11	
2mM Ca ²⁺ + CaMKII ₁₋₂₉₀	Peak current density [pA/pF]	10.96 \pm 1.1	30.81 \pm 1.7**	10.11 \pm 0.72	
	n	18	16	16	
	Activation (G/G_{max})	V_{0.5 act} [mV]	-20.50 \pm 0.68	-27.97 \pm 0.63**	-21.37 \pm 0.78
		Slope_{act} [mV]	7.10 \pm 0.17	5.79 \pm 0.25**	7.60 \pm 0.23
		n	18	16	16
	Inactivation (I/I_{max})	V_{0.5 inact} [mV]	-42.13 \pm 0.55	-45.35 \pm 0.72**	-41.07 \pm 0.57
		Slope_{inact} [mV]	-4.89 \pm 0.16	-5.56 \pm 0.15*	-5.17 \pm 0.08
		I_{non-inact} (%)	6.85 \pm 0.86	3.07 \pm 0.77**	9.02 \pm 1.31
		n	17	16	15
	2mM Ca ²⁺ + CaM	Peak current density [pA/pF]	34.94 \pm 2.54	42.24 \pm 5.98	5.63 \pm 0.36**
r₃₀₀ (%)		-40 mV	53.65 \pm 6.21	49.71 \pm 5.76	73.94 \pm 4.95**
		-30 mV	16.28 \pm 2.27	23.28 \pm 4.21	54.22 \pm 4.50**
		-20 mV	13.01 \pm 1.71	17.27 \pm 2.77	40.13 \pm 2.82**
		-10 mV	13.48 \pm 2.10	16.68 \pm 2.75	36.53 \pm 2.75**

		0 mV	16.37 ± 2.79	16.68 ± 3.46	37.26 ± 3.15**
		n	14	13	19
	Activation (G/G_{max})	V_{0.5 act} [mV]	-30.55 ± 1.31	-30.66 ± 1.39	-23.84 ± 0.69**
		Slope [mV]	4.92 ± 0.26	4.78 ± 0.33	7.05 ± 0.18**
		n	14	11	16
	Inactivation (I/I_{max})	V_{0.5 inact} [mV]	-44.02 ± 0.84	-43.45 ± 0.96	-36.30 ± 0.65**
		Slope [mV]	-4.40 ± 0.18	-4.78 ± 0.10	-4.42 ± 0.16
		I_{non-inact} (%)	3.50 ± 0.65	1.51 ± 0.30	5.64 ± 0.54**
		n	12	13	17
	2mM Ca²⁺ + BsCaMIQ	Peak current density [pA/pF]		3.77 ± 0.45	4.27 ± 0.17
r₃₀₀ (%)		-30 mV	41.87 ± 3.18	45.41 ± 2.27	47.48 ± 3.24
		-20 mV	35.26 ± 2.51	33.08 ± 1.66	36.27 ± 3.21
		-10 mV	33.55 ± 3.05	27.63 ± 1.13	30.47 ± 3.23
		0 mV	30.77 ± 2.91	27.69 ± 1.30	28.02 ± 3.43
		10 mV	32.09 ± 3.07	30.77 ± 1.76	26.74 ± 3.40
		n	14	18	13
Activation (G/G_{max})		V_{0.5 act} [mV]	-20.36 ± 1.13	-21.58 ± 0.74	-22.70 ± 0.81
		Slope [mV]	7.44 ± 0.17	7.37 ± 0.12	8.08 ± 0.39
		n	13	18	12
Inactivation (I/I_{max})		V_{0.5 inact} [mV]	-35.16 ± 0.83	-34.32 ± 0.97	-36.29 ± 0.78
		Slope [mV]	-6.00 ± 0.20	-5.40 ± 0.12	-5.86 ± 0.25
		I_{non-inact} (%)	10.36 ± 1.15	9.72 ± 1.46	12.29 ± 2.27
		n	14	18	10
2mM Ca²⁺ + CaM₁₂₃₄		Peak current density [pA/pF]		29.94 ± 2.47	35.44 ± 1.10
	r₃₀₀ (%)	-40 mV	65.28 ± 2.86	66.95 ± 3.21	71.18 ± 4.44
		-30 mV	54.11 ± 3.17	58.31 ± 2.85	76.47 ± 2.15**
		-20 mV	44.82 ± 2.52	48.89 ± 3.22	68.21 ± 2.72**
		-10 mV	40.81 ± 2.09	42.08 ± 2.63	61.21 ± 2.65**
		0 mV	37.54 ± 1.69	39.52 ± 2.67	56.47 ± 2.15**
		n	14	15	16
	Activation (G/G_{max})	V_{0.5 act} [mV]	-26.19 ± 1.53	-26.17 ± 0.84	-20.93 ± 1.61*
		Slope [mV]	5.93 ± 0.41	5.95 ± 0.21	7.11 ± 0.30*
		n	14	14	16
	Inactivation (I/I_{max})	V_{0.5 inact} [mV]	-38.57 ± 0.78	-38.83 ± 0.51	-33.18 ± 0.52**
		Slope [mV]	-6.15 ± 0.18	-5.97 ± 0.11	-6.23 ± 0.16
		I_{non-inact} (%)	10.12 ± 1.20	8.09 ± 0.78	9.11 ± 0.58
		n	14	13	16

2mM Ba²⁺ + CaM	Peak current density [pA/pF]		30.65 ± 3.37	30.91 ± 2.67	9.97 ± 1.03**
	r₃₀₀ (%)	-40 mV	79.63 ± 2.34	87.34 ± 1.89	83.82 ± 3.18
		-30 mV	75.44 ± 2.70	73.64 ± 3.36	82.46 ± 2.09
		-20 mV	70.23 ± 2.82	67.99 ± 3.64	77.22 ± 2.55
		-10 mV	65.72 ± 2.50	66.39 ± 3.82	76.14 ± 1.91
		0 mV	64.40 ± 2.55	65.05 ± 3.68	74.39 ± 1.91
		n	10	15	17
	Activation (G/G_{max})	V_{0.5 act} [mV]	-35.50 ± 0.74	-35.58 ± 0.86	-29.45 ± 0.94**
		Slope [mV]	5.70 ± 0.34	5.38 ± 0.34	6.13 ± 0.36
		n	9	15	16
	Inactivation (I/I_{max})	V_{0.5 inact} [mV]	-44.96 ± 0.66	-44.99 ± 0.52	-39.36 ± 0.81**
		Slope [mV]	-5.66 ± 0.19	-5.31 ± 0.16	-5.52 ± 0.14
		I_{non-inact} (%)	16.00 ± 0.99	13.71 ± 1.08	16.95 ± 1.47
n		10	13	17	
2mM Ba²⁺	Peak current density [pA/pF]		32.17 ± 2.17	35.02 ± 2.24	19.12 ± 1.82**
	r₃₀₀ (%)	-40 mV	78.62 ± 3.54	81.77 ± 3.38	88.00 ± 5.24
		-30 mV	65.71 ± 2.61	66.71 ± 3.72	78.83 ± 5.38
		-20 mV	58.43 ± 2.09	61.33 ± 3.33	66.52 ± 5.72
		-10 mV	53.72 ± 2.33	58.86 ± 3.03	65.39 ± 6.27
		0 mV	49.20 ± 2.98	57.98 ± 2.70	64.68 ± 7.97
		n	14	12	7
	Activation (G/G_{max})	V_{0.5 act} [mV]	-31.95 ± 1.43	-31.14 ± 0.85	-29.41 ± 1.49
		Slope [mV]	5.72 ± 0.39	4.53 ± 0.28	4.75 ± 0.53
		n	9	11	7
	Inactivation (I/I_{max})	V_{0.5 inact} [mV]	-47.08 ± 0.47	-46.34 ± 1.11	-44.96 ± 1.33
		Slope [mV]	-6.00 ± 0.20	-5.63 ± 0.19	-5.42 ± 0.23
		I_{non-inact} (%)	13.12 ± 0.70	12.36 ± 1.24	16.31 ± 1.07
n		14	11	7	

Table S7.2. ANOVA results of comparing whole-cell recordings investigating S1475 modulation of Ca_v1.3. Table reports F-values and degrees of freedom F (DFn, DFd) and p-values up to three decimal places. Smaller p-values are reported as $p < 0.001$.

ANOVA results comparing WT, S1475A, S1475D			
2mM Ca ²⁺	Peak current density [pA/pF]		F (2, 35) = 44.70 and $p < 0.001$
	r ₃₀₀ (%)	-40 mV	F (2, 35) = 0.891 and $p = 0.419$
		-30 mV	F (2, 35) = 4.458 and $p = 0.019$
		-20 mV	F (2, 35) = 5.654 and $p = 0.008$
		-10 mV	F (2, 35) = 3.396 and $p = 0.047$
		0 mV	F (2, 35) = 2.034 and $p = 0.147$
	Activation (G/G _{max})	V _{0.5 act} [mV]	F (2, 32) = 2.122 and $p = 0.136$
		Slope [mV]	F (2, 32) = 6.372 and $p = 0.005$
	Inactivation (I/I _{max})	V _{0.5 inact} [mV]	F (2, 32) = 5.081 and $p = 0.012$
		Slope [mV]	F (2, 32) = 0.303 and $p = 0.741$
I _{non-inact} [%]		F (2, 32) = 4.787 and $p = 0.015$	
KN-93	Peak current density [pA/pF]		F (2, 35) = 70.54 and $p < 0.001$
CaMKII ₁₋₂₉₀	Peak current density [pA/pF]		F (2, 47) = 81.25 and $p < 0.001$
	Activation (G/G _{max})	V _{0.5 act} [mV]	F (2, 47) = 31.31 and $p < 0.001$
		Slope _{act} [mV]	F (2, 47) = 16.30 and $p < 0.001$
	Inactivation (I/I _{max})	V _{0.5 inact} [mV]	F (2, 45) = 12.00 and $p < 0.001$
		Slope _{inact} [mV]	F (2, 45) = 6.086 and $p = 0.005$
I _{non-inact} (%)		F (2, 45) = 8.161 and $p < 0.001$	
2mM Ca ²⁺ + CaM	Peak current density [pA/pF]		F (2, 43) = 36.49 and $p < 0.001$
	r ₃₀₀ (%)	-40 mV	F (2, 43) = 5.848 and $p = 0.006$
		-30 mV	F (2, 43) = 27.60 and $p < 0.001$
		-20 mV	F (2, 43) = 34.47 and $p < 0.001$
		-10 mV	F (2, 43) = 24.55 and $p < 0.001$
		0 mV	F (2, 43) = 15.53 and $p < 0.001$
	Activation (G/G _{max})	V _{0.5 act} [mV]	F (2, 38) = 14.80 and $p < 0.001$
		Slope [mV]	F (2, 38) = 25.47 and $p < 0.001$
	Inactivation (I/I _{max})	V _{0.5 inact} [mV]	F (2, 39) = 28.66 and $p < 0.001$
		Slope [mV]	F (2, 39) = 1.699 and $p = 0.196$
I _{non-inact} (%)		F (2, 39) = 15.49 and $p < 0.001$	
BsCaMIQ	Peak current density [pA/pF]		F (2, 42) = 0.919 and $p = 0.407$
	r ₃₀₀ (%)	-30 mV	F (2, 42) = 0.847 and $p = 0.436$
		-20 mV	F (2, 42) = 0.455 and $p = 0.638$
		-10 mV	F (2, 42) = 1.451 and $p = 0.246$
		0 mV	F (2, 42) = 0.422 and $p = 0.658$
		10 mV	F (2, 42) = 0.916 and $p = 0.408$

	Activation (G/G_{\max})	$V_{0.5 \text{ act}}$ [mV]	F (2, 40) = 1.498 and p=0.239	
		Slope [mV]	F (2, 40) = 2.771 and p=0.075	
	Inactivation (I/I_{\max})	$V_{0.5 \text{ inact}}$ [mV]	F (2, 39) = 1.047 and p=0.361	
		Slope [mV]	F (2, 39) = 3.403 and p=0.063	
		$I_{\text{non-inact}}$ (%)	F (2, 39) = 0.620 and p=0.543	
2mM Ca^{2+} + CaM_{1234}	Peak current density [pA/pF]		F (2, 42) = 80.61 and p<0.001	
	r_{300} (%)	-40 mV	F (2, 42) = 0.706 and p=0.499	
		-30 mV	F (2, 42) = 19.62 and p<0.001	
		-20 mV	F (2, 42) = 19.64 and p<0.001	
		-10 mV	F (2, 42) = 21.56 and p<0.001	
		0 mV	F (2, 42) = 25.93 and p<0.001	
	Activation (G/G_{\max})	$V_{0.5 \text{ act}}$ [mV]	F (2, 40) = 4.468 and p=0.018	
		Slope [mV]	F (2, 40) = 4.364 and p=0.019	
	Inactivation (I/I_{\max})	$V_{0.5 \text{ inact}}$ [mV]	F (2, 41) = 26.74 and p<0.001	
		Slope [mV]	F (2, 41) = 0.720 and p=0.493	
		$I_{\text{non-inact}}$ (%)	F (2, 41) = 1.204 and p=0.311	
	2mM Ba^{2+} + CaM	Peak current density [pA/pF]		F (2, 39) = 28.18 and p<0.001
		r_{300} (%)	-40 mV	F (2, 39) = 1.749 and p=0.187
-30 mV			F (2, 39) = 3.160 and p=0.053	
-20 mV			F (2, 39) = 2.717 and p=0.079	
-10 mV			F (2, 39) = 4.192 and p=0.023	
0 mV			F (2, 38) = 4.046 and p=0.026	
Activation (G/G_{\max})		$V_{0.5 \text{ act}}$ [mV]	F (2, 37) = 15.20 and p<0.001	
		Slope [mV]	F (2, 37) = 1.219 and p=0.307	
Inactivation (I/I_{\max})		$V_{0.5 \text{ inact}}$ [mV]	F (2, 37) = 20.45 and p<0.001	
		Slope [mV]	F (2, 37) = 1.049 and p=0.361	
		$I_{\text{non-inact}}$ (%)	F (2, 37) = 1.590 and p=0.218	
2mM Ba^{2+}		Peak current density [pA/pF]		F (2, 29) = 10.28 and p<0.001
		r_{300} (%)	-40 mV	F (2, 30) = 1.246 and p=0.302
	-30 mV		F (2, 30) = 3.122 and p=0.059	
	-20 mV		F (2, 30) = 1.263 and p=0.297	
	-10 mV		F (2, 30) = 2.519 and p=0.097	
	0 mV		F (2, 30) = 3.486 and p=0.054	
	Activation (G/G_{\max})	$V_{0.5 \text{ act}}$ [mV]	F (2, 24) = 0.864 and p=0.434	
		Slope [mV]	F (2, 24) = 2.543 and p=0.099	
	Inactivation (I/I_{\max})	$V_{0.5 \text{ inact}}$ [mV]	F (2, 29) = 1.094 and p=0.348	
		Slope [mV]	F (2, 29) = 2.173 and p=0.132	
		$I_{\text{non-inact}}$ (%)	F (2, 29) = 3.058 and p=0.062	

Table S 7.3. p-values of Bonferroni's multiple comparisons test following significant one-way ANOVA investigating S1475 modulation of Ca_v1.3. Table reports p-values up to three decimal places. Smaller p-values are reported by $p < 0.001$.

		WT vs S1475A	WT vs S1475D	S1475A vs S1475D	
2mM Ca ²⁺	Peak current density [pA/pF]	<0.001	<0.001	<0.001	
	r ₃₀₀ (%)	-30 mV	>0.999	0.045	0.029
		-20 mV	>0.999	0.011	0.017
		-10 mV	>0.999	0.128	0.069
	Activation	Slope [mV]	>0.999	0.005	0.031
	Inactivation	V _{0.5 inact} [mV]	0.082	0.015	0.829
I _{non-inact} [%]		0.144	0.877	0.019	
KN-93	Peak current density [pA/pF]	0.889	<0.001	<0.001	
CaMKII ₁₋₂₉₀	Peak current density [pA/pF]	<0.001	>0.999	<0.001	
	Activation	V _{0.5 act} [mV]	<0.001	>0.999	<0.001
		Slope [mV]	<0.001	0.378	<0.001
	Inactivation	V _{0.5 inact} [mV]	0.002	0.741	<0.001
		Slope [mV]	0.003	0.500	0.159
		I _{non-inact} (%)	0.002	0.741	<0.001
2mM Ca ²⁺ + CaM	Peak current density [pA/pF]	0.458	<0.001	<0.001	
	r ₃₀₀ (%)	-40 mV	>0.999	0.035	0.011
		-30 mV	0.764	<0.001	<0.001
		-20 mV	0.846	<0.001	<0.001
		-10 mV	>0.999	<0.001	<0.001
		0 mV	>0.999	<0.001	<0.001
	Activation	V _{0.5 act} [mV]	>0.999	<0.001	<0.001
		Slope [mV]	>0.999	<0.001	<0.001
	Inactivation	V _{0.5 inact} [mV]	>0.999	<0.001	<0.001
		I _{non-inact} (%)	0.056	0.023	<0.001
2mM Ca ²⁺ + CaM ₁₂₃₄	Peak current density [pA/pF]	0.055	<0.001	<0.001	
	r ₃₀₀ (%)	-30 mV	0.861	<0.001	<0.001
		-20 mV	0.983	<0.001	<0.001
		-10 mV	>0.999	<0.001	<0.001
		0 mV	>0.999	<0.001	<0.001
	Activation	V _{0.5 act} [mV]	>0.999	0.041	0.048
		Slope [mV]	>0.999	0.042	0.054
Inactivation	V _{0.5 inact} [mV]	>0.999	<0.001	<0.001	
2mM Ba ²⁺ + CaM	Peak current density [pA/pF]	>0.999	<0.001	<0.001	
	r ₃₀₀ (%)	-10 mV	>0.999	0.078	0.058
		0 mV	>0.999	0.085	0.053
	Activation	V _{0.5 act} [mV]	>0.999	<0.001	<0.001
Inactivation	V _{0.5 inact} [mV]	>0.999	<0.001	<0.001	
Ba ²⁺	Peak current density [pA/pF]	>0.999	0.003	<0.001	

Table S 7.4. Data values of CDI and SAN-AP investigation of S1475 modulation of Ca_v1.3. Table reports values for as mean ± SEM. *p ≤ 0.05 vs WT and #p ≤ 0.05 S1475A vs S1475D in Bonferroni's multiple comparisons test following one-way ANOVA. P-values see Tab S 7.5.

		WT	S1475A	S1475D
CDI	f-value - CaM	44.05 ± 1.41	46.27 ± 1.81	41.78 ± 2.44
	n	10	15	10
	f-value + CaM	57.22 ± 1.71	50.72 ± 2.77	37.10 ± 2.81**
	n	14	13	19
SAN-AP	I_{peak} Depolarization	9.28 ± 1.04	10.71 ± 1.17	2.43 ± 0.39**
	I_{peak} Repolarization	1.74 ± 0.20	1.94 ± 0.20	1.32 ± 0.16
	Area under the curve (AUC)	1.16 ± 0.20	1.63 ± 0.28	0.48 ± 0.10**
	n	7	7	10

Table S 7.5. ANOVA results and p-values of Bonferroni's multiple comparisons for CDI and SAN-AP results. Table reports ANOVA results with F-value and degrees of freedom F (DFn, DFd) and p-values, and p-values of Bonferroni's multiple comparisons test following significant one-way ANOVA. P-values are reported up to three decimal places and smaller values as p < 0.001.

		WT vs S1475A	WT vs S1475D	S1475A vs S1475D
CDI	f-value - CaM	F (2, 32) = 1.332 and p=0.278		
	f-value + CaM	F (2, 43) = 16.95 and p<0.001		
		0.312	<0.001	0.002
SAN-AP	I_{peak} Depolarization	F (2, 21) = 26.45 and p<0.001		
		0.914	<0.001	<0.001
	I_{peak} Repolarization	F (2, 21) = 2.757 and p=0.086		
		F (2, 21) = 10.88 and p<0.001		
Area under the curve (AUC)	0.304	0.039	<0.001	

References

- Adams, P. J., Ben-Johny, M., Dick, I. E., Inoue, T., & Yue, D. T. (2014). Apocalmodulin itself promotes ion channel opening and Ca(2+) regulation. *Cell*, *159*(3), 608-622. <https://doi.org/10.1016/j.cell.2014.09.047>
- Ashcroft, F. M., Proks, P., Smith, P. A., Ammala, C., Bokvist, K., & Rorsman, P. (1994). Stimulus-secretion coupling in pancreatic beta cells. *J Cell Biochem*, *55 Suppl*, 54-65. <https://doi.org/10.1002/jcb.240550007>
- Avery, R. B., & Johnston, D. (1996). Multiple channel types contribute to the low-voltage-activated calcium current in hippocampal CA3 pyramidal neurons. *J Neurosci*, *16*(18), 5567-5582. <https://doi.org/10.1523/JNEUROSCI.16-18-05567.1996>
- Azizan, E. A., Poulsen, H., Tuluc, P., Zhou, J., Clausen, M. V., Lieb, A., Maniero, C., Garg, S., Bochukova, E. G., Zhao, W., Shaikh, L. H., Brighton, C. A., Teo, A. E., Davenport, A. P., Dekkers, T., Tops, B., Kusters, B., Ceral, J., Yeo, G. S., ... Brown, M. J. (2013). Somatic mutations in ATP1A1 and CACNA1D underlie a common subtype of adrenal hypertension. *Nat Genet*, *45*(9), 1055-1060. <https://doi.org/10.1038/ng.2716>
- Baddeley, D., Jayasinghe, I. D., Lam, L., Rossberger, S., Cannell, M. B., & Soeller, C. (2009). Optical single-channel resolution imaging of the ryanodine receptor distribution in rat cardiac myocytes. *Proc Natl Acad Sci U S A*, *106*(52), 22275-22280. <https://doi.org/10.1073/pnas.0908971106>
- Baig, S. M., Koschak, A., Lieb, A., Gebhart, M., Dafinger, C., Nurnberg, G., Ali, A., Ahmad, I., Sinnegger-Brauns, M. J., Brandt, N., Engel, J., Mangoni, M. E., Farooq, M., Khan, H. U., Nurnberg, P., Striessnig, J., & Bolz, H. J. (2011). Loss of Ca(v)1.3 (CACNA1D) function in a human channelopathy with bradycardia and congenital deafness. *Nat Neurosci*, *14*(1), 77-84. <https://doi.org/10.1038/nn.2694>
- Banerjee, R., Yoder, J. B., Yue, D. T., Amzel, L. M., Tomaselli, G. F., Gabelli, S. B., & Ben-Johny, M. (2018). Bilobal architecture is a requirement for calmodulin signaling to Ca(V)1.3 channels. *Proc Natl Acad Sci U S A*, *115*(13), E3026-E3035. <https://doi.org/10.1073/pnas.1716381115>
- Baroudi, G., Qu, Y., Ramadan, O., Chahine, M., & Boutjdir, M. (2006). Protein kinase C activation inhibits Cav1.3 calcium channel at NH2-terminal serine 81 phosphorylation site. *Am J Physiol Heart Circ Physiol*, *291*(4), H1614-1622. <https://doi.org/10.1152/ajpheart.00095.2006>
- Barresi, S., Dentici, M. L., Manzoni, F., Bellacchio, E., Agolini, E., Pizzi, S., Ciolfi, A., Tarnopolsky, M., Brady, L., Garone, G., Novelli, A., Mei, D., Guerrini, R., Capuano, A., Pantaleoni, C., & Tartaglia, M. (2020). Infantile-Onset Syndromic Cerebellar Ataxia and CACNA1G Mutations. *Pediatr Neurol*, *104*, 40-45. <https://doi.org/10.1016/j.pediatrneurol.2019.09.005>
- Bartels, P., Salvesson, I., Coleman, A. M., Anderson, D. E., Jeng, G., Estrada-Tobar, Z. M., Man, K. N. M., Yu, Q., Kuzmenkina, E., Nieves-Cintrón, M., Navedo, M. F., Horne, M. C., Hell, J. W., & Ames, J. B. (2022). Half-calcified calmodulin promotes basal activity and inactivation of the L-type calcium channel Ca(V)1.2. *J Biol Chem*, *298*(12), 102701. <https://doi.org/10.1016/j.jbc.2022.102701>

- Bean, B. P. (1989). Neurotransmitter inhibition of neuronal calcium currents by changes in channel voltage dependence. *Nature*, 340(6229), 153-156. <https://doi.org/10.1038/340153a0>
- Bell, D. C., Butcher, A. J., Berrow, N. S., Page, K. M., Brust, P. F., Nesterova, A., Stauderman, K. A., Seabrook, G. R., Nurnberg, B., & Dolphin, A. C. (2001). Biophysical properties, pharmacology, and modulation of human, neuronal L-type (alpha(1D), Ca(V)1.3) voltage-dependent calcium currents. *J Neurophysiol*, 85(2), 816-827. <https://doi.org/10.1152/jn.2001.85.2.816>
- Ben Johny, M., Yang, P. S., Bazzazi, H., & Yue, D. T. (2013). Dynamic switching of calmodulin interactions underlies Ca²⁺ regulation of Cav1.3 channels. *Nat Commun*, 4, 1717. <https://doi.org/10.1038/ncomms2727>
- Ben-Johny, M., & Yue, D. T. (2014). Calmodulin regulation (calmodulation) of voltage-gated calcium channels. *J Gen Physiol*, 143(6), 679-692. <https://doi.org/10.1085/jgp.201311153>
- Ben-Johny, M., & Dick, I. E. (2022). Calmodulin Regulation of Voltage-Gated Calcium Channels. In G. W. Zamponi & N. Weiss (Eds.), *Voltage-Gated Calcium Channels* (pp. 217-236). Springer International Publishing. https://doi.org/10.1007/978-3-031-08881-0_9
- Bers, D. M. (2002). Cardiac excitation-contraction coupling. *Nature*, 415(6868), 198-205. <https://doi.org/10.1038/415198a>
- Binder, M. D., Powers, R. K., & Heckman, C. J. (2020). Nonlinear Input-Output Functions of Motoneurons. *Physiology (Bethesda)*, 35(1), 31-39. <https://doi.org/10.1152/physiol.00026.2019>
- Birnbaumer, L., Campbell, K. P., Catterall, W. A., Harpold, M. M., Hofmann, F., Horne, W. A., Mori, Y., Schwartz, A., Snutch, T. P., Tanabe, T., & et al. (1994). The naming of voltage-gated calcium channels. *Neuron*, 13(3), 505-506. [https://doi.org/10.1016/0896-6273\(94\)90021-3](https://doi.org/10.1016/0896-6273(94)90021-3)
- Birnbaumer, L., Qin, N., Olcese, R., Tareilus, E., Platano, D., Costantin, J., & Stefani, E. (1998). Structures and functions of calcium channel beta subunits. *J Bioenerg Biomembr*, 30(4), 357-375. <https://www.ncbi.nlm.nih.gov/pubmed/7917287>
- Black, D. J., Leonard, J., & Persechini, A. (2006). Biphasic Ca²⁺-dependent switching in a calmodulin-IQ domain complex. *Biochemistry*, 45(22), 6987-6995. <https://doi.org/10.1021/bi052533w>
- Blesneac, I., Chemin, J., Bidaud, I., Huc-Brandt, S., Vandermoere, F., & Lory, P. (2015). Phosphorylation of the Cav3.2 T-type calcium channel directly regulates its gating properties. *Proc Natl Acad Sci U S A*, 112(44), 13705-13710. <https://doi.org/10.1073/pnas.1511740112>
- Bock, G., Gebhart, M., Scharinger, A., Jangsangthong, W., Busquet, P., Poggiani, C., Sartori, S., Mangoni, M. E., Sinnegger-Brauns, M. J., Herzig, S., Striessnig, J., & Koschak, A. (2011). Functional properties of a newly identified C-terminal splice variant of Cav1.3 L-type Ca²⁺ channels. *J Biol Chem*, 286(49), 42736-42748. <https://doi.org/10.1074/jbc.M111.269951>

- Borchert, T., Hubscher, D., Guessoum, C. I., Lam, T. D., Ghadri, J. R., Schellinger, I. N., Tiburcy, M., Liaw, N. Y., Li, Y., Haas, J., Sossalla, S., Huber, M. A., Cyganek, L., Jacobshagen, C., Dressel, R., Raaz, U., Nikolaev, V. O., Guan, K., Thiele, H., . . . Streckfuss-Bomeke, K. (2017). Catecholamine-Dependent beta-Adrenergic Signaling in a Pluripotent Stem Cell Model of Takotsubo Cardiomyopathy. *J Am Coll Cardiol*, *70*(8), 975-991. <https://doi.org/10.1016/j.jacc.2017.06.061>
- Bourdin, B., Marger, F., Wall-Lacelle, S., Schneider, T., Klein, H., Sauve, R., & Parent, L. (2010). Molecular determinants of the CaVbeta-induced plasma membrane targeting of the CaV1.2 channel. *J Biol Chem*, *285*(30), 22853-22863. <https://doi.org/10.1074/jbc.M110.111062>
- Bourinet, E., Zamponi, G. W., Stea, A., Soong, T. W., Lewis, B. A., Jones, L. P., Yue, D. T., & Snutch, T. P. (1996). The alpha 1E calcium channel exhibits permeation properties similar to low-voltage-activated calcium channels. *J Neurosci*, *16*(16), 4983-4993. <https://doi.org/10.1523/JNEUROSCI.16-16-04983.1996>
- Brandt, A., Striessnig, J., & Moser, T. (2003). CaV1.3 channels are essential for development and presynaptic activity of cochlear inner hair cells. *J Neurosci*, *23*(34), 10832-10840. <https://doi.org/10.1523/JNEUROSCI.23-34-10832.2003>
- Braun, M., Ramracheya, R., Bengtsson, M., Zhang, Q., Karanauskaite, J., Partridge, C., Johnson, P. R., & Rorsman, P. (2008). Voltage-gated ion channels in human pancreatic beta-cells: electrophysiological characterization and role in insulin secretion. *Diabetes*, *57*(6), 1618-1628. <https://doi.org/10.2337/db07-0991>
- Breitenkamp, A. F., Matthes, J., Nass, R. D., Sinzig, J., Lehmkuhl, G., Nurnberg, P., & Herzig, S. (2014). Rare mutations of CACNB2 found in autism spectrum disease-affected families alter calcium channel function. *PLoS One*, *9*(4), e95579. <https://doi.org/10.1371/journal.pone.0095579>
- Breitenkamp, A. F., Matthes, J., & Herzig, S. (2015). Voltage-gated Calcium Channels and Autism Spectrum Disorders. *Curr Mol Pharmacol*, *8*(2), 123-132. <https://dx.doi.org/10.2174/1874467208666150507105235>
- Brickley, K., Campbell, V., Berrow, N., Leach, R., Norman, R. I., Wray, D., Dolphin, A. C., & Baldwin, S. A. (1995). Use of site-directed antibodies to probe the topography of the alpha 2 subunit of voltage-gated Ca²⁺ channels. *FEBS Lett*, *364*(2), 129-133. [https://doi.org/10.1016/0014-5793\(95\)00371-F](https://doi.org/10.1016/0014-5793(95)00371-F)
- Buraei, Z., & Yang, J. (2010). The beta-subunit of voltage-gated Ca²⁺ channels. *Physiol Rev*, *90*(4), 1461-1506. <https://doi.org/10.1152/physrev.00057.2009>
- Carbone, E., & Lux, H. D. (1984). A low voltage-activated, fully inactivating Ca channel in vertebrate sensory neurones. *Nature*, *310*(5977), 501-502. <https://doi.org/10.1038/310501a0>
- Casas-Alba, D., Lopez-Sala, L., Perez-Ordóñez, M., Mari-Vico, R., Bolasell, M., Martínez-Monseny, A. F., Muchart, J., Fernández-Fernández, J. M., Martorell, L., & Serrano, M. (2021). Early-onset severe spinocerebellar ataxia 42 with neurodevelopmental deficits (SCA42ND): Case report, pharmacological trial, and literature review. *Am J Med Genet A*, *185*(1), 256-260. <https://doi.org/10.1002/ajmg.a.61939>
- Castellano, A., Wei, X., Birnbaumer, L., & Perez-Reyes, E. (1993). Cloning and expression of a neuronal calcium channel beta subunit. *J Biol Chem*, *268*(17), 12359-12366. [https://doi.org/10.1016/S0021-9258\(18\)31398-X](https://doi.org/10.1016/S0021-9258(18)31398-X)

- Catterall, W. A. (2000). Structure and regulation of voltage-gated Ca²⁺ channels. *Annu Rev Cell Dev Biol*, 16, 521-555. <https://doi.org/10.1146/annurev.cellbio.16.1.521>
- Catterall, W. A., Perez-Reyes, E., Snutch, T. P., & Striessnig, J. (2005). International Union of Pharmacology. XLVIII. Nomenclature and structure-function relationships of voltage-gated calcium channels. *Pharmacol Rev*, 57(4), 411-425. <https://doi.org/10.1124/pr.57.4.5>
- Catterall, W. A. (2011). Voltage-gated calcium channels. *Cold Spring Harb Perspect Biol*, 3(8), a003947. <https://doi.org/10.1101/cshperspect.a003947>
- Catterall, W. A. (2022). Subunit Architecture and Atomic Structure of Voltage-Gated Ca²⁺ Channels. In G. W. Zamponi & N. Weiss (Eds.), *Voltage-Gated Calcium Channels* (pp. 31-45). Springer International Publishing. https://doi.org/10.1007/978-3-031-08881-0_2
- Cens, T., Rousset, M., Leyris, J. P., Fesquet, P., & Charnet, P. (2006). Voltage- and calcium-dependent inactivation in high voltage-gated Ca(2+) channels. *Prog Biophys Mol Biol*, 90(1-3), 104-117. <https://doi.org/10.1016/j.pbiomolbio.2005.05.013>
- Chan, C. S., Guzman, J. N., Ilijic, E., Mercer, J. N., Rick, C., Tkatch, T., Meredith, G. E., & Surmeier, D. J. (2007). 'Rejuvenation' protects neurons in mouse models of Parkinson's disease. *Nature*, 447(7148), 1081-1086. <https://doi.org/10.1038/nature05865>
- Chemin, J., Siquier-Pernet, K., Nicouleau, M., Barcia, G., Ahmad, A., Medina-Cano, D., Hanein, S., Altin, N., Hubert, L., Bole-Feysot, C., Fourage, C., Nitschke, P., Thevenon, J., Rio, M., Blanc, P., Vidal, C., Bahi-Buisson, N., Desguerre, I., Munnich, A., . . . Cantagrel, V. (2018). De novo mutation screening in childhood-onset cerebellar atrophy identifies gain-of-function mutations in the CACNA1G calcium channel gene. *Brain*, 141(7), 1998-2013. <https://doi.org/10.1093/brain/awy145>
- Chik, C. L., Liu, Q. Y., Li, B., Klein, D. C., Zylka, M., Kim, D. S., Chin, H., Karpinski, E., & Ho, A. K. (1997). Alpha 1D L-type Ca(2+)-channel currents: inhibition by a beta-adrenergic agonist and pituitary adenylate cyclase-activating polypeptide (PACAP) in rat pinealocytes. *J Neurochem*, 68(3), 1078-1087. <https://doi.org/10.1046/j.1471-4159.1997.68031078.x>
- Chung, S. H., & Kennedy, R. A. (1996). Coupled Markov chain model: characterization of membrane channel currents with multiple conductance sublevels as partially coupled elementary pores. *Math Biosci*, 133(2), 111-137. [https://doi.org/10.1016/0025-5564\(95\)00084-4](https://doi.org/10.1016/0025-5564(95)00084-4)
- Cohen, P. (2002). The origins of protein phosphorylation. *Nat Cell Biol*, 4(5), E127-130. <https://doi.org/10.1038/ncb0502-e127>
- Comunanza, V., Marcantoni, A., Vandael, D. H., Mahapatra, S., Gavello, D., Carabelli, V., & Carbone, E. (2010). CaV1.3 as pacemaker channels in adrenal chromaffin cells: specific role on exo- and endocytosis? *Channels (Austin)*, 4(6), 440-446. <https://doi.org/10.4161/chan.4.6.12866>
- D'Agostino. (1986). Tests for Normal Distribution. In S. M. D'Agostino RB, Dekker M (Ed.), *Goodness-Of-Fit Techniques*.
- Davis, M. J., Wu, X., Nurkiewicz, T. R., Kawasaki, J., Gui, P., Hill, M. A., & Wilson, E. (2001). Regulation of ion channels by protein tyrosine phosphorylation. *Am J Physiol Heart Circ Physiol*, 281(5), H1835-1862. <https://doi.org/10.1152/ajpheart.2001.281.5.H1835>

- De Mingo Alemany, M. C., Mifsud Grau, L., Moreno Macian, F., Ferrer Lorente, B., & Leon Carinena, S. (2020). A de novo CACNA1D missense mutation in a patient with congenital hyperinsulinism, primary hyperaldosteronism and hypotonia. *Channels (Austin)*, *14*(1), 175-180. <https://doi.org/10.1080/19336950.2020.1761171>
- Despang, P., Salamon, S., Breitenkamp, A. F., Kuzmenkina, E., Herzig, S., & Matthes, J. (2020). Autism-associated mutations in the Ca(V)beta(2) calcium-channel subunit increase Ba(2+)-currents and lead to differential modulation by the RGK-protein Gem. *Neurobiol Dis*, *136*, 104721. <https://doi.org/10.1016/j.nbd.2019.104721>
- Despang, P., Salamon, S., Breitenkamp, A., Kuzmenkina, E., & Matthes, J. (2022). Inhibitory effects on L- and N-type calcium channels by a novel Ca(V)beta(1) variant identified in a patient with autism spectrum disorder. *Naunyn Schmiedebergs Arch Pharmacol*, *395*(4), 459-470. <https://doi.org/10.1007/s00210-022-02213-7>
- Dick, I. E., Tadross, M. R., Liang, H., Tay, L. H., Yang, W., & Yue, D. T. (2008). A modular switch for spatial Ca²⁺ selectivity in the calmodulin regulation of CaV channels. *Nature*, *451*(7180), 830-834. <https://doi.org/10.1038/nature06529>
- Dixon, R. E., Navedo, M. F., Binder, M. D., & Santana, L. F. (2022). Mechanisms and physiological implications of cooperative gating of clustered ion channels. *Physiol Rev*, *102*(3), 1159-1210. <https://doi.org/10.1152/physrev.00022.2021>
- Dolphin, A. C. (2003). Beta subunits of voltage-gated calcium channels. *J Bioenerg Biomembr*, *35*(6), 599-620. <https://doi.org/10.1023/B:IOBB.0000008026.37790.5a>
- Dolphin, A. C. (2012). Calcium channel alpha(2)delta subunits in epilepsy and as targets for antiepileptic drugs. In J. L. Noebels, M. Avoli, M. A. Rogawski, R. W. Olsen, & A. V. Delgado-Escueta (Eds.), *Jasper's Basic Mechanisms of the Epilepsies* (4th ed.). <https://www.ncbi.nlm.nih.gov/pubmed/22787633>
- Dolphin, A. C. (2013). The alpha2delta subunits of voltage-gated calcium channels. *Biochim Biophys Acta*, *1828*(7), 1541-1549. <https://doi.org/10.1016/j.bbamem.2012.11.019>
- Dolphin, A. C. (2016). Voltage-gated calcium channels and their auxiliary subunits: physiology and pathophysiology and pharmacology. *J Physiol*, *594*(19), 5369-5390. <https://doi.org/10.1113/JP272262>
- Dou, H., Vazquez, A. E., Namkung, Y., Chu, H., Cardell, E. L., Nie, L., Parson, S., Shin, H. S., & Yamoah, E. N. (2004). Null mutation of alpha1D Ca²⁺ channel gene results in deafness but no vestibular defect in mice. *J Assoc Res Otolaryngol*, *5*(2), 215-226. <https://doi.org/10.1007/s10162-003-4020-3>
- Dragicevic, E., Poetschke, C., Duda, J., Schlaudraff, F., Lammel, S., Schiemann, J., Fauler, M., Hetzel, A., Watanabe, M., Lujan, R., Malenka, R. C., Striessnig, J., & Liss, B. (2014). Cav1.3 channels control D2-autoreceptor responses via NCS-1 in substantia nigra dopamine neurons. *Brain*, *137*(Pt 8), 2287-2302. <https://doi.org/10.1093/brain/awu131>
- Dubel, S. J., Starr, T. V., Hell, J., Ahlijanian, M. K., Enyeart, J. J., Catterall, W. A., & Snutch, T. P. (1992). Molecular cloning of the alpha-1 subunit of an omega-conotoxin-sensitive calcium channel. *Proc Natl Acad Sci U S A*, *89*(11), 5058-5062. <https://doi.org/10.1073/pnas.89.11.5058>

- Eckrich, T., Blum, K., Milenkovic, I., & Engel, J. (2018). Fast Ca²⁺ Transients of Inner Hair Cells Arise Coupled and Uncoupled to Ca²⁺ Waves of Inner Supporting Cells in the Developing Mouse Cochlea. *Front Mol Neurosci*, *11*, 264. <https://doi.org/10.3389/fnmol.2018.00264>
- Ellinor, P. T., Yang, J., Sather, W. A., Zhang, J. F., & Tsien, R. W. (1995). Ca²⁺ channel selectivity at a single locus for high-affinity Ca²⁺ interactions. *Neuron*, *15*(5), 1121-1132. [https://doi.org/10.1016/0896-6273\(95\)90100-0](https://doi.org/10.1016/0896-6273(95)90100-0)
- Ellis, S. B., Williams, M. E., Ways, N. R., Brenner, R., Sharp, A. H., Leung, A. T., Campbell, K. P., McKenna, E., Koch, W. J., Hui, A., & et al. (1988). Sequence and expression of mRNAs encoding the alpha 1 and alpha 2 subunits of a DHP-sensitive calcium channel. *Science*, *241*(4873), 1661-1664. <https://www.ncbi.nlm.nih.gov/pubmed/2458626>
- Engel, J., Michna, M., Platzer, J., & Striessnig, J. (2002). Calcium channels in mouse hair cells: function, properties and pharmacology. *Adv Otorhinolaryngol*, *59*, 35-41. <https://doi.org/10.1159/000059243>
- Ertel, E. A., Campbell, K. P., Harpold, M. M., Hofmann, F., Mori, Y., Perez-Reyes, E., Schwartz, A., Snutch, T. P., Tanabe, T., Birnbaumer, L., Tsien, R. W., & Catterall, W. A. (2000). Nomenclature of voltage-gated calcium channels. *Neuron*, *25*(3), 533-535. [https://doi.org/10.1016/S0896-6273\(00\)81057-0](https://doi.org/10.1016/S0896-6273(00)81057-0)
- Evans, R. M., & Zamponi, G. W. (2006). Presynaptic Ca²⁺ channels--integration centers for neuronal signaling pathways. *Trends Neurosci*, *29*(11), 617-624. <https://doi.org/10.1016/j.tins.2006.08.006>
- Fatt, P., & Katz, B. (1953). The electrical properties of crustacean muscle fibres. *J Physiol*, *120*(1-2), 171-204. <https://doi.org/10.1113/jphysiol.1953.sp004884>
- Felix, R., Gurnett, C. A., De Waard, M., & Campbell, K. P. (1997). Dissection of functional domains of the voltage-dependent Ca²⁺ channel alpha2delta subunit. *J Neurosci*, *17*(18), 6884-6891. <https://doi.org/10.1523/JNEUROSCI.17-18-06884>
- Felizola, S. J., Maekawa, T., Nakamura, Y., Satoh, F., Ono, Y., Kikuchi, K., Aritomi, S., Ikeda, K., Yoshimura, M., Tojo, K., & Sasano, H. (2014). Voltage-gated calcium channels in the human adrenal and primary aldosteronism. *J Steroid Biochem Mol Biol*, *144 Pt B*, 410-416. <https://doi.org/10.1016/j.jsbmb.2014.08.012>
- Finkbeiner, S., & Greenberg, M. E. (1998). Ca²⁺ channel-regulated neuronal gene expression. *J Neurobiol*, *37*(1), 171-189. <https://www.ncbi.nlm.nih.gov/pubmed/9777740>
- Fleckenstein, A. (1983). History of calcium antagonists. *Circ Res*, *52*(2 Pt 2), 13-16. <https://www.ncbi.nlm.nih.gov/pubmed/6339106>
- Flucher, B. E., & Beam, K. G. (2022). The Skeletal Muscle Calcium Channel. In G. W. Zamponi & N. Weiss (Eds.), *Voltage-Gated Calcium Channels* (pp. 449-474). Springer International Publishing. https://doi.org/10.1007/978-3-031-08881-0_16
- Gao, L., Blair, L. A., Salinas, G. D., Needleman, L. A., & Marshall, J. (2006). Insulin-like growth factor-1 modulation of CaV1.3 calcium channels depends on Ca²⁺ release from IP3-sensitive stores and calcium/calmodulin kinase II phosphorylation of the alpha1 subunit EF hand. *J Neurosci*, *26*(23), 6259-6268. <https://doi.org/10.1523/JNEUROSCI.0481-06.2006>

- Garcia-Donaire, J. S., C. Cerezo, L.M. Ruilope. (2008). Calcium channel blockers and cardiovascular protection. *European Society of Cardiology*, 6(21).
- Garcia-Palomero, E., Renart, J., Andres-Mateos, E., Solis-Garrido, L. M., Matute, C., Herrero, C. J., Garcia, A. G., & Montiel, C. (2001). Differential expression of calcium channel subtypes in the bovine adrenal medulla. *Neuroendocrinology*, 74(4), 251-261. <https://doi.org/10.1159/000054692>
- Garcia, J., Nakai, J., Imoto, K., & Beam, K. G. (1997). Role of S4 segments and the leucine heptad motif in the activation of an L-type calcium channel. *Biophys J*, 72(6), 2515-2523. [https://doi.org/10.1016/S0006-3495\(97\)78896-9](https://doi.org/10.1016/S0006-3495(97)78896-9)
- Grabner, M., Dirksen, R. T., Suda, N., & Beam, K. G. (1999). The II-III loop of the skeletal muscle dihydropyridine receptor is responsible for the Bi-directional coupling with the ryanodine receptor. *J Biol Chem*, 274(31), 21913-21919. <https://www.ncbi.nlm.nih.gov/pubmed/10419512>
- Graham, F. L., & van der Eb, A. J. (1973). A new technique for the assay of infectivity of human adenovirus 5 DNA. *Virology*, 52(2), 456-467. [https://doi.org/10.1016/0042-6822\(73\)90341-3](https://doi.org/10.1016/0042-6822(73)90341-3)
- Guzman, J. N., Sanchez-Padilla, J., Chan, C. S., & Surmeier, D. J. (2009). Robust pacemaking in substantia nigra dopaminergic neurons. *J Neurosci*, 29(35), 11011-11019. <https://doi.org/10.1523/JNEUROSCI.2519-09.2009>
- Hamill, O. P., Marty, A., Neher, E., Sakmann, B., & Sigworth, F. J. (1981). Improved patch-clamp techniques for high-resolution current recording from cells and cell-free membrane patches. *Pflugers Arch*, 391(2), 85-100. <https://doi.org/10.1007/BF00656997>
- Hao, L. Y., Xu, J. J., Minobe, E., Kameyama, A., & Kameyama, M. (2008). Calmodulin kinase II activation is required for the maintenance of basal activity of L-type Ca²⁺ channels in guinea-pig ventricular myocytes. *J Pharmacol Sci*, 108(3), 290-300. <https://doi.org/10.1254/jphs.08101fp>
- Heerwig, A., Kick, A., Sommerfeld, P., Eimermacher, S., Hartung, F., Laube, M., Fischer, D., Pietzsch, H. J., Pietzsch, J., Loser, R., Mertig, M., Pietsch, M., & Wodtke, R. (2023). The Impact of N(epsilon)-Acryloyllysine Piperazides on the Conformational Dynamics of Transglutaminase 2. *Int J Mol Sci*, 24(2). <https://doi.org/10.3390/ijms24021650>
- Hell, J. W., Westenbroek, R. E., Warner, C., Ahlijanian, M. K., Prystay, W., Gilbert, M. M., Snutch, T. P., & Catterall, W. A. (1993). Identification and differential subcellular localization of the neuronal class C and class D L-type calcium channel alpha 1 subunits. *J Cell Biol*, 123(4), 949-962. <https://doi.org/10.1083/jcb.123.4.949>
- Helton, T. D., Xu, W., & Lipscombe, D. (2005). Neuronal L-type calcium channels open quickly and are inhibited slowly. *J Neurosci*, 25(44), 10247-10251. <https://doi.org/10.1523/JNEUROSCI.1089-05.2005>
- Hering, S., Zangerl-Plessl, E. M., Beyl, S., Hohaus, A., Andranovits, S., & Timin, E. N. (2018). Calcium channel gating. *Pflugers Arch*, 470(9), 1291-1309. <https://doi.org/10.1007/s00424-018-2163-7>
- Herzig, S., Patil, P., Neumann, J., Staschen, C. M., & Yue, D. T. (1993). Mechanisms of beta-adrenergic stimulation of cardiac Ca²⁺ channels revealed by discrete-time Markov analysis of slow gating. *Biophys J*, 65(4), 1599-1612. [https://doi.org/10.1016/S0006-3495\(93\)81199-8](https://doi.org/10.1016/S0006-3495(93)81199-8)

- Herzig, S., Khan, I. F., Grundemann, D., Matthes, J., Ludwig, A., Michels, G., Hoppe, U. C., Chaudhuri, D., Schwartz, A., Yue, D. T., & Hullin, R. (2007). Mechanism of Ca(v)1.2 channel modulation by the amino terminus of cardiac beta2-subunits. *FASEB J*, *21*(7), 1527-1538. <https://doi.org/10.1096/fj.06-7377com>
- Hess, P., Lansman, J. B., & Tsien, R. W. (1984). Different modes of Ca channel gating behaviour favoured by dihydropyridine Ca agonists and antagonists. *Nature*, *311*(5986), 538-544. <https://doi.org/10.1038/311538a0>
- Hille, B. (2001). *Ion Channels of Excitable Membranes* (Vol. Third Edition). Sinauer Associates.
- Hill, C. L., & Stephens, G. J. (2021). An Introduction to Patch Clamp Recording. In M. Dallas & D. Bell (Eds.), *Patch Clamp Electrophysiology: Methods and Protocols* (pp. 1-19). Springer US. https://doi.org/10.1007/978-1-0716-0818-0_1
- Hirtz, J. J., Braun, N., Griesemer, D., Hannes, C., Janz, K., Lohrke, S., Muller, B., & Friauf, E. (2012). Synaptic refinement of an inhibitory topographic map in the auditory brainstem requires functional Cav1.3 calcium channels. *J Neurosci*, *32*(42), 14602-14616. <https://doi.org/10.1523/JNEUROSCI.0765-12.2012>
- Hoda, J. C., Zaghetto, F., Koschak, A., & Striessnig, J. (2005). Congenital stationary night blindness type 2 mutations S229P, G369D, L1068P, and W1440X alter channel gating or functional expression of Ca(v)1.4 L-type Ca²⁺ channels. *J Neurosci*, *25*(1), 252-259. <https://doi.org/10.1523/JNEUROSCI.3054-04.2005>
- Hodgkin, A. L., & Huxley, A. F. (1952). The components of membrane conductance in the giant axon of Loligo. *J Physiol*, *116*(4), 473-496. <https://doi.org/10.1113/jphysiol.1952.sp004718>
- Hofer, N. T., Tuluc, P., Ortner, N. J., Nikonishyna, Y. V., Fernandes-Quintero, M. L., Liedl, K. R., Flucher, B. E., Cox, H., & Striessnig, J. (2020). Biophysical classification of a CACNA1D de novo mutation as a high-risk mutation for a severe neurodevelopmental disorder. *Mol Autism*, *11*(1), 4. <https://doi.org/10.1186/s13229-019-0310-4>
- Hofmann, F., Lacinova, L., & Klugbauer, N. (1999). Voltage-dependent calcium channels: from structure to function. *Rev Physiol Biochem Pharmacol*, *139*, 33-87. <https://doi.org/10.1007/BFb0033648>
- Huang, H., Ng, C. Y., Yu, D., Zhai, J., Lam, Y., & Soong, T. W. (2014). Modest CaV1.342-selective inhibition by compound 8 is beta-subunit dependent. *Nat Commun*, *5*, 4481. <https://doi.org/10.1038/ncomms5481>
- Huang, H., Hu, Z., Yeow, S. Q. Z., & Soong, T. W. (2022). Splicing and Editing to Fine-Tune Activity of High Voltage-Activated Calcium Channels. In G. W. Zamponi & N. Weiss (Eds.), *Voltage-Gated Calcium Channels* (pp. 47-72). Springer International Publishing. https://doi.org/10.1007/978-3-031-08881-0_3
- Hullin, R., Khan, I. F., Wirtz, S., Mohacsi, P., Varadi, G., Schwartz, A., & Herzig, S. (2003). Cardiac L-type calcium channel beta-subunits expressed in human heart have differential effects on single channel characteristics. *J Biol Chem*, *278*(24), 21623-21630. <https://doi.org/10.1074/jbc.M211164200>

- Hung, A. Y., Futai, K., Sala, C., Valtschanoff, J. G., Ryu, J., Woodworth, M. A., Kidd, F. L., Sung, C. C., Miyakawa, T., Bear, M. F., Weinberg, R. J., & Sheng, M. (2008). Smaller dendritic spines, weaker synaptic transmission, but enhanced spatial learning in mice lacking Shank1. *J Neurosci*, *28*(7), 1697-1708. <https://doi.org/10.1523/JNEUROSCI.3032-07.2008>
- Hurley, M. J., Brandon, B., Gentleman, S. M., & Dexter, D. T. (2013). Parkinson's disease is associated with altered expression of CaV1 channels and calcium-binding proteins. *Brain*, *136*(Pt 7), 2077-2097. <https://doi.org/10.1093/brain/awt134>
- Imredy, J. P., & Yue, D. T. (1994). Mechanism of Ca(2+)-sensitive inactivation of L-type Ca²⁺ channels. *Neuron*, *12*(6), 1301-1318. [https://doi.org/10.1016/0896-6273\(94\)90446-4](https://doi.org/10.1016/0896-6273(94)90446-4)
- Ismailov, II, & Benos, D. J. (1995). Effects of phosphorylation on ion channel function. *Kidney Int*, *48*(4), 1167-1179. <https://doi.org/10.1038/ki.1995.400>
- Jangsangthong, W., Kuzmenkina, E., Khan, I. F., Matthes, J., Hullin, R., & Herzig, S. (2010). Inactivation of L-type calcium channels is determined by the length of the N terminus of mutant beta(1) subunits. *Pflugers Arch*, *459*(3), 399-411. <https://doi.org/10.1007/s00424-009-0738-z>
- Johnson, B. A., Javors, M. A., Lam, Y. W., Wells, L. T., Tiouririne, M., Roache, J. D., Ait-Daoud, N., & Lawson, K. (2005). Kinetic and cardiovascular comparison of immediate-release isradipine and sustained-release isradipine among non-treatment-seeking, cocaine-dependent individuals. *Prog Neuropsychopharmacol Biol Psychiatry*, *29*(1), 15-20. <https://doi.org/10.1016/j.pnpbp.2004.08.014>
- Jurkat-Rott, K., & Lehmann-Horn, F. (2004). The impact of splice isoforms on voltage-gated calcium channel alpha1 subunits. *J Physiol*, *554*(Pt 3), 609-619. <https://doi.org/10.1113/jphysiol.2003.052712>
- Kang, M. G., & Campbell, K. P. (2003). Gamma subunit of voltage-activated calcium channels. *J Biol Chem*, *278*(24), 21315-21318. <https://doi.org/10.1074/jbc.R300004200>
- Kang, S., Cooper, G., Dunne, S. F., Dusel, B., Luan, C. H., Surmeier, D. J., & Silverman, R. B. (2012). CaV1.3-selective L-type calcium channel antagonists as potential new therapeutics for Parkinson's disease. *Nat Commun*, *3*, 1146. <https://doi.org/10.1038/ncomms2149>
- Karmazinova, M., & Lacinova, L. (2010). Measurement of cellular excitability by whole cell patch clamp technique. *Physiol Res*, *59* Suppl 1, S1-S7. <https://doi.org/10.33549/physiolres.932000>
- Kim, E. Y., Rumpf, C. H., Fujiwara, Y., Cooley, E. S., Van Petegem, F., & Minor, D. L., Jr. (2008). Structures of CaV2 Ca²⁺/CaM-IQ domain complexes reveal binding modes that underlie calcium-dependent inactivation and facilitation. *Structure*, *16*(10), 1455-1467. <https://doi.org/10.1016/j.str.2008.07.010>
- Kim, J., Ghosh, S., Nunziato, D. A., & Pitt, G. S. (2004). Identification of the components controlling inactivation of voltage-gated Ca²⁺ channels. *Neuron*, *41*(5), 745-754. [https://doi.org/10.1016/S0896-6273\(04\)00081-9](https://doi.org/10.1016/S0896-6273(04)00081-9)
- Kim, S., & Rhim, H. (2011). Effects of amyloid-beta peptides on voltage-gated L-type Ca(V)1.2 and Ca(V)1.3 Ca(2+) channels. *Mol Cells*, *32*(3), 289-294. <https://doi.org/10.1007/s10059-011-0075-x>

- Klabunde, R. (2016). Cardiovascular Physiology Concepts. www.cvphysiology.com, Richard E. Klabunde. <https://www.cvphysiology.com/Arrhythmias/SAN%20action%20potl.gif>
- Koch, P., Herzig, S., & Matthes, J. (2016). An expert protocol for immunofluorescent detection of calcium channels in tsA-201 cells. *J Pharmacol Toxicol Methods*, 82, 20-25. <https://doi.org/10.1016/j.vascn.2016.07.001>
- Koh et al., N. S., Zhai J, Tuck Wah Soong. (2021). *Neuronal L-type calcium channels in aging*. Academic Press. <https://doi.org/10.1016/B978-0-12-817990-1.00019-6>
- Koschak, A., Reimer, D., Huber, I., Grabner, M., Glossmann, H., Engel, J., & Striessnig, J. (2001). alpha 1D (Cav1.3) subunits can form l-type Ca²⁺ channels activating at negative voltages. *J Biol Chem*, 276(25), 22100-22106. <https://doi.org/10.1074/jbc.M101469200>
- Koschak, A., Obermair, G. J., Pivotto, F., Sinnegger-Brauns, M. J., Striessnig, J., & Pietrobon, D. (2007). Molecular nature of anomalous L-type calcium channels in mouse cerebellar granule cells. *J Neurosci*, 27(14), 3855-3863. <https://doi.org/10.1523/JNEUROSCI.4028-06.2007>
- Kuzmenkina, E., Novikova, E., Jangsangthong, W., Matthes, J., & Herzig, S. (2019). Single-Channel Resolution of the Interaction between C-Terminal Ca(V)1.3 Isoforms and Calmodulin. *Biophys J*, 116(5), 836-846. <https://doi.org/10.1016/j.bpj.2019.01.025>
- Labster, T. (2018). The cardiac conducting system. In theory.labster.com/: Labster Theory. https://labster-image-manager.s3.amazonaws.com/77d9ff3c-cccf-4ae3-b7da-d612a7f7c395/6_CAM_Pacemaker2.en.x512.png
- Lauven, M., Handrock, R., Muller, A., Hofmann, F., & Herzig, S. (1999). Interaction of three structurally distinct Ca²⁺ channel activators with single L-type Ca²⁺ channels. *Naunyn Schmiedeberg's Arch Pharmacol*, 360(2), 122-128. <https://doi.org/10.1007/s002109900059>
- Lee, A., Wong, S. T., Gallagher, D., Li, B., Storm, D. R., Scheuer, T., & Catterall, W. A. (1999). Ca²⁺/calmodulin binds to and modulates P/Q-type calcium channels. *Nature*, 399(6732), 155-159. <https://doi.org/10.1038/20194>
- Lemke, T., Welling, A., Christel, C. J., Blaich, A., Bernhard, D., Lenhardt, P., Hofmann, F., & Moosmang, S. (2008). Unchanged beta-adrenergic stimulation of cardiac L-type calcium channels in Ca v 1.2 phosphorylation site S1928A mutant mice. *J Biol Chem*, 283(50), 34738-34744. <https://doi.org/10.1074/jbc.M804981200>
- Lieb, A., Scharinger, A., Sartori, S., Sinnegger-Brauns, M. J., & Striessnig, J. (2012). Structural determinants of CaV1.3 L-type calcium channel gating. *Channels (Austin)*, 6(3), 197-205. <https://doi.org/10.4161/chan.21002>
- Liljelund, P., Netzeband, J. G., & Gruol, D. L. (2000). L-Type calcium channels mediate calcium oscillations in early postnatal Purkinje neurons. *J Neurosci*, 20(19), 7394-7403. <https://doi.org/10.1523/JNEUROSCI.20-19-07394.2000>
- Limpitikul, W. B., Dick, I. E., Ben-Johny, M., & Yue, D. T. (2016). An autism-associated mutation in CaV1.3 channels has opposing effects on voltage- and Ca(2+)-dependent regulation. *Sci Rep*, 6, 27235. <https://doi.org/10.1038/srep27235>

- Limpitikul, W. B., Dick, I. E., Tester, D. J., Boczek, N. J., Limphong, P., Yang, W., Choi, M. H., Babich, J., DiSilvestre, D., Kanter, R. J., Tomaselli, G. F., Ackerman, M. J., & Yue, D. T. (2017). A Precision Medicine Approach to the Rescue of Function on Malignant Calmodulinopathic Long-QT Syndrome. *Circ Res*, *120*(1), 39-48. <https://doi.org/10.1161/CIRCRESAHA.116.309283>
- Liu, X., Yang, P. S., Yang, W., & Yue, D. T. (2010). Enzyme-inhibitor-like tuning of Ca(2+) channel connectivity with calmodulin. *Nature*, *463*(7283), 968-972. <https://doi.org/10.1038/nature08766>
- Llinas, R., & Yarom, Y. (1981). Properties and distribution of ionic conductances generating electroresponsiveness of mammalian inferior olivary neurones in vitro. *J Physiol*, *315*, 569-584. <https://doi.org/10.1113/jphysiol.1981.sp013764>
- Llinas, R., Sugimori, M., Lin, J. W., & Cherksey, B. (1989). Blocking and isolation of a calcium channel from neurons in mammals and cephalopods utilizing a toxin fraction (FTX) from funnel-web spider poison. *Proc Natl Acad Sci U S A*, *86*(5), 1689-1693. <https://doi.org/10.1073/pnas.86.5.1689>
- Loya-Lopez, S., Sandoval, A., Gonzalez-Ramirez, R., Calderon-Rivera, A., Avalos-Fuentes, A., Rodriguez-Sanchez, M., Caballero, R., Tovar-Soto, D., Felix, R., & Floran, B. (2020). Cdk5 phosphorylates Ca(V)1.3 channels and regulates GABA(A)-mediated miniature inhibitory post-synaptic currents in striato-nigral terminals. *Biochem Biophys Res Commun*, *524*(1), 255-261. <https://doi.org/10.1016/j.bbrc.2020.01.084>
- Mangoni, M. E., Couette, B., Bourinet, E., Platzer, J., Reimer, D., Striessnig, J., & Nargeot, J. (2003). Functional role of L-type Cav1.3 Ca²⁺ channels in cardiac pacemaker activity. *Proc Natl Acad Sci U S A*, *100*(9), 5543-5548. <https://doi.org/10.1073/pnas.0935295100>
- Martin-Aragon Baudel, M., Flores-Tamez, V. A., Hong, J., Reddy, G. R., Maillard, P., Burns, A. E., Man, K. N. M., Sasse, K. C., Ward, S. M., Catterall, W. A., Bers, D. M., Hell, J. W., Nieves-Cintrón, M., & Navedo, M. F. (2022). Spatiotemporal Control of Vascular Ca(V)1.2 by alpha1(C) S1928 Phosphorylation. *Circ Res*, *131*(12), 1018-1033. <https://doi.org/10.1161/CIRCRESAHA.122.321479>
- Martinez-Rivera, A., Hao, J., Rice, R., Inturrisi, C. E., & Rajadhyaksha, A. M. (2023). Ca(v)1.3 L-type Ca(2+) channel-activated CaMKII/ERK2 pathway in the ventral tegmental area is required for cocaine conditioned place preference. *Neuropharmacology*, *224*, 109368. <https://doi.org/10.1016/j.neuropharm.2022.109368>
- Marx, S.O. and Kushnir, A. (2018). Voltage-Gated Calcium Channels. In J. J. Douglas P. Zipes, William G. Stevenson (Ed.), *Cardiac Electrophysiology: From Cell to Bedside* (Vol. 7, pp. 12-24). Elsevier. <https://doi.org/10.1016/B978-0-323-44733-1.00002-X>
- Matthes, J., Yildirim, L., Wietzorrek, G., Reimer, D., Striessnig, J., & Herzig, S. (2004). Disturbed atrio-ventricular conduction and normal contractile function in isolated hearts from Cav1.3-knockout mice. *Naunyn Schmiedebergs Arch Pharmacol*, *369*(6), 554-562. <https://doi.org/10.1007/s00210-004-0940-7>
- Matthes, J., & Herzig, S. (2010). Less is more, or enough is enough? Ca(2+)-dependent inactivation revisited. *J Physiol*, *588*(Pt 1), 15-16. <https://doi.org/10.1113/jphysiol.2009.184846>
- McKinney, B. C., Sze, W., Lee, B., & Murphy, G. G. (2009). Impaired long-term potentiation and enhanced neuronal excitability in the amygdala of Ca(V)1.3 knockout mice. *Neurobiol Learn Mem*, *92*(4), 519-528. <https://doi.org/10.1016/j.nlm.2009.06.012>

- Mercado, J., Baylie, R., Navedo, M. F., Yuan, C., Scott, J. D., Nelson, M. T., Brayden, J. E., & Santana, L. F. (2014). Local control of TRPV4 channels by AKAP150-targeted PKC in arterial smooth muscle. *J Gen Physiol*, *143*(5), 559-575. <https://doi.org/10.1085/jgp.201311050>
- Michels, G., Matthes, J., Handrock, R., Kuchinke, U., Groner, F., Cribbs, L. L., Pereverzev, A., Schneider, T., Perez-Reyes, E., & Herzig, S. (2002). Single-channel pharmacology of mibefradil in human native T-type and recombinant Ca(v)3.2 calcium channels. *Mol Pharmacol*, *61*(3), 682-694. <https://doi.org/10.1124/mol.61.3.682>
- Michna, M., Knirsch, M., Hoda, J. C., Muenkner, S., Langer, P., Platzer, J., Striessnig, J., & Engel, J. (2003). Cav1.3 (alpha1D) Ca²⁺ currents in neonatal outer hair cells of mice. *J Physiol*, *553*(Pt 3), 747-758. <https://doi.org/10.1113/jphysiol.2003.053256>
- Moosmang, H. (2009). Cav1.3 Voltage-Gated Calcium Channel. In F. H. S. Moosmang, S.J. Enna, D.B. Bylund (Ed.), *xPharm: The Comprehensive Pharmacology Reference* (pp. 1-5). Elsevier. <https://doi.org/10.1016/B978-008055232-3.60396-4>
- Moreno, C. M., Dixon, R. E., Tajada, S., Yuan, C., Opitez-Araya, X., Binder, M. D., & Santana, L. F. (2016). Ca²⁺ entry into neurons is facilitated by cooperative gating of clustered CaV1.3 channels. *Elife*, *5*. <https://doi.org/10.7554/eLife.15744>
- Morgenstern, T. J., Park, J., Fan, Q. R., & Colecraft, H. M. (2019). A potent voltage-gated calcium channel inhibitor engineered from a nanobody targeted to auxiliary Ca(V)beta subunits. *Elife*, *8*. <https://doi.org/10.7554/eLife.49253>
- Morgenstern, T. J., & Colecraft, H. M. (2021). Controlling ion channel trafficking by targeted ubiquitination and deubiquitination. *Methods Enzymol*, *654*, 139-167. <https://doi.org/10.1016/bs.mie.2021.03.007>
- Morgenstern, T. J., Nirwan, N., Hernandez-Ochoa, E. O., Bibollet, H., Choudhury, P., Laloudakis, Y. D., Ben Johnny, M., Bannister, R. A., Schneider, M. F., Minor, D. L., Jr., & Colecraft, H. M. (2022). Selective posttranslational inhibition of Ca(V)beta(1)-associated voltage-dependent calcium channels with a functionalized nanobody. *Nat Commun*, *13*(1), 7556. <https://doi.org/10.1038/s41467-022-35025-7>
- Mori, Y., Friedrich, T., Kim, M. S., Mikami, A., Nakai, J., Ruth, P., Bosse, E., Hofmann, F., Flockerzi, V., Furuichi, T., & et al. (1991). Primary structure and functional expression from complementary DNA of a brain calcium channel. *Nature*, *350*(6317), 398-402. <https://doi.org/10.1038/350398a0>
- Morrill, J. A., & Cannon, S. C. (1999). Effects of mutations causing hypokalaemic periodic paralysis on the skeletal muscle L-type Ca²⁺ channel expressed in *Xenopus laevis* oocytes. *J Physiol*, *520 Pt 2*, 321-336. <https://doi.org/10.1111/j.1469-7793.1999.00321.x>
- Mosharov, E. V., Larsen, K. E., Kanter, E., Phillips, K. A., Wilson, K., Schmitz, Y., Krantz, D. E., Kobayashi, K., Edwards, R. H., & Sulzer, D. (2009). Interplay between cytosolic dopamine, calcium, and alpha-synuclein causes selective death of substantia nigra neurons. *Neuron*, *62*(2), 218-229. <https://doi.org/10.1016/j.neuron.2009.01.033>
- Nagasamy Venkatesh, D., Meyyanathan, S. N., Shanmugam, R., Kamatham, S. S., Campos, J. R., Dias-Ferreira, J., Sanchez-Lopez, E., Cardoso, J. C., Severino, P., & Souto, E. B. (2021). Physicochemical, pharmacokinetic, and pharmacodynamic characterization of isradipine tablets for controlled release. *Pharm Dev Technol*, *26*(1), 92-100. <https://doi.org/10.1080/10837450.2020.1839495>

- Namkung, Y., Skrypnik, N., Jeong, M. J., Lee, T., Lee, M. S., Kim, H. L., Chin, H., Suh, P. G., Kim, S. S., & Shin, H. S. (2001). Requirement for the L-type Ca²⁺ channel alpha(1D) subunit in postnatal pancreatic beta cell generation. *J Clin Invest*, 108(7), 1015-1022. <https://doi.org/10.1172/JCI13310>
- Navedo, M. F., Cheng, E. P., Yuan, C., Votaw, S., Molkentin, J. D., Scott, J. D., & Santana, L. F. (2010). Increased coupled gating of L-type Ca²⁺ channels during hypertension and Timothy syndrome. *Circ Res*, 106(4), 748-756. <https://doi.org/10.1161/CIRCRESAHA.109.213363>
- Neely, A., Wei, X., Olcese, R., Birnbaumer, L., & Stefani, E. (1993). Potentiation by the beta subunit of the ratio of the ionic current to the charge movement in the cardiac calcium channel. *Science*, 262(5133), 575-578. <https://www.ncbi.nlm.nih.gov/pubmed/8211185>
- Neher, E., & Sakmann, B. (1976). Noise analysis of drug induced voltage clamp currents in denervated frog muscle fibres. *J Physiol*, 258(3), 705-729. <https://doi.org/10.1113/jphysiol.1976.sp011442>
- Neher, E., Sakmann, B., & Steinbach, J. H. (1978). The extracellular patch clamp: a method for resolving currents through individual open channels in biological membranes. *Pflugers Arch*, 375(2), 219-228. <https://doi.org/10.1007/BF00584247>
- Noble et al., D. D., Denyer JC. (1989). Ionic mechanisms in normal and abnormal cardiac pacemaker activity. In J. JW (Ed.), *Neuronal and cellular oscillators* (pp. 59-85). Marcel Dekker, New York.
- Nystoriak, M. A., Nieves-Cintrón, M., Patriarchi, T., Buonarati, O. R., Prada, M. P., Morotti, S., Grandi, E., Fernandes, J. D., Forbush, K., Hofmann, F., Sasse, K. C., Scott, J. D., Ward, S. M., Hell, J. W., & Navedo, M. F. (2017). Ser1928 phosphorylation by PKA stimulates the L-type Ca²⁺ channel CaV1.2 and vasoconstriction during acute hyperglycemia and diabetes. *Sci Signal*, 10(463). <https://doi.org/10.1126/scisignal.aaf9647>
- Obermair, G. J., Szabo, Z., Bourinet, E., & Flucher, B. E. (2004). Differential targeting of the L-type Ca²⁺ channel alpha 1C (CaV1.2) to synaptic and extrasynaptic compartments in hippocampal neurons. *Eur J Neurosci*, 19(8), 2109-2122. <https://doi.org/10.1111/j.0953-816X.2004.03272.x>
- Ogden, D. a. S., P. (1994). Patch clamp techniques for single channel and whole-cell recording. In *Plymouth workshop handbook* (2 ed.). Company of Biologists Limited.
- Olson, P. A., Tkatch, T., Hernandez-Lopez, S., Ulrich, S., Ilijic, E., Mugnaini, E., Zhang, H., Bezprozvanny, I., & Surmeier, D. J. (2005). G-protein-coupled receptor modulation of striatal CaV1.3 L-type Ca²⁺ channels is dependent on a Shank-binding domain. *J Neurosci*, 25(5), 1050-1062. <https://doi.org/10.1523/JNEUROSCI.3327-04.2005>
- Omata, K., Anand, S. K., Hovelson, D. H., Liu, C. J., Yamazaki, Y., Nakamura, Y., Ito, S., Satoh, F., Sasano, H., Rainey, W. E., & Tomlins, S. A. (2017). Aldosterone-Producing Cell Clusters Frequently Harbor Somatic Mutations and Accumulate With Age in Normal Adrenals. *J Endocr Soc*, 1(7), 787-799. <https://doi.org/10.1210/js.2017-00134>
- Ortner, N. J., Bock, G., Vandael, D. H., Mauersberger, R., Draheim, H. J., Gust, R., Carbone, E., Tuluc, P., & Striessnig, J. (2014). Pyrimidine-2,4,6-triones are a new class of voltage-gated L-type Ca²⁺ channel activators. *Nat Commun*, 5, 3897. <https://doi.org/10.1038/ncomms4897>
- Ortner, N. J., Bock, G., Dougalis, A., Kharitonova, M., Duda, J., Hess, S., Tuluc, P., Pomberger, T., Stefanova, N., Pitterl, F., Ciossek, T., Oberacher, H., Draheim, H. J., Kloppenburg, P., Liss, B.,

- & Striessnig, J. (2017). Lower Affinity of Isradipine for L-Type Ca(2+) Channels during Substantia Nigra Dopamine Neuron-Like Activity: Implications for Neuroprotection in Parkinson's Disease. *J Neurosci*, 37(28), 6761-6777. <https://doi.org/10.1523/JNEUROSCI.2946-16.2017>
- Ortner, N. J., Kaserer, T., Copeland, J. N., & Striessnig, J. (2020). De novo CACNA1D Ca(2+) channelopathies: clinical phenotypes and molecular mechanism. *Pflugers Arch*, 472(7), 755-773. <https://doi.org/10.1007/s00424-020-02418-w>
- Parkinson Study Group, S.-P. D. I. I. I. I. (2020). Isradipine Versus Placebo in Early Parkinson Disease: A Randomized Trial. *Ann Intern Med*, 172(9), 591-598. <https://doi.org/10.7326/M19-2534>
- Patriarchi, T., Qian, H., Di Biase, V., Malik, Z. A., Chowdhury, D., Price, J. L., Hammes, E. A., Buonarati, O. R., Westenbroek, R. E., Catterall, W. A., Hofmann, F., Xiang, Y. K., Murphy, G. G., Chen, C. Y., Navedo, M. F., & Hell, J. W. (2016). Phosphorylation of Cav1.2 on S1928 uncouples the L-type Ca²⁺ channel from the beta2 adrenergic receptor. *EMBO J*, 35(12), 1330-1345. <https://doi.org/10.15252/emj.201593409>
- Pellicena, P., & Schulman, H. (2014). CaMKII inhibitors: from research tools to therapeutic agents. *Front Pharmacol*, 5, 21. <https://doi.org/10.3389/fphar.2014.00021>
- Perez-Reyes, E. (2003). Molecular physiology of low-voltage-activated t-type calcium channels. *Physiol Rev*, 83(1), 117-161. <https://doi.org/10.1152/physrev.00018.2002>
- Peterson, B. Z., DeMaria, C. D., Adelman, J. P., & Yue, D. T. (1999). Calmodulin is the Ca²⁺ sensor for Ca²⁺ -dependent inactivation of L-type calcium channels. *Neuron*, 22(3), 549-558. [https://doi.org/10.1016/S0896-6273\(00\)80709-6](https://doi.org/10.1016/S0896-6273(00)80709-6)
- Peterson, B. Z., Lee, J. S., Mulle, J. G., Wang, Y., de Leon, M., & Yue, D. T. (2000). Critical determinants of Ca(2+)-dependent inactivation within an EF-hand motif of L-type Ca(2+) channels. *Biophys J*, 78(4), 1906-1920. [https://doi.org/10.1016/S0006-3495\(00\)76739-7](https://doi.org/10.1016/S0006-3495(00)76739-7)
- Pinggera, A., Lieb, A., Benedetti, B., Lampert, M., Monteleone, S., Liedl, K. R., Tuluc, P., & Striessnig, J. (2015). CACNA1D de novo mutations in autism spectrum disorders activate Cav1.3 L-type calcium channels. *Biol Psychiatry*, 77(9), 816-822. <https://doi.org/10.1016/j.biopsych.2014.11.020>
- Pinggera, A., Mackenroth, L., Rump, A., Schallner, J., Beleggia, F., Wollnik, B., & Striessnig, J. (2017). New gain-of-function mutation shows CACNA1D as recurrently mutated gene in autism spectrum disorders and epilepsy. *Hum Mol Genet*, 26(15), 2923-2932. <https://doi.org/10.1093/hmg/ddx175>
- Pinggera, A., Negro, G., Tuluc, P., Brown, M. J., Lieb, A., & Striessnig, J. (2018). Gating defects of disease-causing de novo mutations in Ca(v)1.3 Ca(2+) channels. *Channels (Austin)*, 12(1), 388-402. <https://doi.org/10.1080/19336950.2018.1546518>
- Platzer, J., Engel, J., Schrott-Fischer, A., Stephan, K., Bova, S., Chen, H., Zheng, H., & Striessnig, J. (2000). Congenital deafness and sinoatrial node dysfunction in mice lacking class D L-type Ca²⁺ channels. *Cell*, 102(1), 89-97. [https://doi.org/10.1016/S0092-8674\(00\)00013-1](https://doi.org/10.1016/S0092-8674(00)00013-1)
- Pragnell, M., De Waard, M., Mori, Y., Tanabe, T., Snutch, T. P., & Campbell, K. P. (1994). Calcium channel beta-subunit binds to a conserved motif in the I-II cytoplasmic linker of the alpha 1-subunit. *Nature*, 368(6466), 67-70. <https://doi.org/10.1038/368067a0>

- Putzier, I., Kullmann, P. H., Horn, J. P., & Levitan, E. S. (2009). Cav1.3 channel voltage dependence, not Ca²⁺ selectivity, drives pacemaker activity and amplifies bursts in nigral dopamine neurons. *J Neurosci*, 29(49), 15414-15419. <https://doi.org/10.1523/JNEUROSCI.4742-09.2009>
- Qian, H., Patriarchi, T., Price, J. L., Matt, L., Lee, B., Nieves-Cintrón, M., Buonarati, O. R., Chowdhury, D., Nanou, E., Nystoriak, M. A., Catterall, W. A., Poomvanicha, M., Hofmann, F., Navedo, M. F., & Hell, J. W. (2017). Phosphorylation of Ser1928 mediates the enhanced activity of the L-type Ca²⁺ channel Cav1.2 by the beta2-adrenergic receptor in neurons. *Sci Signal*, 10(463). <https://doi.org/10.1126/scisignal.aaf9659>
- Qu, Y., Baroudi, G., Yue, Y., El-Sherif, N., & Boutjdir, M. (2005). Localization and modulation of alpha1D (Cav1.3) L-type Ca channel by protein kinase A. *Am J Physiol Heart Circ Physiol*, 288(5), H2123-2130. <https://doi.org/10.1152/ajpheart.01023.2004>
- Ramadan, O., Qu, Y., Wadgaonkar, R., Baroudi, G., Karnabi, E., Chahine, M., & Boutjdir, M. (2009). Phosphorylation of the consensus sites of protein kinase A on alpha1D L-type calcium channel. *J Biol Chem*, 284(8), 5042-5049. <https://doi.org/10.1074/jbc.M809132200>
- Randall, A., & Tsien, R. W. (1995). Pharmacological dissection of multiple types of Ca²⁺ channel currents in rat cerebellar granule neurons. *J Neurosci*, 15(4), 2995-3012. <https://doi.org/10.1523/JNEUROSCI.15-04-02995.1995>
- Reuter, H. (1967). The dependence of slow inward current in Purkinje fibres on the extracellular calcium-concentration. *J Physiol*, 192(2), 479-492. <https://doi.org/10.1113/jphysiol.1967.sp008310>
- Rhoads, A. R., & Friedberg, F. (1997). Sequence motifs for calmodulin recognition. *FASEB J*, 11(5), 331-340. <https://doi.org/10.1096/fasebj.11.5.9141499>
- Rios, E., Pizarro, G., & Stefani, E. (1992). Charge movement and the nature of signal transduction in skeletal muscle excitation-contraction coupling. *Annu Rev Physiol*, 54, 109-133. <https://doi.org/10.1146/annurev.ph.54.030192.000545>
- Rosholm, K. R., Boddum, K., & Lindquist, A. (2021). Perforated Whole-Cell Recordings in Automated Patch Clamp Electrophysiology. In M. Dallas & D. Bell (Eds.), *Patch Clamp Electrophysiology: Methods and Protocols* (pp. 93-108). Springer US. https://doi.org/10.1007/978-1-0716-0818-0_5
- Sahu, G., Asmara, H., Zhang, F. X., Zamponi, G. W., & Turner, R. W. (2017). Activity-Dependent Facilitation of Ca(V)1.3 Calcium Channels Promotes KCa3.1 Activation in Hippocampal Neurons. *J Neurosci*, 37(46), 11255-11270. <https://doi.org/10.1523/JNEUROSCI.0967-17.2017>
- Sala, C., Piech, V., Wilson, N. R., Passafaro, M., Liu, G., & Sheng, M. (2001). Regulation of dendritic spine morphology and synaptic function by Shank and Homer. *Neuron*, 31(1), 115-130. [https://doi.org/10.1016/S0896-6273\(01\)00339-7](https://doi.org/10.1016/S0896-6273(01)00339-7)
- Sandoval, A., Duran, P., Gandini, M. A., Andrade, A., Almanza, A., Kaja, S., & Felix, R. (2017). Regulation of L-type Ca(V)1.3 channel activity and insulin secretion by the cGMP-PKG signaling pathway. *Cell Calcium*, 66, 1-9. <https://doi.org/10.1016/j.ceca.2017.05.008>
- Sang, L., Vieira, D. C. O., Yue, D. T., Ben-Johny, M., & Dick, I. E. (2021). The molecular basis of the inhibition of Ca(V)1 calcium-dependent inactivation by the distal carboxy tail. *J Biol Chem*, 296, 100502. <https://doi.org/10.1016/j.jbc.2021.100502>

- Scharinger, A., Eckrich, S., Vandael, D. H., Schonig, K., Koschak, A., Hecker, D., Kaur, G., Lee, A., Sah, A., Bartsch, D., Benedetti, B., Lieb, A., Schick, B., Singewald, N., Sinnegger-Brauns, M. J., Carbone, E., Engel, J., & Striessnig, J. (2015). Cell-type-specific tuning of Cav1.3 Ca²⁺-channels by a C-terminal automodulatory domain. *Front Cell Neurosci*, *9*, 309. <https://doi.org/10.3389/fncel.2015.00309>
- Schneider, T., Wei, X., Olcese, R., Costantin, J. L., Neely, A., Palade, P., Perez-Reyes, E., Qin, N., Zhou, J., Crawford, G. D., & et al. (1994). Molecular analysis and functional expression of the human type E neuronal Ca²⁺ channel alpha 1 subunit. *Receptors Channels*, *2*(4), 255-270. <https://www.ncbi.nlm.nih.gov/pubmed/7536609>
- Scholl, U. I., Goh, G., Stolting, G., de Oliveira, R. C., Choi, M., Overton, J. D., Fonseca, A. L., Korah, R., Starker, L. F., Kunstman, J. W., Prasad, M. L., Hartung, E. A., Mauras, N., Benson, M. R., Brady, T., Shapiro, J. R., Loring, E., Nelson-Williams, C., Libutti, S. K., . . . Lifton, R. P. (2013). Somatic and germline CACNA1D calcium channel mutations in aldosterone-producing adenomas and primary aldosteronism. *Nat Genet*, *45*(9), 1050-1054. <https://doi.org/10.1038/ng.2695>
- Schulla, V., Renstrom, E., Feil, R., Feil, S., Franklin, I., Gjinovci, A., Jing, X. J., Laux, D., Lundquist, I., Magnuson, M. A., Obermuller, S., Olofsson, C. S., Salehi, A., Wendt, A., Klugbauer, N., Wollheim, C. B., Rorsman, P., & Hofmann, F. (2003). Impaired insulin secretion and glucose tolerance in beta cell-selective Ca(v)1.2 Ca²⁺ channel null mice. *EMBO J*, *22*(15), 3844-3854. <https://doi.org/10.1093/emboj/cdg389>
- Seitter, H., & Koschak, A. (2018). Relevance of tissue specific subunit expression in channelopathies. *Neuropharmacology*, *132*, 58-70. <https://doi.org/10.1016/j.neuropharm.2017.06.029>
- Semenova, N. A., Ryzhkova, O. R., Strokova, T. V., & Taran, N. N. (2018). [The third case report a patient with primary aldosteronism, seizures, and neurologic abnormalities (PASNA) syndrome de novo variant mutations in the CACNA1D gene]. *Zh Nevrol Psikhiatr Im S S Korsakova*, *118*(12), 49-52. <https://doi.org/10.17116/jnevro201811812149>
- Shistik, E., Ivanina, T., Puri, T., Hosey, M., & Dascal, N. (1995). Ca²⁺ current enhancement by alpha 2/delta and beta subunits in Xenopus oocytes: contribution of changes in channel gating and alpha 1 protein level. *J Physiol*, *489* (Pt 1), 55-62. <https://doi.org/10.1113/jphysiol.1995.sp021029>
- Sigworth, F. J., & Sine, S. M. (1987). Data transformations for improved display and fitting of single-channel dwell time histograms. *Biophys J*, *52*(6), 1047-1054. [https://doi.org/10.1016/S0006-3495\(87\)83298-8](https://doi.org/10.1016/S0006-3495(87)83298-8)
- Sinden, R. R. (1994). Introduction to the Structure, Properties, and Reactions of DNA. In R. R. Sinden (Ed.), *DNA Structure and Function* (pp. 1-57). Academic Press.
- Singh, A., Hamedinger, D., Hoda, J. C., Gebhart, M., Koschak, A., Romanin, C., & Striessnig, J. (2006). C-terminal modulator controls Ca²⁺-dependent gating of Ca(v)1.4 L-type Ca²⁺ channels. *Nat Neurosci*, *9*(9), 1108-1116. <https://doi.org/10.1038/nn1751>
- Singh, A., Gebhart, M., Fritsch, R., Sinnegger-Brauns, M. J., Poggiani, C., Hoda, J. C., Engel, J., Romanin, C., Striessnig, J., & Koschak, A. (2008). Modulation of voltage- and Ca²⁺-dependent gating of CaV1.3 L-type calcium channels by alternative splicing of a C-terminal regulatory domain. *J Biol Chem*, *283*(30), 20733-20744. <https://doi.org/10.1074/jbc.M802254200>

- Splawski, I., Timothy, K. W., Sharpe, L. M., Decher, N., Kumar, P., Bloise, R., Napolitano, C., Schwartz, P. J., Joseph, R. M., Condouris, K., Tager-Flusberg, H., Priori, S. G., Sanguinetti, M. C., & Keating, M. T. (2004). Ca(V)1.2 calcium channel dysfunction causes a multisystem disorder including arrhythmia and autism. *Cell*, *119*(1), 19-31. <https://doi.org/10.1016/j.cell.2004.09.011>
- Stanfield, O. a. (1987). Introduction to single channel recording. In G. P. Standen NB, Whitaker MJ (Ed.), *The Plymouth workshop handbook* (pp. 63-82). The Company of Biologists Limited.
- Stanika, R. I., Flucher, B. E., & Obermair, G. J. (2015). Regulation of Postsynaptic Stability by the L-type Calcium Channel CaV1.3 and its Interaction with PDZ Proteins. *Curr Mol Pharmacol*, *8*(1), 95-101. <https://www.ncbi.nlm.nih.gov/pubmed/25966696>
- Stanika, R., Campiglio, M., Pinggera, A., Lee, A., Striessnig, J., Flucher, B. E., & Obermair, G. J. (2016). Splice variants of the CaV1.3 L-type calcium channel regulate dendritic spine morphology. *Sci Rep*, *6*, 34528. <https://doi.org/10.1038/srep34528>
- Stotz, S. C., Hamid, J., Spaetgens, R. L., Jarvis, S. E., & Zamponi, G. W. (2000). Fast inactivation of voltage-dependent calcium channels. A hinged-lid mechanism? *J Biol Chem*, *275*(32), 24575-24582. <https://doi.org/10.1074/jbc.M000399200>
- Stotz, S. C., Jarvis, S. E., & Zamponi, G. W. (2004). Functional roles of cytoplasmic loops and pore lining transmembrane helices in the voltage-dependent inactivation of HVA calcium channels. *J Physiol*, *554*(Pt 2), 263-273. <https://doi.org/10.1113/jphysiol.2003.047068>
- Striessnig, J. (1999). Pharmacology, structure and function of cardiac L-type Ca(2+) channels. *Cell Physiol Biochem*, *9*(4-5), 242-269. <https://doi.org/10.1159/000016320>
- Striessnig, J., Hoda, J. C., Koschak, A., Zaghetto, F., Mullner, C., Sinnegger-Brauns, M. J., Wild, C., Watschinger, K., Trockenbacher, A., & Pelster, G. (2004). L-type Ca²⁺ channels in Ca²⁺ channelopathies. *Biochem Biophys Res Commun*, *322*(4), 1341-1346. <https://doi.org/10.1016/j.bbrc.2004.08.039>
- Striessnig, J., Koschak, A., Sinnegger-Brauns, M. J., Hetzenauer, A., Nguyen, N. K., Busquet, P., Pelster, G., & Singewald, N. (2006). Role of voltage-gated L-type Ca²⁺ channel isoforms for brain function. *Biochem Soc Trans*, *34*(Pt 5), 903-909. <https://doi.org/10.1042/BST0340903>
- Striessnig, J., Bolz, H. J., & Koschak, A. (2010). Channelopathies in Cav1.1, Cav1.3, and Cav1.4 voltage-gated L-type Ca²⁺ channels. *Pflugers Arch*, *460*(2), 361-374. <https://doi.org/10.1007/s00424-010-0800-x>
- Striessnig, J. (2021). Voltage-Gated Ca(2+)-Channel alpha1-Subunit de novo Missense Mutations: Gain or Loss of Function - Implications for Potential Therapies. *Front Synaptic Neurosci*, *13*, 634760. <https://doi.org/10.3389/fnsyn.2021.634760>
- Striessnig, J., Nakao, A., & Mori, Y. (2022). Voltage-Gated Ca²⁺ Channels. Lessons from Knockout and Knock-in Mice. In G. W. Zamponi & N. Weiss (Eds.), *Voltage-Gated Calcium Channels* (pp. 255-357). Springer International Publishing. https://doi.org/10.1007/978-3-031-08881-0_11

- Strom, T. M., Nyakatura, G., Apfelstedt-Sylla, E., Hellebrand, H., Lorenz, B., Weber, B. H., Wutz, K., Gutwillinger, N., Ruther, K., Drescher, B., Sauer, C., Zrenner, E., Meitinger, T., Rosenthal, A., & Meindl, A. (1998). An L-type calcium-channel gene mutated in incomplete X-linked congenital stationary night blindness. *Nat Genet*, *19*(3), 260-263. <https://doi.org/10.1038/940>
- Sumi, M., Kiuchi, K., Ishikawa, T., Ishii, A., Hagiwara, M., Nagatsu, T., & Hidaka, H. (1991). The newly synthesized selective Ca²⁺/calmodulin dependent protein kinase II inhibitor KN-93 reduces dopamine contents in PC12h cells. *Biochem Biophys Res Commun*, *181*(3), 968-975. [https://doi.org/10.1016/0006-291x\(91\)92031-e](https://doi.org/10.1016/0006-291x(91)92031-e)
- Sun, L., Tong, C. K., Morgenstern, T. J., Zhou, H., Yang, G., & Colecraft, H. M. (2022). Targeted ubiquitination of sensory neuron calcium channels reduces the development of neuropathic pain. *Proc Natl Acad Sci U S A*, *119*(20), e2118129119. <https://doi.org/10.1073/pnas.2118129119>
- Sun, P., Enslin, H., Myung, P. S., & Maurer, R. A. (1994). Differential activation of CREB by Ca²⁺/calmodulin-dependent protein kinases type II and type IV involves phosphorylation of a site that negatively regulates activity. *Genes Dev*, *8*(21), 2527-2539. <https://doi.org/10.1101/gad.8.21.2527>
- Surmeier, D. J., Guzman, J. N., & Sanchez-Padilla, J. (2010). Calcium, cellular aging, and selective neuronal vulnerability in Parkinson's disease. *Cell Calcium*, *47*(2), 175-182. <https://doi.org/10.1016/j.ceca.2009.12.003>
- Tajada, S., Moreno, C. M., O'Dwyer, S., Woods, S., Sato, D., Navedo, M. F., & Santana, L. F. (2017). Distance constraints on activation of TRPV4 channels by AKAP150-bound PKC α in arterial myocytes. *J Gen Physiol*, *149*(6), 639-659. <https://doi.org/10.1085/jgp.201611709>
- Takimoto, K., Li, D., Nerbonne, J. M., & Levitan, E. S. (1997). Distribution, splicing and glucocorticoid-induced expression of cardiac α 1C and α 1D voltage-gated Ca²⁺ channel mRNAs. *J Mol Cell Cardiol*, *29*(11), 3035-3042. <https://doi.org/10.1006/jmcc.1997.0532>
- Tan, B. Z., Jiang, F., Tan, M. Y., Yu, D., Huang, H., Shen, Y., & Soong, T. W. (2011). Functional characterization of alternative splicing in the C terminus of L-type CaV1.3 channels. *J Biol Chem*, *286*(49), 42725-42735. <https://doi.org/10.1074/jbc.M111.265207>
- Tan, G. C., Negro, G., Pinggera, A., Tizen Laim, N. M. S., Mohamed Rose, I., Ceral, J., Ryska, A., Chin, L. K., Kamaruddin, N. A., Mohd Mokhtar, N., AR, A. J., Sukor, N., Solar, M., Striessnig, J., Brown, M. J., & Azizan, E. A. (2017). Aldosterone-Producing Adenomas: Histopathology-Genotype Correlation and Identification of a Novel CACNA1D Mutation. *Hypertension*, *70*(1), 129-136. <https://doi.org/10.1161/HYPERTENSIONAHA.117.09057>
- Tanabe, T., Takeshima, H., Mikami, A., Flockerzi, V., Takahashi, H., Kangawa, K., Kojima, M., Matsuo, H., Hirose, T., & Numa, S. (1987). Primary structure of the receptor for calcium channel blockers from skeletal muscle. *Nature*, *328*(6128), 313-318. <https://doi.org/10.1038/328313a0>
- Tang, L., Gamal El-Din, T. M., Swanson, T. M., Pryde, D. C., Scheuer, T., Zheng, N., & Catterall, W. A. (2016). Structural basis for inhibition of a voltage-gated Ca(2+) channel by Ca(2+) antagonist drugs. *Nature*, *537*(7618), 117-121. <https://doi.org/10.1038/nature19102>

- Tanskanen, A. J., Greenstein, J. L., O'Rourke, B., & Winslow, R. L. (2005). The role of stochastic and modal gating of cardiac L-type Ca²⁺ channels on early after-depolarizations. *Biophys J*, *88*(1), 85-95. <https://doi.org/10.1529/biophysj.104.051508>
- Thomas, G., Chung, M., & Cohen, C. J. (1985). A dihydropyridine (Bay k 8644) that enhances calcium currents in guinea pig and calf myocardial cells. A new type of positive inotropic agent. *Circ Res*, *56*(1), 87-96. <https://doi.org/10.1161/01.RES.56.1.87>
- Tokumitsu, H., Chijiwa, T., Hagiwara, M., Mizutani, A., Terasawa, M., & Hidaka, H. (1990). KN-62, 1-[N,O-bis(5-isoquinolinesulfonyl)-N-methyl-L-tyrosyl]-4-phenylpiperazine, a specific inhibitor of Ca²⁺/calmodulin-dependent protein kinase II. *J Biol Chem*, *265*(8), 4315-4320. <https://www.ncbi.nlm.nih.gov/pubmed/2155222>
- Török, F., Tezcan, K., Filippini, L., Fernandez-Quintero, M. L., Zanetti, L., Liedl, K. R., Drexel, R. S., Striessnig, J., & Ortner, N. J. (2022). Germline de novo variant F747S extends the phenotypic spectrum of CACNA1D Ca²⁺ channelopathies. *Hum Mol Genet*. <https://doi.org/10.1093/hmg/ddac248>
- Toyoda, F., Mesirca, P., Dubel, S., Ding, W. G., Striessnig, J., Mangoni, M. E., & Matsuura, H. (2017). Ca(V)_{1.3} L-type Ca²⁺ channel contributes to the heartbeat by generating a dihydropyridine-sensitive persistent Na⁺ current. *Sci Rep*, *7*(1), 7869. <https://doi.org/10.1038/s41598-017-08191-8>
- Van Petegem, F., Clark, K. A., Chatelain, F. C., & Minor, D. L., Jr. (2004). Structure of a complex between a voltage-gated calcium channel beta-subunit and an alpha-subunit domain. *Nature*, *429*(6992), 671-675. <https://doi.org/10.1038/nature02588>
- Vandael, D. H., Mahapatra, S., Calorio, C., Marcantoni, A., & Carbone, E. (2013). Cav1.3 and Cav1.2 channels of adrenal chromaffin cells: emerging views on cAMP/cGMP-mediated phosphorylation and role in pacemaking. *Biochim Biophys Acta*, *1828*(7), 1608-1618. <https://doi.org/10.1016/j.bbamem.2012.11.013>
- Veitinger. (2011). *The Patch-Clamp Technique* <https://www.leica-microsystems.com/science-lab/life-science/the-patch-clamp-technique/>
- Verkerk, A. O., van Borren, M. M., Peters, R. J., Broekhuis, E., Lam, K. Y., Coronel, R., de Bakker, J. M., Tan, H. L., & Wilders, R. (2007). Single cells isolated from human sinoatrial node: action potentials and numerical reconstruction of pacemaker current. *Annu Int Conf IEEE Eng Med Biol Soc*, *2007*, 904-907. <https://doi.org/10.1109/IEMBS.2007.4352437>
- Vivas, O., Moreno, C. M., Santana, L. F., & Hille, B. (2017). Proximal clustering between BK and Ca(V)_{1.3} channels promotes functional coupling and BK channel activation at low voltage. *Elife*, *6*. <https://doi.org/10.7554/eLife.28029>
- Wang, Q. M., Xu, Y. Y., Liu, S., & Ma, Z. G. (2017). Isradipine attenuates MPTP-induced dopamine neuron degeneration by inhibiting up-regulation of L-type calcium channels and iron accumulation in the substantia nigra of mice. *Oncotarget*, *8*(29), 47284-47295. <https://doi.org/10.18632/oncotarget.17618>
- West, J. W., Patton, D. E., Scheuer, T., Wang, Y., Goldin, A. L., & Catterall, W. A. (1992). A cluster of hydrophobic amino acid residues required for fast Na⁺-channel inactivation. *Proc Natl Acad Sci U S A*, *89*(22), 10910-10914. <https://doi.org/10.1073/pnas.89.22.10910>

- Wilders, R., Jongsma, H. J., & van Ginneken, A. C. (1991). Pacemaker activity of the rabbit sinoatrial node. A comparison of mathematical models. *Biophys J*, *60*(5), 1202-1216. [https://doi.org/10.1016/S0006-3495\(91\)82155-5](https://doi.org/10.1016/S0006-3495(91)82155-5)
- Wilders, R. (2007). Computer modelling of the sinoatrial node. *Med Biol Eng Comput*, *45*(2), 189-207. <https://doi.org/10.1007/s11517-006-0127-0>
- Williams, M. E., Marubio, L. M., Deal, C. R., Hans, M., Brust, P. F., Philipson, L. H., Miller, R. J., Johnson, E. C., Harpold, M. M., & Ellis, S. B. (1994). Structure and functional characterization of neuronal alpha 1E calcium channel subtypes. *J Biol Chem*, *269*(35), 22347-22357. <https://www.ncbi.nlm.nih.gov/pubmed/8071363>
- Wirtz, S., & Herzig, S. (2004). Molecular mechanisms of vasoselectivity of the 1,4-dihydropyridine lercanidipine. *Br J Pharmacol*, *142*(2), 275-284. <https://doi.org/10.1038/sj.bjp.0705786>
- Xu, W., & Lipscombe, D. (2001). Neuronal Ca(V)1.3alpha(1) L-type channels activate at relatively hyperpolarized membrane potentials and are incompletely inhibited by dihydropyridines. *J Neurosci*, *21*(16), 5944-5951. <https://doi.org/10.1523/JNEUROSCI.21-16-05944.2001>
- Yaney, G. C., Wheeler, M. B., Wei, X., Perez-Reyes, E., Birnbaumer, L., Boyd, A. E., 3rd, & Moss, L. G. (1992). Cloning of a novel alpha 1-subunit of the voltage-dependent calcium channel from the beta-cell. *Mol Endocrinol*, *6*(12), 2143-2152. <https://doi.org/10.1210/mend.6.12.1337146>
- Yang, G., Shi, Y., Yu, J., Li, Y., Yu, L., Welling, A., Hofmann, F., Striessnig, J., Juntti-Berggren, L., Berggren, P. O., & Yang, S. N. (2015). CaV1.2 and CaV1.3 channel hyperactivation in mouse islet beta cells exposed to type 1 diabetic serum. *Cell Mol Life Sci*, *72*(6), 1197-1207. <https://doi.org/10.1007/s00018-014-1737-6>
- Yang, J., Ellinor, P. T., Sather, W. A., Zhang, J. F., & Tsien, R. W. (1993). Molecular determinants of Ca²⁺ selectivity and ion permeation in L-type Ca²⁺ channels. *Nature*, *366*(6451), 158-161. <https://doi.org/10.1038/366158a0>
- Yang, P. S., Alseikhan, B. A., Hiel, H., Grant, L., Mori, M. X., Yang, W., Fuchs, P. A., & Yue, D. T. (2006). Switching of Ca²⁺-dependent inactivation of Ca(v)1.3 channels by calcium binding proteins of auditory hair cells. *J Neurosci*, *26*(42), 10677-10689. <https://doi.org/10.1523/JNEUROSCI.3236-06.2006>
- Yang, T., & Poovaiah, B. W. (2003). Calcium/calmodulin-mediated signal network in plants. *Trends Plant Sci*, *8*(10), 505-512. <https://doi.org/10.1016/j.tplants.2003.09.004>
- Yao, X., Gao, S., & Yan, N. (2022). Structural basis for pore blockade of human voltage-gated calcium channel Ca(v)1.3 by motion sickness drug cinnarizine. *Cell Res*, *32*(10), 946-948. <https://doi.org/10.1038/s41422-022-00663-5>
- Yokokura, H., Okada, Y., Terada, O., & Hidaka, H. (1996). HMN-709, a chlorobenzenesulfonamide derivative, is a new membrane-permeable calmodulin antagonist. *Jpn J Pharmacol*, *72*(2), 127-135. <https://doi.org/10.1254/jjp.72.127>
- Yuan, G., Cao, C., Cao, D., Li, B., Li, X., Li, H., Shen, H., Wang, Z., & Chen, G. (2023). Receptor-interacting protein 3-phosphorylated Ca(2+) /calmodulin-dependent protein kinase II and mixed lineage kinase domain-like protein mediate intracerebral hemorrhage-induced neuronal necroptosis. *J Neurochem*, *164*(1), 94-114. <https://doi.org/10.1111/jnc.15731>

-
- Zamponi, G. W., An, M. T., & Zamponi, G. W. (2005). Voltage-dependent inactivation of voltage gated calcium channels. *Voltage-Gated Calcium Channels*, 194-204.
- Zamponi, G. W., Striessnig, J., Koschak, A., & Dolphin, A. C. (2015). The Physiology, Pathology, and Pharmacology of Voltage-Gated Calcium Channels and Their Future Therapeutic Potential. *Pharmacol Rev*, 67(4), 821-870. <https://doi.org/10.1124/pr.114.009654>
- Zhang, H., Maximov, A., Fu, Y., Xu, F., Tang, T. S., Tkatch, T., Surmeier, D. J., & Bezprozvanny, I. (2005). Association of CaV1.3 L-type calcium channels with Shank. *J Neurosci*, 25(5), 1037-1049. <https://doi.org/10.1523/JNEUROSCI.4554-04.2005>
- Zhang, Z., Xu, Y., Song, H., Rodriguez, J., Tuteja, D., Namkung, Y., Shin, H. S., & Chiamvimonvat, N. (2002). Functional Roles of Ca(v)1.3 (alpha(1D)) calcium channel in sinoatrial nodes: insight gained using gene-targeted null mutant mice. *Circ Res*, 90(9), 981-987. <https://doi.org/10.1161/01.RES.0000018003.14304.E2>
- Zuhlke, R. D., Pitt, G. S., Deisseroth, K., Tsien, R. W., & Reuter, H. (1999). Calmodulin supports both inactivation and facilitation of L-type calcium channels. *Nature*, 399(6732), 159-162. <https://doi.org/10.1038/20200>

Acknowledgements

Scientific achievement is never one person's accomplishment. Therefore I would like to express my sincere gratitude to everyone who supported me throughout this thesis.

First, I would like to sincerely thank my supervisor PD Dr. Jan Matthes for being able to conduct my thesis in his research group and his guidance throughout this journey. I am grateful for his invaluable advice, continuous support, and his trust in me and my work.

My sincere gratitude also goes to Prof. Dr. Tatiana Korotkova and Prof. Dr. Dirk Isbrandt for being my tutors and evaluating this thesis. I am very grateful for the knowledge and expertise they generously provided in our encouraging meetings. Special thanks goes to Prof. Dr. Dirk Isbrandt for allowing me to temporarily use the equipment in his research group, and to Dr. Malte Stockebrand and Marina Velichkova for assisting me herein.

I am very grateful to Prof. Dr. Heike Endepols for being my mentor. She instantly and patiently guided me whenever I needed personal or professional support.

I would like to extend my gratitude to our collaborators. I thank Prof. Dr. Jörg Striessnig and Dr. Nadine Ortner for their interest and trust in my single-channel patch-clamp abilities. It has been inspiring to work with such distinguished experts in the field of disease-associated Cav1.3 mutations. I also thank Dr. Manu Ben-Johny for sharing his expertise in collaborating on the FRET experiments.

Special thanks go to our former postdocs. I sincerely thank Dr. Elza Kuzmenkina for arousing my interest in Cav1.3 and her biophysical expertise, and Dr. Patrick Despang for scientific discussions and sharing his knowledge on whole-cell patch-clamp.

I also sincerely thank my current lab members Cora Fried for her indispensable technical assistance in molecular biological techniques, and Nour Katnahji for being my fellow PhD student and friend, for better or for worse.

Last, but definitely not least, my heartfelt gratitude goes to my loved ones for their continuous support, keeping me harmonious and enduring lectures on voltage-gated calcium channels.

Thank you!

Sarah Salamon 

Eidesstattliche Erklärung

Hiermit versichere ich an Eides statt, dass ich die vorliegende Dissertationsschrift selbstständig und ohne die Benutzung anderer als der angegebenen Hilfsmittel angefertigt habe. Alle Stellen - einschließlich Tabellen, Karten und Abbildungen -, die wörtlich oder sinngemäß aus veröffentlichten und nicht veröffentlichten anderen Werken im Wortlaut oder dem Sinn nach entnommen sind, sind in jedem Einzelfall als Entlehnung kenntlich gemacht. Ich versichere an Eides statt, dass diese Dissertationsschrift noch keiner anderen Fakultät oder Universität zur Prüfung vorgelegen hat; dass sie - abgesehen von unten angegebenen Teilpublikationen - noch nicht veröffentlicht worden ist sowie, dass ich eine solche Veröffentlichung vor Abschluss der Promotion nicht ohne Genehmigung der/des Vorsitzenden des IPHS-Promotionsausschusses vornehmen werde. Die Bestimmungen dieser Ordnung sind mir bekannt. Die von mir vorgelegte Dissertation ist von PD Dr. med. Jan Matthes betreut worden.

Darüber hinaus erkläre ich hiermit, dass ich die Ordnung zur Sicherung guter wissenschaftlicher Praxis und zum Umgang mit wissenschaftlichem Fehlverhalten der Universität zu Köln gelesen und sie bei der Durchführung der Dissertation beachtet habe und verpflichte mich hiermit, die dort genannten Vorgaben bei allen wissenschaftlichen Tätigkeiten zu beachten und umzusetzen.

Übersicht der Publikationen: *Siehe nachfolgende Seite.*

Ich versichere, dass ich alle Angaben wahrheitsgemäß nach bestem Wissen und Gewissen gemacht habe und verpflichte mich, jedmögliche, die obigen Angaben betreffenden Veränderungen, dem IPHS-Promotionsausschuss unverzüglich mitzuteilen.

Köln, den 04.10.2023



Sarah Salamon

Eidesstattliche Erklärung – Publikationen

Übersicht der Teilpublikationen:

Salamon S., Kuzmenkina E., Fried C., Matthes J. EF-hand phosphorylation site S1475 modulates Cav1.3 whole-cell and single-channel currents. Under revision. *The Journal of Physiology*.

Salamon S., Török F, Zanetti L, Ortner N.J., Striessnig J., Matthes J. Cav1.3 missense variant F747S induces a novel kind of gating cooperativity. To be submitted to *Neurobiology of Disease*.

Teilpublikationen im Rahmen von Konferenzbeiträgen:

Salamon S., Kuzmenkina E., Fried C., Matthes J. (2022) Cav1.3 whole-cell current modulation involving EF-hand phosphorylation site S1475. 66th Biophysical Society Annual Meeting, San Francisco, USA

Salamon S., Kuzmenkina E., Fried C., Matthes J. (2022) EF-hand phosphorylation site S1475 modulates Cav1.3 whole-cell and single-channel currents. 4th European Calcium Channel Conference, Alpbach, Austria

Salamon S., Török F., Ortner N., Striessnig J., Matthes J. (2022) Neurodevelopmental disorder associated Cav1.3 mutations lead to gain-of-function single-channel gating. 4th European Calcium Channel Conference, Alpbach, Austria

Salamon S., Kuzmenkina E., Fried C., Matthes J. (2022) Alteration of EF-hand phosphorylation site affects Cav1.3 calcium channel whole-cell currents. 7th German Pharm-Tox Summit, Bonn, Germany

Salamon S., Kuzmenkina E., Fried C., Matthes J. (2019) Influence of EF-hand phosphorylation on biophysical gating properties of Cav1.3 voltage-gated calcium channels. 4th German Pharm-Tox Summit, Stuttgart, Germany

Köln, den 04.10.2023



Sarah Salamon